Exploring the high-energy transient sky with ANTARES and KM3NeT neutrino telescopes

Author:
Angela Zegarelli

Supervisors:
Prof. Antonio Capone
Prof.ssa Silvia Celli

Coordinator:
Prof. Nicola Vittorio

Vice-Coordinator:
Prof. Francesco Piacentini

A thesis submitted in fulfilment
of the requirements for the degree of
Doctor of Philosophy

Department of Physics
PhD course in Astronomy, Astrophysics and Space Science
Faculty of Mathematical, Physical and Natural Sciences

Academic Year 2022-2023 (XXXV cycle)

Exploring the high-energy transient sky with ANTARES and KM3NeT neutrino telescopes, © February 2023

Author:
Angela Zegarelli

Supervisors:
Prof. Antonio Capone
Prof.ssa Silvia Celli

Institute:
Tor Vergata University, Rome, Italy Sapienza University, Rome, Italy

Ai miei genitori, che mi hanno sempre lasciato libera di volare senza costrizioni e condizionamenti.
A mio fratello, da sempre mio discreto sostenitore.
Alla piccola Sofia, che ci ha riempito il cuore e colorato le nostre vite.

A Michael, mio fulcro, e alla nostra forza.

A Donatella, sempre al mio fianco in questi anni.

"Remember to look up at the stars and not down at your feet. Try to make sense of what you see and wonder about what makes the universe exist. Be curious. And however difficult life may seem, there is always something you can do and succeed at. It matters that you don't just give up."

Stephen Hawking

"The more I want to get something done, the less I call it work."

Richard Bach

CONTENTS

ABSTRACT

With the discovery, in 2013, of a diffuse flux of astrophysical neutrinos (νs), high-energy neutrino astronomy entered a new era. Since then, in the last few years, several associations between active galactic nuclei and high-energy νs have emerged. Despite the exploration of synergies between different instruments, we still are not able to explain the origin of the diffuse neutrino flux. High-energy astrophysical νs originate in processes involving very high-energy primary hadrons, through collisions of Cosmic Rays (CRs) with high-density matter and/or radiation fields, where both νs and gamma (γ) rays are released. Among those, νs are peculiar particles because they can cross the Universe preserving the directional information about their production site, allowing to unambiguously identify the most efficient sites of particle acceleration. Gamma-Ray Bursts (GRBs) have long been predicted as promising candidates for emitting νs, as hadronic acceleration mechanisms have long been believed to occur inside their relativistic jets. In such sources, the neutrino energy depends on the site of the jet region where acceleration takes place: multi-GeV νs are expected to be produced as a result of the dissipation of the jet kinetic energy through nuclear collisions occurring around the photosphere, below which the jet is still optically thick to high-energy radiation (*inelastic collisional scenario*); at higher distance from the GRB central engine, TeV-PeV νs can be produced at shocks inside the jet between shells of plasma during ultra-high-energy CR acceleration (*internal shock scenario*).

So far, neutrino emissions in GRBs from the former scenario have been poorly investigated from an experimental point of view. In the present thesis, I discuss the prospects for identifying νs produced in such collisionally heated GRBs with the large-volume ν telescopes KM3NeT and IceCube, including their low-energy extensions, KM3NeT/ORCA and DeepCore, respectively. To this aim, I evaluate the detection sensitivity for νs from both individual and stacked searches for coincident GRBs. As a result of my analysis, I find that it is possible to detect a significant flux of νs from a stacking sample of ~ 900 long GRBs (i.e., with prompt γ-ray emission lasting more than 2 seconds) already with DeepCore and KM3NeT/ORCA. The detection sensitivity increases with the inclusion of data from the high-energy telescopes, IceCube and KM3NeT/ARCA, respectively.

Acceleration at internal shocks in GRBs might, in turn, be responsible for the multi-TeV energies required to contribute to the observed diffuse astrophysical ν flux. I investigate this possibility through a search for upward going muon neutrinos in ANTARES data in spatial and temporal coincidence with 784 GRBs occurred from 2007 to 2017. For each GRB, I computed the expected ν flux by the model quantifying, for the first time in this kind of analysis, the impact of the lack of knowledge of source redshifts and other intrinsic parameters of the emission mechanism. For the selected sources, I analyse ANTARES data by maximising the discovery probability of the stacking sample through an extended maximum-likelihood strategy. Although no neutrino event passed the quality cuts set by

the optimisation procedure, the 90% confidence level upper limits (with their uncertainty), estimated according to the model, are found to constrain the contribution of GRBs to the observed diffuse astrophysical ν flux around 100 TeV to less than 10%.

To help identifying and characterising the cosmic sources in the selection of the most promising ones contributing to this flux, multimessenger observations are crucial. In particular, real-time ν alerts for triggering prompt multiwavelength follow-ups constitute a great thrust forward the detection of transient sources; in fact, Cherenkov-based ν telescopes, being characterised by a field of view comprising the whole sky, are ideally suited to detect and inform in very short time other instruments about interesting events. KM3NeT is moving towards this direction, being progressively fully integrating into the multimessenger global network. I here present the online pipeline developed for the real-time reconstruction of events in KM3NeT/ARCA, which is optimised for the detection of TeV-PeV neutrinos. I show that, for the current operational detector (21 detection lines), the response time of the online system is on average ~ 4 seconds, a short enough timescale to allow pointing instruments to perform quasi-simultaneous observations. Fast analyses performed with events reconstructed in real-time can significantly increase the discovery potential of transient cosmic accelerators in the sky.

PUBLICATIONS

This thesis is based on the original results obtained by the author. Part of them have been already published in several conference proceedings (not here reported) and in the following peer-reviewed journal papers:

- A. **Zegarelli**, S. Celli, A. Capone, S. Gagliardini, and I. Di Palma, *Detection prospects for multi-GeV neutrinos from collisionally heated GRBs*, Phys. Rev. D 105.8, 083023 (2022), DOI: 10.1103/PhysRevD.105.083023
- A. Albert et al. (**A. Zegarelli as corresponding author**), *Constraining the contribution of Gamma-Ray Bursts to the high-energy diffuse neutrino flux with 10 yr of ANTARES data*, MNRAS 500.4 (2021), DOI: 10.1093/mnras/staa3503

The author has also primarily contributed to further studies not discussed in the thesis:

- M. Fasano, S. Celli, D. Guetta, A. Capone, A. **Zegarelli**, and I. Di Palma. *Estimating the neutrino flux from choked gamma-ray bursts*, JCAP 09, 044 (2021), DOI: 10.1088/1475-7516/2021/09/044
- S. Gagliardini, S. Celli, D. Guetta, A. **Zegarelli**, A. Capone, S. Campion, and I. Di Palma. *On the hadronic origin of the TeV radiation from GRB 190114C*, submitted, arXiv:2209.01940

The author is as a member of the ANTARES/KM3NeT Collaborations and THESEUS[1] Collaboration, and is co-author of the following peer-reviewed papers:

- ANTARES and HAWC Collaborations, *Search for Gamma-Ray and Neutrino Coincidences Using HAWC and ANTARES Data*, ApJ 944, 166 (2023): DOI: 10.3847/1538-4357/acafdd
- KM3NeT Collaboration, *KM3NeT Broadcast Optical Data Transport System*, JINST 18, T02001 (2023), DOI: 10.1088/1748-0221/18/02/T02001
- KM3NeT Collaboration. *Limits on the nuclearite flux using the ANTARES neutrino telescope*, JCAP 01, 012 (2023), DOI: 10.1088/1475-7516/2023/01/012
- KM3NeT Collaboration. *Nanobeacon: A time calibration device for the KM3NeT neutrino telescope*, Nuclear Instruments and Methods in Physics Research A 1040, 167132 (2022) DOI: 10.1016/j.nima.2022.167132
- ANTARES Collaboration, IceCube Collaboration, Pierre Auger Collaboration, and Telescope Array Collaboration. *Search for Spatial Correlations of Neutrinos with Ultra-high-energy Cosmic Rays*, ApJ 934, 164 (2022), DOI: 10.3847/1538-4357/ac6def
- KM3NeT Collaboration. *The KM3NeT multi-PMT optical module*, JINST 17, P07038 (2022), P07038, DOI: 10.1088/1748-0221/17/07/P07038

1 Transient High-Energy Sky and Early Universe Surveyor (THESEUS) is a space telescope mission proposal by the European Space Agency that would study gamma-ray bursts and X-rays: `https://www.isdc.unige.ch/theseus/`.

- ANTARES Collaboration. *Search for non-standard neutrino interactions with 10 years of ANTARES data*, Journal of High Energy Physics 7, 48 (2022), DOI: 10.1007/JHEP07(2022)048

- ANTARES Collaboration. *Search for magnetic monopoles with ten years of the ANTARES neutrino telescope*, Journal of High Energy Astrophysics 34 (2022), DOI: 10.1016/j.jheap.2022.03.001

- ANTARES Collaboration. *Search for secluded dark matter towards the Galactic Centre with the ANTARES neutrino telescope*, JCAP 06, 028 (2022), DOI: 10.1088/1475-7516/2022/06/028

- ANTARES Collaboration. *Search for solar atmospheric neutrinos with the ANTARES neutrino telescope*, JCAP 06, 018 (2022), DOI: 10.1088/1475-7516/2022/06/018

- KM3NeT Collaboration. *Combined sensitivity of JUNO and KM3NeT/ORCA to the neutrino mass ordering*, Journal of High Energy Physics 03, 55 (2022), DOI: 10.1007/JHEP03(2022)055

- KM3NeT Collaboration. *Determining the neutrino mass ordering and oscillation parameters with KM3NeT/ORCA*, European Physical Journal C 82, 26 (2022), DOI: 10.1140/epjc/s10052-021-09893-0

- R. Ciolfi et al. *Multi-messenger astrophysics with THESEUS in the 2030s*, Experimental Astronomy 52 (2021), DOI: 10.1007/s10686-021-09795-9

- KM3NeT Collaboration. *Sensitivity to light sterile neutrino mixing parameters with KM3NeT/ORCA*, Journal of High Energy Physics 10, 180 (2021), DOI: 10.1007/JHEP10(2021)180

- ANTARES Collaboration. *Search for Neutrinos from the Tidal Disruption Events AT2019dsg and AT2019fdr with the ANTARES Telescope*, ApJ 920, 50 (2021), DOI: 10.3847/1538-4357/ac16d6

- ANTARES Collaboration. *Measurement of the atmospheric ν_e and ν_μ energy spectra with the ANTARES neutrino telescope*, Physics Letters B 816, 136228 (2021), DOI: 10.1016/j.physletb.2021.136228

- KM3NeT Collaboration. *The KM3NeT potential for the next core-collapse supernova observation with neutrinos*, European Physical Journal C 81, 445 (2021), DOI: 10.1140/epjc/s10052-021-09187-5

- ANTARES Collaboration and S. Buson. *ANTARES Search for Point Sources of Neutrinos Using Astrophysical Catalogs: A Likelihood Analysis*, ApJ 911, 48 (2021), DOI: 10.3847/1538-4357/abe53c

- ANTARES Collaboration. *ANTARES upper limits on the multi-TeV neutrino emission from the GRBs detected by IACTs*, JCAP 3, 092 (2021), DOI: 10.1088/1475-7516/2021/03/092

- ANTARES Collaboration. *Monte Carlo simulations for the ANTARES underwater neutrino telescope*, JCAP 1, 064 (2021), DOI: 10.1088/1475-7516/2021/01/064

- ANTARES Collaboration. *Observation of the cosmic ray shadow of the Sun with the ANTARES neutrino telescope*, Phys. Rev. D 102, 122007 (2020), DOI: 10.1103/PhysRevD.102.122007

- KM3NeT Collaboration. *Deep-sea deployment of the KM3NeT neutrino telescope detection units by self-unrolling*, JINST 15 (2020), DOI: 10.1088/1748-0221/15/11/ P11027
- KM3NeT Collaboration. *gSeaGen: The KM3NeT GENIE-based code for neutrino telescopes*, Computer Physics Communications 256, 107477 (2020), DOI: 10.1016/j.cpc.2020.107477
- KM3NeT Collaboration. *The Control Unit of the KM3NeT Data Acquisition System*, Computer Physics Communications 256, 107433 (2020), DOI: 10.1016/j.cpc.2020.107433
- ANTARES Collaboration and Icecube Collaboration. *Combined search for neutrinos from dark matter self-annihilation in the Galactic Center with ANTARES and IceCube*, Phys. Rev. D 102, 082002 (2020), DOI: 10.1103/PhysRevD.102.082002
- KM3NeT Collaboration. *Event reconstruction for KM3NeT/ORCA using convolutional neural networks*, JINST 15 (2020), DOI: 10.1088/1748-0221/15/10/P10005
- ANTARES Collaboration. *Search for dark matter towards the Galactic Centre with 11 years of ANTARES data*, Physics Letters B 805, 135439 (2020), DOI: 10.1016/j.physletb.2020.135439
- ANTARES Collaboration. *Search for neutrino counterparts of gravitational-wave events detected by LIGO and Virgo during run O2 with the ANTARES telescope*, European Physical Journal C 80, 487 (2020), DOI: 10.1140/epjc/s10052-020-8015-6
- ANTARES Collaboration and Icecube Collaboration. *ANTARES and IceCube Combined Search for Neutrino Point-like and Extended Sources in the Southern Sky*, ApJ 892.2, 92 (2020), p. 92. DOI:10.3847/1538-4357/ab7afb
- KM3NeT Collaboration. *Dependence of atmospheric muon flux on seawater depth measured with the first KM3NeT detection units*, European Physical Journal C 80, 99 (2020), DOI: 10.1140/epjc/s10052-020-7629-z
- KM3NeT Collaboration. *KM3NeT front-end and readout electronics system: hardware, firmware, and software*, Journal of Astronomical Telescopes, Instruments, and Systems 5, 046001 (2019), DOI: 10.1117/1.JATIS.5.4.046001

PREFACE

This thesis explores several topics in the context of high-energy neutrino astronomy. In particular, it is focused on cosmic neutrinos, produced as a result of cosmic ray hadronuclear and photohadronic interactions with matter and photon fields, respectively.

The thesis is organised as follows:

Chapter 1 provides background information relevant to understand my field of research. In particular, it aims at introducing the several cosmic messengers used to explore the Universe, within the framework of the new frontiers provided by the *multimessenger astronomy*: cosmic rays, photons, neutrinos, and gravitational waves. Their characteristics, their propagation to the Earth, and the physical processes responsible for their production are outlined. Moreover, the strong connection between cosmic messengers is highlighted, in order to demonstrate the importance of common observational strategies between neutrino telescopes, cosmic-ray observatories, gamma-ray instruments, and interferometers for gravitational waves detection.

Chapter 2 is dedicated to neutrinos, the main messenger around which this thesis is developed. Their properties, as well as all aspects related to the detection of high-energy neutrinos are explained. In particular, the chapter pays special attention to ANTARES and KM3NeT detectors in the Mediterranean Sea, being the author part of the two collaborations. ANTARES was dismantled at the beginning of 2022; KM3NeT is under construction and currently operating with a partial detector configuration. Technical descriptions and expected performances of the two detectors are provided.

Chapter 3 focusses on one of the most promising sources to be studied in the framework previously described in the thesis, namely Gamma-Ray Bursts (GRBs). These extragalactic sources can in principle explain particle acceleration of cosmic rays to ultra-high-energies, from whose interactions high-energy neutrinos come from. After a general description of GRBs and of the physical mechanisms responsible for gamma-ray and possible neutrino emission, the chapter presents the result of a study carried out by the author, aiming at evaluating the detection prospects for KM3NeT (in its full detector configuration) of $\sim$GeV neutrinos, expected to be produced in one of the several scenarios capable of explaining GRB emission (i.e., via inelastic collisions between protons and neutrinos occurring around the photosphere of the GRB jet). In addition, the author also provides estimates for the current IceCube detector.

Chapter 4 describes the procedure and results of an analysis performed by the author on behalf of the ANTARES Collaboration, searching for temporal and spatial correlations between TeV-PeV neutrinos and GRBs using 10 years of ANTARES data.

Here, an alternative scenario (internal shocks between plasma of shells in the jet) with respect to the one investigated in the previous chapter is considered. Thanks to this analysis, a new constraint of the GRB population contribution to the existing astrophysical diffuse flux discovered by IceCube in 2013, and whose origin is still unknown, is provided. For the very first time, the derived limits are evaluated in association with the uncertainty that possible not well-known parameters of the model can introduce in the neutrino flux evaluation.

Chapter 5 presents the studies carried out by the author within the KM3NeT Collaboration in the multimessenger context. The fast-response online pipeline, developed for the reconstruction in real time of data collected by KM3NeT/ARCA (i.e. the KM3NeT telescope optimised for the detection of TeV-PeV neutrinos), is presented. The characteristics of the events reconstructed through this pipeline are studied. Additionally, the performances of such pipeline for a future fully funded detector configuration are also investigated. Finally, the results of the first quasi-real-time analysis performed on a transient source (GRB 221009A) taking advantage of data reconstructed in real time are shown.

Chapter 6 summarises and discusses the results presented in this thesis.

At the end, the thesis includes the following appendices:

Appendix A presents some calibration activities on the KM3NeT/ARCA detector, in which the author has contributed.

Appendix B summarises the Monte Carlo event simulation and reconstruction algorithms of ANTARES and KM3NeT, both adopted in this thesis.

Appendix C presents the author's computation of an energy correction that was applied in the first follow-up analysis performed by KM3NeT for the search of neutrinos in association with a gamma-ray source.

1 MESSENGERS FROM THE HIGH-ENERGY UNIVERSE

Over the last decades, the way of performing astronomical studies has changed profoundly. Originally, astronomy was centred only on what we were able to see with our own eyes. Since the beginning of the seventeenth century, when the first optical telescopes were built thanks to Galileo Galilei's contribution, the Universe has long been studied using exclusively optical light. Nowadays, this view has been expanded. Visible light no longer constitutes the only message that the cosmos is sending us. Astronomers can benefit the information coming from the entire electromagnetic spectrum, from radio to gamma-rays, unveiling a Universe filled by sources of various nature and characteristics from vast distances and early epochs. Beyond light, other astrophysical particles, as Cosmic Rays (CRs), neutrinos, and gravitational waves can be used to investigate the cosmos.

Astronomy is living now the so-called *multimessenger era*: particles travelling through space and then pelting Earth and ripples in spacetime are tracked with the aim of providing unique and valuable insights into the properties of the Universe and underlying processes. Indeed, a deep understanding of the physical processes governing individual cosmic sources in the cosmos, related among others to their particle composition, radiation and acceleration mechanisms operating inside them, can arise from the complementary information carried by the four aformentioned messengers, namely photons, gravitational waves, neutrinos, and CRs. Through this approach and by accumulating statistics by all those messengers, the possibility to more and more figure out the properties of the sources populating the Universe increases and, consequently, different source populations may be characterised.

In this chapter, the several messengers coming from the high-energy Universe, namely CRs, photons, neutrinos and gravitational waves, are described in Sects. 1.1, 1.2, 1.3, and 1.4, respectively. Their production mechanisms are outlined in Sect. 1.5. Finally, the connection between the messengers and the current observing scenario defined within the multimessenger community are the topics of Sect. 1.6.

1.1 COSMIC RAYS

At the beginning of the twentieth century, a series of experiments revealed an increasing ionisation rate with an altitude greater than 1 kilometre with respect to sea level [1–4]. At that time, the nature of the discovered radiation was completely unknown. Today, it is firmly associated with charged particles impacting the Earth's atmosphere, called CRs. It is remarkable that CRs with energy up to three orders of magnitude higher than that protons have at the Large Hadron Collider (LHC) at CERN[1] are observed (see Fig. 1.1).

The main properties of CRs are discussed in Sect. 1.1.1. Afterwards, the focus is moved to the highest-energy CRs, which are most likely related to the cosmic sources investigated in the present thesis. These CRs are first described in Sect. 1.1.2, while their connection with astrophysical sources is presented in Sect. 1.1.3 as resulting from the experimental point of view. Later, in Sect. 1.1.4, some theoretical considerations about candidate sources are introduced.

1.1.1 *Energy spectrum and mass composition*

Observationally, it is well established that CRs are ordinary atomic nuclei accelerated to very high energies which arrive in the neighborhood of the Earth from outside the solar system (except for those associated to solar flares, which are not of interest for this thesis). These high-energy particles are mainly (89%) protons, but also include a fraction of ∼10% helium nuclei and smaller abundances of heavier nuclei (∼1%) [5]. Our atmosphere is continually crossed by such *primary CRs*, uniformly and isotropically, that impact the atmosphere originating the so-called *secondary CRs*. The energetic particles that arise from this process collide in turn with other nuclei producing Extensive Air Showers (EAS), namely cascade of particles. The latter, being detected by ground-based experiments, allow us to infer the properties of high-energy CRs.

The observed CR flux extends in energy over ten orders of magnitude, from ~ 1 GeV up to ~ 100 EeV, steeply falling with increasing energy. In fact, the differential cosmic-ray spectrum (number of particles per unit energy) is well described by the following power law:

$$\frac{\mathrm{d}N}{\mathrm{d}E} \propto E^{-\alpha}, \tag{1.1}$$

that results from the convolution of several physical processes undergone by the charged particles, including their acceleration at the source and their propagation in Galactic and/or extragalactic environments. As CRs are accelerated in various astrophysical environments, several effects are responsible for the observed spectrum, and the slope of the power law varies with energy. The flux of all nuclear components that make up CRs (the so-called *all-particle spectrum*) is shown in Fig. 1.1, where the differential CR spectrum in Eq. (1.1) is multiplied by a factor of E^2 to appreciate the observed features. Two main characteristics are easily recognisable. The first one is the so-called *knee* at about 3×10^6 GeV ($= 3$ PeV), where the spectral slope of the differential spectrum steepens from $\alpha = 2.7$ to $\alpha = 3.1$, and the other one is the *ankle*, at about 3×10^9 GeV ($= 3$ EeV), where the spectrum flattens again ($\alpha = 2.6$). At low energies (below ∼30 GeV), where the flux of detectable

1 LHC is the world's largest and most powerful particle accelerator, located in Geneva (Switzerland). It consists of a 27-kilometre ring of superconducting magnets with a number of accelerating structures to boost the energy of the particles along the way.

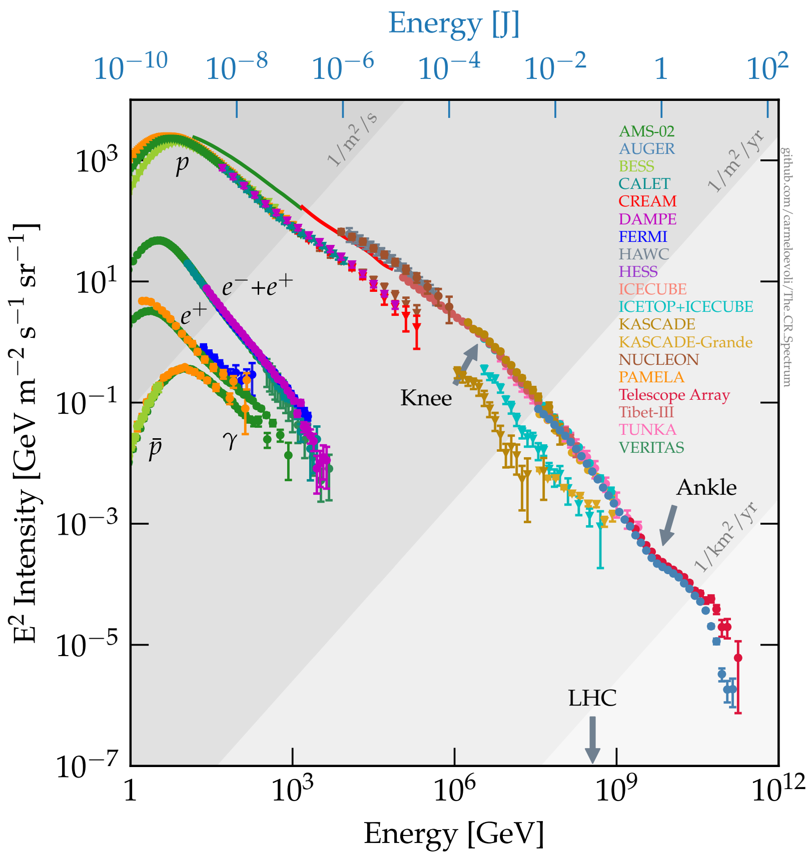

Figure 1.1: Cosmic-ray energy spectrum measured by several experiments in the past two decades. This plot has been produced by using the public Git project [6]. References to each data set shown in the plot are listed in the corresponding dedicated GitHub repository: https://github.com/carmeloevoli/The_CR_Spectrum.

particles is large (greater than 1 particle/m^2/s), the flux is influenced by the solar modulation. The number of observed particles is modulated on different timescales by the 11-year cycle of the heliosphere magnetic fields (e.g., [7–9]). The origin of the steepening of the CR spectrum around 3 PeV is a long-standing debated point. It has long been suspected to correspond to the energy beyond which the efficiency of Galactic sources of CRs is steadily exhausted [10]. However, this consideration is strongly model-dependent. The experimental signature that now is considered to explain this characteristic is the change in CR composition around the knee. CRs appear to be increasingly more dominated by heavier nuclei at high energy, at least up to a few $\sim 10^{17}$ eV [11–14]. Thus, as the maximum cosmic ray energy at the source depends on the rigidity[2] [10], more massive particles are expected to show the corresponding break at higher energies. Indeed, if the maximum energy of protons could reach $E_{\text{knee}} \simeq 3$ PeV, then a heavier nucleus with charge Z would reach Z times larger energies: in this scenario, Fe would have an energy of $26E_{\text{knee}}$. This fits with the model for which shocks in Supernova Remnants (SNRs) [3] constitute the main

2 The rigidity of a particle is $R = p/q$, where p is the momentum and $q = Ze$ its charge (e is the electron charge and Z is the atomic number of the nucleus).

3 A supernova remnant is the structure resulting from the explosion of a star in a supernova. The supernova remnant is bounded by an expanding shock wave, and consists of ejected material expanding from the explosion, and the interstellar material it sweeps up and shocks along the way.

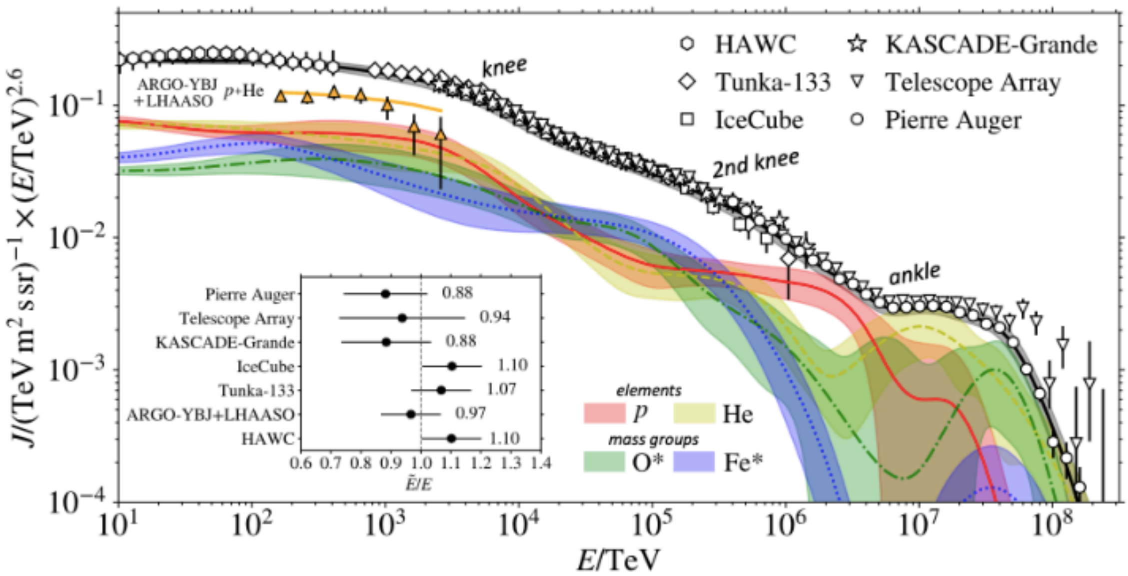

Figure 1.2: CR energy spectrum and mass composition by combining results obtained by different experiments. In the y-label there is the differential energy CR spectrum multiplied by $E^{2.6}$ to make clear the visibility of the second knee feature around 400 PeV. Image credit: [24].

Galactic CR accelerators [15, 16]. The composition change is believed to be the cause of an additional feature emerging in the energy spectrum after the enormous progress made in CR detections, i. e. the *second knee* around 4×10^{17} eV (400 PeV), where the spectral index becomes even steeper than above the knee (from $\alpha = 3.1$ to $\alpha = 3.3$) [17–20]. Heavy elements, although subdominant below the knee, could be accelerated to higher energies until the iron component falls steeply around 400 PeV. For this reason, this bending is also known as *iron knee*. Hence, the region between the knee and the second knee would result from the superposition of cutoffs in the spectra of different chemical elements (e.g., [21–23]). This is visible in Fig. 1.2, which shows the CR energy spectrum together with the information on the mass composition depending on the CR energy, obtained by combining results from different experiments operating in the last decades. Finally, the flattening of the spectrum at the ankle suggests the existence of a further component influencing the spectrum. In this region, the CR energies are so high that in a standard Galactic magnetic field of 3μG the Larmor radii, i. e. the radii of their circular motion in the presence of a uniform magnetic field, are comparable to the thickness of the Galaxy. For a particle with energy E, charge $q = Ze$ and $\beta = v/c$ (v is the velocity of the particle and c the speed of light), immersed in a magnetic field B, the Larmor radius is defined as

$$r_L = \frac{E}{ZeB\beta c} \rightarrow \frac{r_L}{1\ \text{kpc}} \simeq \left(\frac{E}{1\ \text{EeV}}\right)\left(\frac{B}{1\ \mu\text{G}}\right)^{-1}. \tag{1.2}$$

Eq. (1.2) shows that a relativistic proton with energy 10^{18} eV is characterised by a Larmor radius $r_L \simeq 330$ pc, whose value is close to the vertical dimension of the Galactic disk ($\sim$300 pc). This consideration demonstrates that the bulk of CRs between the knee and the ankle probably has a local Galactic origin; meanwhile CRs with higher energies cannot be magnetically bound to the Galaxy and are most likely extragalactic. Thus, the ankle can be considered, as a first approximation, the energy region where the transition between Galactic and extragalactic CRs occurs. Recent observations have confirmed this view, providing evidence for CRs to be accelerated to energies above 10^{15} eV in the Galaxy [25–27]. However, the nature of the sources and the mechanisms by which they accelerate CRs remain, in general, not firmly established. In particular, whether particles can be effectively accelerated to the rigidity of the second knee in SNRs is still under debate; see, e.g., [28].

1.1.2 *Ultra-high-energy cosmic rays*

CRs with energies from a few 10^{18} eV to beyond 10^{20} eV are commonly called Ultra-High-Energy Cosmic Rays (UHECRs). Since their first observation in the 1960s [29], through the EAS generated as a consequence of their interaction with nuclei in the upper atmosphere, the study of UHECRs has continued, with increasingly large detector arrays to compensate for their incredibly low frequency (less than 1 particle per km^2 per year). The flux of CRs with energies above a certain threshold E_{min} is on the order of $10^2(E_{\mathrm{min}}/\mathrm{EeV})^{-2}$ particles per square kilometre per year [30]. Hence, below about 10^{15} eV it is possible to observe CRs directly in spacecraft with a square-metre-size detector or, after correcting for atmospheric overburden, from balloons; while, UHECRs need to be studied through the detection of EASs of particles using ground-based detectors covering vast areas. The most recent ones are the Pierre Auger Observatory (PAO) in Argentina, the largest CR observatory available today, covering a land area of 3000 km^2 [31], and Telescope Array (TA), in USA, with an area of 700 km^2 [32].

Despite the huge technological and scientific progress achieved in this field, the only certainty that scientists have about UHECRs is their extragalactic origin because at these energies the Galactic magnetic field is not strong enough to contain them, as previously discussed. Quite recently, the first observational piece of evidence for an extragalactic origin of CRs beyond the ankle occurred: the Pierre Auger Collaboration, by using CR data with $E > 8$ EeV, discovered an anisotropic signal consistent with a dipolar modulation over $\sim$85% of the sky covered by the detector. The amplitude of this dipole appears consistent with an anisotropic distribution of UHECR sources within a few hundred Mpc, and its direction lies 125° from the Galactic centre [33]. Among several other sources investigated, nearby starburst galaxies appear to be the more plausible partners to UHECRs, having these sources provided the strongest indication of anistropy (4.2σ) at the highest CR energies to date [34] (see Sect. 1.1.3 for a more detailed treatment of this topic). Nevertheless, many aspects of the nature of UHECRs remain an enigma, as for example the origin of these particles and what process is able to accelerate them to such extreme energies. For a detailed review about open questions and prospects for progresses in UHECR research, see [35].

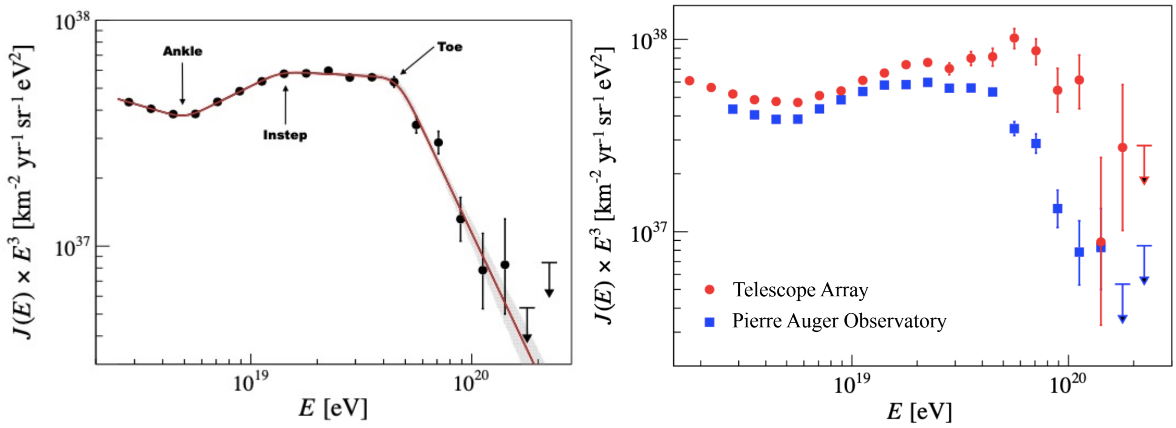

(a) (b)

Figure 1.3: (a) UHECR energy spectrum obtained by the Pierre Auger experiment. The red line shows the best fit (see Eq. (9) in [36]). The shaded grey band indicates the statistical uncertainty of the fit. The main features (angle, instep, and toe) are also highlighted in the plot, that has been adapted from Fig. (9) in [36]. (b) Comparison between the Pierre Auger UHECR spectrum presented in [36] (in blue) and the TA one [41] (in red). The spectra are scaled by E^3 for better readability. Images credit: [36].

Spectrum of UHECRs

Thanks to the high-quality data collected over the past decade by several UHECR observatories, it has been possible to study the features of the all-particle energy spectrum with unprecedented precision. A recent spectrum produced by the Pierre Auger Collaboration for UHECRs [36] is shown in Fig. 1.3(a). In addition to the distinct features discussed in Sect. 1.1.1, several new deviations from a simple power law are visible. A new spectral break is identified at $10^{19.2}$ eV, where the spectral index increases from $\alpha \sim 2.6$ to $\alpha \sim 3.0$. This feature, dubbed the *instep*, seems to reflect the interplay of light-to-intermediate nuclei [36]. Finally, a suppression of the total flux above $10^{19.7}$ eV, claimed for the first time by the HiRes Collaboration [37], is also observed with $\alpha \sim 5$ [36, 38–41]. This cutoff, commonly called *toe*, can be related either to the Greisen-Zatsepin-Kuzmin (GZK) suppression [42, 43], an effect responsible for the limited horizon of UHECRs due to their absorption in the scattering off the low-energy photons of the Cosmic Microwave Background (CMB), either to the maximum energy that extragalactic sources would provide to particle acceleration. Note that the spectrum measured by TA agrees in shape with the one measured by PAO but shows a different energy break and flux normalisation for energies above $10^{19.5}$ eV (see Fig. 1.3(b)), even once scaling factors due to different energy calibrations and systematic uncertainties of the detectors, as well as the declination dependence of the TA spectrum[4], are taken into account. A joint effort between the two collaborations is underway to better understand the reasons of the observed differences and to study their impact on the spectral features.

4 The energy spectrum measured by Auger does not show any significant declination dependence, but TA does.

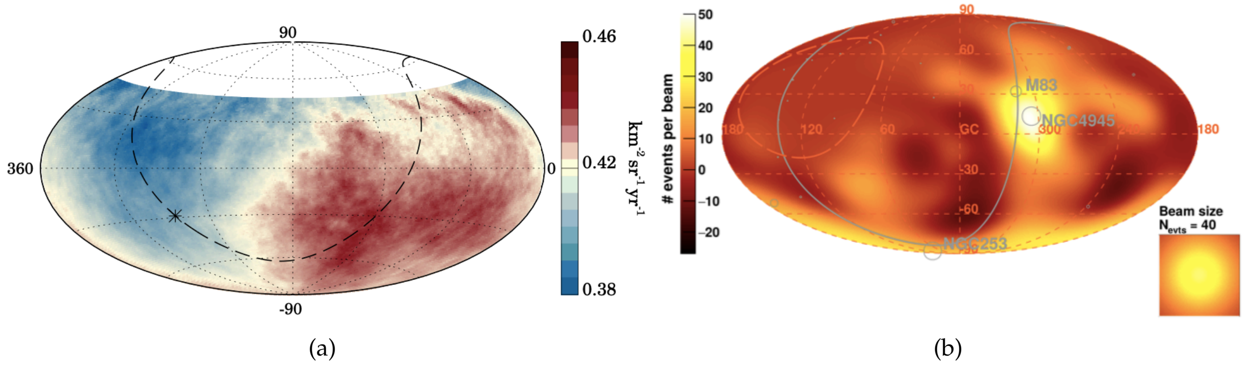

Figure 1.4: (a) Sky map in Galactic coordinates showing the CR flux measured by PAO above 8 EeV. The Galactic center is marked with an asterisk and the Galactic plane is shown by a dashed line. The color scale indicates the number of events per km^2 per yr per sr. Image credit: [33]. (b) Observed excess map showing the UHECR hotspot in correspondence of the Centaurus A / M 83 / NGC 4995 group. The color scale indicates the number of events per smearing beam. The supergalactic plane is shown as a solid gray line. An orange dashed line delimits the field of view of the array. Image credit: [55].

Composition at ultra-high energies

It is well known that, for energies between the second knee and the ankle, the composition of the primaries is a mix of protons and medium-mass (e.g., nitrogen) nuclei, gradually becoming lighter with increasing energy [44, 45]. Then, in the ankle region, the composition is mixed and both pure elements or (p+He)-only mixtures are excluded with significance $> 6\sigma$ [46]. Above the ankle, the mass composition of UHECRs appears to be increasingly heavier and less mixed [47], although with larger statistical uncertainties, suggesting that the UHECR spectrum is the superposition of elements with progressively heavier mass, each with a steep cutoff (see Fig. 1.2). The composition of CRs gives us important information about the transition from their Galactic to extragalactic nature. The picture appears to be much more complicated than that described in Sect. 1.1.1, where the transition was considered to occur at the ankle. The mixed composition visible just above the second knee could be provided by comparable contributions from a Galactic and an extragalactic component [23, 48–53]. Very recently, considering both energy spectrum and composition data, the Pierre Auger Collaboration studied two different astrophysical scenarios for UHECR sources, with different extragalactic components for the region below and above the ankle, and an additional Galactic contribution [54]. A definite conclusion about the presence of a Galactic component contributing at the UHECR spectrum was not reached; however, it was possible to infer that a medium-mass nuclei composition is needed to explain the observed spectrum. In addition, homogeneous source distributions across cosmic history seem to be favoured with respect to very strong source evolutions, that would otherwise cause a flux of secondary particles at the ankle exceeding the observed spectrum [54].

1.1.3 *Correlation of UHECRs with astrophysical sources*

From the study of the arrival directions of UHECRs, it is possible to retain some information on the possible location of the astrophysical sources that accelerate them to such extreme energies. Since UHECRs are elettrically charged, their trajectories are deflected by intergalactic and Galactic magnetic fields, so it is not straightforward to reconstruct the position of their sources from their arrival directions. For this kind of studies, particles characterised by an energy with at least a few tens of EeV are particularly indicated. Indeed, at those energies, the deflections due to magnetic fields permeating the Universe are small enough to allow CRs to retain some directional information on the position of their sources, at least for nuclei with a sufficiently small charge (e.g., [56, 57]). Additionally, the cosmological volume to investigate is quite limited, due to the GZK effect and the low mean free path values for particle energies losses[5]; this limits the sources of UHECRs to be searched in the local Universe ($\lesssim 100$ Mpc). For energies below 4 EeV, the observed distribution of the arrival directions of UHECR is consistent with being isotropic [58, 59]. At higher energies, a dipole with amplitude $d \simeq 5(E/10\ \text{EeV})\%$ towards an extragalactic direction is present [33] (see Fig. 1.4(a)), as already pointed out at the beginning of Sect. 1.1.2; this result has now reached a statistical significance level of 6.6σ [60]. Interestingly, the direction of the dipole is also consistent at the 2σ level with nearby galaxy stellar mass distribution (2MASS survey[6] [61]). At even higher energies, a recent study by the Pierre Auger Collaboration, that includes more than 2,600 events with energies $E > 39$ EeV taken in 17 years of data acquisition and with accumulated exposure of 122,000 km^2 sr yr, shows anisotropies in the toe region [34]. An excess at $\sim 4\sigma$ is found with the Centaurus region, which contains the most prominent active and star-forming galaxy expected to contribute at these energies. This result confirms the previous founding in [55], whose excess map with the UHECR hotspot identified in correspondence of Centaurus A is shown in Fig. 1.4(b). Catalogue-based searches endorse this association, establishing the largest signal coming from starbursts (4.2σ), as well as an association at $\sim 3\sigma$ with jetted Active Galactic Nuclei (AGN). A similar search was previously carried out by the TA Collaboration for events with E>43 EeV; unfortunately, it was unable to give a constraint between the isotropy hypothesis and the association with starburst galaxies [62]. In addition, a study has been conducted with combined data between PAO and TA, in the Southern and Northern hemispheres, respectively [63]. Again, a weak association with the overall galaxy distribution was found, as well as a stronger association with nearby starburst galaxies, but unfortunately still short of the discovery level. In the future, once new data will be accumulated, allowing to add more statistics to the present studies, and deflections of CRs will be better understood (currently these are subject to large uncertainties because of the not well-known charge of these particles), it will be reasonably possible to corroborate or not this excess.

---

5 At 100 EeV the loss length is of the order of 200-300 Mpc for proton and iron, and 3-6 Mpc for intermediate nuclei such as helium and nitrogen [30].

6 The 2MASS redshift survey maps the distribution of galaxies out to a redshift of $z \simeq 0.03$ (about 115 Mpc).

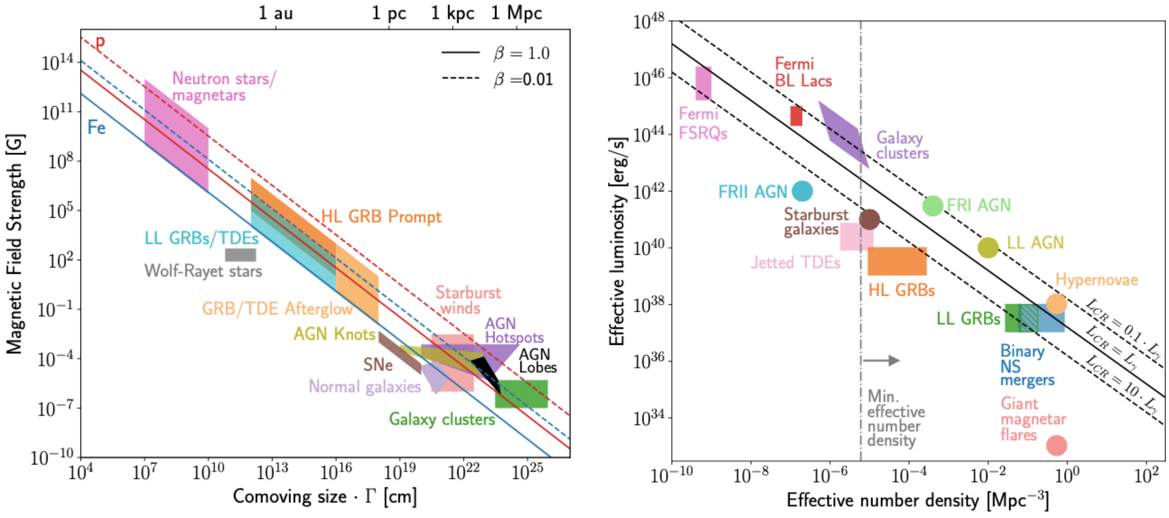

(a) (b)

Figure 1.5: (a) Hillas plot showing candidate UHECRs acceleration sites as colored areas on the $B - R$ plane (magnetic field versus size of the accelerating region multiplied by its Lorentz factor Γ with respect to the observer). The acceleration up to 10^{20} eV is possible only above the diagonal lines, that define the minimal value for the BR product needed to satisfy the Hillas condition. The results are shown for protons and iron nuclei, in red and blue respectively, through solid lines for maximum shock velocity ($\beta = 1$) and dashed lines in the case of slower shocks ($\beta = 0.01$). (b) Effective luminosity versus effective number density. For transient sources a characteristic lifetime of 3×10^5 yr is assumed. The black solid line shows the UHECRs energy production rate of 5×10^{44} erg Mpc^{-3} yr^{-1}. The gray vertical line gives the lower limit on the UHECRs source number density derived in [64]. Uncertainties on the source parameters are taken into account and are represented by the extension of each colored region. Images credit: [35].

1.1.4 *Origin of the bulk of UHECRs*

Since the discovery of UHECRs, understanding their origin has attracted a great deal of attention among scientists. In 1984, A. M. Hillas proposed a criterion, which takes his name (*Hillas criterion*), to find the minimal condition that a source must satisfy to be able to accelerate CRs up to energies as high as 10^{20} eV [65]. That condition states that particles can stay in the acceleration region as long as their Larmor radius is smaller than their size. Indeed, a necessary condition (but not sufficient) for particles to be accelerated is that they are confined in the accelerator. Accounting for a possible relativistic motion of the acceleration site with Lorentz factor Γ with respect to the observer[7], the maximum achievable energy in a source with characteristic size R and magnetic field strength B can be estimated as

$$E_{\max} = \Gamma q B R. \tag{1.3}$$

A recent version of the Hillas plot has been produced [35] (see Fig. 1.5(a)), where the typical magnetic field of several sources as a function of their characteristic size is shown.

7 The Lorentz factor is defined as $\Gamma = 1/\sqrt{1 - v^2/c^2} = 1/\sqrt{1 - \beta^2}$.

Solid diagonal lines define the minimum value of BR required to accelerate protons (red) and iron nuclei (blue) to 10^{20} eV. Hence, by using the Hillas criterion, it is possible to identify the plausible CR accelerators as those located above those lines. Note that two different cases are considered, e.g., fast and low shock waves, characterised by a velocity of the shock in unit of the speed of light equal to $\beta = 1$ and $\beta = 0.01$. As shown with the dashed diagonal lines, the required BR value results to be higher for slower shock. From the Hillas plot it is possible to infer that sources as normal galaxies, namely without a Black Hole (BH) at its centre, supernovae, and stars that drive massive magnetised winds such as Wolf-Rayet stars do not satisfy the confinement condition dictated by the Hillas criterion of 10^{20} eV particles. For all the other sources, such as Gamma-Ray Bursts (GRBs), AGN, and starbursts, the condition is instead satisfied. Nonetheless, it is worth pointing out that the Hillas condition-only just discussed is not sufficient to fully constrain the cosmic-ray accelerators up to ultra-high energies. Indeed, to ensure the efficiency of the acceleration process, one should also take into account the actual production of particles at the maximum energy, resulting from the specifics of the acceleration mechanisms, namely how the acceleration timescale $t_{\rm acc}$ compares with the typical energy loss timescale $t_{\rm loss}$ and escape timescale $t_{\rm esc}$ for energy losses in the source environment. In other words, the following condition should also be satisfied:

$$t_{\rm acc} \leq \min(t_{\rm age}, t_{\rm esc}, t_{\rm loss}), \tag{1.4}$$

$t_{\rm age}$ being the age of the source. The effects induced by radiation losses in different acceleration regimes on the simplistic Hillas condition are studied in [66]. For a more detailed discussion about the influence of $t_{\rm age}$ and $t_{\rm esc}$ on the acceleration mechanism of CRs, see Sect. 1.5.1.

A further independent consideration of possible UHECR accelerators comes from energy-budget speculations. As astrophysical sources need to output sufficient energy in UHECRs to support the flux observed on Earth, the UHECR production rate can be compared with the rate of occurrence of the potential sources. The result carried out by one of these kind of studies is shown in Fig. 1.5(b). The energy budget of various source classes based on infrared, radio, X-ray and gamma-ray observations, is compared to a recent estimation of the UHECR energy-production rate, amounting to $\dot{\rm U} \sim 5 \times 10^{44}$ erg Mpc^{-3} yr^{-1} [67, 68]. The effective number density for the sources investigated has been found using their luminosity density at redshift $z = 0$; this is motivated by the fact that local UHECRs must originate in the nearby Universe ($z \lesssim 0.02 - 0.03$, corresponding to sources within $\sim$ 100 Mpc), as previously discussed in Sect. 1.1.3. The solid diagonal line in the plot represents the minimum energy budget condition that a source needs to satisfy to be able to accelerate up to the highest energies, in case the UHECR luminosity of the source $L_{\rm cr}$ is equal to the radiated luminosity L_γ in the wavelength studied. Through the black dashed lines, the region between $L_{\rm cr} = 0.1 L_\gamma$ and $L_{\rm cr} = 10 L_\gamma$ is delimited. In addition, the grey dashed line shows the lower bound on the density of UHECR sources from the lack of significant clustering in the arrival directions of the highest energy events ($E > 70$ EeV) detected at the PAO [64]. However, it is worth highlighting that the results in Fig. 1.5(b) and discussed here are not to be considered definitive, since they are hypotheses-dependent. E.g., the effective number density for UHECRs from transient sources depends on the observed burst rate ρ and the apparent burst duration τ as $n_{\rm eff} = (3/5)\rho\tau$ [69]. For any bursting source considered in Fig. 1.5(b), $\tau = 3 \times 10^5$ yr has been assumed, resulting in a mean extragalactic magnetic field strength of 1 nG [70]:

$$\tau \simeq 3 \times 10^5 \text{ yr} \left(\frac{D}{100 \text{ Mpc}}\right)^2 \left(\frac{B}{1 \text{ nG}}\right)^2 \left(\frac{E/Z}{100 \text{ EeV}}\right)^{-2}, \tag{1.5}$$

D being the distance travelled by the UHECR and Z the atomic number of UHECR nuclei. Eq. (1.5) shows that stronger magnetic fields would imply larger τ values and hence a larger effective number density. In addition, the UHECR energy budget depends on several factors, such as the source-by-source injected spectrum, composition, and luminosity evolution of the sources, and thus no definitive statement can be made yet.

From the state-of-art so far pointed out, it appears clear that understanding the origin of UHECRs is a perennial challenge since the beginning, and it still constitutes an active field of research despite the interesting results achieved in the last years and huge progresses on UHECR knowledge. Indeed, it is not yet possible to make claims about the sources of the highest-energy particles known in the Universe. In the case of UHECRs, the astrophysical source identification is complicated by their deflection in magnetic fields inside and outside our Galaxy and by the time delay of 10^4 yr between arrival of CRs and secondary gamma-rays/neutrinos created during their propagation through the environment surrounding their source and through extragalactic space (see Sect. 1.5.2 for the discussion about the production mechanisms of such secondary particles).

These constitute the main reasons why the origin of the most energetic CRs is still unknown. A phenomenological and multimessenger approach might help shedding light on these dedicated issues; in fact, an indirect way to identify potential UHECR sources is based on the detection of gamma-ray fluxes and very high-energy neutrinos resulting from the interaction of UHECRs with matter or photon fields in the vicinity of the cosmic accelerators.

1.2 PHOTONS

Current knowledge of the Universe has been historically acquired throughout centuries via detection of electromagnetic (EM) signals from several types of astronomical sources. In particular, as already mentioned at the beginning of the present chapter, astronomical observations started with visible light. Afterwards, the observation range was expanded to all the EM spectrum spanning over 20 orders of magnitude, including radio, infrared, optical, ultraviolet, X-ray, and gamma-ray frequencies. There is a wealth of information in photons, with different wavelengths typically carrying the signatures of distinct processes. Gamma rays, that are the most energetic photons in the EM spectrum, are of specific interest for this thesis. Being emitted by the most energetic objects in the Universe, these are typically related to nuclear phenomena occurring in such high-energy astrophysical sources. Specifics of gamma-ray observations and detection techniques are described in Sect. 1.2.1, followed by the explanation of the absorption effect that these suffer during their propagation to Earth in Sect. 1.2.2, making challenging their detection for energies above TeV.

1.2.1 *Gamma rays*

Gamma rays are photons with energies greater than 100 keV. They are considered particularly interesting cosmic messengers, as they provide a valuable probe of the largest energy transfer throughout the Universe. Thousands of gamma-ray sources are visible in the high-energy (HE) regime (100 MeV $< E <$ 100 GeV), and hundreds in the very-high-energy (VHE) one (100 GeV $< E <$ 100 TeV)[8]. Some are generated by transient events, such as solar flares, supernovae, and GRBs; others are produced by steady sources like the supermassive BHs at the hearts of galaxies. The large interaction cross section of gamma rays[9] and their rates facilitate their detection in the HE regime by using moderate-sized particle detectors space-born missions (e.g., Swift [71] and Fermi [72, 73] satellites), in the VHE regime using arrays of Cherenkov Telescopes deployed on ground at moderate altitudes (e.g., MAGIC [74, 75], HESS [76, 77], VERITAS [78]), and high-altitude extended detector arrays (e.g., HAWC [79, 80], ARGO [81], LHAASO[82]), which measure gamma rays from 100 GeV to multi-TeV energies.

Gamma rays are characterized by an important property that distinguishes them from CRs: they are able to propagate in straight lines from their site of origin. Indeed, photons (thus, gamma rays too) are electrically neutral, and they are not deflected by magnetic fields. Nevertheless, understanding the processes involved in the production of gamma rays is not trivial, since they may be produced both in the interaction of protons and heavier nuclei (hadronic emission), and by lower-energy photons undergoing inverse-Compton scattering on high-energy electrons (leptonic emission), as outlined in Sect. 1.5.2. Another effect influencing gamma-rays observation is their absorption because of the interaction with the background photon field filling the Universe, discussed in Sect. 1.2.2.

1.2.2 *Gamma ray absorption*

During their propagation to Earth, high-energy gamma rays are characterised by a certain probability of being converted into electron-positron pairs because of the presence in the Universe of a background radiation field. The maximum contribution comes from the CMB, whose number density is about 410 photons per cubic centimetre. Of particular interest is the so-called Extragalactic Background Light (EBL). The EBL is the integrated

8 NASA's top 10 gamma-ray sources in the Universe:
https://www.space.com/13838-nasa-gamma-ray-targets-blazars-fermi.html.

9 The US National Institute of Standards and Technology published online a complete and detailed database of cross section values of X-ray and γ-ray interactions with different materials in different energies (last update in 2010). It is called XCOM and it is reachable at https://www.nist.gov/pml/xcom-photon-cross-sections-database.

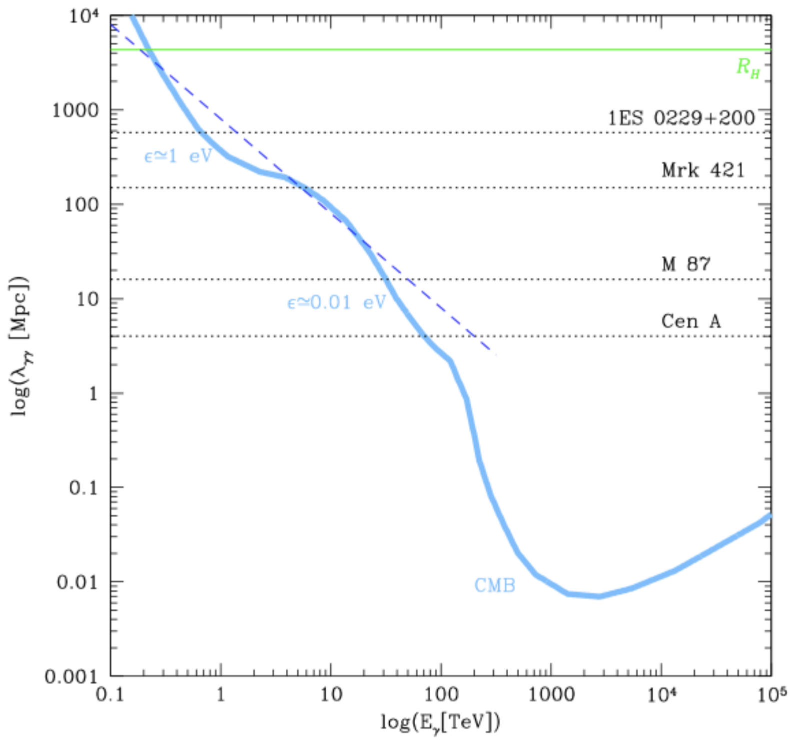

Figure 1.6: Mean free path of VHE γ-rays as a function of the photon energy at $z = 0$. Labels along the curve mark the energies of soft photons with which gamma rays interact. The horizontal green line shows the Hubble radius $R_H = c/H_0 \simeq 13.7$ billions of light-years, i.e. the radius of the observable Universe. Dotted black lines mark distances to some known VHE γ-ray sources. The dashed blue line shows the relation in Eq. (1.9). Image credit: [86].

intensity of all the light permeating the Universe that has been emitted throughout its history in the infrared, optical, and ultraviolet regions of the EM spectrum. Even if it has not been completely measured nor explained yet, it is believed to be associated with either primordial phenomena, such as photons emitted by stars, galaxies, and AGN or other radiative processes. From gamma rays to radio, the integrated intensity values in units of $\mathrm{nW/m^2/sr^1}$ for the various photon background components are ~ 0.015 (gamma-ray), ~ 0.3 (X-ray), $\sim 0.01 - 0.02$ (lower and upper limits at 4.9 nm for Extreme UV), $24 \sim 4$ (with an additional ± 5 systematic; optical), $\sim 30 \pm 10$ (cosmic infrared background), 960 (CMB), and < 0.001 (radio), respectively. The EBL may also contain diffuse and extended signals, including high-energy photons associated with dark-matter particle decays or annihilation [83–85]. The pair production process $\gamma + \gamma_{\mathrm{bkg}} \to e^+ + e^-$ becomes possible when the center-of-mass energy in the photon-photon collision exceeds twice the electron mass. By considering a high photon energy, namely a γ ray with E_γ, and a softer photon energy ϵ, the γ-ray energy threshold to produce e^+e^- pairs is [87]

$$E_\gamma \geq \frac{m_e^2}{\epsilon} \simeq 250 \left(\frac{\epsilon}{1\ \mathrm{eV}}\right)^{-1} \mathrm{GeV}. \tag{1.6}$$

Thus, whenever photons are characterised by an energy greater than that in Eq. (1.6), the γ-ray source starts to become opaque to gamma rays. For example, gamma rays with energies above $E_\gamma = 100$ TeV could produce pairs in interactions with CMB photons (with energy 10^{-6} keV) and be absorbed. The probability for a photon of observed energy $E_{\rm obs}$ to survive absorption along its path from its source at redshift z to the observer plays the role of an *attenuation factor* for the radiation flux, and is expressed as

$$P = e^{-\tau(E_{\rm obs},z)}. \tag{1.7}$$

The coefficient $\tau(E_{\rm obs},z)$ is called *optical depth*, and is defined as

$$\tau(E_{\rm obs},z) = \int_0^z \lambda_{\gamma\gamma}^{-1}(E,z)\frac{\mathrm{d}l}{\mathrm{d}z}\mathrm{d}z, \tag{1.8}$$

where $l(z)$ is the distance as a function of the redshift, depending on cosmological parameters[10], and $\lambda_{\gamma\gamma}$ is the photon mean free path given by the following equation:

$$\lambda_{\gamma\gamma} = \frac{\int\limits_{\epsilon} (\sigma_{\gamma\gamma}(\epsilon) n_{\rm bkg}(\epsilon))^{-1}\mathrm{d}\epsilon}{\int\limits_{\epsilon}\mathrm{d}\epsilon}, \tag{1.9}$$

where $\sigma_{\gamma\gamma}(\epsilon)$ is the pair production cross section which reaches its maximum at $\sigma_{\gamma\gamma}^{\rm max}(\epsilon) \simeq 10^{-25}$ cm^2, and $n_{\rm bkg}(\epsilon)$ is the density of the considered photon background component. For gamma rays with energy between $\sim$10 GeV and 100 TeV, the EBL is the dominant background; instead, the CMB overtakes the EBL for energies above 100 TeV and 10 EeV; for higher energies, the main source of opacity of the Universe is the radio background. In Fig. 1.6 the dependence of $\lambda_{\gamma\gamma}$ with the observed γ-ray energy is shown. The mean free path of gamma rays is comparable to typical distances of extragalactic γ-ray sources in the TeV band. At PeV γ-ray energies, $\lambda_{\gamma\gamma}$ lowers. For example, considering CMB photons with $n_{\rm CMB} = 400$ cm^{-3}, the mean free path value amounts to $\lambda_{\gamma\gamma} \simeq 8$ kpc. Thus, PeV γ rays are not able to escape from the host galaxy of the source, typically characterised by sizes of 10-100 kpc.

The energy dependence of $\tau(E_{\rm obs},z)$ leads to appreciable modifications of the observed source spectrum with respect to the emitted one, even for small differences in the optical depth value, due to the exponential dependence in Eq. (1.7). Because the absorption coefficient increases with energy, the observed flux is steeper than the emitted one.

The absorption of extragalactic gamma rays in the intergalactic medium defines the so-called *gamma-ray horizon*, that is the distance corresponding to the redshift z for which the attenuation factor equals unity. It is marked by the boundary of the black area in Fig. 1.7, where the distance horizon (distance from the Earth) that defines the visible Universe as a function of the energy is shown. In addition to photons, neutrinos and cosmic-ray energies are also included. While lower-energy photons can travel to us from the farthest Universe, the highest-energy photons (TeV-PeV gamma rays) and CRs are attenuated after short distances due to interaction with the EBL and GZK effect (discussed in Sect. 1.1), respectively. The gamma-ray horizon is set at a redshift of about $z = 1$ at $E \sim 100$ GeV. Hence, the

10 $\frac{\mathrm{d}l}{\mathrm{d}z} = \frac{c}{H_0(1+z)[(1+z)^2(\Omega_M z+1)-\Omega_\Lambda z(z+2)]^{1/2}}$, where Ω_0 is the Hubble constant, Ω_M is the matter (baryonic and cold dark matter)) density, and Ω_Λ is the dark energy density.

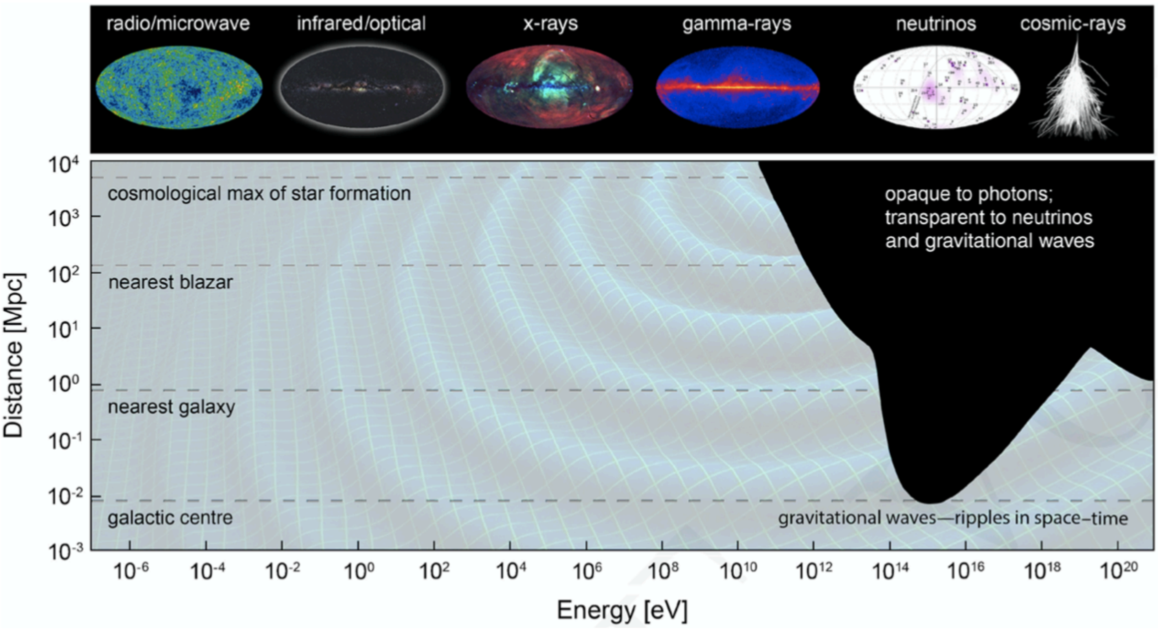

Figure 1.7: Distance horizon that defines the visible Universe as a function of the energy of cosmic messengers. The plot shows the distance at which the Universe becomes optically thick to electromagnetic radiation. The horizon is marked by the boundary of the black area. Image credit: [88].

most distant Universe can be studied only through other messengers, i. e. neutrinos (see Sect. 1.3) and gravitational waves (see Sect. 1.4).

1.3 NEUTRINOS

Shock accelerated particles interacting with matter and radiation in and around astrophysical sources may produce neutrinos. Neutrinos are elementary particles present in huge abundances throughout space. Neutrinos play a special role in particle astrophysics. Their interaction cross section is very small (the lowest among elementary particles), then they can leave the production site without interacting, carrying information about the core of the astrophysical objects where they are originated. Being electrically neutral and weakly interacting particles, they can reach Earth from cosmological distances without suffering absorption (unlike gamma rays) and with no deflection (unlike CRs). Thus, they have a powerful capacity to escape from the accelerators where CRs are born, being able to point in the direction of the source from which they come. These properties make them ideal cosmic messengers. A brief overview on neutrino spectrum components is given in the following (Sect. 1.3.1), with particular attention to atmospheric (Sect. 1.3.2) and cosmic neutrinos (Sect. 1.3.3), whose distinction is crucial in high-energy neutrino astronomy, as it will be clear later in the thesis. More aspects related to neutrinos will be further analysed in Chapter 2, dedicated to neutrino astronomy.

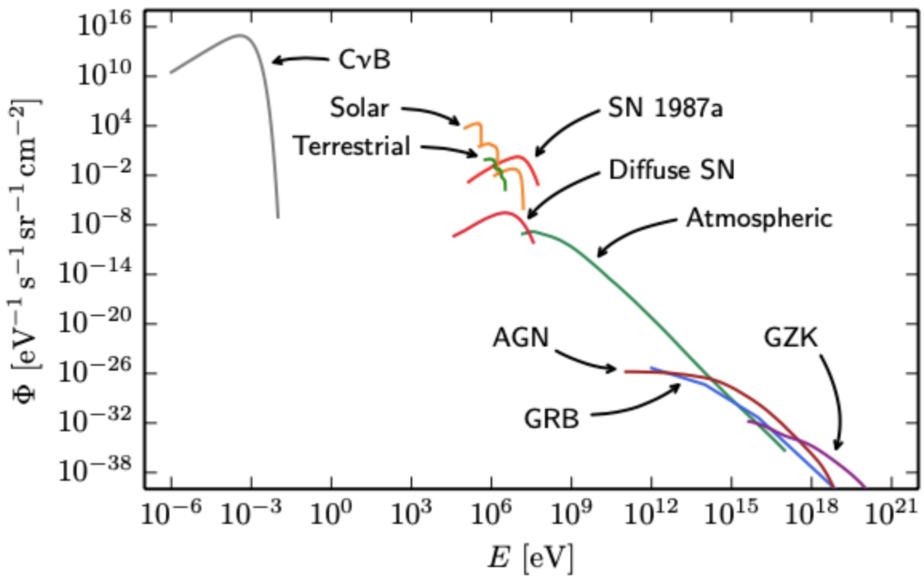

Figure 1.8: Neutrino energy spectrum. Predictions from several sources are shown: neutrino spectra of the cosmic neutrino background (gray), solar neutrinos (light orange), terrestrial neutrinos (dark orange), neutrinos from SN 1987A and the diffuse supernova neutrino background (red), atmospheric neutrinos (green), neutrinos from AGNs and from GRBs (dark red and cyan, respectively), and cosmogenic neutrinos (violet). Image credit: [89].

1.3.1 *Neutrino energy spectrum*

Many sources, either astrophysical or terrestrial, produce neutrinos observed in many different processes. In this regard, Fig. 1.8 shows the whole neutrino energy spectrum over a broad energy range (from 10^{-6} eV to EeV) with predicted and/or observed neutrino and antineutrino fluxes produced by several sources. This is commonly called in the community *Grand Unified Neutrino Spectrum* (GUNS), described in detail in a recent review [90]. Between 10^{-6} eV and 10^{-3} eV, a huge flux due to the cosmic neutrino background (CνB) [91], a thermal relic from the early Universe when it was just 1 second old, is expected. Despite the very high particle density (it should constitute the highest neutrino flux at Earth with a number density of $n_{\nu,\mathrm{C}\nu\mathrm{B}} \simeq 110$ cm^{-3}), the CνB has never been directly observed, because low-energy neutrinos interact very weakly with normal matter. Moving to higher energies, in the MeV range, the flux is dominated by solar neutrinos; indeed, the 2.3% of the energy produced by the Sun is carried by electron neutrinos ν_e (2×10^{38} neutrinos per second), carrying each $\sim 1-10$ MeV. They arise during the process of nuclear fusion in the Sun, from the reaction $4p + 2e^- \rightarrow^4 \mathrm{He} + 2\nu_e + 26.73$ MeV, which proceeds through several reaction chains and cycles. The average distance between the Earth and the Sun of $\simeq 1.5 \times 10^{13}$ cm implies a ν_e number density on Earth of $n_{\nu,\mathrm{Sun}} = 2.17$ cm^{-3} [92]. About 100 billion solar neutrinos pass through our thumbnail every second [11]. At MeV energies, other neutrino fluxes at Earth are also observed, as terrestrial neutrinos, also called geoneutrinos, produced by radioactive decays inside the Earth [94]. The flux from SN 1987A and the

11 The value of number density at Earth changes by ±3.4% in the course of the year due to the ellipticity of the Earth's orbit [93].

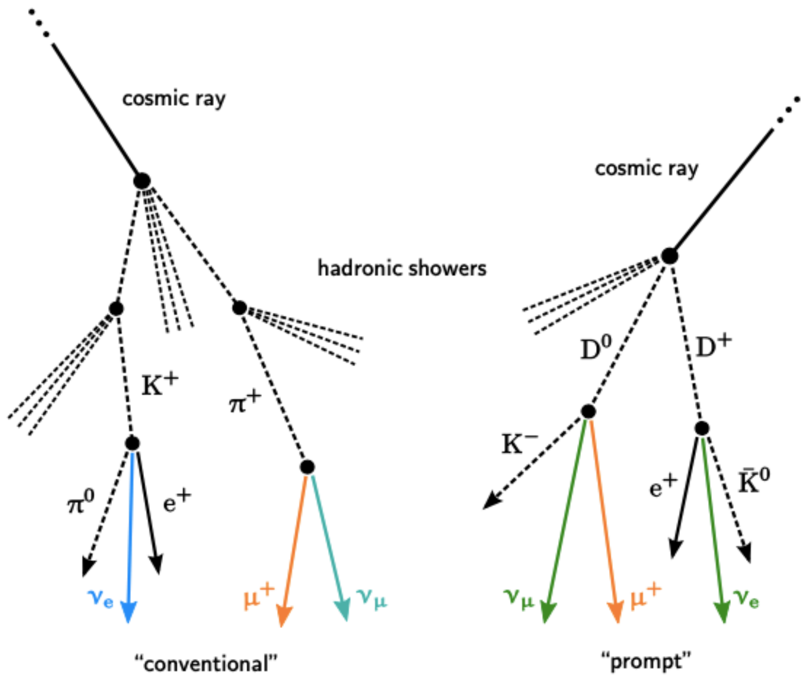

Figure 1.9: Sketch of the two types of atmospheric air shower resulting from the CR interaction with nuclei in the Earth's atmosphere. Muons and neutrinos from pion and kaon decays are referred to as conventional; those from the decay of charm mesons as prompt. Image credit: [89].

associated diffuse supernova neutrino background are shown too [95]. At higher energy, the neutrino's sky is dominated by atmospheric neutrinos, produced by CR interactions in the atmosphere [96]. Above ~ 100 TeV, it is expected that this flux is exceeded by astrophysical ν fluxes produced in extragalactic sources such as AGNs and GRBs [97–100]. Such neutrinos are produced by CR collisions with photons or nuclei near the acceleration regions (see Sect. 1.5.2). When CRs collide with CMB (this is the case for UHECRs that suffer from the GZK effect), cosmogenic neutrinos (GZK neutrinos) are produced [101].

1.3.2 *High-energy neutrinos of atmospheric origin*

As it will be better discussed in Chapter 2, the main background we must account for, when performing a search for astrophysical neutrinos, comes from neutrinos with $E_\nu > 100$ GeV produced in the Earth's atmosphere. They are the result of CR interactions with nuclei constituting the atmosphere through the production of unstable secondary particles, which in turn decay and produce atmospheric neutrinos. Depending on the nature of the secondary particles produced, there are two kinds of atmospheric neutrinos, which is usually referred to: *conventional* (modelled, e.g., in [102, 103]) and *prompt* neutrinos (e.g., [104]). As visible in Fig. 1.9, conventional atmospheric neutrinos are created from the decay of charged pions and kaons; the prompt component, instead, results from decay of mesons that contain heavy quarks (mostly charm quarks), such as D-mesons (or, more generally, charm mesons). Neutrinos and antineutrinos of atmospheric origin are dominantly electron neu-

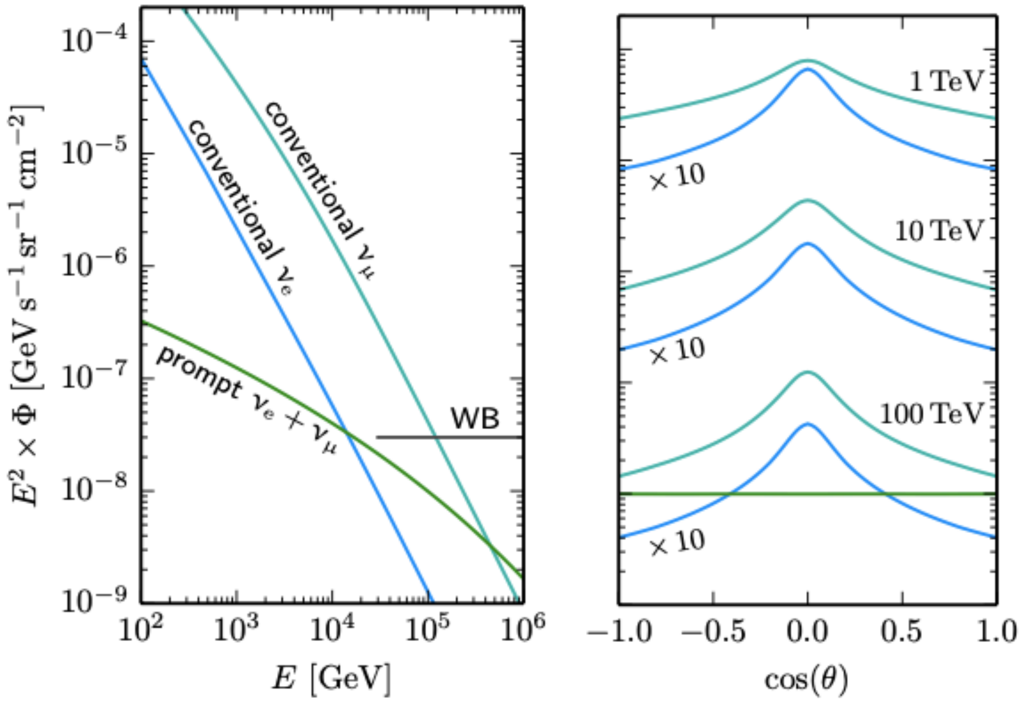

(a)

(b)

Figure 1.10: (a) Fluxes of conventional [103] and prompt neutrinos [104] as a function of the neutrino energy. Electron and muon conventional neutrinos are shown separately, through the cyan and teal lines, respectively; the prompt neutrino flux is shown in green as sum of the muon and electron component. The Waxman-Bahcall bound [100, 107], i. e. an upper limit on the flux of high-energy neutrinos derived from the observed flux of UHECRs (see Sect. 1.6.1), is also shown by the gray line. (b) Same fluxes as in (a) as a function of the cosine of the zenith angle θ. The vertical axes are scaled with E^2 for better readability. Images credit: [89]

trinos ν_e and muon neutrinos ν_μ[12]. In particular, conventional ν_μ and ν_e are produced with proportion $N_{\nu_\mu} \simeq 2N_{\nu_e}$, since pions predominantly decay into ν_μ rather than ν_e (see Fig. 1.10(a))[13]. Note that when CRs interact, they also produce neutral pions that decay to photons ($\pi^0 \to \gamma\gamma$), establishing a connection between high-energy photons and neutrinos (see Sect. 1.5). Pions and kaons, instead of decaying, can also interact with air molecules. In fact, each particle is characterised by a *critical energy* below which decay prevails and above which interaction is more likely. For example, for charged pions, the critical energy amounts to ~ 115 GeV, and for charged and neutral kaons it is ~ 850 GeV and ~ 205 GeV, respectively. Therefore, the higher the pions/kaons energy, the smaller their chance to decay before losing a significant fraction of energy. This explains the spectrum of conventional atmospheric neutrinos, which behaves as the one of primary CRs at energies up to energies lower than 100 GeV ($\sim E_\nu^{-2.7}$), and then, in the region 100 GeV – 100 TeV, becomes steeper ($\sim E_\nu^{-3.7}$). For even higher energies, the neutrino flux is less and less polluted by the atmospheric component. The same is true for other secondary particles as

12 There is a small fraction of prompt atmospheric tau neutrinos from the decay of D_S mesons, but this flux is suppresses with respect to electron and muon ones by a factor ~ 20 [104].
13 More details on the decay channels and their branching ratios can be found in [105, 106].

well. This can be understood by considering, for example, the pion decay process. The most energetic pions carry away $\sim 1/5$ of the energy of the primary CR ($E_\pi \sim 1/5 E_p$ in case of protons), then every particle produced in turn carries away, on average, a similar amount of energy. Since there are two gamma rays from the π^0 decay and four particles from the $\pi^\pm$ and subsequent $\mu^\pm$ decay, it can be considered that, on average, the resulting photons are twice more energetic than the corresponding neutrinos, thus

$$\langle E_\gamma \rangle \simeq \frac{\langle E_p \rangle}{10} \rightarrow \langle E_\nu \rangle \simeq \frac{\langle E_\gamma \rangle}{2} \simeq \frac{\langle E_p \rangle}{20}. \tag{1.10}$$

From this result, recalling that above the so-called knee (around 3 PeV) the CR spectrum steepens, it is expected that the atmospheric neutrino spectrum extends up to $E_{\text{knee}}/20 \sim 100$ TeV: for $E_\nu > 100$ TeV the sky starts to become more and more free from conventional neutrinos, leaving possible cosmic neutrinos (described in Sect. 1.3.3) to emerge. Prompt neutrinos follow a spectrum shape that reflects the CR one, that is $\sim E_\nu^{-2.7}$. In fact, charm mesons, characterised by lifetimes of 10^{-12} s or less and critical energies above 10 PeV [5], immediately decay with a tiny interaction possibility with other nuclei in the atmosphere. Thus, since above $\sim$ 100 TeV the prompt neutrino flux decreases less strongly with increasing energy than the conventional one, it presumably exceeds the conventional spectrum at high energies. So far, prompt neutrinos have not yet been experimentally identified and it has not been possible to constrain their theoretical predictions, which remain highly uncertain due to poor knowledge of the charm-meson production processes [108, 109]. Quite recent calculations have shown that, by taking into account the latest measurements of the hadronic cross sections, the expected flux of prompt neutrinos should be lower than its previous estimations [110]. Fig. 1.10 shows the fluxes of conventional and prompt atmospheric neutrinos, as described above, as a function of the neutrino energy (Fig. 1.10(a)), as well as of the zenith angle θ (Fig. 1.10(b)). A higher quantity of conventional neutrinos is expected towards the horizon ($\cos\theta = 0$), because pions and kaons coming from vertical directions are able to reach very fast the denser regions of the Earth's atmosphere, where the interaction is more likely than decay.

1.3.3 *Cosmic neutrinos*

To date, neutrinos from extragalactic sources have been detected. The first detection of neutrinos in coincidence with an astrophysical source goes back to more than forty years ago, when the observation of solar neutrinos was claimed [111]. Then, in 1987, both Kamiokande II [112] (the biggest neutrino experiment at that time) and Irvine-Michigan-Brookhaven (IBM) [113] detectors observed a neutrino burst from the supernova SN 1987A in the Large Magellanic Cloud. The former showed that neutrinos are massive particles with a tiny mass, unexpected by the Standard Model of particle physics. The latter confirmed that core-collapse SN phenomena emit neutrinos, as only theoretically predicted until then. Both such observations are considered milestones in neutrino astronomy, on which this thesis is focused.

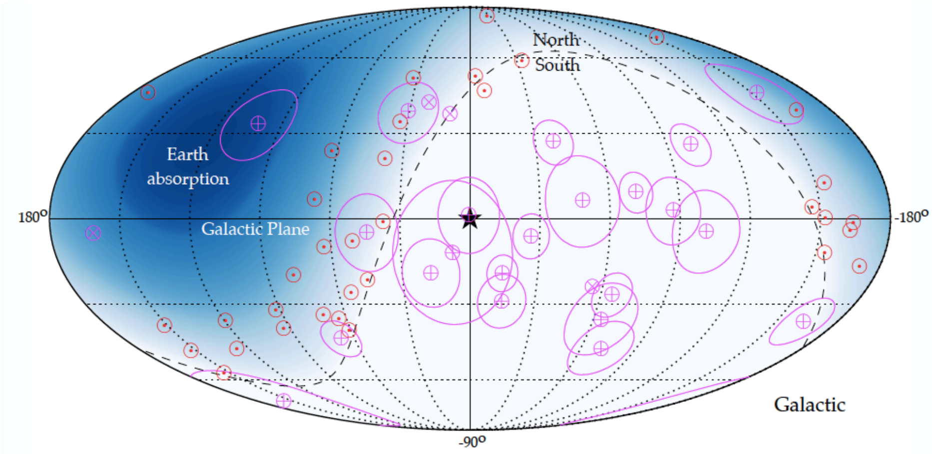

Figure 1.11: Map in Galactic coordinates showing the most energetic astrophysical neutrino events discovered by the IceCube neutrino telescope. HESE events in 6 years of data are shown in magenta; $\nu_\mu + \bar{\nu}_\mu$ tracks in 8 years of data are shown in red. Circles around each event give an indication of the uncertainty on their reconstructed direction. Image credit: [116].

However, only after decades, high-energy neutrino astronomy had its turning point in 2013, with the discovery by IceCube (the high-energy neutrino telescope located in the Southern Hemisphere and presented in Sect. 2.7.1), of a diffuse flux of TeV-PeV neutrinos (more than 6σ of statistical significance), without evidence of preferred directions in the sky, in excess with respect to atmospheric neutrinos [114, 115]. This discovery allowed us to state that extremely energetic astrophysical neutrino sources exist, but their identity is still unknown. Since the first discovery, the search for cosmic neutrinos has continued through multiple detection channels. These aspects will be explained in detail in Sect. 2. Some concepts useful for understanding what is described in the following are introduced here. In neutrino experiments, neutrino-induced events are detected: charged current (CC) ν_μ interactions result in a muon that at high energies can travel many kilometres producing a long track-like signature in the detector with typical angular resolution $< 1^\circ$ (these are the so-called *track events*); in addition, neutral current (NC) ν_μ interactions and CC interactions of both ν_e and ν_τ produce a shower of particles of short size with relatively poor angular resolution, i. e. few degrees (*shower events*, also called *cascade events*). Taking advantage of their features, neutrino events can be classified for different analyses in several ways. The IceCube detector, for example, has firmly established the existence of the high-energy astrophysical neutrinos mentioned above with all-sky measurements using events with interaction vertices contained in the detector fiducial volume (*high-energy starting events*, HESE) and *through-going muon tracks* (ν_μ tracks traversing the whole detector). Some of these events are shown in Fig. 1.11, where it is visible that their angular distribution is consistent with an extragalactic origin. Assuming an isotropic astrophysical neutrino flux at Earth in flavor equipartition[14], the differential energy flux ($\phi_\nu \simeq \frac{\mathrm{d}\phi_\nu}{\mathrm{d}E}$) can

14 Under the assumption the neutrinos are produced in charged meson decays, their flux at the souce has a flavor composition of $\nu_e : \nu_\mu : \nu_\tau = 1:2:0$. Vacuum oscillations over cosmic distances produce equipartition in the three flavours at Earth: $\nu_e : \nu_\mu : \nu_\tau = 1:1:1$.

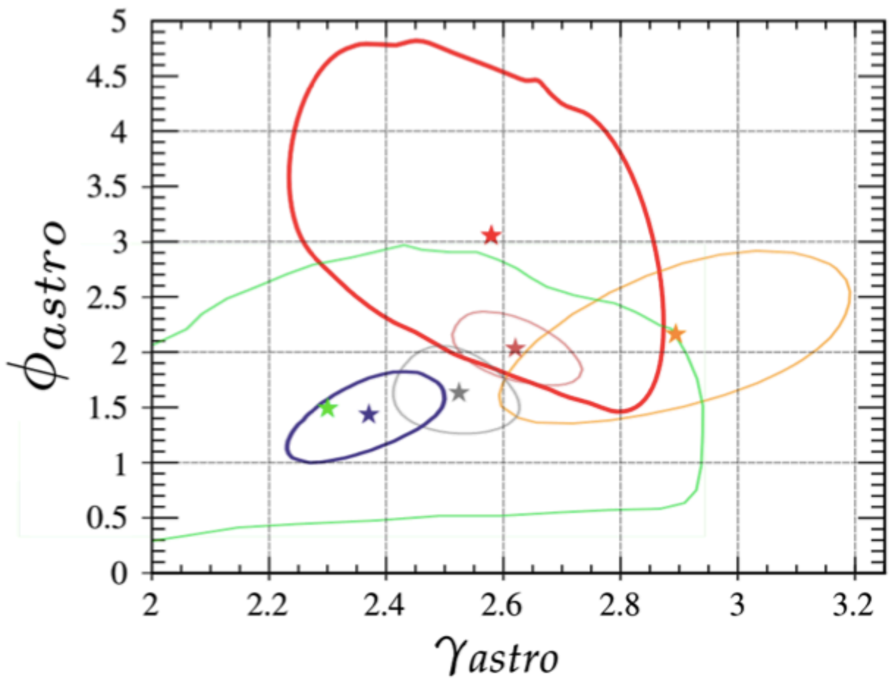

Figure 1.12: Summary of all diffuse neutrino flux measurements. Best-fit parameters and uncertainty contours at 68% CL for the single power-law hypothesis (see Eq. (1.11)) are drawn for IceCube studies based on HESE (7.5 years, full-sky) [117] in yellow, cascade-like events (6 years, full-sky) [119] in gray, through-going tracks (9.5 years, Northern hemisphere) [118] in dark blue, and an inelasticity study [120] in light red. The ANTARES result obtained through the combination of tracks and cascades (6 years, full-sky) [121] is shown in green. Recent Baikal-GVD results (2018-2021, upward-going cascade analysis) are shown in red. Image credit: [122].

be well modelled by a single power law with spectral index γ_{astro} and normalisation ϕ_0^{astro},

$$\phi_{\nu+\bar{\nu}}^{\text{astro}} = c_{\text{units}} \times \phi_0^{\text{astro}} \left(\frac{E_\nu}{100\ \text{TeV}} \right)^{-\gamma_{\text{astro}}}, \tag{1.11}$$

with $c_{\text{units}} = 10^{-18}\ \text{GeV}^{-1}\ \text{cm}^{-2}\ \text{s}^{-1}\ \text{sr}^{-1}$. The latest published results by IceCube for the best-fit spectral index and flux normalisation values are summarised in the following:

- HESE sample, collected in 7.5 years of data ($E_\nu > 60$ TeV) with six neutrino species combined [117]: $\gamma_{\text{astro}} = 2.87^{+0.20}_{-0.19}$ and $\phi_0^{\text{astro}} = 6.37^{+1.46}_{-1.62}$;
- astrophysical muon neutrinos from the Northern hemisphere in 9.5 years of data (15 TeV – 5 PeV) [118]: $\gamma_{\text{astro}} = 2.28^{+0.08}_{-0.09}$ and $\phi_0^{\text{astro}} = 1.44^{+0.25}_{-0.24}$;
- showers events in 6 years of data (16 TeV – 2.6 PeV) [119]: $\gamma_{\text{astro}} = 2.53^{+0.07}_{-0.07}$ and $\phi_0^{\text{astro}} = 1.66^{+0.25}_{-0.27}$.

Despite some differences in γ_{astro} values arising from different analyses, they are all consistent within uncertainties. It has recently been demonstrated that, through combined analyses using both high-energy cascades and through-going muon tracks in 10 years of IceCube data, the spectrum characteristics can be inferred as $\gamma_{\text{astro}} = 2.37^{+0.04}_{-0.05}$ and $\phi_0^{\text{astro}} = 1.36^{+0.09}_{-0.15}$

[123]. In addition, the ANTARES neutrino telescope, operative in the Northern Hemisphere until the early 2022 (refer to Chapter 2 for a detailed description of the instrument), provided some valuable information on the study of this diffuse flux of cosmic neutrinos [121, 124]. The last published results refer to 9 years of ANTARES data collected from 2007 to 2018 in both the track and shower channels. A mild excess of events was found over the expected atmospheric backgrounds (1.8σ excess), unfortunately without reaching the minimum significance needed to claim a detection. The best-fit cosmic flux yields $\gamma_{\rm astro} = 2.3^{+0.4}_{-0.4}$ and $\phi_0^{\rm astro} = 1.5^{+1.0}_{-1.0}$ [121]. Interestingly, very recently the Baikal-GVD Collaboration published its first measurements of the astrophysical neutrino flux using samples of cascade events collected in 2018-2021 [122]. Two different analyses have been performed: one using a sample of high-energy showers with energy greater than 70 TeV from all-sky directions, and another one using a subsample of upward moving cascades with energy greater than 15 TeV. In the latter case, an excess of the expected number of atmospheric background was estimated with a 3.05σ significance. By performing a global fit of all the selected neutrino data, information about the astrophysical neutrino flux were extracted: assuming a single power law model with identical contribution from each neutrino flavor, the spectral index $\gamma_{\rm astro} = 2.58^{+0.27}_{-0.33}$ and the flux normalisation $\phi_0^{\rm astro} = 3.04^{+1.52}_{-1.21}$ per one flavor at 100 TeV were found as best-fit parameters values. These results are in good agreement with the previous fits derived by IceCube and ANTARES and represent the first confirmation (at 3σ significance level) of the astrophysical neutrino flux detected by IceCube. Fig. 1.12 collects all the results discussed so far, including also another independent estimation given by IceCube from the study of the ratio between the energy in hadronic cascades produced in ν_μ CC interactions and the energy of the interacting neutrino itself (this quantity is called *inelasticity*) [120]. The diffuse flux level agrees across analyses, within their overlapping energy regions. However, there are mild tensions between spectral indexes for a single power law for energies above 1 PeV, where softer ones seem to be statistically more favourable at 2σ level [118].

In principle, the observed diffuse flux should contain contributions from both Galactic and extragalactic sources, as well as from the diffuse Galactic Plane emission. Taking advantage of the ANTARES detector visibility, which also includes the Galactic centre because of its location, a joint analysis between IceCube and ANTARES (note that IceCube and ANTARES have complementary field of view) allowed constraining the Galactic contribution to the diffuse flux to be subdominant ($< 10\%$) between 10 PeV and 1 TeV [125], namely the region where the transition between Galactic and extragalactic CR acceleration is expected to occur (see Sect. 1.1). Moreover, no significant steady or transient emission from known Galactic and extragalactic sources has been found so far, even if some interesting candidates have been identified. In 2017, the blazar TXS 0506+056, an AGN with a relativistic jet pointing towards the Earth, was identified as the first possible extragalactic astrophysical source that emits neutrinos (with significance at the 3σ level) and thus accelerates CRs [126]. This constitutes the first multimessenger neutrino-gamma detection, result of extensive multiwavelength monitoring by several telescopes (see Sect. 1.6.2 dedicated to the real-time analysis strategy in multimessenger studies). Driven by this association, IceCube also looked at their archival data, and interestingly found independent evidence (3.5σ) of a flare in neutrinos (four times higher than that in γ rays) from the same direction of the sky between September 2014 and March 2015. A second possible source very recently associated with astrophysical neutrinos (4.2σ significance) is the starburst galaxy NGC 1068 [127], whose first indications of neutrino emission arose few years ago with significance a bit below 3σ [128]. In addition to these sources, other studies have also shown some indications of correlations between the tidal disruption event[15] AT2019dsg [129] and radio-bright AGNs [130] with astrophysical neutrinos. However, all these results are insufficient to explain the origin of the observed diffuse astrophysical neutrino flux, which still remains an open and actively discussed point in the field of neutrino astronomy.

An important point to highlight here is that all these studies were made possible thanks to the combination of multimessenger observations. Refer to Sect. 1.6.1 for a more detailed treatment of the connections between the cosmic messengers discussed, and Sect. 1.6.2 for the description of the real-time analysis strategy adopted by multimessenger instruments with the aim of sharing information coming from their observations.

1.4 GRAVITATIONAL WAVES

The most violent cosmic events produce a form of radiation that is distinct from those discussed so far and is directly related to gravity. Indeed, space-time is curved by massive objects and their gravity. As a massive object moves, it induces oscillations of the space-time metrics that propagate away, travelling at the speed of light. These changes are called Gravitational Waves (GW) and were predicted at the beginning of the last century by the general theory of relativity developed by A. Einstein. Their coupling with matter and radiation is extremely weak, so these messengers can propagate without significant attenuation, scattering, or dispersion on their way through the Universe.

GWs have been the last messengers discovered observationally. On September 2015 the first GW was detected by the two Laser Interferometer Gravitational Wave Observatory (LIGO) detectors, based in the USA, in collaboration with the Italian interferometer Virgo (located close to Pisa, in Tuscany) [131]. For the first time, there was observational evidence of the inspiral of two stellar-mass BHs and the subsequent merger into a more massive BH resulting from this process; this event occurred 1.3 billion lightyears away. This detection represents the dawn of gravitational wave astronomy: gravitational waves, can be used as a new fundamental messenger to explore the Universe and probe its most energetic events.

Many GW detections have followed from 2015 until now (the number of known gravitational wave sources has increased to ~ 100), among which GW 170817 deserves a particular mention: it is indeed the first GW associated with the observation of an electromagnetic event [132], namely the short GRB 170817A (gamma-ray explosion with duration less than 2 seconds), detected through other multiwavelength signals [133]. GW 170817 was gener-

15 A tidal disruption event is an astronomical phenomenon that occurs when a star approaches sufficiently close to a supermassive black hole to be pulled apart and shredded by the black hole's tidal force, producing a luminous flare.

ated by the merger of a binary system containing a Neutron Star (NS) and a BH. In such a case, the fast movement of the NS and BH around each other and the presence of a lot of NS material allowed the engine resulting from the merger to create a cataclysmic explosion that produced gamma-ray emission, optical light, X-rays, and radio waves. It is also important to point out here that this discovery was fundamental for GRB progenitor theories, because it was the experimental confirmation of the fact that short GRBs bursting in the sky originate from the merger of two compact objects (for details, see Chapter 3). This was also the first experimental evidence of a kilonova [134], a type of transient event expected from neutron star mergers where heavy elements are produced through the so-called *r*-process nucleosynthesis[16].

Even many years before the GW discovery, it was expected that the same astrophysical sources that are able to accelerate CRs and subsequently produce gamma rays and neutrinos also emit transient gravitational wave signals. Now there is the probe of this assumption and GWs have very actively started to play in the field of multimessenger astronomy helping in making clearer the understanding of the sources filling our cosmos. In particular, since the gravitational-wave spectrum ranges over more than twenty orders of magnitude, from 10^{-9} Hz to thousands Hz, several classes of astrophysical sources can in principle be investigated, as super-massive BH[17] inspiral and merger, extreme-mass-ratio inspirals (when a neutron star or stellar-mass BH collides with a super-massive BH), compact binary inspiral and merger, pulsar, supernovae. To this aim, gravitational-wave detectors sensitive to different frequency ranges can be used. Terrestrial interferometers, as LIGO and Virgo, operate in the ν range between ~ 10 Hz and ~ 10 kHz, and with the current technology they are able to reveal coalescing binary BH and NS systems and (as yet to be observed) supernovae and isolated neutron stars. Future space-based interferometers, such as the Laser Interferometer Space Antenna (LISA) [135], will target GW sources from milliseconds up to hundreds of microseconds and trace the evolution of BHs from the early Universe; it will also be able to map the curvature of spacetime at the event horizons of massive BHs. For an overview about recent discoveries and the potential science with future GW observations, the reader can refer to [136].

Gravitational waves are unique messengers able to reveal information on the dynamics of cosmic events, as the formation and evolution of compact objects. The knowledge obtained thanks to GWs can be combined with those of the other cosmic messengers (CRs, photons, and neutrinos) that instead carry information about accretion, particle acceleration, and interactions. Note that, since the acceleration of particles by compact objects is still not well understood, a coincident observation of neutrinos could be the "smoking gun" for evidencing the occurrence of hadronic processes and help in understanding the dissipation mechanisms active in relativistic outflows. Unfortunately, no neutrino-GW combined detection has occurred so far.

16 *Rapid neutron capture nuclear process*: a nucleus rapidly increases its atomic number by repeatedly capturing neutrons in a neutron-rich environment.

17 Super-massive BHs are characterized by masses between 10^5 and 10^6 solar masses. This kind of BH forms when galaxies merge and is present at the centre of most galaxies.

1.5 cosmic messenger production mechanisms

To better understand how the cosmic messengers described so far can be used to extract information on the properties of astrophysical sources, it is important to discuss the physical mechanisms responsible for the production of such particles. In the present section, the connection between the observed photon spectra and the charged CRs is explained, as well as the models that make possible an associated neutrino production in astrophysical sources. In particular, in Sect. 1.5.1 the model commonly used for the acceleration of charged CRs is outlined; then, Sect. 1.5.2 describes the radiative processes responsible for the production of high-energy photons and high-energy neutrinos, providing a direct link between CRs, photons and neutrinos.

1.5.1 *Acceleration of charged cosmic rays: the Fermi mechanisms*

A basic hypothesis that allows the acceleration of charged CRs produced by particle injection in several possible astrophysical sources is the presence of variable magnetic fields. These, indeed, may induce variable electric fields that can accelerate particles many times, through many acceleration cycles.

This idea was developed for the first time in 1949 by Enrico Fermi, who proposed a mechanism in which particles are accelerated in stochastic collisions with magnetic field irregularities (*magnetic mirrors*) moving isotropically in the interstellar medium [137]. The energy after collision with a cloud velocity $\beta = v/c$ increases on average by a factor

$$\left\langle \frac{\Delta E}{E} \right\rangle \sim \frac{4}{3}\beta^2. \tag{1.12}$$

For this reason, this mechanism is also known as *Fermi acceleration at second order* in β. Despite the natural prediction of power-law spectra for accelerated particles, matching the observation that the energy spectrum of CRs at Earth follows a power law over wide energy ranges (see Sect. 1.1), this model is not very effective. The random velocities of interstellar clouds in typical environments are very small, i. e. $\beta \sim 10^{-4}$, and this makes the process described inefficient.

An energy gain linear in β is instead needed to improve the efficiency of the acceleration mechanism, and this happens in the Diffusive Shock Acceleration (DSA) [138–142], also dubbed *first order Fermi acceleration mechanism*. This model improves the efficiency of the acceleration processes by considering the direction of the clouds strongly correlated, instead of being randomly distributed: they constitute strong shock wave fronts moving in the interstellar medium with supersonic velocities. For example, this happens when a supernova ejects a sphere of hot gas into the interstellar medium and, moving faster than the local speed of sound (i. e. of the speed of the pressure wave), is brought into a stationary gas that, in turn, behaves as an obstacle of expansion. In this situation, shown in Fig. 1.13, the shock wave propagates with a locally plane wave front; ahead and behind it there are two flows, one not yet reached by the shock (*upstream*) and the other one already

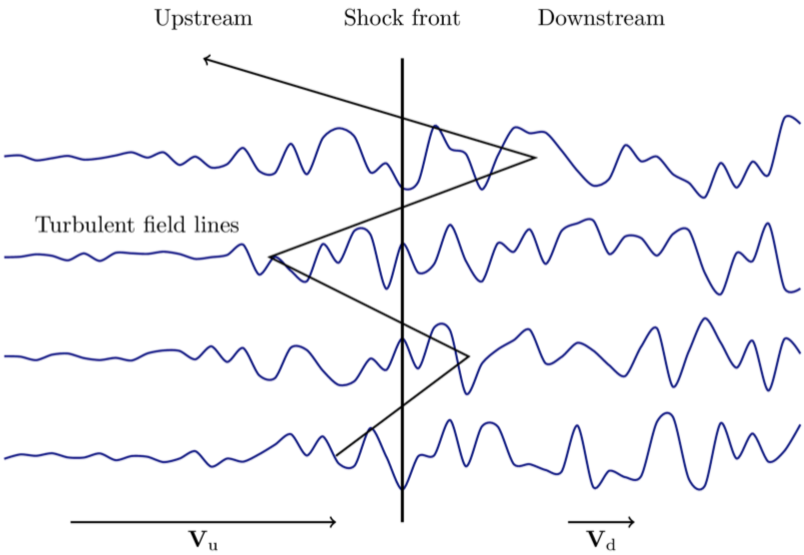

Figure 1.13: CR acceleration for a diffusing shock wave, in the reference frame of the shock. Image credit: http://sprg.ssl.berkeley.edu/~pulupa/illustrations/.

reached and exceeded by it (*downstream*), respectively. In the reference frame of the shock front, which behaves as a discontinuity between the two regions, the upstream flow passes through the shock with a supersonic velocity v_u, while the downstream one moves away with a velocity v_d. Let ρ_u and ρ_d be the gas densities in the upstream and downstream fluid, respectively; according to the kinetic theory of gases, in a supersonic shock propagating through a monoatomic gas (fully ionised gas) $v_d \sim v_u/4$. In the laboratory system, particles can pass through the shock in either direction by starting a series of diffusion processes, owing to the presence of a local turbulent magnetic field (bound-rebound cycle), causing particle acceleration. Here, the DSA is simply explained, following the derivation in [5], to which the reader is referred for a more detailed explanation. By considering the reference frame of one of the clouds (upstream or downstream), each bound-rebound cycle is equivalent from the point of view of the energy gain to a collision in the laboratory with a head-on component into a cloud moving with a certain velocity. Following the setup in Fig. 1.14, let us consider a charged particle with initial energy E_1 and velocity u crossing a shock front back and forth, returning to the unshocked medium with final energy E_2. In practise, the particle is scattering against a moving boundary between regions of different density (a partially ionised gas cloud). Due to the chaotic magnetic fields generated by its charged particles, the cloud, characterised by a velocity $\beta = v/c < u$, acts as a massive scatterer. The initial and final scattering angles, which are the angles between, respectively, the initial and final particle momentum and the cloud velocity, are θ_1 and θ_2. The energy of the particle in the cloud reference frame is given by (neglecting the particle mass with respect to its kinetic energy)

$$E_1' = \frac{E_1(1-\beta\cos\theta_1)}{\sqrt{1-\beta^2}}. \tag{1.13}$$

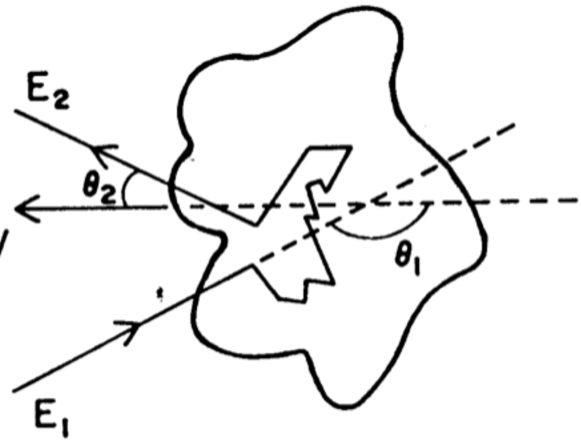

Figure 1.14: Scattering of a CR by a moving gas cloud. Image credit: [5].

After having passed through the shock front, the particle does multiple elastic scatterings, namely the cloud acts as a magnetic mirror. Thus, just before crossing again back into the unshocked medium, in the cloud reference frame $E_2^{'} = E_1^{'}$, and in the laboratory frame, the energy of the particle after the collision is

$$E_2 = \frac{E_2^{'}(1+\beta\cos\theta_2^{'})}{\sqrt{1-\beta^2}} = \frac{E_1(1-\beta\cos\theta_1)(1+\beta\cos\theta_2^{'})}{1-\beta^2}. \tag{1.14}$$

The relative energy gain is given by

$$\frac{\Delta E}{E} = \frac{(1-\beta\cos\theta_1)(1+\beta\cos\theta_2^{'})}{1-\beta^2} - 1. \tag{1.15}$$

and consequently the energy after the collision increases on average by a factor linear in β, as shown in the following,

$$\left\langle \frac{\Delta E}{E} \right\rangle = \frac{1+\frac{4}{3}\beta+\frac{4}{9}\beta^2}{1-\beta^2} - 1 \simeq \frac{4}{3}\beta \equiv \xi, \tag{1.16}$$

where $\langle\cos\theta_1\rangle \approx -2/3$ and $\left\langle\cos\theta_2^{'}\right\rangle \approx 2/3$, being $-1 \leq \cos\theta_1 \leq 0$ and $0 \leq \cos\theta_2^{'} \leq 1$. The amount of energy that increases after n collisions for an accelerated CR with initial energy E_0 becomes

$$E_n = E_0(1+\xi)^n, \tag{1.17}$$

and the number of cycles needed to reach it is

$$n = \frac{\ln\left(\frac{E}{E_0}\right)}{\ln(1+\xi)}. \tag{1.18}$$

The probability for a particle to cross the shock n times is given by $P_{E_n} = (1-P_\mathrm{e})^n$, considering that at each cycle a particle may escape from the shock region with some probability P_e. As the number of particles N with energy E_n is $N = N_0 P_{E_n}$, the probability that a particle is confined until it achieves an energy E_n is given by the ratio between the involved number of particles N and the initial one N_0, i. e.

$$P_{E_n} = N/N_0. \tag{1.19}$$

From Eq. (1.18) and Eq. (1.19), it is possible to obtain

$$\frac{N}{N_0} = \left(\frac{E}{E_0}\right)^{-\delta} \Rightarrow \frac{\mathrm{d}N}{\mathrm{d}E} \propto \left(\frac{E}{E_0}\right)^{-\Gamma}, \tag{1.20}$$

with $\delta = \ln P_{E_n} / \ln(1+\xi)$ and $\Gamma = \delta + 1$. Hence, the first-order Fermi acceleration mechanism predicts, with a more efficient energy gain with respect to the original model proposed by Fermi, that the cosmic-ray energy spectrum follows a power law. According to the classical kinetic theory, $\Gamma = 2$. However, the detected spectrum at Earth is steeper, as seen in Sect. 1.1. This difference can be explained by including diffusion processes that modify the CR energy spectrum during its propagation, as described in detail, e.g., in [5]. Thus, the first-order Fermi model provides remarkable agreement with the observed CR spectrum. Note that a different numerical treatment is needed to account for the relativistic speed. Because of these features and of the fact that shock fronts are common in astrophysical environments, e.g., in SNRs, the diffuse shock acceleration model is a widespread model for cosmic-ray acceleration. An extension of the simple model considered so far can be found in [143], where it is supposed that accelerated particles themselves can amplify the magnetic field at shocks during the acceleration process via plasma instabilities; in this way, the maximum attainable cosmic-ray energy increases.

However, as already highlighted in Sect. 1.1.4, the CR acceleration is limited by several contributions: energy loss processes (Bethe-Heitler production, pair production, nuclear photodisintegration, pion production, synchrotron radiation), finite acceleration sites (Hillas criterion) and the duration of the shocks. This last point can be explored taking advantage of the treatment used for the DSA. The acceleration time must satisfy the condition of Eq. (1.4). The probability for a particle to escape from a shocked region can be approximated as $P_e = T_{\mathrm{cycle}}/t_{\mathrm{esc}}$, where T_{cycle} and t_{esc} are the characteristic time for an acceleration cycle and for escape from the acceleration region, respectively. If an accelerator is characterised by a lifetime t_{age}, the number of cycles in an acceleration process that has been working in the meantime can be expressed as $n = t_{\mathrm{age}}/T_{\mathrm{cycle}}$. It follows that the energy of an accelerated CR (in Eq. (1.17)) needs to satisfy the following condition:

$$E \leq E_0(1+\xi)^{t_{\mathrm{age}}/T_{\mathrm{cycle}}}. \tag{1.21}$$

From Eq. (1.21) it is evident that (i) higher-energy particles take longer to accelerate than low-energy ones; (ii) if E_0 is the typical energy of injection into the accelerator, the maximum energy it can reach is constrained by its lifetime t_{age}[18].

18 Typically ~ 1000 years for the active phase of a supernova remnant.

To summarise, magnetic fields and shock waves are fundamental ingredients for CR acceleration. Both are expected to be present in several types of astrophysical source, i. e. SNRs, AGNs, and GRBs. In these objects, indeed, accelerated charged particles can interact with a cloud of molecular species, dust, photon gas expected from bremmstrahlung and synchrotron radiation.

1.5.2 *Leptonic and hadronic radiative processes*

Gamma rays, coming either from sources in our Galaxy and beyond, can be produced by radiative processes whose nature depend on the composition of the astrophysical sources that produce them. If these come from a population of sources made of only leptons or hadrons, we refer to *leptonic* and *hadronic* emission, respectively. The former case usually occurs when the astrophysical environment is full of relativistic leptons and is permeated by a magnetic field; in particular, the flux of gamma rays of leptonic origin is traced by the electron density and by the radiation fields. On the other hand, the flux of gamma rays of hadronic origin is due to the interaction of CRs with radiation fields and, thus, depends on the CR density and the target gas density. It is worth highlighting as of now that these hadronic interactions are responsible at the same time for a correlated production of high-energy neutrinos, crucial for the purposes of the present thesis.

In the following, leptonic processes are discussed. Many of the arguments presented here are taken from, e.g., [144–147]. Finally, hadronic processes are also described, together with the correlated production of high-energy neutrinos.

Synchrotron radiation

The synchrotron radiation is one of the most significant radiative processes, generated by a high-energy charged particle spiralling around magnetic field lines. The radiation from charges accelerated by magnetic fields in a non-relativistic regime is called cyclotron emission. When relativistic particles are considered, synchrotron radiation is created. For example, relativistic particles accelerated in astrophysical environments, where magnetic fields are present, emit this kind of radiation. According to the Larmor formula, the total radiated power emitted by the charged relativistic particle in a magnetic field with strength B, mass m, and charge number Z is

$$P_{\rm synch} = \left(\frac{\mathrm{d}E}{\mathrm{d}t}\right)_{\rm synch} = \frac{4}{3}\sigma_{\rm T} c U_B \beta^2 c^2 = \frac{3}{4}\sigma_{\rm T} Z^4 \left(\frac{m_e}{m}\right)^2 c\beta^2\gamma^2\frac{B^2}{8\pi} \tag{1.22}$$

where $\gamma = (1-(v/c)^2)^{-1/2}$ is the Lorentz factor of the particle moving with $\beta = v/c$, $\sigma_{\rm T} \simeq 6.65 \times 10^{-25}$ cm ^{2} is the Thomson cross section and $U_B = B^2/(8\pi)$ is the magnetic field energy density. Eq. (1.22) shows that synchrotron radiation is produced more efficiently by electrons, since the mass of an electron is about 1/2000 the mass of a proton ($m_e/m_p \sim 5\times 10^{-4}$). As a consequence, the radiated energy of electrons is a factor $\sim 10^{13}$ higher than that produced by protons that lose energy to synchrotron radiation only for extremely high energies and large magnetic fields. Most of the radiation from the charged particle is emitted around the *critical frequency* ω_c,

$$\omega_c = \frac{3qB\sin\alpha}{2mc}\gamma^2, \tag{1.23}$$

where α is the *pitch angle*, namely the angle between the particle's velocity vector and the local magnetic field. By considering that the energy of the primary shock-accelerated particle is $E_p = \gamma mc^2$, it is possible to derive the spectral shape of synchrotron radiation from an ensemble of particles. Since shock-accelerated primaries follow a power-law distribution with spectral index α_p[19],

$$\frac{\mathrm{d}N_p}{\mathrm{d}E_p}\mathrm{d}E_p \propto E_p^{-\alpha_p}\mathrm{d}E_p, \tag{1.24}$$

the total radiated power $P_{\text{tot}}(\omega)$, which depends on the frequency ω, can be expressed as

$$P_{\text{tot}}(\omega) \propto \int_{E_{p,1}}^{E_{p,2}} P(\omega)E_p^{-\alpha_p}\mathrm{d}E_p \propto \int_{E_{p,1}}^{E_{p,2}} F(x)E_p^{-\alpha_p}\mathrm{d}E_p. \tag{1.25}$$

In Eq. (1.25) we have considered that the power in Eq. (1.22) can be written in terms of a function that depends only on the variable $x = \omega/\omega_c$. Taking into account that $E_p \propto \gamma \propto \omega_c^{1/2}$, the total radiated power by synchrotron emission in Eq. (1.25) can be written as

$$P_{\text{tot}}(\omega) \propto \omega^{-\frac{(\alpha_p-1)}{2}} \int_{x_1}^{x_2} F(x)x^{\frac{(\alpha_p-3)}{2}}\mathrm{d}x. \tag{1.26}$$

Since the integral in Eq. (1.26) does not depend on the frequency, it has been derived that synchrotron emission is a nonthermal process[20]: the total synchrotron spectrum for accelerated primaries follows a power law with spectral index

$$s = (\alpha_p - 1)/2. \tag{1.27}$$

The final spectrum is interpreted as the superposition of various contributions of each single particle emitting at its own characteristic frequency. The observed photon spectrum depends on the emitting particles energy distribution; the differential spectral index of this secondary radiation is $\alpha_\gamma = -s - 1$, with $\mathrm{d}N_\gamma/\mathrm{d}E_\gamma \propto E_\gamma^{\alpha_\gamma}$. This is true in the so-called *slow cooling regime*, where the dynamical timescale of the system is much shorter than the cooling timescale of electrons due to radiation losses [148]. In the opposite case (*fast cooling regime*), the photon spectrum is flatter by a factor of 1/2.

The synchrotron spectrum can be altered by further radiation effects. For example, if the intensity of synchrotron radiation within a source becomes sufficiently high, then re-absorption of the radiation by the synchrotron electron themselves becomes important. This re-absorption of radiation is known as *synchrotron self-absorption*, and drastically mod-

19 Electrons and protons follow the same distribution, i. e. the spectral index of electrons is the same as for the protons.
20 The energy spectrum of charged particles does not follow a Maxwellian distribution.

ifies the synchrotron spectrum of the source at low energies, typically sharpening the cutoff.

Compton scattering and inverse Compton process

Compton scattering occurs when high-energy photons scatter on electrons, and a new photon with lower energy emerges; part of the energy of the initial photon is transferred to the recoiling electron. However, in astrophysical applications it is the *Inverse Compton* (IC) scattering that plays an important role than the Compton scattering itself. This process occurs when high-energy electrons interact with a low-energy photon: the photons gain energy and the electrons lose energy. It is called "inverse" because the electrons lose energy rather than the photons, the opposite of the standard Compton effect. The power that characterises the radiation obtained with the IC scattering is given by

$$P_{\mathrm{IC}} = \frac{4}{3}\sigma_{\mathrm{T}} c U_{\gamma} \beta^2 c^2, \tag{1.28}$$

similarly to that of synchrotron radiation, in Eq. 1.22. Both IC and synchrotron radiation are, in fact, due to accelerated electrons. However, the energy densities differ since, in the case of the IC process, U_B is replaced by the energy density of seed photons, U_γ: the radiation losses due to synchrotron emission and the IC effect are in the same ratio as the magnetic field energy density and photon energy density. This is related to the different origin of the electric field that accelerates electrons. As regards the synchrotron radiation, the constant accelerating electric field is associated with the motion of the electron through the magnetic field; instead, in the case of IC scattering, it is the sum of all the electric fields of the electromagnetic waves incident on electron. The IC spectrum, i.e. the radiation produced by scattering of a photon with a certain frequency by an electron, is very peaked, even more than the synchrotron $F(x)$ function (see Eq. (1.26)). Scattered photons gain a factor γ^2 in frequency, and thus in energy. Thanks to the similarity between IC and synchrotron emission, it is possible to use the same procedure as the one adopted in the case of synchrotron radiation to work out the spectrum of radiation produced by a power-law distribution of electron energies. The spectral index of the scattered radiation results to be the same as in Eq. (1.27).

The results discussed above are very important in astrophysics because it is well known that there are several astrophysical sources in which electrons are characterised by Lorentz factor with values $\gamma \sim 10 - 1000$. In such cases, these electrons scatter any low-energy photon to much higher energies; for example, from radio, far-infrared, and optical photons, electrons with $\gamma = 1000$ are able to create high-energy UV photons, X-rays, and γ-rays, respectively. IC scattering is likely to be an important source of X-rays and γ-rays, for example, in intense extragalactic γ-ray sources, as GRBs discussed in Chapter 3.

Synchrotron Self-Compton

When IC occurs in synchrotron self-absorbed sources, the process is known as *Synchrotron Self-Compton* (SSC). Ultrarelativistic electrons accelerated in a magnetic field generate synchrotron photons, with an energy peaking in the infrared/X-ray range (eV-keV). Such photons, in turn, interact via IC scattering with the same population of ultrarelativistic particles producing the radiation. In such a way, the energy of photons is highly increased (from eV to TeV). Let us consider a population of relativistic electrons with energy E_e and soft photons with energy ϵ_e, described by a power law with a differential spectral index q and a black-body spectrum (Maxwellian distribution), respectively. For scattered photons with energy E_γ, the following relations can be derived:

$$\langle E_\gamma \rangle \simeq \frac{4}{3}\gamma_e^2 \langle \epsilon_e \rangle \,, \tag{1.29}$$

$$\frac{\mathrm{d}N_\gamma}{\mathrm{d}E_\gamma} \propto E_\gamma^{-\frac{q+1}{2}} \,. \tag{1.30}$$

Eq. (1.29) and Eq. (1.30) are valid for $\gamma_e \epsilon_e \ll m_e c^2$, called *Thomson regime*. A useful approximate relation between the energy of the scattered photons E_γ, the energy of the parent electron E_e, and the energy of the seed photon ϵ_e is given by

$$E_\gamma \simeq 6 \left(\frac{E_e}{\mathrm{GeV}} \right)^2 \left(\frac{\epsilon_e}{\mathrm{eV}} \right) \ \mathrm{TeV}. \tag{1.31}$$

When $\gamma_e \epsilon_e \gg m_e c^2$ (*Klein-Nishina regime*) the cross section becomes smaller than σ_T and decreases with increasing photon energy as ν^{-1}. In this case, the following relations become valid:

$$\langle E_\gamma \rangle \simeq \frac{1}{2} \langle E_e \rangle \,, \tag{1.32}$$

$$\frac{\mathrm{d}N_\gamma}{\mathrm{d}E_\gamma} \propto E_\gamma^{-(q+1)} \ln E_\gamma . \tag{1.33}$$

Therefore, in the Klein-Nishina regime the IC gamma-ray spectrum is expected to be significantly steeper (compare Eq. (1.30) and Eq. (1.33)).

The energy spectrum resulting from the SSC is the sum of the synchrotron and IC components, peaking at keV and GeV-TeV energies, respectively. This behaviour has been verified with high precision in the Crab Nebula (e.g., [149]), and several other sources such as AGNs and GRBs.

Hadronic origin of gamma rays and neutrinos

The leptonic processes discussed so far create high-energy γ-ray photons, that in turn can also be produced in π^0 decays. Neutral pions are produced in collisions between relativistic protons and nuclei of atoms and ions of the interstellar gas, as well as from proton interaction with photon fields. Such a hadronic scenario leads to the production of high-energy neutrinos from the decay of charged mesons.

The hadronic interaction of protons with radiation fields occurs mainly with the production of the Δ^+ hadron ($m_{\Delta^+} = 1232$ MeV$/c^2$). Indeed, its largest cross section corresponds to the Δ rest energy (resonant Δ^+ production), with a value of $\sigma_{p\gamma} = \sigma_\Delta \simeq 5 \times 10^{-28}$ cm^2. The delta barion has two main decay channels:

$$p + \gamma \xrightarrow{\Delta^+} \begin{cases} p + \pi^0, & \text{fraction } 2/3 \\ n + \pi^+, & \text{fraction } 1/3 \end{cases} \tag{1.34}$$

Neutral pions immediately decay (their lifetime at rest is $\sim 8.5 \times 10^{-17}$ s), and produce high-energy gamma rays:

$$\pi^0 \to \gamma + \gamma. \tag{1.35}$$

As a result of the neutral pion decay from hadronic interactions, a distinct bell-type feature is present in the energy spectrum of γ rays between 100 MeV and few GeV, and it is commonly known as *pion bump* [150]. The resulting broad-band γ-ray spectra have been studied in various astrophysical environments such as solar flares, interstellar medium, SNRs, molecular clouds, galaxy clusters [151–153], and have been claimed to be detected towards several young SNRs [154–156]. This was interpreted as evidence of the acceleration of CRs in SNRs. However, the pion bump is not easy to recognise in gamma-ray spectra; several processes can distort the spectrum around the pion bump feature, as investigated in [157].

The production of an energy flux of neutrinos is led by the decay of charged pions (their lifetime at rest is 2.6×10^{-8} s) and the subsequent muon decay, in analogy to atmospheric neutrino production (see Sect. 1.3.2):

$$\begin{aligned} \pi^+ \to & \mu^+ + \nu_\mu \\ & \mu^+ \to e^+ + \nu_e + \bar{\nu}_\mu \end{aligned}$$

Note that the Δ^+ production can be also non-resonant if the $p\gamma$ centre-of-mass energy is larger than the Δ mass; in this case the probability of meson production is about $1/2$ both for neutral and charged pions. The energy related to the secondary pion (this quantity is called *inelasticity*) is $k_\pi \simeq 0.2$ [158].

With regard to inelastic pp and pn interactions, the reaction chains are shown in the following:

$$p + p \to \begin{cases} p + p + \pi^0 \\ p + n + \pi^+ \end{cases} \tag{1.36}$$

$$p + n \to \begin{cases} p + n + \pi^0 \\ p + p + \pi^+ \end{cases} \tag{1.37}$$

The cross section for π production is almost energy independent and assumes the value $\sigma_{pp} \simeq \sigma_{pn} \simeq 2 \times 10^{-26}$ cm^2. Gamma-ray and neutrino production occurs in the same way as in proton-photon interactions. By analogy, in pn collisions, the resulting negative pions are responsible for neutrino production ($\pi^- \to \mu^- + \bar{\nu}_\mu$; $\mu^- \to e^- + \bar{\nu}_e + \nu_\mu$). In hadronic collisions positive, negative and neutral pions are produced with equal probability 1/3, and the inelasticity is $k_\pi \simeq 0.5$ [158]. In charged-pion decays, the energy of each neutrino can be approximated as $\sim 25\%$ of the pion energy ($k_\nu \simeq 1/4$), corresponding to $\sim 5\%$ of the energy of the initial proton. Taking into account the proton redshift energy loss from the astrophysical source to Earth, the resulting neutrino energy is $E_{\nu,\mathrm{obs}} = 5\ \mathrm{PeV}\frac{E_{p,\mathrm{source},17}}{(1+z)}$, where $E_{p,\mathrm{source},17}$ is the proton energy at the source in units of 10^{17} eV. This relation suggests that PeV neutrinos could be produced by pion photoproduction by protons with energies close to $\sim 10^{17}$ eV, namely the second knee. In neutral pion decays, the energy of each photon is $\sim 50\%$ of the pion energy ($k_\gamma \simeq 1/2$). Neutrinos are also produced by the beta decay of neutrons in Eq. (1.34) and Eq. (1.37): $n \to p + e^- + \bar{\nu}_e$. Note that neutrinos are produced by cosmic accelerators with a flavour mixture ($\nu_e : \nu_\mu : \nu_\tau = 1:2:0$), but arrive on Earth with a modified ratio ($\nu_e : \nu_\mu : \nu_\tau = 1:1:1$) due to neutrino oscillations.

Detailed model predictions exist for various source classes (see, e.g., [159] for a review of sources).

1.6 THE MULTIMESSENGER PICTURE

A diffuse flux of cosmic neutrinos has been detected in the last years (see Sect. 1.3.3), proving the existence of some CR accelerators in the Universe, most likely extragalactic, though still unassociated to any specific source population. Because of the consistency of the arrival directions of such neutrinos with an isotropic distribution, after correcting for the angular acceptance of the detector and Earth absorption, the neutrino signal is likely to originate from a population of relatively weak extragalactic sources. High-energy neutrinos can be produced only through hadronic models that require the acceleration of CRs in astrophysical environments. For this reason, these cosmic messengers are believed to be related to each other. In Sect. 1.6.1, the cosmic messengers connection is explained, while Sect. 1.6.2 gives an overview of the common approach adopted by current instruments working in the multimessenger field: these cooperate and share between each other part of their observational results with the idea of triggering as many studies as possible, namely through CRs, γ-rays, νs, and GWs, to achieve a deeper and deeper view of the sources populating our Universe.

1.6.1 *Cosmic messengers connection*

In Fig. 1.15, the IceCube diffuse cosmic neutrino flux measurements are compared with the isotropic extragalactic γ-ray background observed by Fermi [160] and UHECRs data collected by Pierre Auger. It is possible to see that their energy densities are comparable, so we can conclude that the same amount of gamma rays, neutrinos, and CRs of extreme energies is injected into our Universe. This consideration suggests that the three particle populations might be connected and originate from the same source class (e.g., [116, 161]). As we have already discussed before, hadronic models can produce both γ rays and neutrinos via CR interaction with ambient matter or radiation and subsequent pion decay (see Sect. 1.5). Let us discuss in the following several points emerging from Fig. 1.15:

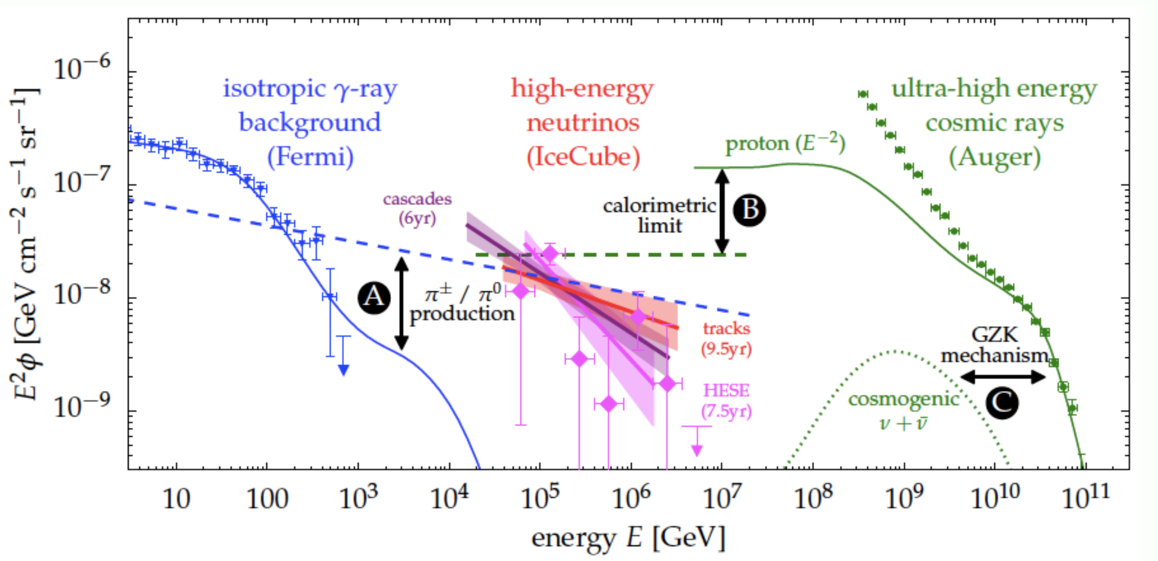

Figure 1.15: Comparison between spectral flux of unresolved extragalactic γ-ray sources, cosmic neutrinos, and UHECRs. The various multimessenger relations explained in the text are highlighted. **A.** The joined production of π^+ and π^0 in UHECR interactions leads to the emission of neutrinos (dashed blue line) and gamma rays (solid blue line) fitting the data. **B.** The classical CRs acceleration model treated in Sect. 1.5.1 (solid green line) implies a maximal flux of neutrinos produced by the same sources accelerating UHECRs (dashed green line). **C.** Cosmogenic neutrinos peaking at EeV energies are predicted by UHECR collisions with CMB photon (GZK mechanism). Image credit: [116], adapted with updated neutrino data (see Sect. 1.3.3).

- **A.** The joint production of $\pi^{\pm}$ and π^0 in CR interactions leads to the simultaneous emission of neutrinos (dashed blue line) and γ rays (solid blue line). In extragalactic sources, however, γ rays suffer from a strong absorption because of the $\gamma\gamma$ interaction with EBL and CMB (see Sect. 1.2.2). Fermi γ-ray observations in GeV-TeV range can be explained by electromagnetic cascades initiated by high-energy leptons and interacting with the CMB through repeated IC scattering and pair production. It is important to point out here that the observed neutrino flux below 10 TeV slightly exceeds the bound set by the model, represented by the dashed blue line. This poses a challenge for emission models in which optically thin sources produce elusive gamma rays and neutrinos and would suggest that some neutrino sources "hidden" to gamma rays could exist (e.g., [162]).

- **B.** UHECRs, while trapped in astrophysical environments through their diffusion in magnetic fields, can produce γ rays and neutrinos through collision with gas. If so, this mechanism can be so efficient that the total energy stored in UHECRs is converted to that of γ-rays and neutrinos. The efficiency of this process is related to the total energy stored in the source under the assumption that it is calorimetric. Under the hypothesis that sources work as perfect calorimeters and that the UHECR proton spectrum scales as E^{-2} (green solid line), as predicted by the first-order Fermi acceleration (see Sect. 1.5.1), a maximal flux of neutrinos from the same sources is expected. This limit (shown by the green dashed line) is called *calorimetric* or Waxman-Bahcall limit [100, 107]. It is worth noticing that this limit was derived under the hypotheses of optically thin sources for high-energy protons to photohadronic and hadronuclear interactions, and without any magnetic fields. Note also that the standard model of UHECR protons with a spectrum $\propto E^{-2}$ could account only for the most energetic CRs (green data). CR data below 10^{10} GeV is not accounted for by this model and must be supplied by additional sources, not discussed here.

- **C.** The same CR acceleration and diffusion model as in B. predicts the production of cosmogenic neutrinos from the collision of CRs with CMB (GZK mechanism), as explained in Sect. 1.3. Future measurements of the diffuse PeV-EeV neutrino emission can provide supporting evidence for the UHECR connection; this is the goal of the proposed space-based POEMMA experiment [163].

As all cosmic messengers are tightly connected, they need to be understood in the context of multimessenger and multiwavelength observations.

Interestingly, it is possible to obtain a relation providing the minimum power density necessary to produce the neutrino flux observed by IceCube. The diffuse neutrino intensity on Earth from extragalactic sources can be approximated as [107]

$$\phi_\nu = \xi \frac{L_\nu n_s R_H}{4\pi}, \tag{1.38}$$

where ξ accounts for the redshift evolution of sources (its typical value for sources following the evolution of the star formation rate density is 2-3), n_s is the source density, L_ν is the neutrino effective source luminosity and $R_H = c/H_0 \simeq 400$ Mpc is the Hubble radius. By pugging into Eq. (1.38) the IceCube diffuse flux level, amounting to $\sim 3 \times 10^{-8}$ GeV cm^{-2} s^{-1} sr^{-1} (see Sect. 1.3.3 and Fig. 1.15), the minimum power density necessary to produce the observed diffuse astrophysical neutrino flux can be obtained [164]:

$$n_s L_\nu \sim 10^{43} \text{ erg Mpc}^{-3} \text{ yr}^{-1}. \tag{1.39}$$

Viable astrophysical neutrino sources need to be characterised by $n_s L_\nu$ values higher than that in Eq. (1.39). Fig. 1.16 shows the results of a similar calculation dating back to 2015 [165]. This study can be used in combination with the similar one presented for UHECRs in Sect. 1.1.2 (see Fig. 1.5(a) and Fig. 1.5(b)), in order to investigate which sources could in principle produce the observed fluxes of UHECRs and neutrinos, e.g., AGNs and GRBs. However, they seem to be excluded as dominant sources of the diffuse flux of neutrinos discovered by IceCube. The contribution of GRBs to the neutrino flux is disfavored by IceCube investigations, as well as by ANTARES analyses: further insights into this topic will

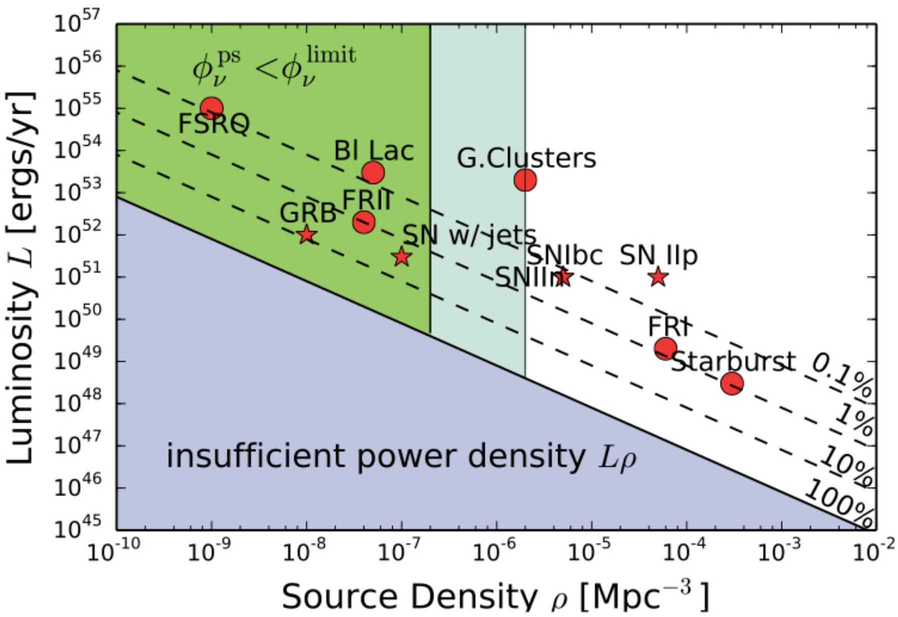

Figure 1.16: Constraints on potential transient and steady sources, responsible for the diffuse astrophysical flux detected by IceCube. The individual source populations are represented by their density and typical luminosity in a characteristic wavelength band. The transient sources are indicated by red stars. Steady sources are shown through red circles. The solid diagonal line marks the neutrino power density boundary (similarly to Eq. (1.39)). Sources above the line release sufficiently abundant energy in electromagnetic radiation to potentially explain the diffuse neutrino flux. Dashed lines indicate the same boundary condition for fractional energy release in neutrinos. Sources in the vertical left regions can be excluded as the dominant source of the diffuse flux, since they would result in a signal within dedicated searches (the green and cyan color refers to limits derived on steady and transient sources, respectively.). Image credit: [165].

be provided in the following Chapters 3 and 4, dedicated to the analysis I have performed to explore GRB neutrino emissions.

Recently, the ANTARES, IceCube, Pierre Auger, and TA Collaborations tested the UHECR-ν connection [166], by looking for ν correlations with nearby steady extragalactic sources of UHECRs with energies > 50 EeV. Neutrinos created by UHECRs are expected to carry $\sim 5\%$ of the original proton energy, which means hundreds of PeV and above for the UHECRs selected in this study. The same sources would also emit neutrinos detectable by the IceCube and ANTARES detectors. Using three different approaches, they searched for an excess of: (i) neutrino clustering in the vicinity of UHECR directions; (ii) UHECRs in the direction of the highest-energy neutrinos; (iii) pairs of UHECR and high-energy neutrinos on different angular scales. Unfortunately, none of the analyses has found a significant excess, and, moreover, from the constraints derived, the assumption of no common sources of UHECRs and neutrinos cannot be excluded. In fact, the uncertainties in the analyses performed are too large to make any statement. More research is needed, e.g., on the propagation of the charged messengers through the Galactic magnetic field, which influence the deflection of UHECRs.

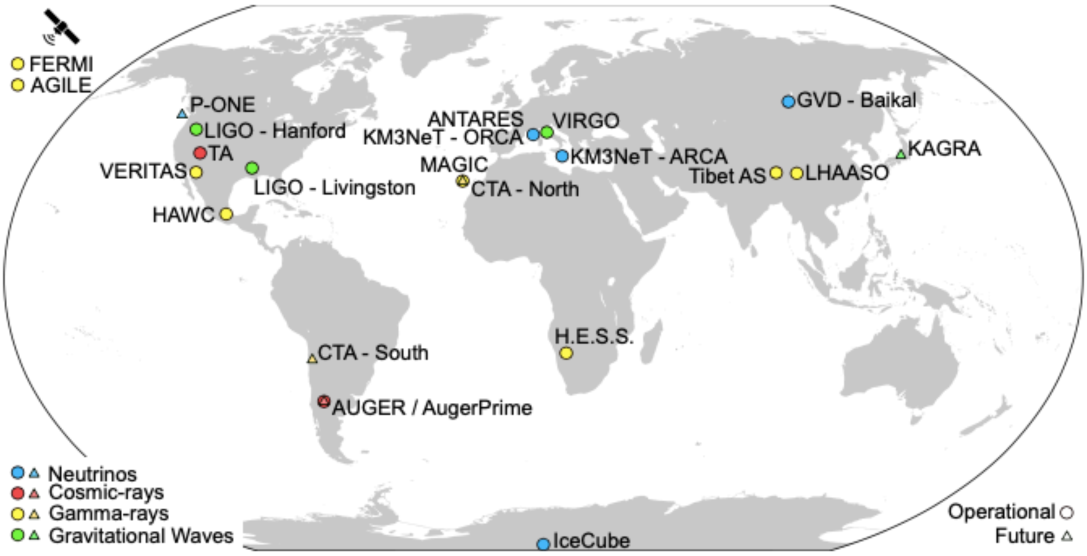

Figure 1.17: Earth map indicating the location of several multimessenger observatories and satellites (neutrinos in cyan, CRs in red, gamma rays in yellow, and gravitational waves in green) that are either currently operating (circles) or planned (triangles). Image credit: [167].

1.6.2 *Observational strategies: real-time analyses*

In the previous sections, the characteristics of all cosmic messengers, their propagation to the Earth, the physical processes responsible of their production and finally the interconnections between each other have been outlined. The importance to collect as much as possible wide multiwavelength and multiprobe information coming from the Universe has emerged, with the aim of studying and discriminating physical processes working in astrophysical sources.

In this context, efficient communication between several collaborations is crucial. For pointing instruments and transient sources, the exchange of information also needs to be fast. A global network of multimessenger instruments is already in place. Neutrino telescopes, cosmic-ray observatories, gamma-ray satellite and ground-based telescopes, interferometers for the detection of gravitational waves continuously cooperate and share recorded events. The map in Fig. 1.17 shows the location of a selection of multimessenger observatories and satellites that are either currently operating or planned, among which a particular mention goes to neutrino detectors located in the Mediterranean Sea, ANTARES and KM3NeT, as the present thesis is developed around them. If interesting events are found using any of these instruments, public alerts are sent to the community. Several methods for information exchange exist; the most widely used are the Gamma-ray Coordinate Network (GCN, `https://gcn.gsfc.nasa.gov`), a fast dispatcher of triggers and results, and the Astronomer Telegram (ATel, `https://astronomerstelegram.org`), namely a publication service for briefly reporting information on new astronomical observations. In addition to these public alerts, private programmes are also established between different collaborations, defined by the so-called Memorandum of Understanding (MoU), such as TaToo [168] between ANTARES and optical telescopes, and the Astrophysical Multimessenger Observatory Network (AMON) [169], combining data from different experiments to increase the significance of sub-threshold events that alone would not be sufficient to claim a detection.

By using the multimessenger approach, the probability of detecting a source is enhanced, and this helps in understanding the physics of many astrophysical sources, often characterised by a variety of timescales and electromagnetic spectral features recognised during the years. The presence of neutrinos is the "smoking gun" to identify sources as hadronic cosmic accelerators. See, e.g., [170] for a review of transient astrophysical sources in the high-energy multimessenger context.

Two main events, occurring just a few years ago, marked the birth of real-time extragalactic multimessenger astronomy: the combined detection of GW 170817 and GRB 170817A (GW-γ multimessenger connection; see Sect. 1.4), and the detection of the IceCube neutrino event IC 170922A in association with the blazar TXS 0506+056 (ν-γ multimessenger connection; see Sect. 1.3.3). Most of the operating high-energy neutrino telescopes has an alert system in place; e.g., IceCube, after the implementation of an event alert system in 2016 [171], upgraded in 2019 [172], has been sending tens of public alerts per year[21]. IC 170922A was one of these: this neutrino event was promptly classified with a good probability to be of astrophysical origin, and in a few minutes the IC alert system automatically circulated an alert to the whole astronomical community. Many similar associations between high-energy neutrinos and their potential astrophysical counterparts have been studied in the last years; e.g., 58 analyses were performed by the IceCube Collaboration between 2016 and 2020 [172]. It is worth mentioning that a dedicated real-time pipeline, fully automated, was also operational for the ANTARES detector since 2014 up to its dismantling, in February 2022. All the external triggers by electromagnetic, neutrino, and gravitational wave instruments occurring in positions of the sky below the ANTARES horizon were followed. For a review of all the online analyses performed with ANTARES refer to [173]. The next generation neutrino telescope KM3NeT is also developing a framework for real-time analyses. Part of the activities within this thesis has been dedicated to the implementation of the required software for online event processing, as it will be described in Chapter 5 (see Sect. 5.2), where also the first KM3NeT analyses results are outlined.

21 In particular, 10 *gold* alerts and 20 *bronze* alerts, with $> 50\%$ and $> 30\%$ probability to be astrophysical, respectively.

2 HIGH-ENERGY NEUTRINO TELESCOPES IN THE MEDITERRANEAN SEA

In the 1930s, through the study of β decay[1], it was theoretically clear that a third unknown particle, with nearly no mass and with neutral charge, was needed to be involved to save the principle of energy conservation. The existence of this particle, dubbed "neutrino" by Enrico Fermi, was experimentally proved in 1956. In the subsequent years, the observation of neutrinos from the Sun and from the supernova SN1987A, posed the idea that they could represent good astrophysical messengers. Neutrino interaction with matter is extremely feeble because of its characteristics. Therefore, astrophysical neutrinos, produced in high-energy hadronic processes, may reach the Earth without any absorption and deflection by magnetic field effects. However, their weak interaction constitutes a strong impediment to their observations; huge particle detectors with a large volume of free and natural target for neutrino interactions are required to collect cosmic neutrinos in statistically significant numbers. Following the Markov's proposal in 1960 [174], big efforts have been concentrated over the years on installing large detectors deep in water and ice able to collect the Cherenkov light induced by the propagation of charged particles resulting from neutrino interactions with nuclei in the detector volume. These efforts have led towards the construction of bigger and bigger detectors all over the world. Among them, it is worth mentioning the IceCube neutrino telescope at the South Pole, that firstly detected cosmic neutrinos (see Sect. 1.3.3), the Gigaton Volume Detector Baikal (Baikal-GVD) below the surface of Lake Baikal in Russia [175], and the two detectors in the depths of the Mediterranean Sea on which this work is focused: ANTARES (dismantled at the beginning of 2022) and KM3NeT (at the time of writing, under construction).

This chapter starts with the discussion of the high-energy neutrino detection principles in Sect. 2.1. Then, seawater properties and detection techniques used by underwater neutrino detectors are discussed in Sect. 2.2 and Sect. 2.3, respectively. Then, their general properties are outlined in Sect. 2.4. In Sect. 2.5, the ANTARES and KM3NeT telescopes and their performance are described. In Sect. 2.6, the methodologies used to calibrate the detectors and attain the needed level of precision before described are summarised. Finally, for completeness, a brief description of other high-energy neutrino telescopes currently operating, i.e., IceCube and Baikal-GVD, is provided in in Sect. 2.7.

1 Radioactive decay in which an atomic nucleus is converted into a nucleus with atomic number increased/decreased by one, while emitting an electron/positron and a electron antineutrino/neutrino:

$$ {}^{A}_{Z}X_{N} \rightarrow {}^{A}_{Z\pm 1} Y_{N\mp 1} + e^{\mp} + \begin{pmatrix} \bar{\nu}_e \\ \nu_e \end{pmatrix} $$

2.1 DETECTION PRINCIPLE OF HIGH-ENERGY NEUTRINOS

High-energy neutrinos can be indirectly revealed by making use of detectors capable of capturing the Cherenkov light that secondary relativistic charged particles, resulting from neutrino interactions, induce crossing transparent media. This section aims at explaining why and how Cherenkov radiation (presented in Sect. 2.1.1) originates after neutrino interactions with nuclei (in Sect. 2.1.2), as well as to outline the event signatures that neutrino telescopes look for (in Sect. 2.1.3).

2.1.1 *Cherenkov radiation*

When a charged particle passes through a transparent medium with a speed exceeding that of light in the medium, optical photons are produced by the Cherenkov effect [176]. During propagation in a medium with refractive index n, a charged particle with velocity v polarises the molecules around its trajectory and emits wavefronts of light that travel at speed c/n. Cherenkov light is emitted when the electrons of the medium restore themselves to equilibrium after the perturbation has passed.

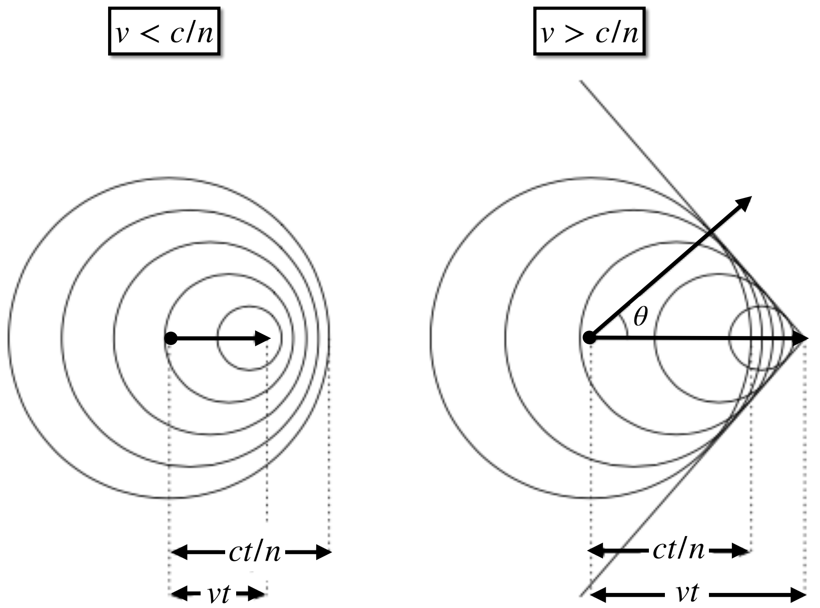

Figure 2.1: Sketch showing a particle propagating for a time t with a velocity v in a medium characterized by a refractive index n, and the wave fronts of light moving at velocity c/n (circles) emitted at the passage of the charged particle. Image credit: [89].

As shown in Fig. 2.1, if $v > c/n$, these radiations are coherently summed up on the surface of a cone with a characteristic angle θ_C given by

$$\cos\theta_C = \frac{c/n}{v} = \frac{1}{\beta n}, \tag{2.1}$$

where β is the particle speed in units of c. Relativistic particles ($\beta \simeq 1$) in seawater, where light moves $\sim 75\%$ slower than in vacuum ($n \approx 1.35$ [177]), induce Cherenkov photons within a cone with $\theta_C \simeq 42°$.

The number of Cherenkov photons N_γ emitted because of this effect per unit path length x of the charged particle and wavelength λ can be written as [178]

$$\frac{\mathrm{d}^2 N_\gamma}{\mathrm{d}x \mathrm{d}\lambda} = \frac{2\pi\alpha}{\lambda^2}\left(1 - \frac{1}{n^2(\lambda)\beta^2}\right), \tag{2.2}$$

where $\alpha \approx 1/137$ is the fine structure constant[2]. Eq. (2.2) shows that shorter wavelengths are more intense in Cherenkov radiation. In fact, most of the Cherenkov radiation is emitted in the ultraviolet spectrum and is observed in blue. In the transparency window of water, i. e. (350-500 nm)[3], the number of photons emitted per track length is ~ 250 cm^{-1}.

2.1.2 *Interaction signatures of high-energy neutrinos*

Neutrinos are subatomic particles, very similar to electrons, but without electrical charge and very small mass ($m_\nu < 0.8$ eV$/c^2$ [179]). According to their energy and to the momentum transferred to the hadronic system, we could classify neutrino-nucleus interactions into elastic, quasi-elastic, and deeply inelastic. Since in this work we refer to neutrino telescopes that aim at the detection of high-energy νs of cosmic origin, here only neutrino interactions at high energies are discussed. For a more general overview about all the ν scattering mechanisms mentioned above, see e.g [180].

High-energy neutrinos weakly interact with quarks via the exchange of W$^\pm$ and Z gauge bosons. Two main channels are possible:

- charged current (CC) interactions, with the production in the final state of a charged lepton,

$$\overset{(-)}{\nu}_l + N \rightarrow l^\pm + X; \tag{2.3}$$

- neutral current (NC) interactions, where the neutrino instead emerges at the final state,

$$\overset{(-)}{\nu}_l + N \rightarrow \overset{(-)}{\nu}_l + X. \tag{2.4}$$

In Eq. (2.3) and Eq. (2.4), l indicates the leptonic flavour ($l = e, \mu, \tau$), and X is the hadronic shower system that starts at the interaction point. The cascade is present both in NC and CC interactions and, even if constituted mostly by hadronic particles, contains also an EM component constantly increasing because of π^0 decays. Regarding the leptonic part of the final state, in NC interactions this is a neutrino with unchanged flavour; meanwhile, in CC interactions, the charged lepton corresponds to the flavour of the initial ν. Fig. 2.2 shows all

2 Fundamental physical constant which quantifies the strength of the electromagnetic interaction between elementary charged particles.

3 Where PMTs are typically more sensitive.

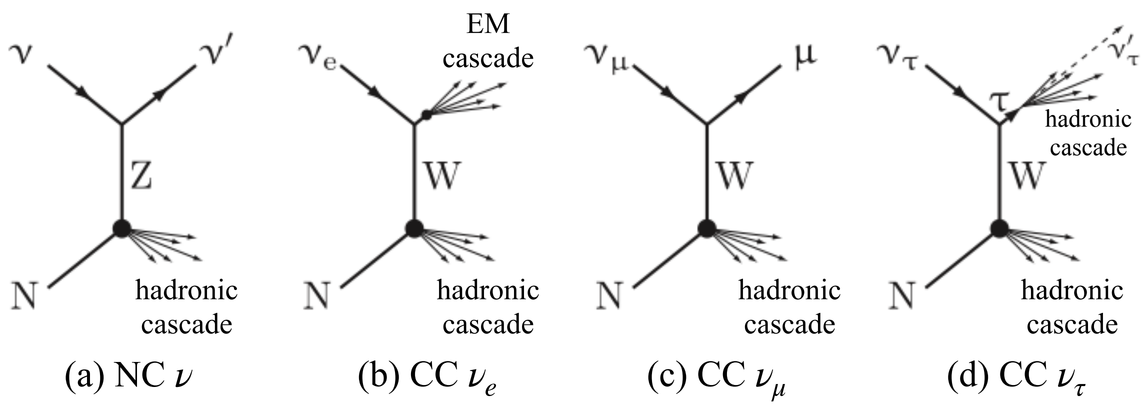

Figure 2.2: Neutrino interaction channels and their products visible to neutrino telescopes: (a) Neutral current ν interaction; (b) Charged current ν_e interaction; (c) Charged current ν_μ interaction; (d) Charged current ν_τ interaction.

the ν interaction channels visible to high-energy neutrino telescopes thanks to detection of the Cherenkov radiation they produce in transparent media. They are explained as follows:

- **(a) NC ν interactions** As the outgoing neutrino does not have a visible signature, only the hadronic shower is seen;
- **(b) CC ν_e interactions** $e^\pm$ immediately initiate a EM cascade producing radiation via bremsstrahlung;
- **(c) CC ν_μ interactions** The resulting $\mu^\pm$, having a mass more than a factor of 200 higher than $e^\pm$ ($m_\mu \simeq 105$ MeV/c^2), can travel large distances with little energy loss, producing a well-distinguishable *muon track* in the detector;
- **(d) CC ν_τ interactions** $\tau^\pm$, with high mass ($m_\mu \simeq 1778$ MeV/c^2) but very short lifetime ($\tau_\tau \simeq 2.9 \times 10^{-13}$ s at rest), are not able to propagate for long distances[4] and decay producing in about 2/3 of the cases another hadronic cascade. Since the two cascades are separated by an appropriate distance, they can be detected individually (*double-bang* signature).

The neutrino cross sections $\sigma_{\nu N}$ for scattering at high energies (DIS regime) are visible in Fig. 2.3. Neutrinos, being weakly interacting, have a low probability of interaction with matter: e.g., at 1 TeV (PeV), the inelastic cross section per nucleon is $\sigma_{\nu N} \sim 10^{-35}(10^{-33})$ cm^2. For $E_\nu \lesssim 10^4$ GeV, $\sigma_{\nu N}$ increases linearly with E_ν, while after it grows more slowly ($\sigma_{\nu N} \propto E_\nu^{0.4}$). For a detailed treatment of the cross sections for the interactions of ultrahigh-energy neutrinos with nucleons, see e.g., [181]. Fig. 2.3 shows also $\sigma_{\nu N}$ for the so-called *Glashow resonance*, namely the scattering of electron antineutrinos with electrons ($\bar{\nu}_e + e^- \to W^- \to X$) [182]: the interaction probability of this process is characterised by a peak in the rest frame of electrons at $E_{\bar{\nu}} \simeq 6.3$ PeV, where it dominates with respect to the others. In such a case, the event signature detectable in neutrino telescopes is a shower with energy compatible with that of the interacting neutrino. Note that this process is

4 Except for very high energies, i. e. $E_\nu \gtrsim 1$ PeV

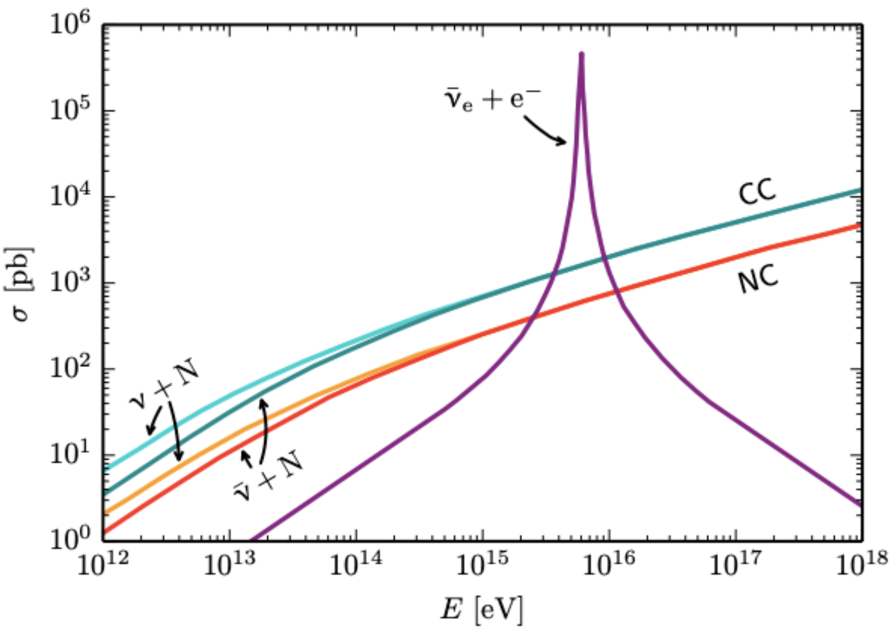

Figure 2.3: Neutrino and anti-neutrino cross sections per nucleon at high energies for CC and NC interactions in DIS, and for the Glashow resonance. Cross section values are given in picobarn (1 pb = 10^{-36} cm ^{2}). Image credit: [89].

the only one, among the interactions in Fig. 2.2, allowing to distinguish between ν and $\bar{\nu}$ through neutrino telescopes. For other neutrino energies, the interaction with electrons can be neglected. In fact, $\sigma_{\nu N}$ is proportional to the mass of the target particle and this leads to a much larger cross section for the neutrino scattering on nucleons than scattering on electrons.

2.1.3 *Propagation of neutrino interaction products*

All the charged secondary particles emerging as final products of neutrino interactions in water (muons, taus, EM and hadronic showers) can induce, if relativistic, Cherenkov radiation that neutrino telescopes can identify through different patterns (track and/or shower), according to the type of interaction occurring. Charged particles travel through the medium until they either decay or stop having lost their kinetic energy, so their path depends on the amount of energy they lose per interaction.

The average path lengths in water for μ, τ, EM, and hadronic cascades, resulting from ν interactions, are shown in Fig. 2.4. When a ν_μ CC interaction occurs, often only the muon track is detected, as its propagation in water exceeds that of the cascade by more than three orders of magnitude for energies above TeV. Indeed, muons, with respect to all the other signatures, can propagate over long distances. For example, for a neutrino with $E_{\nu_\mu} > 1$ TeV interacting with or close to the detector, the final product μ travels in water ~ 10 km. This demonstrates the fact that events generating high-energy muon tracks in neutrino detectors can have the interaction point outside the instrumented volume, extending the so-called *effective volume* of the detector (see Sect. 2.4). The muon path length usually ex-

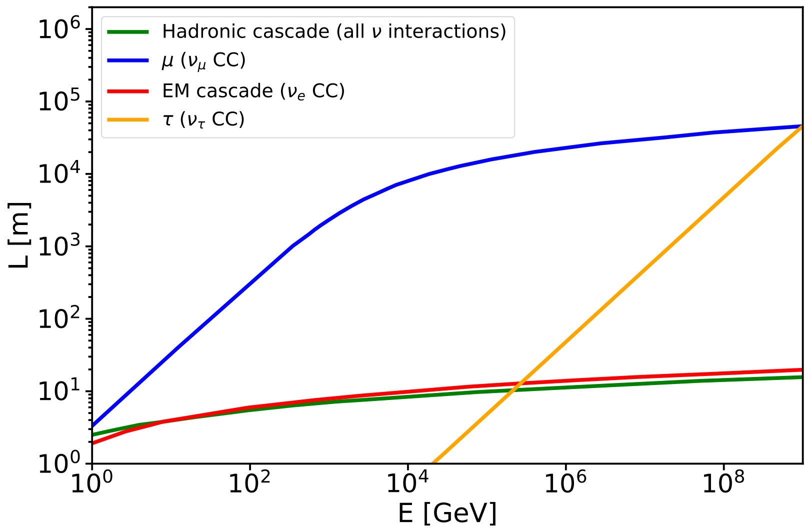

Figure 2.4: Average propagation distances of muons (blue), taus (orange), electromagnetic cascades (red) and hadronic cascades (green) resulting from neutrino interactions in water. Plot reproduced with data taken from [183].

ceeds the spatial resolution of neutrino detectors, so that tracks produced by high-energy ν CC interactions can be easily detected, and constitute the main signature that neutrino telescopes look for.

Muon propagation

Given its importance, let us focus on muon propagation. Along the μ track, additional Cherenkov light is emitted (shower-like) due to muon energy losses due to ionisation and some stochastic processes[5] as bremsstrahlung, pair production, and photonuclear interactions. The total energy loss per unit length can be parameterised as [184]

$$\frac{\mathrm{d}E_\mu}{\mathrm{d}x} = a(E_\mu) + b(E_\mu)E_\mu, \tag{2.5}$$

where $a(E_\mu)$ refers to ionisation and $b(E_\mu) = b_{\text{pair}} + b_{\text{brems}} + b_{\text{photonuc}}$ includes the contribution given by the other radiative losses. The mechanism of ionisation energy loss does not depend strongly on E_μ (see a in Eq. (2.5)), while pair production, bremsstrahlung, and photonuclear reactions increase linearly with energy. In water, $a \simeq 2$ MeV cm^{-1} and $b \simeq (1.7 + 1.2 + 0.6) \times 10^{-6}$ cm^{-1} [185], as shown in Fig. 2.5. For E_μ lower than ~ 1 TeV, ionisation dominates; above this threshold, instead, muons start to lose more energy because of stochastic processes ($b(E_\mu) = \simeq 3.5 \times 10^{-6}$ cm^{-1}). However, as already pointed out, muons with energies higher than TeV propagate in water with a path several orders of magnitude longer than cascades, and tracks can be clearly recognised. Note that muon propagation in water affects the energy resolution of neutrino detectors, namely their ability to accurately determine the energy carried by a muon event, as discussed in Sect. 2.4.

5 Muons deposit their energy at irregular intervals rather than continuously.

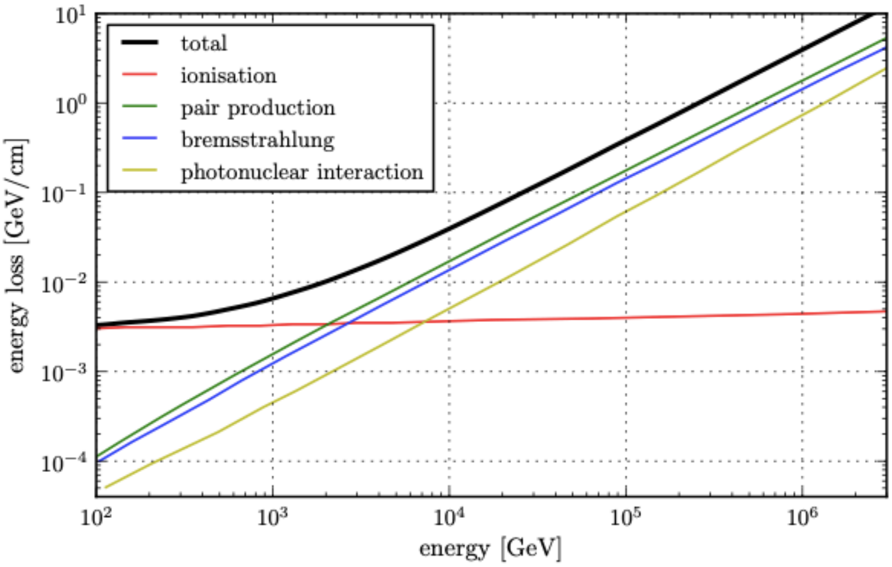

Figure 2.5: Energy loss of muons during their propagation in water: ionisation (red), pair production (green), bremsstrahlung (blue), and photonuclear interaction (yellow). The black line shows the total energy loss. Image credit: [186].

Muon detection and neutrino direction reconstruction

From the reconstruction of the direction of muon tracks resolved by neutrino telescopes, it is possible to trace back the original direction of incoming neutrinos that CC interact in water and produce the track signature. The final state muon, indeed, follows the initial ν direction with an average mismatch angle $\theta_{\nu\mu}(E_\nu)$, usually called *kinematic angle*, that can be approximated as [187]

$$\theta_{\nu\mu}(E_\nu) \leq \frac{0.7^\circ}{(E_\nu\ [\text{TeV}])^{0.7}}. \tag{2.6}$$

Note that the higher the neutrino energy, the smaller the kinematic angle value. The relation in Eq. (2.6) represents the basic principle for the ν_μ directional reconstruction, but at the same time it sets a kinematical limit to the detector angular resolution (see Sect. 2.4).

Let us consider a CC interaction of a muon neutrino with energy E_{ν_μ}; the probability that the final muon reaches the detector with a minimum detectable energy E_μ^{min} depends on the cross section $\sigma^{\text{CC}}_{\nu_\mu N}$ and on the *effective muon range* $L_{\mu,\text{eff}}$, namely the length path after which the muon has decreased its energy to E_μ^{min} [164]:

$$\mathrm{P}_{\nu\to\mu}(E_{\nu_\mu}, E_\mu^{\text{min}}) = N_A \int_{E_{\mu,\text{min}}}^{E_\nu} \mathrm{d}E_\mu \frac{\mathrm{d}\sigma^{\text{CC}}_{\nu_\mu N}}{\mathrm{d}E_\mu} \cdot L_{\mu,\text{eff}}(E_\mu^{\text{min}}, E_\mu), \tag{2.7}$$

being N_A the Avogadro constant. For water and $E_\mu^{\min} = 1$ GeV, it is possible to adopt the following approximation:

$$P_{\nu\to\mu} = 1.3 \times 10^{-6} \left(\frac{E_{\nu_\mu}}{1\ \text{TeV}}\right)^{2.2} \qquad E_{\nu_\mu} < 1\ \text{TeV} \tag{2.8}$$

$$= 1.3 \times 10^{-6} \left(\frac{E_{\nu_\mu}}{1\ \text{TeV}}\right)^{0.8} \qquad E_{\nu_\mu} > 1\ \text{TeV} \tag{2.9}$$

This means that a neutrino telescope can detect a muon event induced by a neutrino with $E_{\nu_\mu} \sim 1$ TeV with probability $\sim 10^{-6}$, if the telescope is on the neutrino path.

Shower detection

The Cherenkov light due to the development in the medium of the EM and hadronic cascades is distributed over a pattern much wider than tracks. It is, indeed, the result of the sum of multiple Cherenkov cones produced by all charged particles constituting the shower. This clearly makes the fit accuracy of the neutrino direction producing the shower event worse than that of tracks. On the other hand, since the length of showers in water increases like the logarithm of the cascade energy, all shower events typically release their entire energy in a compact region into the detector volume, allowing for a more precise energy reconstruction with respect to tracks.

Refer to Sect. 2.3 for an explanation of the experimental and technological technique used to detect the neutrino-induced events mentioned so far.

2.2 SEAWATER AS DETECTOR MEDIUM

The construction of optical Cherenkov neutrino telescopes in deep seawater is a clever way to provide a very large target mass for neutrino interactions, to cope with the small neutrino-nucleon cross sections, as well as to reduce the huge amount of background coming from atmospheric particles produced in CR interactions with Earth's atmosphere (this will be clearer in Sect. 2.3.2). However, the usage of seawater as detector medium leads to absorption and scattering of photons during light propagation underwater (treated in Sect 2.2.1 and Sect 2.2.2, respectively), and to an irreducible natural optical background (discussed in Sect 2.2.3). When working with water Cherenkov neutrino telescopes, which use the position of measured photons and their arrival time on PMTs to characterise neutrino-induced events, it is necessary to take into account all these effects; they must be permanently monitored and the instruments calibrated.

2.2.1 *Photon absorption*

The light absorption reduces the amplitude of the Cherenkov wavefront, namely, the total amount of light arriving on PMTs. The intensity $I(x, \lambda)$ of light towards the optical path x traversed by it at a certain wavelength λ is expressed by the following relation:

$$I(x, \lambda) = I_0(\lambda) e^{-x/L(\lambda)}, \tag{2.10}$$

where $L(\lambda)$ represents a length depending on the properties of the medium and the effect considered. In the case of absorption, $L(\lambda)$ represents the absorption length $L_a(\lambda)$, which defines the distance at which the probability that a particle has not been absorbed drops to $1/e$. Measurements made in the past in the Mediterranean Sea showed that $L_a(\lambda) \simeq 60$ m for blue light and $L_a(\lambda) \simeq 26$ m in the UV band [188].

2.2.2 *Scattering of photons*

The scattering of photons with particles in seawater changes the direction of Cherenkov radiation during its propagation. This affects the distribution of the arrival times of the hits on the PMTs, which degrades the measurement of the direction of the incoming neutrinos. The scattering properties of water are commonly described by the same relation in Eq. (2.10), in analogy to absorption, with $L(\lambda)$ equal to the scattering length $L_s(\lambda)$. A complete description of light scattering also involves knowledge of the scattering angle distribution, that is a mixture of Rayleigh [189, 190] and Mie [191] scattering processes. Photon directions can be deviated multiple times before reaching PMTs. On average, they advance at an angle of $\langle \cos\theta \rangle$ a distance of $L_s(\lambda)$ between each scatter. Hence, after n scatters, this effect is described by the *effective scattering length*, namely $L_s(\lambda)$ averaged over scattering angles:

$$L_s^{\text{eff}}(\lambda) \simeq \frac{L_s(\lambda)}{1 - \langle \cos\theta \rangle}. \tag{2.11}$$

In seawater, this quantity was estimated to be $L_s^{\text{eff}}(\lambda) \simeq 265(122)$ m for blue(UV) light [188]. Due to a combination of absorption and scattering phenomena, the light intensity scales with the depth D as

$$I(x, \lambda) = \frac{I_0(\lambda)}{D^2} e^{-cx}, \tag{2.12}$$

where $c = (L_a + L_s)/(L_a \cdot L_s)$ is called *attenuation coefficient*. Its variation with depth in water is small, unlike that of ice, where absorption and scattering coefficients strongly change. However, differently from neutrino detectors built in ice, in deep seawater the light propagation is affected by seasonal variations in water parameters and bio-matter.

For a comparison with the properties of water in Lake Baikal and ice in the South Pole, where Baikal-GVD and IceCube operate, respectively, see, e.g., [192, 193].

2.2.3 *Optical background*

Working with the Mediterranean Sea also means having to deal with additional optical light produced by decays of radioactive elements and by bioluminescent organisms living in the deep sea.

Seawater contains potassium, whose isotope potassium-40 (^{40}K) is the most abundant. The main decay channel of ^{40}K is:

$$^{40}\mathrm{K} \rightarrow ^{40}\mathrm{Ca} + e^- + \bar{\nu}_e \qquad (89.3\%)$$

The electron produced in the β decay above has an energy of 1.3 MeV and leads to the production of Cherenkov light when travelling in water[6]. Another possibility is given by the electron capture channel

$$^{40}\mathrm{K} + e^- \rightarrow ^{40}\mathrm{Ar} + \nu_e + \gamma \qquad (10.7\%)$$

where the photon, with $E_\gamma = 1.46$ MeV, Compton scatters with water molecules and produces fast electrons, which in turn emit Cherenkov radiation. The background due to ^{40}K is more or less constant and is estimated to add a rate of hundreds of photons per second per cm^2 of photocatode area (e.g., [194]).

Furthermore, organisms living in deep sea emit either a continuous signal (due to steady glow of bacteria) and bursts of photons (produced by other sea animals) typically lasting few seconds, with intensity several order of magnitudes greater than the ^{40}K noise. Note that the higher the velocity of the sea current, the greater the bioluminescence [193]. The distribution of luminescent organisms varies with location, depth, and seasonal variations, and generally its abundance decreases with depth [195]. Together with the shielding effect for atmospheric muons (see Sect. 2.3.2), this is another important reason why neutrino telescopes in the Mediterranean are located in deep sea (at least 2500 m, as will become clear later in the text.)

Optical noise can worsen the reconstruction performances of detectors, as the noise rate in PMTs can look like a low-energy muon event. In particular, this is true for muons with energy $\ll$1 TeV that produce only a few Cherenkov photons. This background is usually suppressed by looking for coincidences in neighbouring PMTs, considering the fact that the probability of random coincidences by ^{40}K or bioluminescence hits is low. Another possibility is to use only hits above a certain amplitude threshold that should guarantee the cut of signals from ^{40}K decays, whose amplitudes generally correspond to a single photoelectron.

2.3 DETECTION TECHNIQUES

In neutrino telescopes, light is detected by making use of transparent spherical glasses hosting several photomultiplier tubes (PMTs) with readout electronics. The glass sphere

6 Electrons with kinetic energy greater than 250 keV emit light in water by Cherenkov effect.

protects PMTs from pressure and other environmental factors (like salinity), and at the same time allows Cherenkov photons to reach PMT photocathodes that convert photons into an electrical pulse. The electrical charge pulse is read out using dedicated electronics located in the sphere. Each sphere is the basic elements of neutrino detectors and is usually defined as Optical Module (OM). Cherenkov photons detected on OMs at a certain time constitute what is usually called *hit*. At each hit, a position, time, and collected charge are associated, which are used to reconstruct the direction and energy of each event. Several OMs are structured in vertical detector lines (called *strings*), namely cables for mechanical support and data transfer, which in water are moored on the ground and held vertically by buoys. The distances between strings and modules themselves are optimised for different energies at which neutrino telescopes aim, as well as depending on the level of expected optical background hits for the medium in which they are located. In practise, a three-dimensional array of PMTs is built, through which the properties of interacting neutrinos can be inferred with high-precision measurements of the number and arrival times of Cherenkov photons on PMTs; in this regard, the following Sect. 2.3.1 and Sect. 2.3.2 explain how events are triggered and reconstructed by neutrino telescopes, and the huge atmospheric background polluting neutrino detections, respectively. More details about the modules installed in the ANTARES and KM3NeT detectors and their design are given in Sect. 2.5.1 and Sect. 2.5.2, dedicated to their description.

It is worth noting that there are also other possibilities, not considered in this work, such as the detection of acoustic (e.g., [196]) or radio signals (e.g., [197]) generated by EeV neutrinos in a huge volume of water (acoustic) or ice (acoustic and radio).

2.3.1 *Triggering and event reconstruction*

Once the data is collected, they need to be filtered and saved to permanent storage for future analyses. This is done through trigger algorithms, which continuously operate on data arriving in real-time. They split the data stream into discrete *events* and, among them, filter those data that is not likely to contain useful information. In practise, trigger algorithms decide whether an event containing a set of hits collected on PMTs should be recorded or not. Using information on the position, time, and amplitude of each hit, specific algorithms are used to reconstruct events. As already seen in Sect. 2.1.2, a neutrino interaction, depending on the neutrino flavour, can result in a muon coming out of the interaction point, namely a track, or can create a cascade of particles (hadrons or electrons), which is termed shower. Fig. 2.6 shows how these patterns are detected by neutrino telescopes. The reconstruction of each event consists of the characterisation of its direction and energy, from which it is possible to trace the same information for the interacting neutrino. Since tracks and showers produce very different patterns, specific reconstruction algorithms are applied on each event to define the most likely origin. These software are usually developed on their own by each neutrino telescope collaboration, to take into account the distinct detector technologies as well as the properties of the medium in which they operate. The influence of environmental noise (mainly by ^{40}K and bioluminescence) is reduced by dedicated selec-

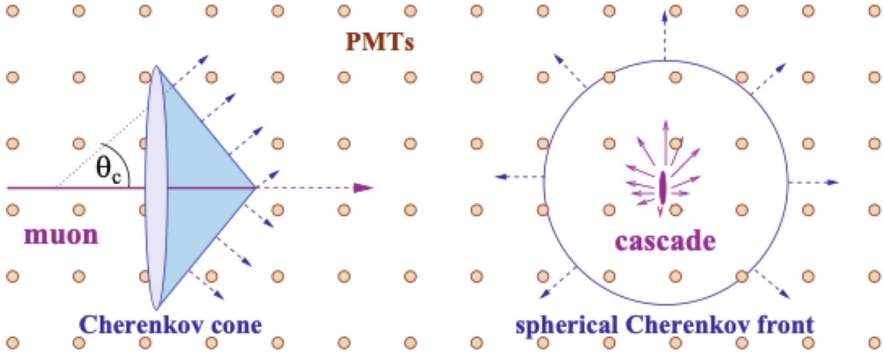

Figure 2.6: Detection principles for muon tracks (left) and showers (right) in neutrino detectors. Image credit: [192].

tion algorithms. Information on background light, response on PMTs to photon hits, and energy losses by particles in the medium are considered at reconstruction processes. The parameters assessing the reconstruction quality can be used to select well-reconstructed events. Namely, some *cuts* on the reconstruction parameters are applied and only events satisfying certain conditions are accepted.

In Appendix B the entire Monte Carlo (MC) chain used in ANTARES and KM3NeT to simulate and reconstruct events is presented.

2.3.2 *Atmospheric background and neutrino selection*

Underwater neutrino telescopes are facing different backgrounds, that make difficult the detection of cosmic neutrinos. In addition to natural irreducible optical backgrounds such as the natural radioactivity of elements in water (mainly ^{40}K), and the luminescence produced by organisms living in the deep sea (see Sect. 2.2.3), there is constant rain of Earth-penetrating neutrinos and muons from cosmic-ray collisions with the atmosphere.

When CRs interact with nuclei in the atmosphere, both neutrinos and muons are produced. Even if atmospheric neutrinos constitute an irreducible background, they strongly lower going at very high energies, where their energy spectrum is much softer than the signal neutrino spectrum expected from astrophysical sources (see Sect. 1.3.1). In this situation, cosmic neutrinos can emerge with respect to the background. In addition, when a neutrino signal is searched from a well-known position in the sky where a potential emitter is present, the large amount of background events can be cut by selecting only events occurring in a defined space angle around the source direction (*point-source analysis*). For details about high-energy neutrinos of atmospheric origin, the reader can refer to Sect. 1.3.2.

The most abundant background is due to atmospheric muons, produced in association with atmospheric neutrinos (see Fig. 1.9). As an air shower usually produces more than one muon, most of them arrive in bundles with a nearly uniform direction and energy loss pattern. These muons can penetrate several kilometres in the detector and the signature they leave can be confused with that of cosmic neutrino signals. The parameterisation of

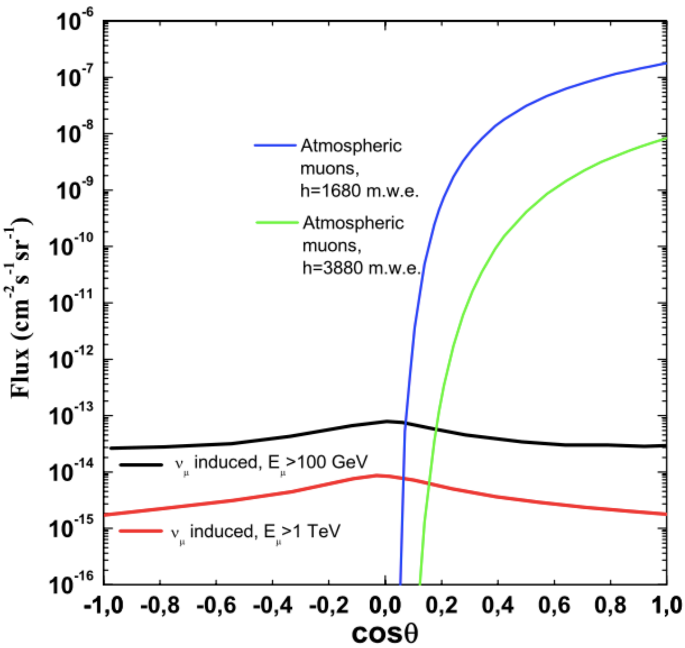

Figure 2.7: Atmospheric muon and neutrino fluxes as a function of the cosine of the zenith angle. Atmospheric muons are shown for two different depths in seawater: 1680 m (blue) and 3880 (green). For neutrinos, the thresholds $E_{\nu_\mu} > 100$ GeV (black) and $E_{\nu_\mu} > 1$ TeV (red) are reported. Image credit: [193].

the flux, lateral distribution, and energy spectrum in deep water for single and multiple muons is discussed in [198]. As shown in Fig. 2.7, atmospheric muons can be discarded by using the Earth as a muon shield and selecting only *up-going* events occurring below the horizon of the telescopes, i. e. with $\cos\theta < 0$, θ being the track zenith angle. By adopting this event selection, the only atmospheric background to account for is constituted by neutrinos. Therefore, neutrino telescopes predominantly look at these events. Even if they are usually deployed in deep transparent media taking advantage of their shielding effect (the atmospheric muons decreases with depth), a large flux of high-energy *down-going* muons ($\cos\theta > 0$) can however reach the detectors and a small fraction of them can be wrongly reconstructed as up-going. Typically, in these cases, the poor quality of the track fit allows us to discard those events.

It is worth highlighting that looking for up-going events works only up to $\sim$ PeV energies; above this threshold the Earth starts to become opaque to neutrinos. Indeed, the higher the neutrino energy, the lower its survival probability through the Earth [199]. At energies above few hundred TeV, neutrino-generated events start to arrive preferentially from directions close to the horizon and, at EeV energies, they come essentially only from the upper hemisphere. At PeV energies, where the atmospheric background is very small, it is not possible to select only up-going events, since neutrinos cannot be seen. However, the atmospheric background rate at these energies is low enough to allow a good reconstruction of such high-energetic tracks, even if they are only seen from above the horizon (e.g., [200]).

2.4 CHERENKOV DETECTOR PROPERTIES

To make a decisive contribution towards the multimessenger astronomy field, discussed in Chapter 1, neutrino detectors need to be able to reconstruct with high precision the direction of the sky from which neutrino events come and, at the same time, be characterised by enough target volume and sensitivity to catch the low rate of cosmic neutrinos hidden among the huge atmospheric background. Before going into the specific performances of ANTARES and KM3NeT (see Sect. 2.5.3), general properties of neutrino detectors are introduced below: angular and energy resolution (in Sect. 2.4.1 and Sect. 2.4.2, respectively), effective volume and area (in Sect. 2.4.3), and sensitivity and discovery potential (in Sect. 2.4.4).

2.4.1 *Angular resolution*

The angular resolution of a detector corresponds to its capacity to resolve the direction of reconstructed events with a small error to trace back as precisely as possible to the direction of the incoming neutrino. This important quality of a neutrino telescope depends on the geometrical layout of the detector, the photocatode area through the number of PMTs, and also on the quality of the reconstruction techniques adopted. The angular resolution as a function of the neutrino energy is commonly evaluated for each detector through the median of the space angle between the direction of neutrino events given by MC simulations and that reconstructed. The typical resolution for neutrino telescopes in water for muon track reconstruction is less than 1° for high-energy events. Note that, as neutrinos are not detected directly, rather via the secondary particles produced in neutrino interactions, the angular resolution is limited by kinematics, i. e. by the angle between the primary neutrino and the muon (in Eq. (2.6)). Since both the kinematic angle and the quality of the reconstruction depend on the energy of the involved particles, the angular resolution improves with increasing energy. On the other hand, compared to track events, the angular resolution is worse for showers because of their spread and quite compact pattern.

2.4.2 *Energy resolution*

To well characterise an event, in addition to its direction, it is important to determine its energy. This evaluation is affected by uncertainties on the physical processes that characterise neutrino interactions, as well as on instrumental uncertainties. When considering the favourite channel for neutrino detectors, namely track-like events, their response to neutrino energy depends on: (i) the fraction of energy transferred to the muon, (ii) the energy lost by the muon outside the detector, and (iii) the energy resolution of the detector. This property is usually determined by several methods depending on different energy ranges. For a better understanding of the topic presented here, the reader can refer to Sect. 2.1.3, where the propagation in water of charged particles produced in neutrino interactions is discussed. Below 100 GeV the ionisation dominates; muons lose in water ~ 2.5 MeV cm^{-1}, and their energy can be estimated from the length travelled totally into the detector size. Above 100 GeV, the fact that muons can start or finish their path outside the detector volume prevents the usage of the previous method. However, it is still possible to determine the minimum energy by means of a measure of the limited range, useful for partially contained events (starting events in which the vertex point is measured inside the detector and stopping events in which the endpoint is measured). At energies greater than 1 TeV, muon energy losses are a function of energy itself (see Eq. (2.5)) and the track length increases $\sim$logarithmically with the muon energy. The stochastic nature of the energy-loss processes here dominating makes the energy reconstruction challenging. In summary, the energy resolution for track-like events degrades with energy. On the other hand, the energy of shower events, characterised by a short length contained in the instrumented detector volume, is usually better evaluated, despite the difficulty in determining the original direction of the incoming neutrino.

2.4.3 *Effective volume and area*

An important parameter that describes the efficiency of a neutrino telescope is the so-called neutrino effective volume, which represents the volume on which all neutrinos crossing the detector would be revealed (100% detection efficiency). This property can be obtained by Monte Carlo simulations. Consider N_{gen} the number of generated events distributed over a volume V_{gen}, which geometrically contains and exceeds the detector, and N_{det} the number of detected events (triggered or reconstructed). The efficiency to detect a neutrino of a given energy E_ν is expressed by the effective volume as

$$V_{\text{eff}}(E_\nu) = V_{\text{gen}}(E_\nu)\frac{N_{\text{det}}(E_\nu)}{N_{\text{gen}}(E_\nu)}. \tag{2.13}$$

Eq. (2.13) highlights that V_{eff} can be higher than the geometrical volume. For example, in high-energy CC ν_μ interactions, even if the interaction point is outside the instrumented volume, the muon tracks produced are so long that they can pass through the detector emitting Cherenkov photons that reach PMTs. In this way, the effective volume of the detector is enhanced. Instead, for cascade events V_{eff} is quite close to it.

Related to the effective volume, the neutrino effective area can be likewise defined. For a given neutrino energy E_ν with incident zenith angle θ, it is expressed as

$$A_{\text{eff}}(E_\nu,\theta) = V_{\text{eff}}(E_\nu,\theta)\sigma_{\nu N}(E_\nu)\rho N_A \text{P}_{\text{Earth}}(E_\nu,\theta), \tag{2.14}$$

where ρ is the medium (i. e. seawater) density, and P_{Earth} is the neutrino transmission probability through the Earth. For up-going events ($\cos\theta < 0$), A_{eff} increases with energy and, otherwise, starts to decrease at few hundred of TeV because of the absorption of neutrinos in the Earth. Note that these detector properties are not fixed. When cuts on reconstruction parameters are applied, and thus it is required to select only events satisfying particular criteria (see Sect. 2.3.1), the detection capability lowers with respect to that at the trigger level. Furthermore, A_{eff} and V_{eff} are analysis dependent, with the latter optimised through different event selection criteria. This is reflected into N_{det} in Eq. (2.13), which full-fledged represents the number of events surviving analysis cuts. Note that A_{eff} and V_{eff} can also be estimated for muons, with respect to which neutrino effective volume and area are many orders of magnitude smaller, due to the small neutrino interaction cross section.

By knowing the detection efficiency of a neutrino telescope through the effective area, for a predicted astrophysical neutrino flux $\phi_\nu(E_\nu,\theta) = \mathrm{d}N_\nu/(\mathrm{d}E_\nu \mathrm{d}t \mathrm{d}A \mathrm{d}\Omega)$, the expected number of events in the detector and in a defined time interval can be computed as

$$N_\nu = \int \phi_\nu(E_\nu,\theta) A_{\text{eff}}(E_\nu,\theta) \mathrm{d}E_\nu \mathrm{d}t \mathrm{d}\Omega. \tag{2.15}$$

By considering that $A_{\text{eff}} \propto V_{\text{eff}} \propto N_{\text{det}}$ (see Eq. (2.14) and Eq. (2.13)), where N_{det} in turn depends on the neutrino energy and direction, there are two consequences: (i) sources with similar ϕ but different spectral index produce a different response in neutrino telescopes (the harder the spectral index, the better the source can be seen); (ii) due to Earth motion, the position in the detector frame of a given source in the sky changes with daytime. For this reason, the effective area needs to be computed for each declination by averaging over the local coordinates (zenith and azimuth angles).

2.4.4 *Sensitivity and discovery potential*

One of the most important goals of a neutrino telescope is to search for cosmic neutrino signals. This is very challenging, as previously discussed, because of the existence of a large background. Therefore, appropriate statistical methods need to be used when looking for such a small signal from a given astrophysical source in the recorded data and, in the negative case, to set exclusion limits to neutrino production for that source. In the case described here, the detector properties considered are *discovery potential* [201] and *sensitivity* [202].

The former is usually evaluated through the Model Discovery Potential (MDP) [203], i. e. the probability of observing an excess at a given level of significance assuming the signal predicted by the theoretical model. In this case, cuts are optimised to obtain the minimum number of signal events necessary to claim a discovery.

If no significant signal is found, upper limits are set using the Model Rejection Factor (MRF) [202], as

$$\phi_{90\%} = \phi_\nu \cdot \text{MRF} = \phi_\nu \frac{\bar{\mu}_{90\%}(\langle n_{\text{bkg}} \rangle)}{\langle n_{\text{s}} \rangle}, \tag{2.16}$$

where ϕ_ν is the expected flux level by the model, and MRF is defined as the ratio between the average experimental upper limit at 90% confidence level (C.L.) $\bar{\mu}_{90\%}$ on the number of signal events n_{s} and the expected average number of n_{s} from a source with a given ϕ_ν. The parameter $\bar{\mu}_{90\%}$ depends on the mean number of background events n_{bkg} and is calculated following the Feldman-Cousing approach [202]. Again, the optimal set of cuts used in an analysis can be found by minimising the MRF. Thus, the detector flux sensitivity can be calculated as

$$\phi_{\text{sens}} = \text{MRF} \cdot \phi_{\nu}. \tag{2.17}$$

The quantity in Eq. (2.17) represents the largest flux that can be excluded by the detector with a given C.L., which is typically considered at 90%.

2.5 ASTROPHYSICAL NEUTRINOS DETECTION IN THE MEDITERRANEAN SEA

Neutrino telescopes are three-dimensional arrays of PMTs distributed in huge and deep areas characterised by a transparent medium so that: (i) a large volume of free and natural target for neutrino interactions is available; (ii) the medium shields against secondary atmospheric particles produced by CRs; (iii) the Cherenkov light induced by the path of relativistic particles produced by neutrino interaction can be visible to PMTs. If seawater is used as the medium, neutrino telescope sites need to be located far enough from coasts and river estuaries to avoid turbulent currents and preserve the purity of water. Moreover, at the same time, they should be close to the scientific and logistic infrastructures on shore. With all such requirements, the Mediterranean Sea offers optimal conditions on a worldwide scale. A first generation neutrino telescope in the Mediterranean Sea has been fully operative between 2008 and the beginning of 2022 off the French coast. This detector, named ANTARES [205], was characterised by an instrumented volume of about 1% cubic kilometre and has proved the feasibility of neutrino detection in seawater, providing a wealth of experience in the field. However, unfortunately it has not identified neutrinos of cosmic origin, even if important constraints to astrophysical models were defined thanks to its data. In fact, it can be estimated that at least a km^3 volume is needed to perform successful neutrino astronomy, as demonstrated by the results obtained by the cubic-kilometre-size neutrino telescope IceCube, built in deep ice at the south pole and operative for about twelve years. Based on the ANTARES experience, a km^3 Mediterranean Neutrino Telescope (KM3NeT) is currently under construction and is already taking data. With the partial detector configuration active at the time of writing, the volume of KM3NeT results is already greater than that of ANTARES[7]. The presence of neutrino detectors in both hemispheres is fundamental for the visibility of the whole neutrino sky without being obscured by the large flux of cosmic neutrinos. Fig. 2.8 shows the total sky visibility by combining the Mediterranean-based neutrino telescopes and IceCube at the South Pole. In the following, the two telesopes ANTARES and KM3NeT are described, in Sect. 2.5.1 and Sect. 2.5.2, respectively.

7 When the KM3NeT volume reached the one of ANTARES, the dismantling of the latter started.

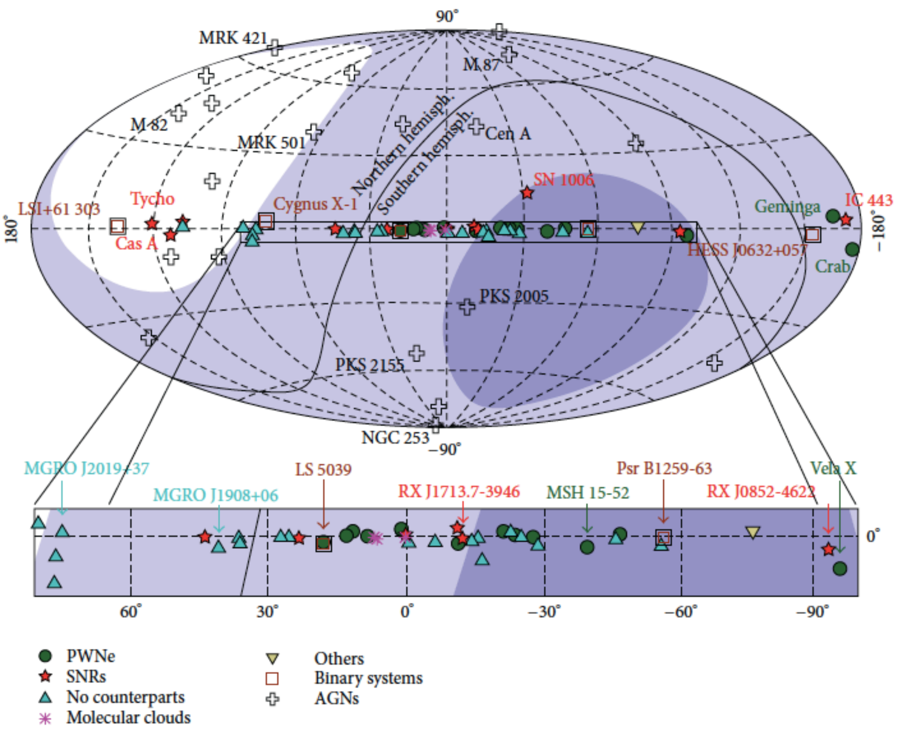

Figure 2.8: Sky map in Galactic coordinates showing the combination of the field of view of Mediterranean-based neutrino telescope (i. e. the Southern Hemisphere) and IceCube at the South Pole (i. e. the Northern Hemisphere) 2π downward coverage. Shades of blue indicate the fraction of time during which sources are visible for Northern telescopes: >25% and >75% of the time for light and dark areas. The white area corresponds to a non-visible region of the sky. The location of some sources of high-energy gamma rays, candidates for neutrino emission, are also indicated. Image credit: [204].

2.5.1 *The first undersea neutrino telescope: ANTARES*

ANTARES, which stands for Astronomy with a Neutrino Telescope and Abyss environmental RESearch project, with an instrumented volume of ~ 0.05 km^3, has been for a long time (2008-2020[8]) the largest neutrino observatory in the Northern Hemisphere. It was located at a depth of ~ 2500, 40 km offshore the coast of Toulon (France). A total of 12 strings, distant 70 m between each other, were anchored on the sea bed at a depth of ~ 2500 m and tensioned by buoys at the top. In a string, 75 optical modules (OM) were distributed over 25 *storeys*, each equipped with 3 OMs that form a triplet. OMs were 17" glass spheres each housing a 10" PMT. The 3 PMTs in a storey were arranged with axis pointing at 45° below the horizontal plane for an increased efficiency for upgoing muon detection [206]. In this way, in the lower hemisphere, there was overlap in angular acceptance between modules, allowing an event trigger based on coincidences from this overlap. Since the strings were subject to sea current (their shape and orientation could change), they were equipped with different sensors and instrumentation was present for time and position calibration (LED beacons, hydrophones, compasses, and tiltmeters). An additional *instrumentation line*, dedicated to carry devices for environmental monitoring, was also present [208, 209]. In

8 Up to the completion of Baikal-GVD.

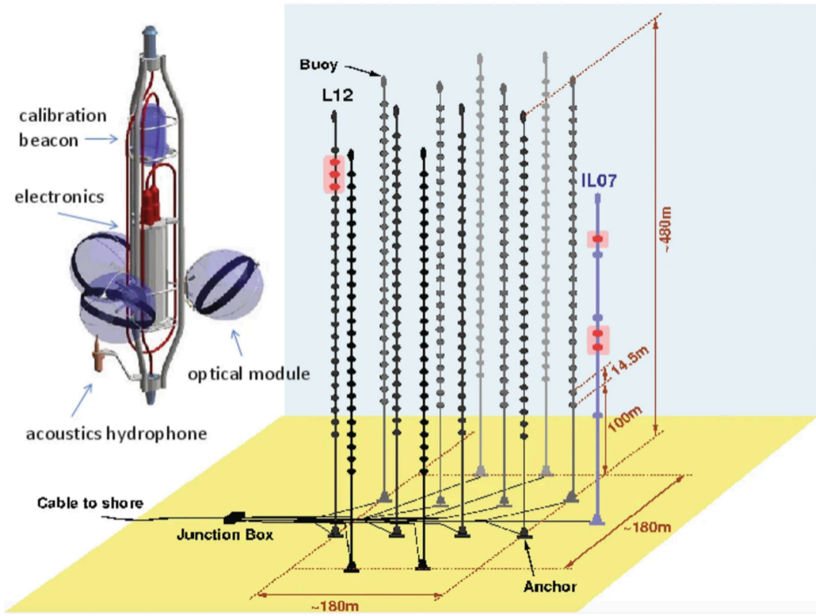

Figure 2.9: Schematic view of the ANTARES detector, with 12 strings (from L1 to L12), and the instrumentation line (IL07) with environmental equipment. A storey (with 3 OMs, calibration, and electronic devices) is visible. Image credit: [207].

Fig. 2.9, the schematic layout of ANTARES and its component are shown. The detector was connected to a shore station using an electro-optical telecommunications cable, providing power and allowing the transmission of information from sea to shore and viceversa. For a detailed description of the detector and Data AcQuisition system (DAQ), see [205, 210]. The total ANTARES sky coverage was 3.5π sr, with an instantaneous overlap of 0.5π sr with that of IceCube. Thanks to its location, the Galactic Centre could be observed 67% of the day time by means of Earth-filtered events [193].

2.5.2 *Cubic kilometre neutrino telescope: KM3NeT*

KM3NeT is a multipurpose neutrino observatory currently being constructed at two sites in the Mediterranean Sea [211]. ARCA (Astroparticle Research with Cosmics in the Abyss), located in Portopalo di Capo Passero close to the Sicilian coast (Italy) at 3500 m of depth, is devoted to the detection of high-energy neutrinos (1 TeV-10 PeV) produced in astrophysical phenomena related to cosmic-rays acceleration; ORCA (Oscillation Research with Cosmics in the Abyss), lying off the coast of Toulon (France) at a depth of about 2500 m (close to the ANTARES location), is optimised for the detection of lower-energy neutrinos (1-100 GeV) and aims to provide information on their fundamental properties. Even if those detectors aim to achieve different scientific goals, they are built with the same innovative technology, based on the so-called Digital Optical Modules (DOMs), pressure-resistant glass spheres containing 31 PMTs, a number of calibration devices, and the read-out electronics. For the first time in a neutrino telescope, the optical module design was modified from a glass sphere equipped with a single large PMT (e.g. that used by the ANTARES detector) to one with the same diameter housing several PMTs (multi-PMT design) [212]. This choice

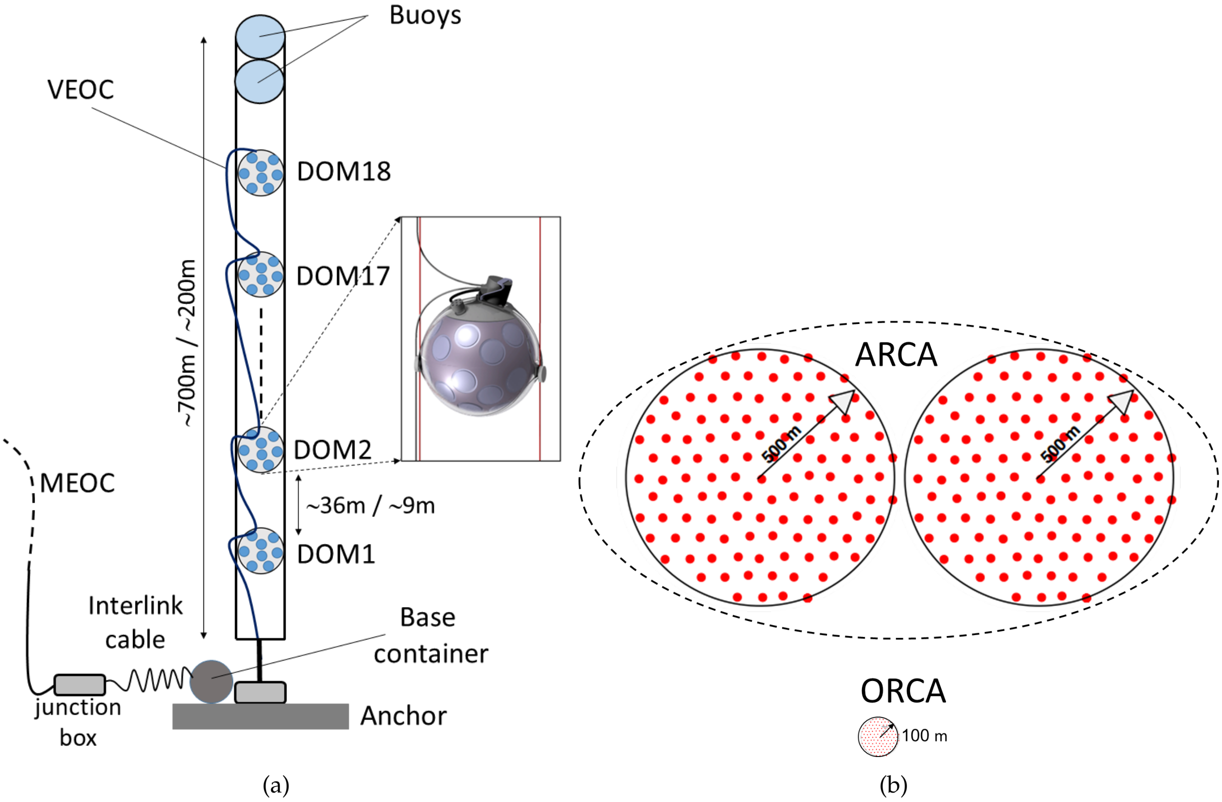

Figure 2.10: (a) Common DU layout for ARCA and ORCA detectors. The DU lengths of ~700(200) and distance between DOMs of ~36(9) m for ARCA(ORCA) are indicated. At the top of each DU, a submerged buoy keeps the structure close to vertical. Attached to the ropes is the VEOC that contains 2 wires for power transmission and 18 optical fibers for data transmission. The VEOC connects the DOMs with the base container and thus to the shore station via the MEOC. (b) Comparison between ARCA and ORCA size, once both detectors will be complete. Image credit: https://www.km3net.org/research/detector/km3net-arca-and-orca/.

provides a large photocathode area, good separation between single-photon and multiple-photon hits, and information on the photon direction. The detector is made of a 3D array of Detection Units (DUs), vertical strings with 18 DOMs each, arranged in a different geometry for ORCA and ARCA to probe distinct ranges of neutrino energies. Each DU, sustained by means of two ropes, is anchored on the seabed. On the top, a buoy is used to keep the DU in a vertical position. A Vertical Electro-Optical data Cable (VEOC) [213] runs along the entire length of the DU with breakout units at each DOM. It is attached to the ropes and contains two copper wires for power transmission (400 VDC) and 18 optical fibres for data transmission. Power and data exchange is possible through a main electro-optical cable (MEOC) between a shore laboratory and the submarine apparatus. A Base Module (BM) is provided for each DU and hosts the power and data communication electronics. The DU layout is shown in Fig. 2.10(a). Analogously to ANTARES, the DAQ is based on the so-called *all-data-to-shore* concept, namely all data collected offshore are digitised and sent without reduction to the onshore control station.

In ORCA, designed for the study of neutrino intrinsic properties, DOMs are arranged in a dense configuration, required for detecting events with energies as low as few GeV.

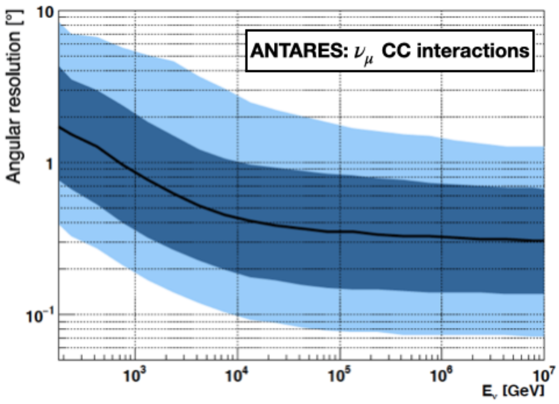

(a)

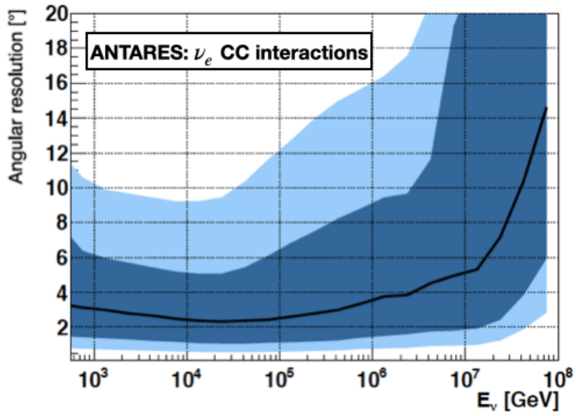

(b)

Figure 2.11: ANTARES median angular resolution for (a) track-like events from ν_μ CC interactions and (b) for shower-like events from ν_e CC interactions. The dark (light) blue band is the 90%(68%) quantile of the distributions. Images credit: [214].

This range is three orders of magnitude lower than the typical energy scale proved by the high-energy detector ARCA. Indeed, being the latter designed for neutrino astroparticle physics studies, the configuration of its array is optimised to detect neutrinos with energy above several hundred of GeV. In particular, the DOMs in the ARCA (ORCA) array are distributed in the seawater volume with an average horizontal distance of about 90 (20) m and a vertical distance of about 36 (9) m, with the lowest modules at about 70 (30) m above the seabed. DUs are grouped into building blocks (BB) of 115 DUs each. The goal is to install 115 DUs (1BB) for ORCA and 230 DUs (2BB) for ARCA within the next few years, to achieve a total instrumented volume of more than one cucib kilometre. For a comparison of the size of the ORCA and ARCA detectors, once complete, see Fig. 2.10(b). At the time of writing, 15 and 21 DUs are operational for ORCA and ARCA, respectively.

2.5.3 *Detector performances and improvements with KM3NeT*

The optical properties of seawater (see Sect. 2.2) allow excellent timing information for the detected light signals, yieding a very good angular resolution for the reconstructed direction of detected neutrino candidates for all event topologies. ANTARES has already proved this during its about fourteen years of full operation; with a relatively small instrumented volume, it was characterised by an excellent angular resolution, that is, in median $< 0.4°$ for track events with E_ν above 10 TeV, and $< 3°$ for showers with E_ν between ~ 1 and ~ 10 TeV (see Fig. 2.11). As regards the energy resolution, for tracks detected by ANTARES its value was $< 50\%$ on $\log_{10} E_\mu$, and $\sim 25\%$ of the shower energy for cascade events. In the case of showers due to ν_e CC interactions, the energy resolution improves to $\sim 10\%$ [214].

With the full KM3NeT/ARCA configuration, these values are expected to improve to $< 0.1°$ for the tracks (see Fig. 2.12(a)) and $< 2°$ for showers with $E_\nu > 10$ TeV. Moreover, recently a refined cascade reconstruction algorithm has been presented by making a more detailed model of neutrino events and including additional information on hit

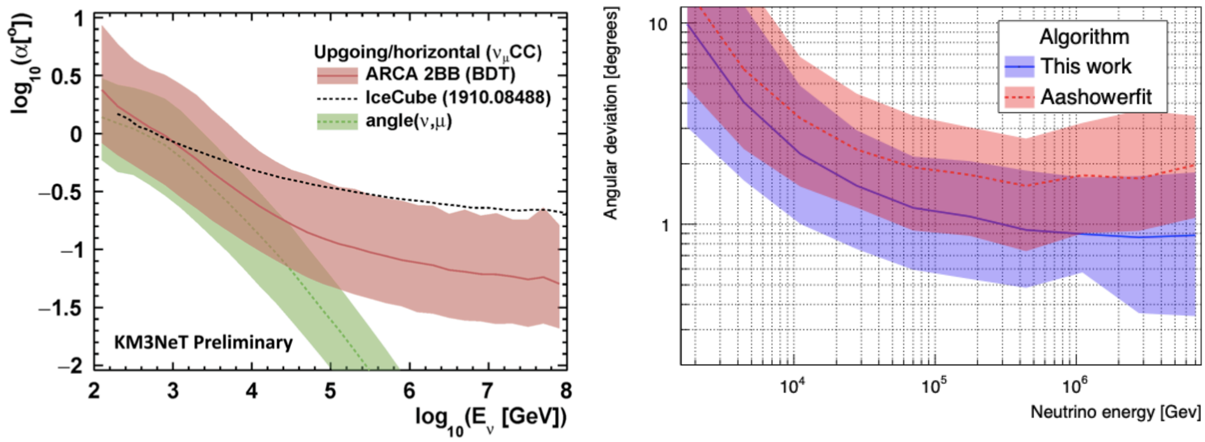

(a) (b)

Figure 2.12: (a) KM3NeT/ARCA 2BB median angular resolution for track-like events from ν_μ CC interactions (red line); the boosted decision tree (BDT) model has been used to select and classify events. The IceCube angular resolution [217] is also shown for comparison by the dashed black line. The green line represents the kinematic angle, in Eq. (2.6), between the incoming neutrino and the secondary muon. Image credits: [218]. (b) KM3NeT/ARCA 2BB median angular resolution for shower-like events with the classical reconstruction algorithm, named *Aashowerfit* (red line), and the new one that makes use also of timing information (blue line). Image credit: [215]. In both figures, the shaded regions represent the 68% quantiles of distributions.

times [215]. According to this novel approach, the median angular resolution of KM3NeT / ARCA improves throughout the energy range and drops below 1° for single cascades of 300 TeV [215]. For a comparison between the performance of the two reconstruction algorithms, see Fig. 2.12(b), where the clear improvement in the median of angular resolution is evident when timing information is included. The energy resolution for the tracks in KM3NeT/ARCA is expected to be better than $\sim 20\%$ in $\log_{10} E_\mu$ for $E_\mu > 10$ TeV [216], while in the cascade channel an energy resolution $< 5\%$ can be achieved for the same energies [215]. Currently, with only one tenth of the operational detector, KM3NeT has already been demonstrated to be capable of reaching an angular resolution better than 1° for $E_\nu > 1$ TeV, as will be shown in the context of results discussed in Chapter 5. Once completed, the instrumented volume of KM3NeT is expected to be $\gtrsim 2$ orders of magnitude greater than ANTARES. Due to this huge detector volume, its effective area will also be larger of the same factor (on average, it will grow from $\sim 10^2$ m^2 at 10 TeV to $\sim 10^3$ m^2 at 100 PeV [218]), and the sensitivity to high-energy neutrino fluxes will be greatly improved with respect to ANTARES. E.g., Fig. 2.13(a) shows the much better sensitivity of ARCA 2BB to point-like cosmic neutrino sources with a flux of E^{-2}, even after a few years of data taking, with respect to that of ANTARES after 13 years [219]. In addition, the KM3NeT detector results will be characterised by a better sensitivity with respect to IceCube, especially for negative declination values. The planned KM3NeT/ARCA detector will allow for the detailed study of cosmic neutrinos also in diffuse-flux mode; Fig. 2.13(b) reports preliminary sensitivity estimates (no systematics are included) of the 68% confidence interval using ARCA 2BB compared to the diffuse astrophysical $\nu_\mu + \bar{\nu}_\mu$ flux detected by IceCube in 9.5 years

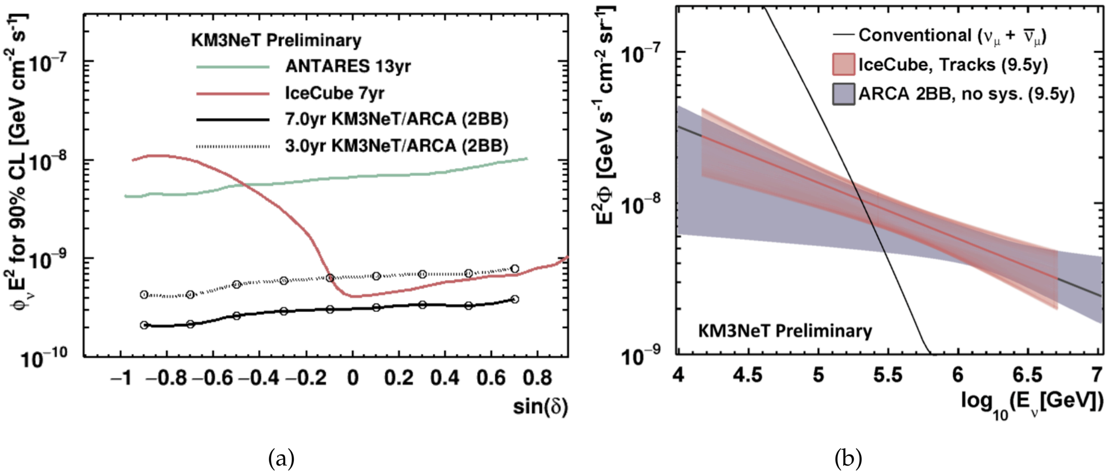

Figure 2.13: (a) KM3NeT/ARCA 2BB sensitivity obtained for upgoing $\nu_\mu + \bar{\nu}_\mu$ tracks and for a point-like source with spectrum $\propto E^{-2}$ after 3 (dashed line) and 7 (solid line) years of data taking, in comparison with that of ANTARES in 13 years of operation (green line) [219], and IceCube in 7 years (red line) [221]. Images credit: [218] (b) KM3NeT/ARCA 2BB sensitivity after 9.5 years (in grey) for the diffuse astrophysical neutrino flux ($\nu_\mu + \bar{\nu}_\mu$) observed by IceCube in the same years of data acquisition (in red). The black line is the conventional atmospheric neutrino flux prediction [103].

.

of data, showing the capability of KM3NeT to observe such high-energy diffuse neutrino flux. The good expected performances of KM3NeT/ARCA will allow us to make definite statements about the cosmic diffuse neutrino flux and neutrino fluxes from point-like extragalactic sources, as well as also from several Galactic candidates, if their γ-ray emission is of hadronic origin, as pointed out in [216, 218].

So far, the performances of ARCA, the high-energy unit of KM3NeT, have been discussed, because devoted to the detection of cosmic neutrinos from astrophysical sources, as its precursor ANTARES. However, also ORCA, optimised for studying fundamental neutrino properties, can contribute to astrophysical studies for a model in which the production of sub-TeV neutrinos is provided, as will be shown in Chapter 3. For the most updated KM3NeT/ORCA detector performances (e.g. effective volume and median angular resolution), the reader can refer to [220].

The MC simulation chain together with the reconstruction algorithms adopted in ANTARES and KM3NeT/ARCA, through which the detectors performance here shown have been obtained, are presented in Appendix B.

2.6 CALIBRATION OF UNDERWATER NEUTRINO DETECTORS

In order to identify the signature of neutrino interactions in underwater neutrino Cherenkov detectors and achieve a good quality in the reconstruction of events, a precise calibration of charge, position and arrival time of the Cherenkov photons reaching the PMTs is mandatory. An accurate charge calibration ensure good energy resolution, as well as a careful position and time calibration is fundamental for a good angular resolution of the reconstruction of the event direction. This is valid for both ANTARES and KM3NeT neutrino telescopes. In the following, the general characteristics of the position, time, and charge calibration procedures that were adopted for ANTARES up to its dismantling and now in use for KM3NeT are summarised in Sect. 2.6.1, 2.6.2 and 2.6.3, respectively.

2.6.1 *Position calibration*

Detection lines constituting underwater neutrino telescope are pulled up by buoys but move because of sea currents and the position of the OMs slowly changes with time. For this reason, a position calibration is needed to determine the position and orientation of each storey in almost real time as well as the absolute detector position. This is required to reach the targeted precision on event reconstruction shown in Sect. 2.5.3.

To this aim, triangulations of the measured acoustic signals at each storey are performed to determine their position through acoustic sensors located at the bottom of each string. In addition, several hydrophones are strategically placed at some detection storeys. The time delay between the emission and reception of the acoustic signals allows us for measuring the distance between the storeys and inferring their position. In fact, by monitoring the sound velocity in seawater using oceanographic instruments, distances can be determined to infer the storey position. Some tiltmeters and compass are also used to measure the orientation of the OMs, allowing for an independent measurement of their position. Finally, the absolute detector position is obtained by the GPS of the boat used during the deployment of lines.

The deviation of the OM position because of sea currents reached several meters at the top of the ANTARES strings. The positioning system of the ANTARES detector is described in [209]. After the calibration, an accurate positioning with an uncertainty of the order of 10 cm is achieved well within specification. The positioning affects the final reconstruction parameters and analysis results significantly, specially when looking at space coincidences with signals observed by other instruments. The same strategy is used for the KM3NeT positioning calibration (e.g., [222, 223]).

2.6.2 *Time calibration*

The time calibration is required to provide accurate timing of the recorded hits across the whole instrumented volume; in particular, a relative time synchronisation between photomultipliers of the nanosecond order is needed to guarantee the required angular resolution of the detector.

Several factors affect the measurements of the time between the photon being detected in a PMT and reaching the shore station, which changes with time. The time offsets between the different lines may also vary with time. For these reasons, the relative time calibration between OMs is regularly monitored in situ. Different methodologies are used to achieve a better time resolution: the time residuals from the reconstruction of muon tracks, coincident events coming from the radioactive ^{40}K decay in sea water, and calibration systems based on LED and laser devices (optical beacons). Combining all of them, different calibrations are carried out: time differences between PMTs in an the same DOM dor KM3NeT (for ANTARES, in the past, between OMs in the same storey), time differences between DOMs (storeys) in a detection line, and time difference between the different strings. In KM3NeT also information of the time delays between the 31 PMTs of a DOM are used, allowing for a more accurate timing. Time calibration devices and procedure are explained for ANTARES in e.g., [224], while for KM3NeT in e.g., [225, 226].

Solutions that facilitate in-situ timing calibration are of paramount importance for the continuous monitoring of timing calibration constants. In this view, prior to the deployment of the detector, a pre-deployment calibration in a dedicated *dark-room* is foreseen after the integration of the structure, in order to measure the initial timing calibration constants. Part of the present thesis also includes this activity, described in Appendix A, where also more details on the time calibration performed in KM3NeT are provided.

2.6.3 *Charge calibration*

Together with the time and the position, the energy reconstruction is the other required ingredient for an accurate reconstruction of the events. A charge calibration is demanded for a best energy estimate. Establishing the relation between the number of photo-electrons and the measured amplitude of the PMT signal is the main goal of the charge calibration.

When a photon impinges on the photocathode area at the entrance window of a PMT, it produces electrons, which are then accelerated by a high-voltage field and multiplied in number within a chain of dynodes by the process of secondary emission. This is the working principle of a PMT, which is based on the amplification of secondary emission of electrons off dynodes via photoelectric effect. The charge of the signal generated by the photo-electrons (p.e.) is digitised by an Analog-to-Voltage Converter (AVC) into a value related to the number p.e. produced in the PMT. To correctly evaluate these quantities, before detector lines deployment, the PMTs are calibrated in the dark-room to measure the single photoelectron signal. Then, in-situ calibration are also performed through specific run of data taking; indeed, over time, the measured values degrade, so regular high voltages tunings of the PMTs need to be performed to maintain the 0.3 p.e. hit threshold, adopted both in ANTARES and KM3NeT.

2.7 OTHER OPERATIVE CUBIC-KILOMETER HIGH-ENERGY NEUTRINO TELESCOPES IN THE WORLD

Beyond the neutrino telescopes subject of this thesis, that exploit the sea water properties to detect neutrinos, world-wide effort in neutrino astronomy is concentrated also in other experiments, as IceCube and Baikal-GVD, that deserve particular attention because of their large volume and sensitivity. Complementary detections by IceCube, Baikal-GVD and KM3NeT allow to collect neutrino data from all directions in the sky and through their combination we expect to achieve in the future important astrophysical results in the context of neutrino astronomy. For this reason, the IceCube and Baikal-GVD experiments are briefly outlined in Sect. 2.7.1 and Sect. 2.7.2 respectively.

2.7.1 *Under-ice neutrino telescope: IceCube*

IceCube [227], a cube of 1 km^3 instrumented in Antartica ices, has been in operation at the South Pole since 2010. The telescope views the ice through approximately 5160 sensors called DOMs. The DOMs are attached to vertical strings, frozen into 86 boreholes, and arrayed over a cubic kilometer from ~ 1.4 km to ~ 2.5 km depth. The strings are deployed on a hexagonal grid with 125 m horizontal spacing and hold 60 DOMs each. The vertical separation of DOMs is 17 m. Eight of these strings at the center of the array were deployed more compactly, with an horizontal separation of about 70 m and a vertical DOM spacing of 7 m. This denser configuration forms the DeepCore subdetector [228], which lowers the neutrino energy threshold to about 10 GeV, creating the opportunity to study neutrino oscillations. However, it is worth introducing here that such low neutrino energies are also interesting in astrophysical studies for specific source models. This statement will be clearer in Chapter 3, where I discuss the capability of low-energy detectors as DeepCore and KM3NeT/ORCA of achieving astrophysical results (for GRBs, in the specific case of this thesis). At the surface, an air shower CR detector array, called IceTop [229], is coupled to the detector completing the IceCube Neutrino Observatory (see Fig. 2.14).

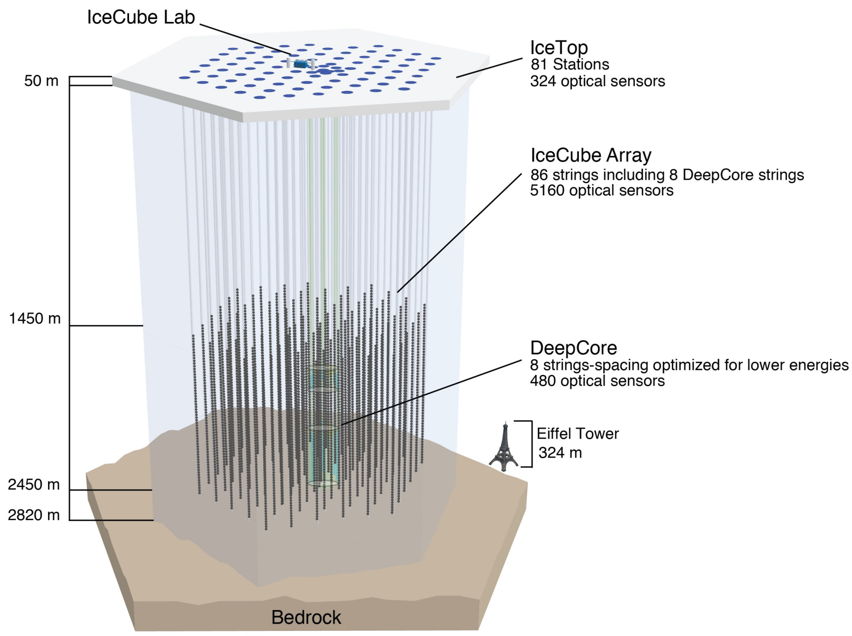

Figure 2.14: The IceCube Neutrino Observatory. Image credit: https://icecube.wisc.edu.

The IceCube detector has achieved remarkable results in neutrino astronomy, namely it allowed the discovery of a diffuse flux of cosmic neutrinos and found first evidence for a cosmic particle acceleration in the jet of an AGN, as widely discussed in the previous chapter. In the future, new important discoveries by IceCube are expected; indeed, the IceCube Collaboration plans to expand the current detector to next-generation instrument called IceCube-Gen2 [230], that will be a ten-cubic kilometer detector characterised by a spacing between light sensors larger than 250 meters, instead of the current 125 meters in IceCube.

2.7.2 *Under-water neutrino telescope: Baikal-GVD*

The underwater neutrino telescope Baikal-GVD [175] is a cubic kilometer scale Cherenkov detector designed to detect neutrinos in the TeV-PeV energy range with a goal to establish their sources. It is located in the Siberian lake Baikal at a depth of approximately 1.4 km and represents an extension of a previous neutrino detector (Baikal NT-200 Detector) [231], whose first test detection units were deployed in the early nineties and that allowed to make a first search for high-energy neutrinos [232]. The configuration of the telescope consists of functionally independent clusters of strings, which are connected to shore by individual electro-optical cables. Each cluster includes 288 OMs arranged along 8 strings where 7 peripheral strings are uniformly located at a 60 m distance around a central one. The distances between the central strings of neighboring clusters are about 300 m. The first full-scale Baikal-GVD cluster was deployed in April 2016. In 2017–2022, nine additional clusters were deployed and commissioned, increasing the total number of optical modules to over 2800 OMs. The current configuration, shown in Fig. 2.15, include ten clusters.

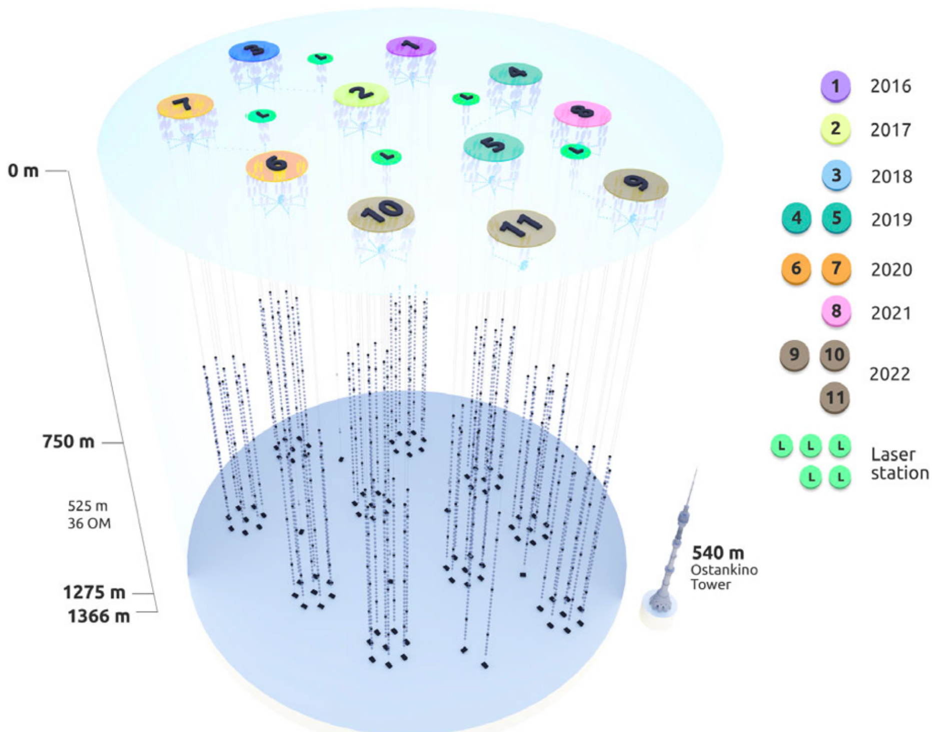

Figure 2.15: Ten Baikal-GVD clusters in the 2022 configuration. Stations with calibration laser light sources and experimental strings are shown. The season of deployment of each cluster is also reported on the right. Image credit: [122].

The first observation of the diffuse cosmic neutrino flux with the Baikal-GVD neutrino telescope, using cascade-like events collected in 2018–2021, has been recently announced

[122]: a significant excess of events over the expected atmospheric background is observed; this excess is consistent with the high-energy diffuse cosmic neutrino flux observed by IceCube (see Sect. 1.3.3).

3

THE ORIGIN OF GAMMA-RAY BURSTS PROMPT EMISSION: AN UNSOLVED PUZZLE

This thesis is mostly focused on Gamma-Ray Bursts (GRBs), flashes of high-energy radiation arising from energetic cosmic explosions. In the context of the multimessenger framework discussed in Chapter 1, GRBs are considered promising sources to be studied, as the combination of large energetic budget and relativistic jet can in principle explain particle acceleration to ultra-high energies (i.e., UHECRs), from whose interactions high-energy neutrinos result.

In Sect. 3.1, GRB characteristics are outlined. The physical mechanisms responsible for gamma-ray emission and possible neutrino production in GRBs are discussed in Sect. 3.2 and Sect. 3.3, respectively. This chapter focusses in particular on neutrinos produced in the so-called *inelastic collisional model*, a scenario capable to explain the GRB emission but still poorly investigated by the experimental neutrino community. Indeed, among the purposes of this thesis, there is the evaluation of the detection prospects for the next generation neutrino telescope KM3NeT (see Sect. 2.5.2 for the detector description) of ~GeV neutrinos expected to be produced in such a model. In addition, estimates for the current IceCube detector are also provided. This work is presented in Sect. 3.4 and is based on results already published in ***Zegarelli A.***, *Celli S., Capone A., et al., 'Detection prospects for multi-GeV neutrinos from collisionally heated GRBs', Physical Review D* ***105****, 083023 (2022)* ([233]).

3.1 GAMMA-RAY BURSTS

Gamma-Ray Bursts (GRBs) are the most luminous astrophysical phenomena currently observed in the Universe. They are detected at a rate of the order of a few per day at random locations in the sky (extragalactic sources) [234–236], as shown in Fig. 3.1 up to very high redshifts: the farthest GRBs observed so far are localised at $z \sim 9.4$ [237], i.e., when the age of the Universe was only ~ 0.5 Gyr, and $z \sim 8.2$ [238, 239], by photometric and spectroscopic measurements, respectively. The released isotropic energy [240] amounts up to $\sim 10^{54}$ erg [241, 242] in a time lasting from a fraction of a second to several thousands of seconds. Since their serendipitous discovery in the late 1960s [243], much has been learnt about these fascinating explosions, thanks to a considerable number of γ-ray/X-ray satellites that have been investigating GRBs over the years (Compton Gamma-Ray Observatory, BeppoSAX, KONUS-Wind, HETE-2, Swift, Integral, AGILE, Fermi) and the follow-up observations carried out by numerous ground-based observatories in the optical, infrared, and radio wavelengths. Indeed, the flash of bright gamma rays (keV-MeV energy range) observed in the first seconds, which is commonly referred to as the *prompt* phase, is followed by the so-called *afterglow*, a long-lived radiation emission detected on a very wide range of frequencies, from γ rays to the radio band, lasting from weeks to months after the explosion and characterised by an exponential decrease in intensity with time. The distinction between the two phases, at the beginning predicted only theoretically [244], was confirmed by the observational discovery of an X-ray afterglow associated with a GRB occurred the 28th of February 1997 (following the common notation adopted, GRB 970228) [245]. The detection of the afterglow radiation is crucial to determine the galaxy hosting the burst and, thus, its distance. In this way, the intrinsic energy released by GRBs can be calculated. Prompt and afterglow emissions are interpreted as two distinct emission phases, as the result of the launch of an ultra-relativistic jet from a newly born compact object (see Sect. 3.2.1). After the first internal dissipation that generates the prompt gamma-ray emission, the ejecta undergoes external dissipation [246], triggered by interaction with the intestellar medium or the wind of the progenitor star. The two processes occur at different typical distances from the central engine, i.e., $R \sim 10^{13} - 10^{14}$ cm and $R \sim 10^{15} - 10^{20}$ cm, respectively.

Today, one of the big questions in GRB research is related to the physical mechanism that causes the prompt emission; indeed, from the observational point of view, GRBs show a wide variety of properties, that make them challenging to be characterised. Another unknown concerns the composition of the jet, as the mechanisms responsible for GRB emission can be either leptonic and hadronic. To reduce the uncertanties and discriminate among the various emission models proposed, neutrinos are a useful tool. If neutrinos were seen in association with a GRB, this would constitute the breakthrough to clearly define the hadronic nature of such sources. Interestingly, from the energy of such neutrinos, it is possible to constrain among the several possible physical mechanisms that are potentially behind GRBs production. In fact, different emission regions are provided by theoretical modelling of GRBs and, for each of those, neutrinos emerge with distinct energies: typically, the farther the emission region from the GRB central engine, the higher the neutrino energy, as will be clear hereafter. To provide a clear explanation of GRB models treated in this chapter, it is necessary to introduce the observational properties of GRB prompt emission, described below: first, GRB light curves are described in Sect. 3.1.1; then, temporal and spectral GRB properties are outlined in Sect. 3.1.2 and Sect. 3.1.3.

3.1.1 *Gamma-ray light curves*

As a result of the gamma-ray radiation emitted during the GRB prompt phase, a wide variety of light curves are observed, with different shapes and no coherent or periodical behaviour. There exist those with a single sharp peak and those that are double or triple peaked, some consist of relatively simple temporal structures with no variability, while others are characterised by a strong variability, or also by a long quiescent period between different peaks (see Fig. 3.2). Light curves are believed to reflect the activity of the

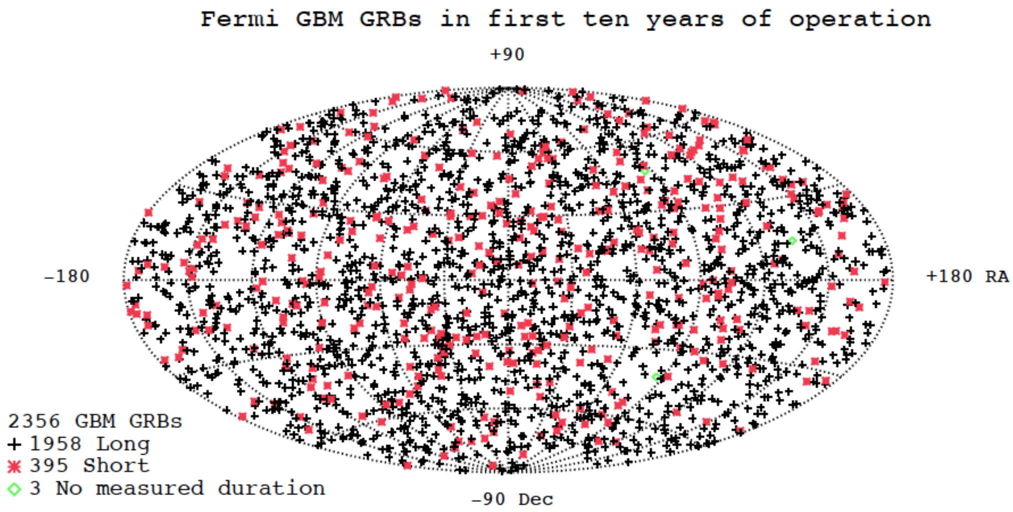

Figure 3.1: Sky distribution in celestial coordinates of GRBs triggered by the Gamma-ray Burst Monitor (GBM) on-board the *Fermi* observatory, over the first 10 years of the mission, starting from the 12nd of July 2008 until the 30th of June 2018. Black crosses, red asterisks and green markers indicate LGRBs, SGRBs and GRB with no measured duration, respectively. Image credit: [247].

GRB central engine [248]. In this regard, an important parameter is the minimum variability timescale t_v, namely the minimum width of peaks that characterises a light curve. In fact, most models attribute it to a physical origin, like the central engine activity, clumpy circumburst medium, or relativistic turbulence [249]. In principle, by exploring the distributions of the t_v values, important information about central engine activity can be inferred; however, these studies are limited by the temporal resolution of each detector[1].

GRBs can exhibit variability times as short as a few milliseconds, indicating that the emission region included in a volume with radius $R \simeq c\Gamma^2 t_v$, with Γ the average Lorentz factor of the relativistic GRB outflow, must be very compact. Such a short variability timescale represented in the 1970s the key parameter to understand the relativistic nature of GRBs [250, 251]. If the source is not relativistic, the emission radius would be simply $R = ct_v$, that implies $R < 10^8$ cm for the observed t_v values of the order of ms. However, such a small R would be problematic. All high-energy photons contained in such a small region would suffer from a large optical depth for the pair production process $\gamma + \gamma \to e^+ + e^-$, which would not allow them to escape. This argument is commonly known as the *compactness problem*. Instead, in a relativistic outflow with Lorentz factor Γ, the size of the emission radius is increased by Γ^2. Because of the relativistic outflow, the observed photons are blueshifted, and their energy in the rest frame of the outflow is reduced by a factor $\sim \Gamma$. Thus, the typical comoving photon energies are much lower than observed.

1 The variability of short-duration GRBs is difficult to be studied, since their duration is closer to the limiting temporal resolution of the detectors.

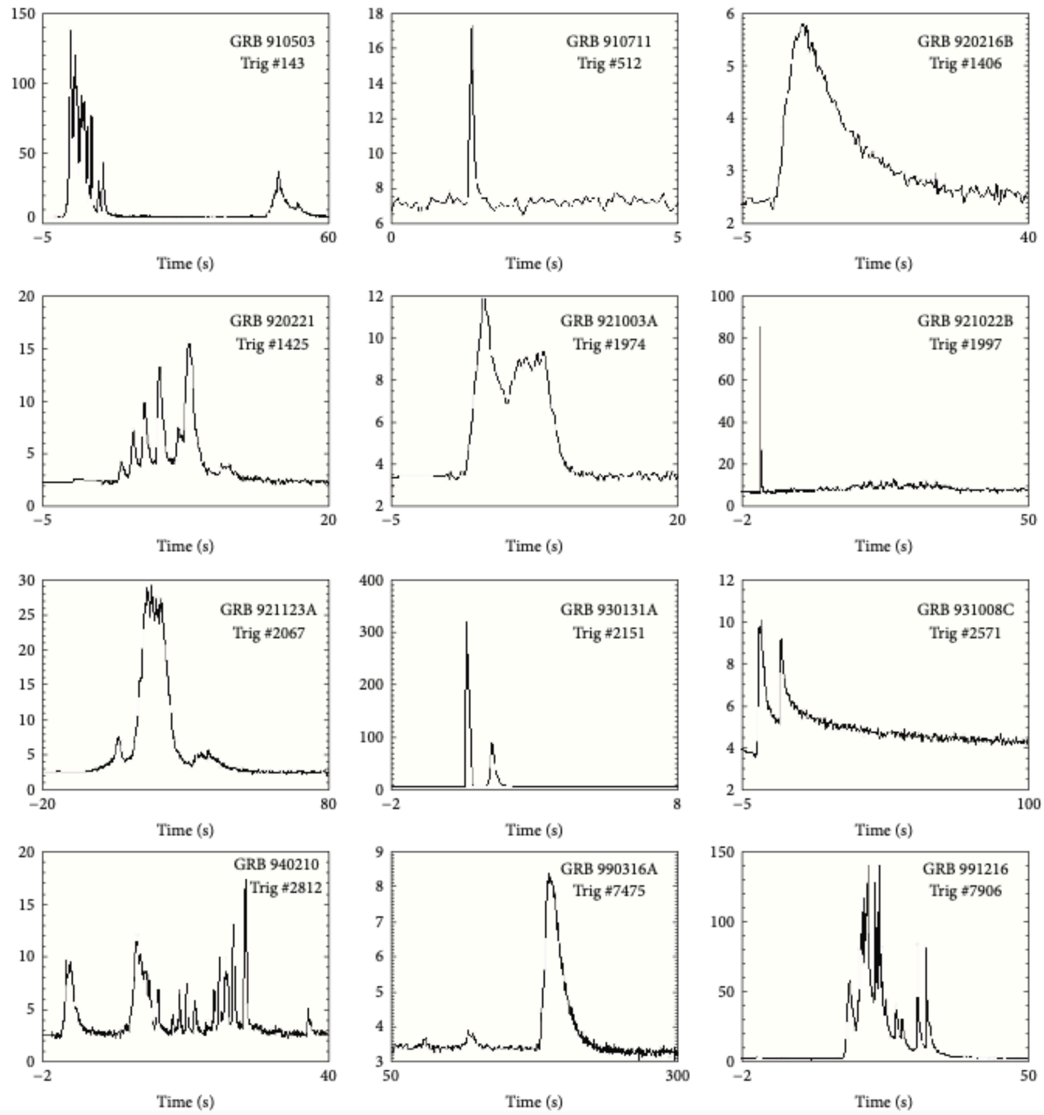

Figure 3.2: Light curves (photon rate in unit of 10^2 counts/s as a function of time) of 12 GRBs detected by BATSE. Image credit: [252].

3.1.2 *GRB properties*

GRB prompt emission lasts from milliseconds to thousands of second. These durations are estimated through the time interval between the 5% and the 95% of their gamma-ray fluence[2] being released, expressed by the parameter T_{90}. The T_{90} measured values appear to have a bimodal distribution since their first detections by the Burst And Transient Source Experiment (BATSE), operative between 1991 and 2000 on board of the Compton Gamma-Ray Observatory (CGRO). This suggests the existence of two distinct GRB populations [235, 253]: short (SGRBs) and long (LGRBs) GRBs, with $T_{90} \lesssim 2$ s and $T_{90} \gtrsim 2$ s, respectively. This classification is also supported by the clustering of SGRBs and LGRBs into two different regions in the T_{90}-hardness diagram. The hardness HR_{32} is typically estimated as the ratio

2 The time-integrated radiant energy per unit area within the detector energy range.

between the fluence obtained through photon counts collected by a given detector in a hard energy band (indicated by the number 3) and a soft one (2):

$$\mathrm{HR}_{32} = \frac{\int_{E_{\mathrm{min},3}}^{E_{\mathrm{max},3}} Ef(E)\mathrm{d}E}{\int_{E_{\mathrm{min},2}}^{E_{\mathrm{max},2}} Ef(E)\mathrm{d}E}, \tag{3.1}$$

where $f(E)$ is the photon differential energy flux at energy E. Note that the hard and soft energy bands are arbitrary and depend on the instrument considered; thus, several different hardness ratios exist. For example, Fig. 3.3 shows the T_{90}-HR$_{32}$ diagram obtained by using data from ~ 3000 GRBs between 2008 and 2021 in the *Fermi*-GBM catalogue. For the HR$_{32}$ estimation, channel 3 is (50-300) keV and channel 2 (8-50) keV. By performing a log-normal bimodal fit of the T_{90} distribution, the short (in red) and long (in blue) components were found to peak at $T_{90} \sim 0.64$ s ($1\sigma = 0.65$ s) and $T_{90} \sim 38.6$ s ($1\sigma = 23.4$ s), respectively. Accordingly to this separation, the median HR$_{32}$ is ~ 2 for SGRBs and ~ 0.8 for LGRBs [254], which means that the spectra of short events are typically harder than those of long ones. Similar results can be obtained by using catalogues containing data collected by other γ-ray satellites as BATSE [255] and Swift [254].

The classification in short/hard and long/soft GRBs[3] generally reflects two different physical phenomena. LGRBs are typically associated with supernovae, indicating that they originate from the collapse of very massive stars at the end of their life (e.g., [256]). The observation of GRB 980425 in conjunction with SN 1998bw showed this connection unambiguously for the first time [257], followed by several more associations in the subsequent years. This assumption however ignores the fact that $\sim 70\%$ of massive stars are found in binary systems, and therefore it is very plausible that most GRBs progenitors are binaries, as considered in the *binary driven hypernova* scenario [258, 259], not discussed in this thesis. SGRBs are generated by the merging of two compact objects, such as two neutron stars (NS), two black holes (BH), or NS+BH. This was observationally proved the 17th of August 2017 by the associated detection of a gravitational wave and short GRB event (see Sect. 1.4). However, it is worth mentioning that the picture in which long GRBs are all physically related to massive star core collapses while short GRBs all physically related to compact star mergers was destroyed some years ago by several observations. E.g., GRB 060614 and GRB 060605 were both nearby long-duration GRBs unassociated with an accompanying supernova [260–263]. More recently the bright GRB 211211A confirmed this statement; despite of its long duration (about a minute), this event seems to stem from NS merger because of the related observation of a kilonova [264, 265]. Therefore, GRBs might be much more difficult to classify than what previously thought. It is no more possible to assume that all short-duration bursts come from neutron-star mergers, whereas long bursts come only from supernovae.

3 It is worth saying that this boundary between short and long GRBs is known to be detector dependent, because the parameters used to discriminate between SGRBs and LGRBs depend on the energy band at which detectors are sensitive.

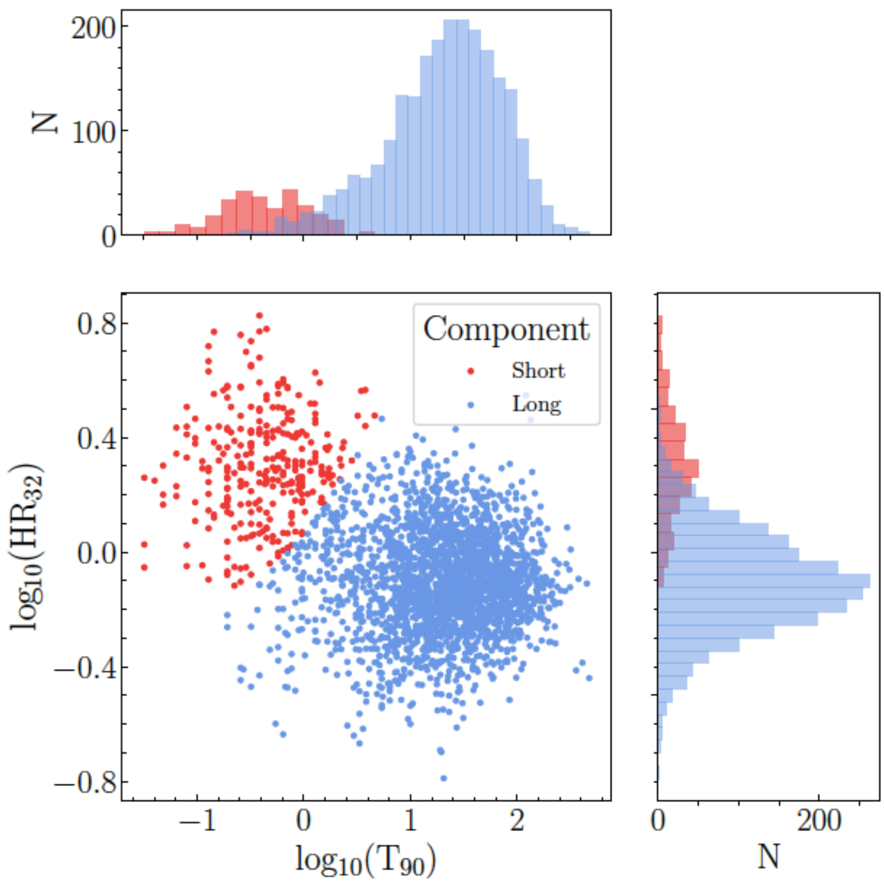

Figure 3.3: Hardness-duration diagram for ~ 3000 GRBs occurred between the 10th of August 2008 and the 17th of March 2021 and detected by the *Fermi*-GBM satellite. The plots attached to the top and right are the projections of the individual distributions of HR_{32} (right) and T_{90}, respectively. Short and long GRBs are indicated in red and blue, respectively. Image credit: [254].

3.1.3 *Spectral template: Band function*

The prompt radiation is a nonthermal high-energy emission characterised by a gamma-ray energy flux peaking at a few hundreds keV in the observer frame and that occasionally extends in a long tail up to the GeV band [249]. When broadband data are available, a typical GRB spectrum, $\mathrm{d}N/\mathrm{d}E$, can be fit between $\sim$ 10 keV and 10^4 keV by two smoothly connected power laws, also known as *Band function* [234]. The photon flux is given by:

$$f_{\mathrm{BAND}}(E) = A \begin{cases} \left(\frac{E}{100\ \mathrm{keV}}\right)^{\alpha} \exp\left(-\frac{E}{E_0}\right), & E < (\alpha-\beta)E_0 \\ \left(\frac{(\alpha-\beta)E}{100\ \mathrm{keV}}\right)^{\alpha-\beta} \exp\left(\beta-\alpha\right)\left(\frac{E}{100\ \mathrm{keV}}\right)^{\beta}, & E \geq (\alpha-\beta)E_0, \end{cases} \tag{3.2}$$

where α and β are the low- and high-energy spectral indeces, respectively, E_0 is related to the energy where the spectral peak occurs as $E_{\mathrm{peak}} = (2+\alpha)E_0$, and A is the normalisation factor at 100 keV in units of photons $\mathrm{s}^{-1}\ \mathrm{cm}^{-2}\ \mathrm{keV}^{-1}$. The E_{peak} distribution is wide and extends from several keV to the MeV range. Apart from the Band model, there are also other empirical functions which can be used to fit GRB spectra: (a) smoothly broken power law (PL), with a more flexible curvature between the power laws modelling the low- and high-energy spectra; (b) simple PL; (c) PL + exponential cutoff. Functions (b) and (c) are typically used in the case of a narrow bandpass of the detectors, so that β could not be well constrained. When the spectrum is observed simultaneously by several instruments it is possible to obtain the global spectrum, and possibly it still complies with a Band function.

The Band function alone does not provide information about the physical process giving rise to the observed radiation, being an empirical function. However, it is possible to compare the values of α and β to the spectral features expected in physical processes (e.g., synchrotron radiation, inverse Compton scattering, emission from the photosphere) to understand the mechanisms that work in GRB jets and produce the observed spectrum, as is discussed also in Sect. 3.2.2.

3.2 GRB EMISSION MODELS

The origin of the emission mechanism powering GRBs has been object of active debates since the early days of their discovery. The commonly accepted picture is the so-called *fireball model* [266, 267], where a mildly relativistic outflow is launched by the compact central engine, most likely a newly formed black hole [249] (see Sect. 3.2.1). Substantial efforts have been made to model the jet outflow dynamics and the subsequent radiative processes, giving rise to a variety of scenarios, such as internal shocks [244, 268], dissipative photospheres [269] and magnetic reconnection phenomena occurring above the photosphere [270–273]. In this section, the two scenarios considered in the works related to this thesis are described. In particular, Sect. 3.2.2 highlights the differences between the internal shock and photospheric frameworks, showing how both can comply with the observed GRB prompt emission.

3.2.1 *The fireball model*

When a massive star collapses or NS-NS/BH-NS mergers occur, a compact object like a stellar mass BH is formed and, around it, the material resulting from this process forms an accretion disk releasing a huge amount of energy. Part of the energy is used to form a matter-dominated fireball, made of baryons (primarily protons and neutrons), electron-positron pairs, and gamma-ray photons. At the beginning, the highly dense fireball is optically thick to photons. Its radiation luminosity is of the order of $10^{50} - 10^{52}$ erg s^{-1}, which is much larger than the Eddington luminosity[4] of $\sim 10^{38}$ erg s^{-1} [274]. As a result, the fireball expands adiabatically and, during this process, converts the internal energy of photons into the bulk kinetic energy of the plasma. The outflow is now in the coasting phase, with a bulk Lorentz factor $\Gamma = E/(Mc^2)$, where E is the total energy released in the burst and M is the matter present in the outflow. Hence, GRBs are produced by dissipation

4 The Eddington luminosity, also referred to as the *Eddington limit*, is the maximum luminosity that a body (such as a star) can achieve when there is balance between the force of radiation acting outward and the gravitational force acting inward.

of kinetic energy of a relativistic expanding wind, i.e. the fireball. When this reaches the circumburst medium, external shocks create the afterglow and the jet is finally decelerated [246]. The remaining kinetic energy powers the observed multiwavelength afterglow.

Although the original model involves a spherical relativistic fireball, the same description still remains valid if the emission occurs in collimated jets. Indeed, GRBs are thought to emit radiation in relativistic outflows characterised by an opening angle of a few degrees, i.e. $\theta \sim 1/\Gamma$, due to the relativistic beaming. Note that an observer on Earth is limited to see only the fraction of emission beamed towards him, and, for this reason, he cannot differentiate between a beamed/collimated outflow and a spherical one. When treating with GRB observable quantities, one usually uses isotropically equivalent values, e.g. for energy and luminosity of the burst, namely those quantities the GRB would have if the observed radiation was emitted over a whole sphere. The true energy in the jet is lower by the fraction of the solid angle subtended by the jet compared to the whole sky (4π).

To generate the observed GRB prompt emission, some physical process must tap into the kinetic energy of the outflow, reconverting it into high-energy radiation. The exact energy dissipation and emission mechanism is still under debate and is closely related to the nature of the ejecta itself. The most prominent models used by the scientific community to explain the GRB prompt emission are compared in the following.

3.2.2 *Prompt emission: internal shock vs photospheric scenarios*

Internal Shock (IS) models are particularly suited for the description of the prompt emission: the powerful and collimated jet produced in the explosion converts a fraction of its kinetic energy into internal energy emitting multiple shells with different speeds. Being characterised by different Lorentz factor values [275], the fastest catch up with the slowest and collide at a typical distance of 10^{13} cm from the central engine [276]. Part of the energy that gets dissipated at the shocks is expected to be transferred to nonthermal particles, achieving relativistic speeds, which hence radiate via synchrotron and inverse Compton (see Sect. 1.5.2 for the description of these emission mechanisms). Despite its ability to explain most of the high-energy properties of the prompt emission phase, including time variability and energetics, some of the observed GRB spectra appear to conflict with this scenario. Indeed, the synchrotron model predicts GRB spectra with $\alpha \sim -1.5$, while the fitted values are often significantly harder. For example, LGRBs show on average $\alpha \sim -1.0$ [277–281]. Some GRBs are even showing spectra beyond the so-called *synchrotron line-of-death* (i. e. $\alpha \geq -2/3$) [282], especially SGRBs [283, 284]. The inconsistencies between the synchrotron model and the observations have revived photospheric models, where the emission takes place closer to the photosphere of the jet. Actually, the photospheric emission is a natural consequence of the fireball model, the fireball being an optically thick expanding plasma made of particles and photons. Photospheric emission from highly relativistic outflows was early considered as an explanation for the prompt emission of GRBs [266, 267]. However, these models did not have a significant impact for many years, as the observed GRB spectra appeared to be non-thermal since their very first observations.

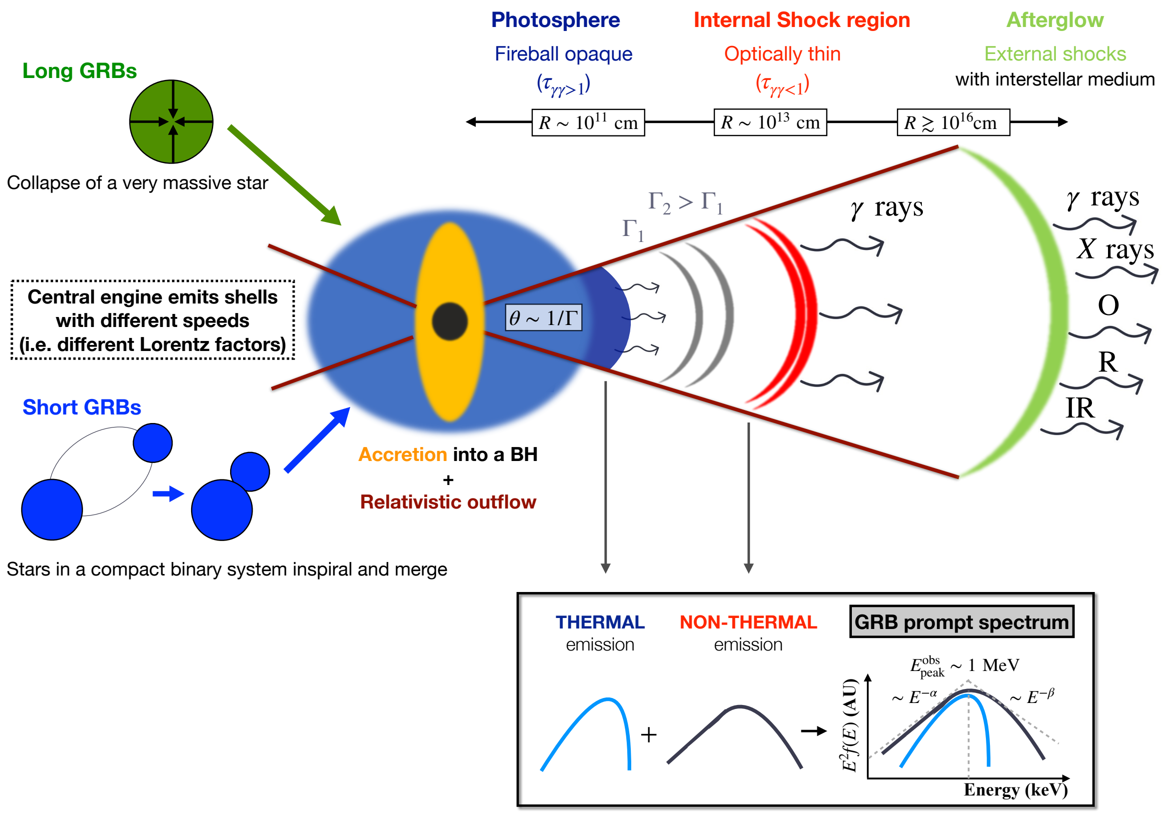

Figure 3.4: Sketch showing fireball model. Different progenitors lead to a common central engine (BH and an accretion disk around it) which emits a relativistic outflow. The thermal and non-thermal emission components, released respectively at the photosphere and as a results of internal shocks occurring between the shells emitted by the central engine, are shown. The final prompt spectrum, typically described by the Band function (in Eq. (3.2)) can be interpreted as the sum of these two components. The afterglow emission (γ rays, X rays, optical, radio, and infrared) is released when the jet interacts with the circumburst medium.

In photospheric models, the emission is expected to be constituted by a freely expanding radiation-dominated outflow with a thermal spectrum (Planck-like) peaked at ~1 MeV in the observer frame. Thus, to explain the observed nonthermal emission, the photospheric component was proposed to be reprocessed into a nonthermal emission arising from optically thin regions (e.g., [285]), as Fig. 3.4 indicates, or to be the result of projection effects. In the former case, several mechanisms have been suggested to operate below the photosphere, e.g., kinetic energy dissipation due to shocks [286–288], collisional processes [289, 290], or magnetic energy dissipation due to field line reconnection [291–294]. In geometric interpretation, in turn, the observed emission would result in a superposition of spectra generated by photons emitted from a wide range of radii and angles, which are detected simultaneously, rendering the inferred photosphere location angle dependent [295, 296]. Overall, it appears clear that the radiation produced at this stage is an unavoidable component in the GRB emission.

The first clear observation of a narrow thermal component in a GRB spectrum occurred in 2009, within the bright long GRB 090902B, detected by *Fermi*-GBM and *Fermi*-LAT [297].

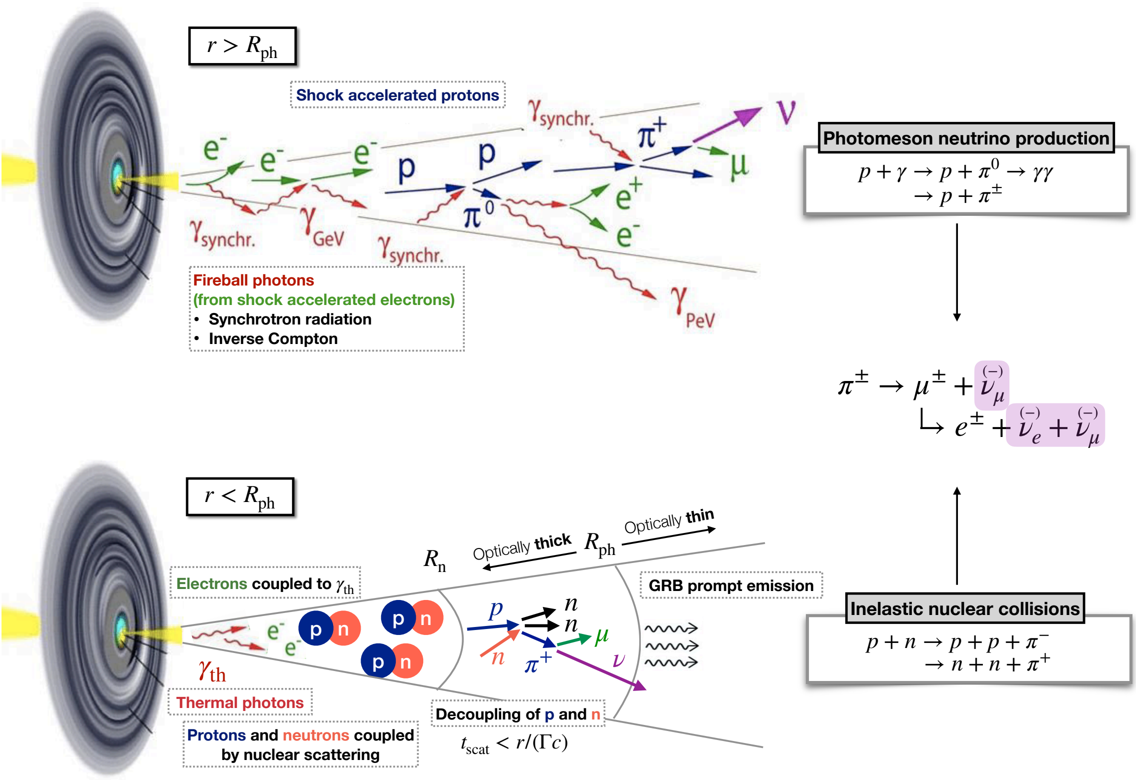

Figure 3.5: Sketch showing the neutrino production mechanisms treated in Sect. 3.3: photomeson ($p\gamma$) interactions of high-energy shock accelerated protons with fireball photons (top), and inelastic pn collisions occurring in the subphotospheric region of the jet (bottom). Both processes lead to charged pion production, with the subsequent neutrino production by charged pion and muon decays.

A time-resolved spectral analysis of such a burst revealed an initial peaked component, with a spectral shape resembling the Planck function, interpreted as a clear sign of photospheric origin, followed by a later broadening of the spectrum described by a Band function with $\alpha = -0.6$ [288]. This would suggest that the photospheric emission lasts during the whole burst duration, with the contribution of an additional component making the spectrum non-thermal. This picture has been corroborated by the discovery of other GRBs with a nonthermal spectrum overlapping the thermal one, e.g., GRB 100724B [298] and GRB 110721A [299]. Given the complexity of the emission observed from the prompt phase of GRBs, both in terms of spectral and temporal features, it is likely that different radiative stages occur. A key issue that still remains to be addressed is to which extent photospheric emission has to be complemented by additional processes and how to identify these different spectral components from observations.

3.3 HIGH-ENERGY NEUTRINOS FROM GRB PROMPT EMISSION

In both models discussed before, a significant fraction of GRB energy is thought to be converted to a burst of high-energy neutrinos (>GeV) produced in correspondence of the observed gamma-rays. Indeed, such neutrinos can originate both by photomeson interactions of high-energy protons with fireball photons (e.g., [107, 300]), as discussed in Sect. 3.3.1, and by processes that instead do not rely CR acceleration. Namely, when neutrons are present in GRB jets, inelastic collisions between bulk flows or neutron diffusion [301] lead to subphotospheric neutrino production, without involving phenomena as internal shocks or magnetic reconnections. It is possible to refer to such neutrinos as *quasi-thermal* neutrinos, being those produced in the deep photosphere. They can be produced during neutron decoupling [302] and/or by internal collisions between neutron-loaded outflows [303, 304]. The latter case, described in Sect. 3.3.2, is the one treated during this thesis project and that lead to the publication in [233].

3.3.1 *Photomeson interactions in IS scenario*

Within the framework of the fireball model, the observed gamma-ray radiation is produced by the synchrotron and IC emission of shock accelerated electrons. In the same region, if the jet is hadronic, also protons are accelerated during internal shocks between shells with different Γ. In such a condition, $p\gamma$ interactions are possible through the Δ^+ resonance production, following the reaction chain in Eq. 1.34, and high-energy neutrinos are produced by the decay of charged pions. See the top part of Fig. 3.5 for a sketch representation of $p\gamma$ interactions occurring in the optical thin region of GRB jets.

In the observer reference frame, the relation between the observed photon energy ϵ_γ and the accelerated proton energy ϵ_p at the photomeson threshold of the Δ^+ resonance is [107]

$$\epsilon_\gamma \epsilon_p = 0.2 \text{ GeV}^2 \Gamma^2. \tag{3.3}$$

For a relativistic jet with $\Gamma = 100 - 1000$ and $\epsilon_\gamma = 1$ MeV, that is the typical observed energy of photons emitted in IS, protons with ϵ_p between $\sim 10^{15}$ eV and $\sim 10^{17}$ eV are required to produce neutrinos from charged pion decay. Since neutrinos receive about 5% of the proton energy (as explained in Sect. 1.5.2), from photomeson interactions occurring at IS, neutrinos with energies between 10 TeV and 1 PeV are expected [268, 276, 300, 305–307].

The TeV-PeV neutrino production in GRBs from photomeson interactions occurring in the classical internal shock model is the topic of the work described in Chapter 4. The reader can refer to it for a more detailed explanation of the model.

3.3.2 *Hadronic collisions in the inelastic collisional scenario*

An alternative high-energy neutrino emission component can originate from colliding neutron-loaded flow, as provided for example by the inelastic collisional model [289, 308, 309]. The basic assumptions of such model are: (i) the presence of a dense, hot and neutron-rich central engine [308, 310]; (ii) a non-magnetized baryonic jet (see [290] for an extension of the model including also a magnetized jet). These two requirements are not far from being realised, since GRB jets are possibly produced by hydrodynamic processes that take place in the accretion disk around a black hole or a neutron star, and the dissociation of nuclei by gamma-ray photons in the inner regions of the disk could produce free neutrons [249]. Initially, neutrons and protons accelerate as a single fluid due to frequent nuclear collisions, while at a later expansion stage the jet evolves into a two-fluid or *compound state*: a slower neutron component with Lorentz factor Γ_n is embedded in a faster proton flow with $\Gamma > \Gamma_n$. This compound flow develops when the timescale for pn collisions becomes longer than the jet expansion time $r/(\Gamma c)$ or, in other words, when the scattering time for proton-neutron nuclear collisions $t_{\rm scat}$ becomes smaller than the same quantity, at radius R_n [301, 302, 308, 310]. The jet becomes transparent to radiation in the photosphere ($R_{\rm ph} \sim (10-20)R_n$), where the thermal emission is effective, as modified by the subphotospheric collisional process. Such a heating mechanism, that is realized in the region of the jet between R_n and $R_{\rm ph}$, injects energy into electron-positron pairs via two branches occurring at comparable heating rates: (i) electrons are heated by Coulomb collisions with protons and consequently radiate; (ii) inelastic pn collisions. As a result, nuclear and Coulomb collisions in GRB jets create a hot $e^{\pm}$ plasma that radiates its energy producing escaping radiation with a well-defined spectrum. In the following, there is a focus on inelastic nuclear collisions, as this channel is responsible for neutrino production within the photosphere.

The region between R_n and $R_{\rm ph}$ is characterized by inelastic nuclear collisions between protons and neutrons, significantly affecting the jet dynamics (sub-photospheric collisional heating), namely

$$\begin{cases} p+n \to p+p+\pi^- \\ p+n \to n+n+\pi^+ \end{cases}, \tag{3.4}$$

as well as

$$\begin{cases} p+p \to p+n+\pi^+ \\ p+p \to p+p+\pi^0 \\ n+n \to p+n+\pi^- \end{cases}. \tag{3.5}$$

The rate of pn collisions per unit volume is given by [289]:

$$\dot{\rm N} = n n_n \Gamma_{\rm rel} \sigma c, \tag{3.6}$$

where $\sigma = 3 \times 10^{-26}$ cm^2 [249] is the nuclear cross section, n and n_n are respectively the proton and neutron number densities, c is the speed of light in vacuum, and $\Gamma_{\rm rel}$ is the relative Lorentz factor of the neutron and proton component of the jet, i. e.

$$\Gamma_{\rm rel} = \frac{1}{2}\left(\frac{\Gamma}{\Gamma_n} + \frac{\Gamma_n}{\Gamma}\right) \simeq \frac{\Gamma}{2\Gamma_n}, \tag{3.7}$$

with $\Gamma \gg \Gamma_n$. Each collision between protons and neutrons dissipates a fraction of kinetic energy, and quasi-thermal nucleons are produced with $E^{\rm th}_{N,c} \simeq k_p \Gamma_{\rm rel} m_p c^2$ in the comoving frame of the interacting flow[5]. Here, $k_p \approx 0.5$ is the nucleon inelasticity (i. e. the fraction of the available center of mass energy used for secondary particles production) [304], and m_p the proton mass. A comparable amount of energy is converted into mildly relativistic pions. Charged pions decay into muons, in turn unstable towards the production of electron/positron pairs:

$$\pi^{\pm} \rightarrow \mu^{\pm} + \nu_\mu/\bar{\nu}_\mu \rightarrow e^{\pm} + \nu_e/\bar{\nu}_e. \tag{3.8}$$

Fig. 3.5 compares the neutrino production in the inelastic collisional model (pn collisions in the sub-photospheric region of the GRB jet) to the one resulting from $p\gamma$ interactions at internal shocks instead occuring in the optical thin region. Despite of the differences between the two models, in both cases neutrinos are produced by charged pion decays.

In addition, from the decay of the neutral pion in Eq. (3.5), high-energy gamma rays are produced that quickly convert to $e^{\pm}$:

$$\pi^0 \rightarrow \gamma + \gamma \rightarrow e^{\pm}. \tag{3.9}$$

Such $e^{\pm}$ pairs, together with the ones produced by the aforementioned Coulomb collisions, can either up-scatter the thermal photons produced at the jet launch site to higher energies (via IC) and/or radiate via synchrotron emission, modifying the radiation spectrum and thus introducing a nonthermal component. The photon spectrum emitted by a collisionally heated jet was first derived by [289], through accurate Monte Carlo simulations of the radiative transfer in the expanding jet. The resulting GRB spectra were shown to peak at $\sim$1 MeV and to extend at higher energies with a photon index $\beta \sim -2.5$, well reproducing the prompt observations [234, 282].

3.4 DETECTION PROSPECTS OF SUB-TEV NEUTRINOS FROM INELASTIC NUCLEAR COLLISIONS

Searching for a coincidence among the GRB prompt emission and high-energy neutrinos is fundamental because it provides information about the nature of accelerated particles in GRBs, as well as the GRB model. If neutrinos were revealed in coincidence with a GRB, they would allow discriminating among the leptonic and hadronic nature of radiation; additionally, the measurement of their characteristic energy could be the key to identify the origin of the GRB prompt radiation (e.g., internal shocks vs photospheric emission). Thus, it is crucial to investigate neutrino emissions in a broad energy range. Until a few years ago, temporal and spatial associations among GRBs and neutrinos have only been searched for in the high-energy domain, mostly because the first-available large-volume neutrino telescopes, as IceCube and ANTARES, were designed to be mainly sensitive to TeV-PeV neutrinos. So far, these searches have not found any $\gamma - \nu$ association; refer to [312–314] for ANTARES analyses (one of those, i.e. [314], is part of this thesis work and

5 Neutrons that survive these collisions travel to larger distances before decaying, possibly affecting the afterglow radiation from GRBs [311].

Chapter 4 is dedicated to its description) and [315, 316] for the IceCube ones. Therefore, after approximately 50 years from the discovery of GRBs, the lack of $\gamma - \nu$ associations still prevents us from undoubtedly establishing the mechanism responsible for the prompt emission of GRB.

Low-energy neutrinos produced in collisionally heated GRBs, i. e. those explained by the inelastic collisional photospheric model, might contribute to solving the puzzle. Some investigations in this direction have led to theoretical calculations of detection prospects of such neutrinos with IceCube [227], the South Pole neutrino observatory, and its low-energy extension, namely DeepCore [228], sensitive to neutrinos with energies as low as $E_\nu \sim$10 GeV. From a sample of bursts observed by BATSE [236], predictions estimated a non-negligible chance for detecting 10-100 GeV neutrinos in 5-10 years by using combined IceCube and DeepCore data [303]. Other authors [304] showed that few neutrino-induced events can be detected by analyzing $\sim$1000-2000 GRBs stacked in a decade. Motivated by this, a first all-flavor search for transient emission of 1-100 GeV neutrinos was carried out using three years of data collected by the IceCube-DeepCore detectors. No significant evidence was found in this sample, and upper limits on the expected volumetric rate of the transient neutrino sources were obtained, by assuming neutrino spectra consistent with the sub-photospheric emission [317, 318]. However, it should be noted that this analysis is time dependent and refers only to individual GRBs characterised by a duration of up to approximately 600 s, a mean neutrino energy of 100 GeV, and a bolometric energy of 10^{52} erg. Recently, an extension of this analysis has been presented [318].

In this work, the possibility to reveal multi-GeV neutrinos from collisionally heated GRBs is investigated for the first time with the new generation neutrino telescope, KM3NeT, currently under construction at two sites in the depth of the Mediterranean Sea (see Sect. 2.5.2). This detector will be sensitive to neutrinos down to few GeV energies thanks to the denser and compact array named KM3NeT/ORCA. Individual and stacked searches on LGRBs and SGRBs are both considered, additionally exploring different bulk Lorentz factor values, ranging from low-luminous GRBs (i. e. those with $\Gamma \sim 100$) to high-luminous ones ($\Gamma \sim 600$).

This section is structured as it follows. In Sect. 3.4.1, I detail the spectral properties of the predicted neutrino fluxes within the framework of the inelastic collisional scenario. In Sect. 3.4.2, I describe the effective areas of neutrino detectors able to investigate the model predictions, both the currently operative ones and those under construction, focusing on the low-energy extensions for which we derived analytical parameterisations. In Sect. 3.4.3, I discuss the neutrino signal and background characteristics, focusing on those parameters that are crucial for clearly assessing GRB-neutrino detections. Afterwards, in Sect. 3.4.4, I derive detector sensitivities with respect to both individual and stacking GRB-neutrino searches, the latter spanning over a GRB sample expected to be collected by the operative gamma-ray satellites in about five years, and at the end I discuss the results achieved through this work.

3.4.1 *Computation of neutrino production at the source*

Neutrinos can be produced as a consequence of hadronic collisions in the subphotospheric region of GRB jets (see Eq. (3.8)). Charged pions on average carry 2/3 of the energy transferred by the protons in hadronic nuclear pn collisions. By considering that neutrinos take $\sim 3/4$ of $\pi^{\pm}$ energy, it is possible to evaluate the average fraction of pion energy that is given to neutrinos, f_ν, as:

$$f_\nu \sim \frac{2}{3} \cdot \frac{3}{4} = \frac{1}{2}. \tag{3.10}$$

Neutrinos, therefore, carry away a significant fraction of the energy $E_{\mathrm{k,diss,s}}$ dissipated in inelastic nuclear collisions, where the subscript s refers to the source rest frame, which is related to the comoving one through the Lorentz boost $E_{\mathrm{s}} = \Gamma E_{\mathrm{c}}$. The corresponding energy of the neutrino burst (which does not suffer any adiabatic cooling) is

$$E_{\nu,\mathrm{s}} = f_\nu E_{\mathrm{k,diss,s}} \simeq \frac{1}{2} E_{\mathrm{k,diss,s}}. \tag{3.11}$$

Therefore, the energy channelled into radiation produced by the GRB jet is the remaining

$$E_{\gamma,\mathrm{s}} = f_{\mathrm{ad}}(1 - f_\nu) E_{\mathrm{k,diss,s}} \simeq \frac{f_{\mathrm{ad}}}{2} E_{\mathrm{k,diss,s}}, \tag{3.12}$$

where $f_{\mathrm{ad}} < 1$ describes the reduction in radiation energy due to adiabatic cooling in the expanding opaque jet below the photosphere.
Hence, the ratio among the neutrino and the radiation burst energies (or their isotropic equivalents) is given by

$$w = \frac{E_{\nu,\mathrm{s}}}{E_{\gamma,\mathrm{s}}} = \frac{E^{\mathrm{iso}}_{\nu,\mathrm{s}}}{E^{\mathrm{iso}}_{\gamma,\mathrm{s}}} = \frac{1}{f_{\mathrm{ad}}}. \tag{3.13}$$

Assuming that half of the energy is dissipated in the adiabatic expansion (i. e. $f_{\mathrm{ad}} = 0.5$), it is expected that

$$E_{\nu,\mathrm{s}} = 2E_{\gamma,\mathrm{s}} \rightarrow E^{\mathrm{iso}}_{\nu,\mathrm{s}} = 2E^{\mathrm{iso}}_{\gamma,\mathrm{s}}. \tag{3.14}$$

By defining the ratio ξ_{N} among the energy dissipated in inelastic nuclear collisions and the gamma-ray energy produced in the GRB jet as

$$\xi_{\mathrm{N}} = \frac{E^{\mathrm{iso}}_{\mathrm{k,diss,s}}}{E^{\mathrm{iso}}_{\gamma,\mathrm{s}}}, \tag{3.15}$$

the benchmark scenario with $f_{\mathrm{ad}} = 0.5$ would imply $\xi_{\mathrm{N}} = 4$ (see Eq. (3.12)).
In the present work, only muon neutrino (and the corresponding anti-neutrino) emissions are considered, since their interactions in charged current with nucleons inside large volume neutrino telescopes are well identified, resulting in long muon tracks, as pointed out

in Chapter 2. By considering the energy carried by ν_μ and $\bar{\nu}_\mu$ only, Eq. (3.14) can be written as:

$$E^{\rm iso}_{\nu_\mu+\bar{\nu}_\mu,\rm s} \sim \frac{2}{3} E^{\rm iso}_{\gamma,\rm s}. \tag{3.16}$$

Thus, the energy flowing into muon neutrinos is estimated to be ∼67% of the gamma ray energy. Such a linear scaling implies that the absolute gamma-ray energy and the model parameter $\xi_{\rm N}$ in Eq. (3.15) are crucial, as they influence the neutrino spectral normalization [304]. The energy of the emitted neutrinos is a function of the Lorentz factor of the jet, Γ, and of the relative Lorentz factor of the proton and neutron components (given in Eq. (3.7)), through [289, 303, 304, 319]:

$$E_\nu \approx 0.1\Gamma\ \Gamma_{\rm rel}\ {\rm m_p c^2} \rightarrow E_\nu \simeq 100\ {\rm GeV} \left(\frac{\Gamma}{500}\right)\left(\frac{\Gamma_{\rm rel}}{2}\right). \tag{3.17}$$

This relation implies an expected neutrino energy of $E_\nu \sim$ 10-100 GeV for Lorentz factors $\Gamma \sim 100 - 1000$. Therefore, measuring the neutrino energy would provide a direct handle on the Lorentz factor of the jet, which is a key in resolving GRB dynamics. The neutrino spectra arising from sub-photospheric collisionally heated model are quasi-thermal, hence their shape is bell-like. The exact details of neutrino spectra have been obtained with detailed Monte Carlo simulations including cooling processes of secondary mesons and leptons (hadronic losses, radiative cooling, and adiabatic expansion) by [304]. The resulting spectra are further discussed in Sect. 3.4.4.

3.4.2 *Current and future low-energy neutrino detectors*

The search for multi-GeV neutrinos from GRBs with Cherenkov telescopes requires compact arrays of 3D photomultiplier sensors, in order to detect the Cherenkov light induced by the propagation of the relativistic particles produced in neutrino interactions.

The IceCube observatory, operating at the South Pole, is complemented by DeepCore [228], an array characterised by a higher concentration of digital optical modules (DOMs), optimised for the detection of neutrinos with energies down to 10 GeV. DeepCore is constituted by 15 strings located in a radius of 125 m at a depth from ∼2100 m to ∼2450 m in the ice. Eigth strings are very close to the bottom centre of IceCube, with a DOM-to-DOM vertical spacing varying between 7 and 17 m. The DeepCore detector is operational since about 10 years. A low-energy in-fill extension to IceCube has also been proposed, named PINGU [320], that will be characterized by an effective mass of about 6 Mton for neutrino energies above few GeV. So far, no public effective area is available for PINGU; thus, it will not be considered in the following estimations.

Currently, another low-energy neutrino detector is under construction in the Northern hemisphere, off the Mediterranean France coast at about 2450 m depth, namely the KM3NeT/ORCA neutrino telescope. Its optical modules are being arranged in the dense configuration required for detecting events with energies as low as few GeV. This range is three orders of magnitude lower that the typical energy scale probed by the high-energy detector KM3NeT/ARCA (currently under construction offshore Sicily, in Italy), designed for neutrino astroparticle physics studies [211]. At the time of writing, KM3NeT/ORCA is taking data with 15 strings[6], with an average horizontal spacing between strings of about 20 m and a vertical spacing between DOMs of about 9 m [211, 220, 321]. Once completed, KM3NeT/ORCA will consist of 115 strings, arranged in a circular footprint with a radius of about 115 m.

The primary goal of low-energy neutrino detectors is to unveil the intrinsic properties of neutrinos, as the mass hierarchy, by investigating neutrino oscillation studies in the atmospheric sector. Still, the low energy domain offers interesting possibilities for exploring astrophysical science cases, e.g., the collisional heating mechanism powering the GRB prompt emission presented above. Therefore, the performances of KM3NeT/ORCA and DeepCore in the context of multi-GeV GRB analyses are investigated. The following part of the current section describes an analytical parameterisation of the detector effective areas, while the next section details expected background rate in each detector.

Detector effective areas

The present study is performed by considering instrument response functions of each detector at trigger level: in particular, effective areas for $\nu_\mu + \bar{\nu}_\mu$ events in IceCube-DeepCore and KM3NeT/ORCA-KM3NeT/ARCA are taken by [228] and [211], respectively, accordingly with the detector configurations. Note that the effective area of KM3NeT / ORCA at trigger level is not directly available from the literature, but it can be obtained by knowing its effective volume $V_{\rm eff}$ towards muon neutrino events, which has been published for the complete detector configuration up to energies of ~ 20 GeV [211]. By defining the muon neutrino charged current cross section $\sigma_{\nu_\mu^{\rm CC}}(E)$, the medium density ρ (i.e. the water density at KM3NeT/ORCA site), and the Avogadro constant N_A, the KM3NeT/ORCA effective area was derived as (see Eq. (2.14))

$$A_{\rm eff}(E) = \sigma_{\nu_\mu^{\rm CC}}(E)\rho N_A V_{\rm eff}(E)\,, \tag{3.18}$$

where the probability for neutrinos to cross the Earth $P_{\rm Earth} \simeq 1$ for the energies considered in the present work. Since GRB-ν flux evaluations require values up to $\sim$1 TeV, the KM3NeT/ORCA effective area behaviour was further extrapolated at higher energies than available, by using the same energy dependence as in DeepCore[7]. A best fit procedure to the DeepCore effective area results into:

$$A_{\rm eff}{}^{\rm DeepCore}(E_{\nu_\mu}) = 15\left(\frac{E_{\nu_\mu}}{100\ {\rm GeV}}\right)^{1.6}\ {\rm cm}^2, \tag{3.19}$$

6 Note that when [233] was published, 10 strings were operational
7 This assumption can be considered valid as both detectors are characterized by a dense configuration of optical modules.

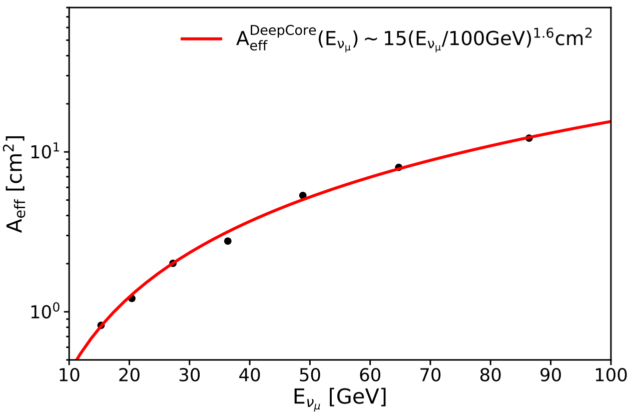

(a)

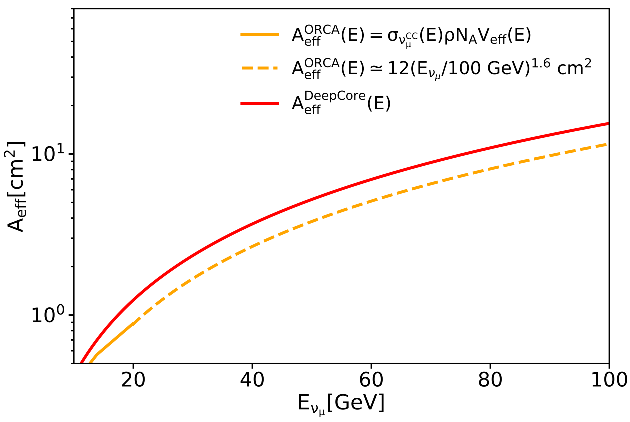

(b)

Figure 3.6: (a) DeepCore effective area at trigger level for neutrino energies between ∼10 GeV and 100 GeV. Black points represent published values from the IceCube Collaboration [228], while the red solid line shows the best fit obtained with Eq. (3.19). (b) KM3NeT/ORCA effective area at trigger level for neutrino energies between ∼10 GeV and 100 GeV (orange line) as compared to the DeepCore effective area (red line). The orange solid line, extending up to ∼20 GeV, shows the computation resulting from Eq. (3.18), namely starting from the detector effective volume $V_{eff}(E)$ [322]. In turn, the orange dashed line $E_{\nu_\mu} > 20\ GeV$ represents its extrapolation, by adopting the same energy dependence as in DeepCore.

as shown in Fig. 3.6. Therefore, the effective area of KM3NeT / ORCA at the trigger level is expected to correspond in the energy range 10 − 100 GeV to (see Fig. 3.6(b))

$$A_{eff}{}^{ORCA}(E_{\nu_\mu}) = 12\left(\frac{E_{\nu_\mu}}{100\ \text{GeV}}\right)^{1.6}\ \text{cm}^2. \tag{3.20}$$

Note that performances at trigger level are the highest possibly achievable by experiments, later reduced by the efficiency of the event selection at analysis level. However, since none of the detectors under investigation has yet implemented analyses tailored to identifying low-energy neutrinos from catalogued GRBs, the trigger level performances are conservatively adopted in the following, in the forms of Eqs. (3.19) and (3.20). Note also that triggering strategy are subject to change: e. g. , recently, a new approach has been developed for KM3NeT/ORCA [220, 322], which is expected to increase the trigger efficiency in the few GeV neutrino energy range with respect to the case here considered.

3.4.3 *Signal and background estimation for GRB-neutrino detections*

Quantitative estimations concerning detection prospects of low-energy neutrinos emerging from collisionally heated GRBs with current (DeepCore and IceCube) and under construction (KM3NeT/ORCA and KM3NeT/ARCA) neutrino telescopes are presented here. As at multi-GeV energies the atmospheric background is severely limiting the identification of cosmic signals, in this search only upward going neutrinos are considered. Indeed, Earth-filtered events allow us to reduce significantly the atmospheric muon background.

Additionally, only events due to ν_μ CC interactions are considered: the muon originated in such interactions, indeed, results into a long track that allows to define with good accuracy the direction of the incoming neutrino. In turn, a worse directional reconstruction is expected for shower-like events, e.g., those originated by ν_e and ν_τ CC interaction channels, as well as by all flavor NC interactions (see Sect. 2.1.2 and Sect. 2.1.3). The addition of this event topology in the present work would require to extend the search cone around each source (particularly for large values of Γ, see Sect. 3.4.4), implying a higher background level affecting the analysis, while at the same time allowing to probe the whole neutrino flux reaching Earth. The exact balance among these two effects deserves a detailed investigation, deferred to a future work because instrumental performances at such low energies are currently not available for all neutrino telescopes under exam.

For the purposes of this analysis, synthetic GRB characteristics are considered: in particular, a source sample reflecting the observed properties of the population is defined, to evaluate the neutrino flux expected on Earth from a GRB population powered by the collisional heating mechanism. Therefore, by collecting satellite's published data, distributions of several quantities are built, such as the burst duration T_{90}, and the gamma-ray fluence F_γ, which are key parameters for the background and signal estimation, respectively. Under the hypotheses of the inelastic collisional model, the neutrino signal would be produced in spatial and temporal coincidence with the prompt phase of GRBs. For this reason a temporal search window around each burst is conservatively defined as wide as $T_{90} \pm 0.3T_{90}$.

The neutrino spectra produced in collisionally heated GRBs are taken from [304] under the following assumptions: i) the neutrino and electromagnetic emission is released at the photosphere (i. e. at R_{ph}), where the optical depth for the pn reactions is close to unity; ii) the relative Lorentz factor between the proton and the neutron component is $\Gamma_{\text{rel}} = 3$ ($\Gamma \simeq 6\Gamma_n$, see Eq. (3.7)); iii) the fraction of gamma-ray energy dissipated in nuclear collision is $\xi_{\text{N}} = 4$. Note that Γ_{rel} influences the characteristic energy of the emitted neutrinos, which scales as $\Gamma_{\text{rel}}/2$ (Eq. (3.17)), namely a faster proton flow within the jet would imply a higher value for the peak of neutrino spectra. In particular, with respect to the reference case with $\Gamma_{\text{rel}} = 3$, a proton flow with $\Gamma \simeq 20\Gamma_n$ gives a typical neutrino energy higher by a factor ~ 3 once the jet Lorentz factor Γ is fixed. In turn, ξ_{N}, in Eq. (3.15), influences neutrino fluence normalisation, since it is related to the ratio between neutrino and gamma ray energies, as demonstrated in Sect. 3.4.1. The inelastic collisional model predicts at most $\xi_{\text{N}} \approx 20$ [304], which corresponds to $f_{\text{ad}} \sim 0.1$ (see Eq. (3.12) and Eq. (3.15)). In such a case, the neutrino fluence normalization would rise by a factor 5 with respect to the benchmark case here considered, thus increasing the expected GRB-emissivity rate of neutrinos. While the spectral details of emission, and hence the expected number of events in neutrino telescopes, might depend on the specific values of the model parameters assumed, the results of the neutrino sensitivity computation presented in the following are quite stable against reasonable variations of these parameters, i. e. $4 \leq \xi_{\text{N}} \leq 20$ and $3 \leq \Gamma_{\text{rel}} \leq 10$. In fact, the sensitivity is rather dominated by the large variety of the GRB population in

	$\Gamma = 100$		$\Gamma = 300$		$\Gamma = 600$	
Detector	$E^*_{\nu_\mu,\max}$ [GeV]	θ^* [deg]	$E^*_{\nu_\mu,\max}$ [GeV]	θ^* [deg]	$E^*_{\nu_\mu,\max}$ [GeV]	θ^* [deg]
KM3NeT/ORCA	27	26	73	13	121	9
KM3NeT/ARCA	-	-	129	9	227	6
DeepCore	27	26	78	13	165	8
IceCube	-	-	156	8	258	5

Table 3.1: Energy values $E^*_{\nu_\mu,\max}$, in GeV, at which each detector is expected to observe the highest number of $\nu_\mu + \bar{\nu}_\mu$ induced events, and corresponding plane angle values θ^*, in degrees, adopted to search for such events around GRBs, corresponding to a solid angle $\Omega = 2\pi(1 - \cos(\theta^*/2))$.

terms of temporal and spectral properties (namely T_{90} and F_γ, which affect, respectively, the number of background and signal events).

The observed neutrino fluence produced in collisionally heated GRBs from a source at redshift z is

$$F_\nu \propto \frac{1+z}{4\pi d_L^2(z)} \int \mathrm{d}E \left(E\frac{\mathrm{d}N}{\mathrm{d}E}\right)_{\nu,\mathrm{s}}, \tag{3.21}$$

where $d_L(z)$ is the luminosity distance of the source and the factor $\frac{1+z}{4\pi d_L^2(z)}$ takes into account the cosmological distance of the source and the dilution of the neutrino energy flux from the source to Earth. It is also worth noting that, as sub-photospheric gamma rays constitute the prompt emission, the neutrino fluence is proportional to the observed gamma-ray fluence through Eq. (3.16), namely $F_\nu \sim F_\gamma$. To characterise the sample of GRBs used for the simulations done in the present work, for each source the spectral parameters F_γ and T_{90} are randomly extracted in accordance to the *Fermi*-GBM distributions[8]. The extracted values are only accepted if their ratio falls into the observed distribution of F_γ/T_{90}. Such a selection was performed in order to ensure that the simulated GRB sample only contains physical sources, i. e. bursts with values of the ratio F_γ/T_{90} compatible with observed GRBs, given that this parameter is a key in the determination of the isotropic gamma-ray luminosity in the observer frame, $L_{\gamma,\mathrm{iso}} = 4\pi d_L^2(z)\frac{F_\gamma}{T_{90}}$. Note, however, that fixing the value of F_γ/T_{90} actually implies that each GRB of the sample is degenerate in $L_{\gamma,\mathrm{iso}}$ and z (through the luminosity distance), since different combinations of these quantities might yield the same value of F_γ/T_{90}. This method was applied to SGRBs and LGRBs, separately, as to correctly characterize the two different populations. To obtain the characteristic of the muon neutrino spectrum of each GRB of the sample, the neutrino production simulation presented in [304] was considered as a reference model. This refers to a high-luminous GRB with bolometric isotropic gamma-ray energy $E_{\gamma,\mathrm{iso}} = 10^{53.5}$ erg at $z = 0.1$, resulting in a gamma-ray bolometric fluence $F^*_\gamma \sim 10^{-2}$ erg cm^{-2}, where the bolometric range is defined between $\mathrm{E}_1 = 1$ keV and $\mathrm{E}_2 = 10$ MeV. Since the fluence values assigned to each GRB of the synthetic sample are extracted from the *Fermi*-GBM catalog, that provides measurements from $e_1 = 10$ keV to $e_2 = 1000$ keV, it is needed to first estimate the corre-

8 *Fermi*-GBM catalogue: https://heasarc.gsfc.nasa.gov/W3Browse/fermi/fermigbrst.html.

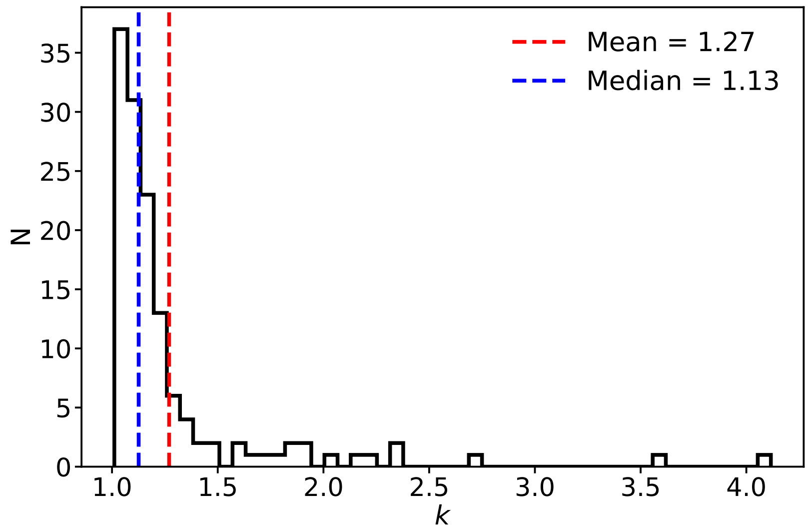

Figure 3.7: k-correction values calculated on the GRB sample collected by *Fermi*-GBM during the first ten years of detector operation, including both LGRBs and SGRBs [324]. The red and blue dashed lines show the mean and the median of the k-correction values, respectively.

sponding gamma-ray fluence in the bolometric range $F_{\gamma,\mathrm{bol}}$. This correction is also known as k-correction [323]:

$$k = \frac{F_{\gamma,\mathrm{bol}}}{F_\gamma} = \frac{F_\gamma\left[\frac{E_1}{1+z}, \frac{E_2}{1+z}\right]}{F_\gamma\left[e_1, e_2\right]}, \tag{3.22}$$

Given the linear scaling among neutrino and gamma-ray fluences predicted by the collisionally heating GRB model, the neutrino fluence predictions can be rescaled from [304] by a factor $\sim F_{\gamma,\mathrm{bol}}/F_\gamma^*$. This factor could be obtained directly from gamma-ray spectra specifically for each GRB. However, since the shape of the gamma-ray spectrum does not enter additionally into the computations, and since most of GRB spectra can be described by the same functional form (the Band function discussed in Sect. 3.1.3), a median correction is included in the analysis. In order to do so, all the k-corrections calculated based on the GRB sample observed by *Fermi*-GBM during the first ten years of its operation and with known redshift ($\sim$4.5% out of the total sample) were collected [324], and the median value of such a distribution was computed. Then, each time a value of gamma-ray fluence was extracted in a synthetic GRB of the sample, this was k-corrected with the median of such distribution, i. e. $\bar{k} = 1.13$ (see Fig. 3.7):

$$F_{\gamma,\mathrm{bol}} = \bar{k} \cdot F_\gamma = 1.13 \cdot F_\gamma. \tag{3.23}$$

In principle, different k-corrections should be applied to the two LGRB and SGRB samples, because these manifestly show different spectral slopes of the emitted prompt radiation. However, the *Fermi*-GBM sample from which the k-correction is extracted [324] is quite limited: it contains only sources with known redshift (amounted to 13 SGRBs and 122 LGRBs). As a result, the sample of SGRBs for which the k-correction has been evaluated is not statistically relevant to derive a physically motivated k correction different from that of LGRBs. Hence, the median value for both populations is adopted.

In the data sample of up-going events collected by a neutrino telescope, the background is mainly constituted by atmospheric neutrinos [325]. The Honda model is adopted as a reference for the atmospheric neutrino flux [103]. The number of events expected in coincidence with the burst depends on: i) its duration, namely the temporal window defined by T_{90}; ii) the search angular window around the GRB position, i. e. the solid angle $\Omega = 2\pi(1 - \cos(\theta/2))$, where θ is the aperture of the search cone. The aperture of the search cone should be carefully chosen to maximise the detection prospects of a signal against the background. Given a model, determined by a specific value of Γ, the same aperture cone angle is adopted for all simulated GRBs, the angle changing with the value of Γ. It was conservatively set to $\theta^* = 3\theta_{\nu\mu}(E^*_{\nu_\mu,\mathrm{max}})$, where $\theta_{\nu\mu}(E_\nu) = 0.7^\circ/(E_\nu[\mathrm{TeV}])^{0.7}$[187] is the kinematic angle between the incoming neutrino and the emerging muon directions, while $E^*_{\nu_\mu,\mathrm{max}}$ is the energy at which each neutrino telescope would observe the maximum number of neutrinos expected according to the model (which depends on Γ). To obtain this value, the energy-dependent effective area $\mathrm{A_{eff}}(E_{\nu_\mu})$ of the detectors was convolved with the expected differential energy fluence $\frac{\mathrm{d}N(E_{\nu_\mu})}{\mathrm{d}E_{\nu_\mu}\mathrm{d}S}$ predicted by the model, obtaining the so-called *parent function*, and then it was multiplied by the width of each energy bin ΔE_{ν_μ}, as follows:

$$N_{\nu_\mu}(E_{\nu_\mu}) = \mathrm{A_{eff}}(E_{\nu_\mu}) \left(\frac{\mathrm{d}N(E_{\nu_\mu})}{\mathrm{d}E_{\nu_\mu}\mathrm{d}S} \right) \Delta E_{\nu_\mu}. \tag{3.24}$$

Then, for each distribution $N_{\nu_\mu}(E_{\nu_\mu})$, the energy $E^*_{\nu_\mu,\mathrm{max}}$ corresponding to the maximum number of expected events for each Γ and each detector was searched. The values so determined are given in Tab. 3.1, together with the corresponding opening angle of the angular window. For the low-energy neutrino telescopes, namely KM3NeT/ORCA and DeepCore, the solid angle opened around each GRB changes from $\Omega \simeq 0.2$ sr to $\Omega \simeq 0.02$ sr for Lorentz factor values from $\Gamma = 100$ to $\Gamma = 600$, respectively. Indeed, according to the model, the higher the value of Γ and the higher the mean energy of the emitted neutrinos (see Eq. (3.17)), hence the higher the energy peak of the detectable neutrino sample. For values of $\Gamma \geq 300$, where the energy peak in the neutrino spectrum is expected beyond 100 GeV, joint analyses that include both low- and high-energy neutrino detectors (namely KM3NeT/ARCA and IceCube) are possible. In the search performed with high-energy neutrino telescopes, the solid angle where background evaluation is performed is rather within the range $\Omega \simeq 0.02$ sr and $\Omega \simeq 0.01$ sr. In the combined investigations, different angular windows are set for the different detectors in order to optimise the search, as given in Tab. 3.1.

Angular windows around GRBs in the background evaluation

Here, the selection of the angular window around each GRB adopted for the background estimation is discussed. In order to reduce the very abundant background from atmospheric muons, only up-going events are considered, thus the remaining background in

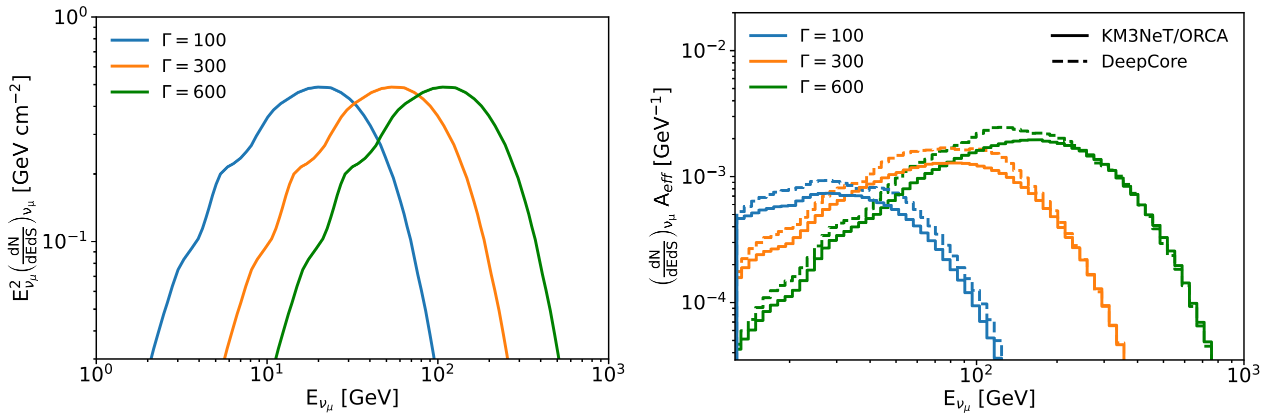

(a) (b)

Figure 3.8: (a) The $\nu_\mu + \bar{\nu}_\mu$ energy fluence for a GRB with observed gamma-ray fluence $F_\gamma \sim 2 \times 10^{-3}$ erg cm^{-2} for Γ=100 (cyan), Γ=300 (orange) and Γ=600 (green). (b) Number of signal events per GeV expected in KM3NeT/ORCA (solid lines) and DeepCore (dotted lines) for the neutrino energy fluences shown in (a). These results are all given at trigger level.

	n_s		
Detector	$\Gamma = 100$	$\Gamma = 300$	$\Gamma = 600$
KM3NeT/ORCA	4×10^{-2}	7×10^{-2}	1×10^{-1}
KM3NeT/ORCA+KM3NeT/ARCA	-	9×10^{-2}	2×10^{-1}
DeepCore	5×10^{-2}	9×10^{-2}	1×10^{-1}
DeepCore+IceCube	-	3×10^{-1}	8×10^{-1}

Table 3.2: Number of events from $\nu_\mu + \bar{\nu}_\mu$ interactions expected from a GRB with gamma-ray fluence $F_\gamma \sim 2 \times 10^{-3}$ erg cm^{-2} in low-energy detectors (KM3NeT/ORCA and DeepCore) alone, or in a combined search with high-energy detectors (KM3NeT/ARCA and IceCube, respectively). These results are all given at the trigger level.

this study is constituted by the irreducible atmospheric neutrinos flux [325], as described by the Honda model [103].

As in Cherenkov telescopes neutrinos are not detected directly, rather via the secondary particles produced in neutrino interactions (tracks of muons originated in CC ν_μ interactions are considered here), two effects need to be carefully considered when inferring the original direction of the neutrino: i) the kinematic angle between the primary neutrino and the induced muon, and ii) the quality of directional reconstruction of muons. Both these factors contribute to the angular resolution of the detector. Their effects depend on the energy of the particles involved, leading to an improved angular resolution with increasing energy. In Fig. 3.9 the energy-dependent kinematic angle $\theta_{\nu\mu}$ [187] is shown, in the form of a band extending from $\theta_{\nu\mu}$ to $3\theta_{\nu\mu}$, as compared to the most updated median angular resolutions available from literature for KM3NeT/ARCA [218], KM3NeT/ORCA [326], DeepCore, and IceCube [221]. Note that the median angular resolution already includes both kinematics and detector effects. Three panels are reported in order to compare the parametrizations of the instrumental angular resolutions with the values of the kinematic angle at $E^*_{\nu_\mu,\max}$, where each detector is expected to observe the highest number of

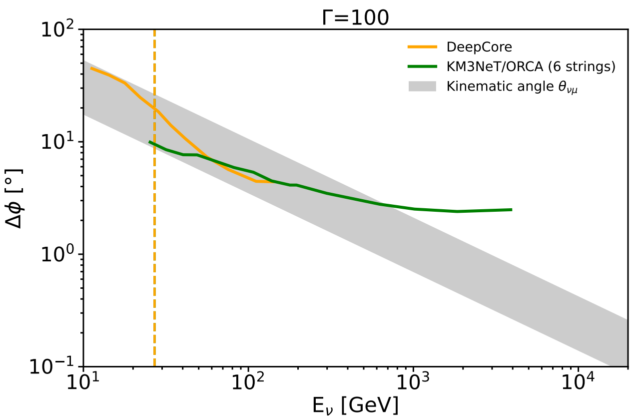

(a)

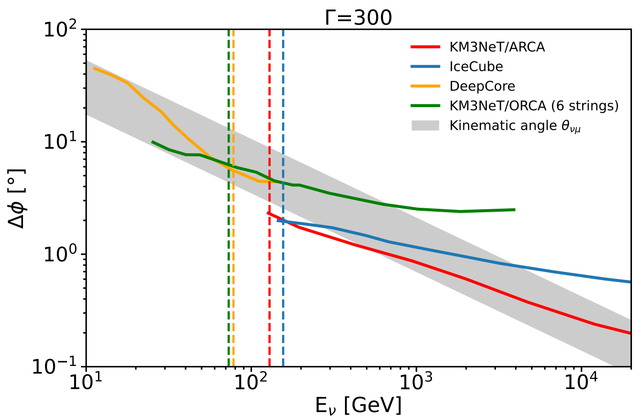

(b)

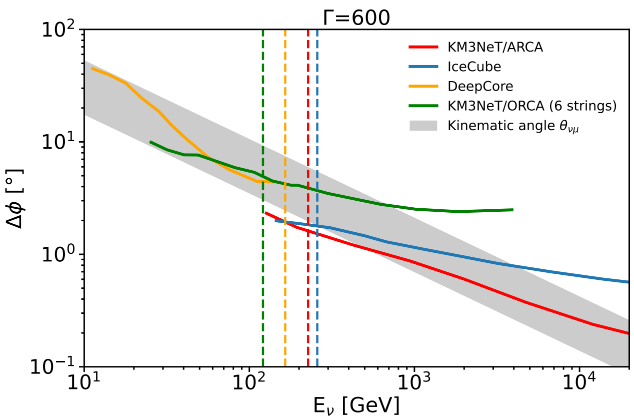

(c)

Figure 3.9: Median angular resolutions of ν_μ charged current events for KM3NeT/ORCA (green) [326], KM3NeT/ARCA (red) [218], DeepCore (orange), and IceCube (blue) [221]. Note that the KM3NeT/ORCA angular resolution refers to a partial configuration with six strings, which is the only one available from the literature. The shaded grey region shows the interval among $\theta_{\nu\mu}$ and $3\theta_{\nu\mu}$, being $\theta_{\nu\mu}$ the kinematic angle between the incoming neutrino and the muon inside the detector. The vertical dashed lines indicate the energy values $E^*_{\nu_\mu,\max}$ at which each detector is expected to observe the highest number of muon neutrinos events (see Tab. 3.1). The three panels differ in the vertical lines, which depend on the model for the signal: in particular, (a) $\Gamma = 100$, (b) $\Gamma = 300$, and (c) $\Gamma = 600$.

ν_μ events for different values of bulk Lorentz factor of the jet, again $\Gamma = 100$, $\Gamma = 300$ and $\Gamma = 600$ (see Sect. 3.4.3 and Tab. 3.1). It is possible to see that, in all cases, the choice of $3\theta_{\nu_\mu}$ as plane angle of the cone opened around each GRB is a conservative one, as it is larger than the median angular resolution of neutrino detectors at $E^*_{\nu_\mu,\max}$. For this reason, in the background estimation, it was conservatively decided to open around each GRB an angular window defined by a solid angle $\Omega = 2\pi(1 - \cos(\theta^*/2))$ with $\theta^* = 3\theta_{\nu\mu}(E^*_{\nu_\mu,\max})$.

3.4.4 *Observational expectations with current and future neutrino telescopes*

It is presented here the estimation whether it would be promising to look for GRB low-energy neutrino emissions with existing and under construction telescopes. Two possibilities are explored in the following: i) the search for neutrinos from individual GRBs, with reference to an extremely bright GRB, that would represent the most optimistic scenario for individual detection of low-energy neutrinos; ii) the quasi-diffuse neutrino search from a population of GRBs with a stacking technique implemented over approximately 5 years of data acquisition.

Detection prospects from an individual extreme GRB

For the purposes of exploring the maximum discovery potential of the collisional heating mechanism in terms of individual neutrino emissions, the case of a very fluentic GRB is here considered, namely with $F_\gamma \sim 2 \times 10^{-3}$ erg cm^{-2}. This value is comparable to that of the highest fluence GRB present in the *Fermi*-GBM catalogue, i. e. GRB130427A. The expected differential neutrino fluence depends on the value of Lorentz factor, particularly because of the maximum energy (see Eq. (3.17)): in Fig. 3.8(a) this dependence for different values of Γ, i. e. $\Gamma = 100$, $\Gamma = 300$ and $\Gamma = 600$ is shown. For comparison with predictions from the internal shock model, refer to Fig. 1 of [313], where the neutrino fluence expectations for GRB130427A are shown. In order to compute the expected number of signal events in each detector, the parent function for each of them was evaluated, as shown in Fig. 3.8(b) for DeepCore and KM3NeT/ORCA. By integrating it over the energy, the results given in Tab. 3.2, concerning the number of muon tracks induced by neutrino interactions, were derived. Although the GRB considered in this example is characterised by a high fluence (comparable to the highest fluence ever observed among all GRBs in the *Fermi*-GBM catalogue), the number of signal events observable in each neutrino telescope is quite limited ($n_\mathrm{s} < 1$), even when the events measured with low-energy detectors are integrated with those collected by high-energy ones. Nonetheless, I suggest to implement a combined search among low and high-energy neutrino detectors, i. e. KM3NeT/ORCA+KM3NeT/ARCA and DeepCore+IceCube, in order to increase the expected signal event rate. Only in the case with $\Gamma = 100$ the high-energy detectors can not provide a significant contribution, as the expected signal is entirely below 100 GeV. According to the performed calculations, to measure $n_\mathrm{s} \geq 1$ from a single GRB in at least one of the detectors considered, this source should be characterised by extreme fluence, as $F_\gamma \geq 10^{-2}$ erg cm^{-2}. So far, no such kind of GRBs has ever been observed, but it is not possible to firmly exclude in the future a serendipitous occurrence of a nearby and very energetic explosion.

Stacking detection prospects

The signal detection rate can be greatly increased when summing up the contribution of many GRBs. However, the same holds for the background, such that stacking techniques are necessary in order to obtain a significant detection level. In fact, selecting events restricted in an angular cone around sources allows the signal to stand out with respect to the background. Here, since the cone aperture around each GRB is not optimized individually, a source ordering in cumulative detection significance is required when sources are summed up. Thanks to the stacking procedure, the cumulative significance results higher since Poissonian fluctuations of the cumulative background are smaller than the sum of background fluctuations expected from a single source. Additionally, stacking techniques take advantage of the transient nature of the sources under investigation. Here, I present a study on expected performances of current and under construction neutrino detectors after $\sim$5 years of stacking analysis in a half-sky search for tracks (namely only upgoing muon neutrinos).

I started by building two synthetic populations of GRBs detectable by current gamma-ray satellites in 5 years of operation, one for long and one for short GRBs, each reproducing the observed rate per year in the half of the sky equal to $\mathrm{N_{SGRB}} = 75\ \mathrm{yr}^{-1}$ and $\mathrm{N_{LGRB}} = 175\ \mathrm{yr}^{-1}$[9]. Each GRB of the sample is described by values of F_γ and T_{90}, randomly extracted from *Fermi*-GBM observed distributions and selected as explained in Sect. 3.4.3. For each extracted source, the expected neutrino fluence for three different values of the Lorentz factor, i. e. $\Gamma = [100, 300, 600]$, was estimated. The average source in the sample is less fluentic than the one considered in the previous section, being characterized by a median value of $F_\gamma \sim 8 \times 10^{-6}$ erg cm^{-2} for LGRBs and $F_\gamma \sim 6 \times 10^{-7}$ erg cm^{-2} for SGRBs. The linear scaling between gamma-ray and neutrino fluence predicted by the inelastic collisional model implies a peak value in the neutrino spectrum at the level of 2×10^{-3} GeV cm^{-2} and 1×10^{-4} GeV cm^{-2} respectively, to be compared with what is shown in Fig. 3.8(a) for an extremely fluent GRB. The stacking approach appears therefore to be a necessary condition to test the model.

The expected background occurring inside the detector in coincidence with the signal from each GRB is estimated in a temporal window as wide as $T_{90} \pm 0.3 T_{90}$, and in an angular window defined by values reported in Tab. 3.1. Once the GRB sample was populated by N objects, the following procedure was adopted:

1. The GRB with the highest level of significance, defined as $\sigma = n_\mathrm{s}/\sqrt{n_\mathrm{b}}$, was selected;
2. Starting from such a GRB, the others were added one by one choosing each time the GRB that provides the maximum increase of the total level of significance σ_tot, defined as:

$$\sigma_\mathrm{tot}(\mathrm{N}) = \frac{n_{\mathrm{s},tot}}{\sqrt{n_{\mathrm{b},tot}}} = \frac{\sum_{i=1}^{\mathrm{N}} n_{\mathrm{s},i}}{\sqrt{\sum_{i=1}^{\mathrm{N}} n_{\mathrm{b},i}}}\,. \tag{3.25}$$

The full procedure was repeated 1000 times, obtaining the median value of significance after stacking 875 LGRBs or 375 SGRBs (acquired in $\sim$5 years of half-sky gamma-ray observations), with an uncertainty band calculated through percentiles at one and two standard

9 Such values are based on observations and were obtained from the Gamma-Ray Bursts Interplanetary Network (IPNGRB) database `https://heasarc.gsfc.nasa.gov/w3browse/all/ipngrb.html`.

deviations. By requiring $\sigma_{\text{tot}} > 3$ and $n_{\text{s},tot} \geq 1$ as minimum conditions to define a detection, I conclude that:

- A detection of subphotospheric neutrinos is possible if LGRBs are included in the search, since SGRBs alone would not provide signal enough to satisfy the requirements above, in spite of the lower background level expected with respect to LGRBs;
- The model with $\Gamma = 100$ is characterized by a median value of σ_{tot} lower than unity;
- Higher values of Γ result into a higher probability of detecting multi-GeV neutrinos in 5 years of observation with KM3NeT/ORCA and DeepCore;
- Such a possibility is increased if high-energy detectors are integrated in the search.

The results obtained with $\Gamma = 300$ for all detectors are shown in Fig. 3.10. Though a higher statistical significance can in principle be obtained by assuming $\Gamma = 600$ (lower amount of background entering the search, mostly because of the smaller angular search window selected, see Tab. 3.1), only the results for $\Gamma = 300$ are here presented, since this value is expected to more realistically describe the entire population of GRBs (see e.g., [327]). With such a value, I obtain that there is a good chance to significantly detect multi-GeV neutrinos by stacking $\sim$900 LGRBs under the hypothesis that their prompt gamma-ray emission is explained by the collisional heating model. As visible, the overall detection significance is characterized by an extended uncertainty band, which is mostly due to the high range of values allowed for the intrinsic properties of the GRB population, namely T_{90} and F_γ. While reflecting the observed distributions, the spread in GRB luminosity can lead to quite different sample realisations, which might impact the analysis results into a non-significant outcome. The situation improves when combining low and high energy detectors, as shown by the case with $\Gamma = 300$ in Figs. 3.10(e) and 3.10(f), such that a sensitivity above 3σ is generally expected to be achieved after analysing a few hundreds of GRBs. Note that the stacking procedure here implemented, once applied within the framework of the classical internal shock scenario of the fireball model, provides results in terms of expected signal neutrinos and analysis significance compatible with the limits set by the IceCube and ANTARES collaborations with respect to such a model [314, 315]. Though minor differences arise because of the adoption of trigger level effective areas and full efficiency for neutrino detectors in this work, the comparison highlights the validity of the methods developed here and the consequent conclusions. In view of the promising results here obtained, I strongly encourage performing optimised stacking analyses for testing the inelastic collisional model and either confirm its occurrence or constrain the amount of GRBs possibly powered by this mechanism.

Note that the quasi-diffuse signal flux expected to arise as a result of the collisionally heating mechanism in the 875 LGRBs of the considered sample would result at the level of $\sim 2 \times 10^{-9}$ GeV cm^{-2} s^{-1} sr^{-1} at $E_\nu \sim 100$ GeV. This value is much smaller than the atmospheric neutrino background flux at the same energy, which is rather of the order of $\sim 5 \times 10^{-4}$ GeV cm^{-2} s^{-1} sr^{-1}. These numbers highlight the challenging task of pure diffuse searches in revealing the presence of a tiny signal, like that from the GRB population, on top of a huge atmospheric background. In turn, as Fig. 3.10 demonstrates, the stacking approach provides a more promising perspective than the pure diffuse analysis. In particular, the IceCube and DeepCore detectors could already have collected enough data to constrain the model here investigated and eventually confirm our finding, with the analysis technique presented here. This result encourages dedicated stacking analyses, optimised for energies lower than 1 TeV, which have not been implemented yet in relation to the GRB population at such low energies.

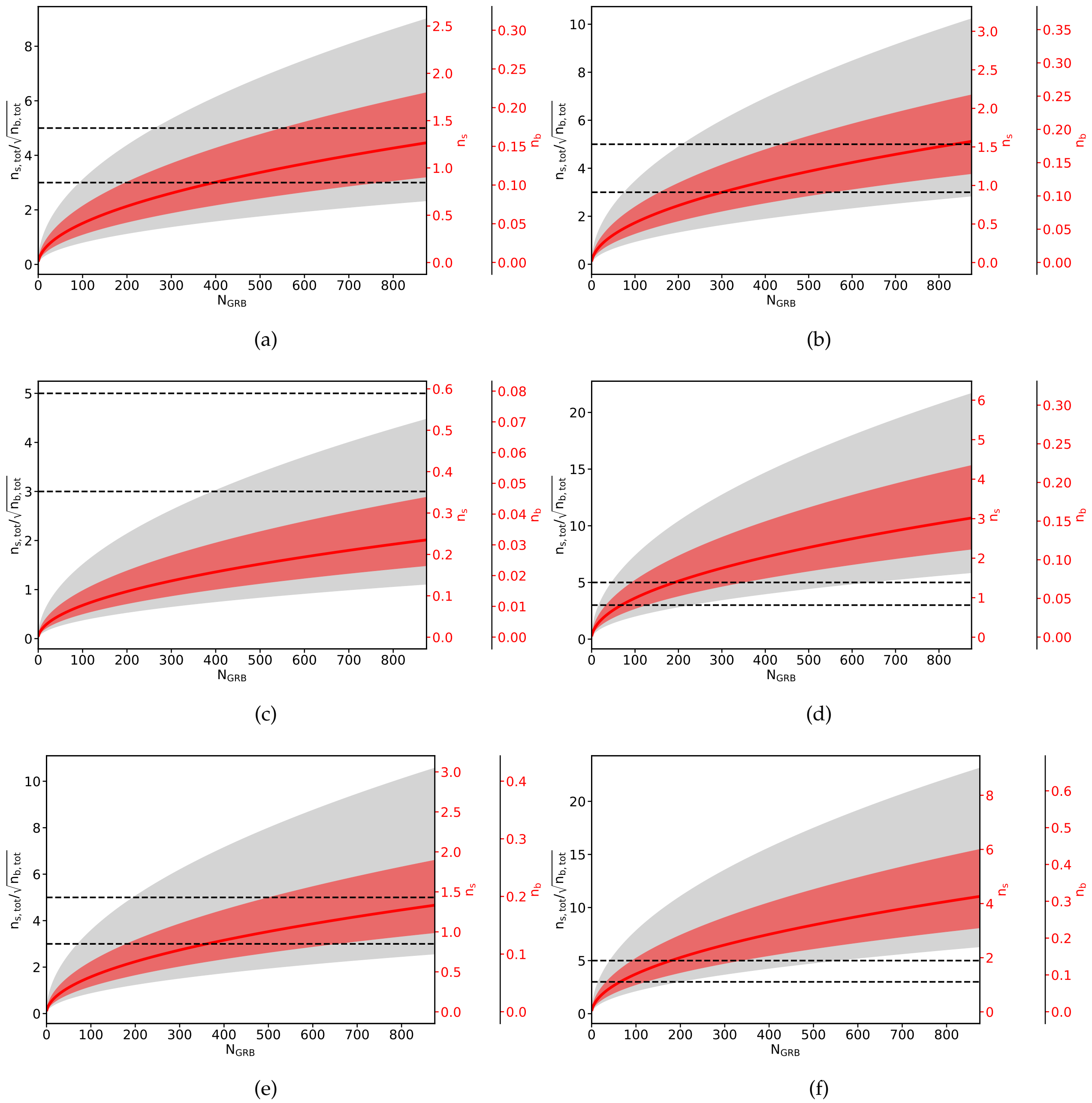

Figure 3.10: Level of significance $n_{s,tot}/\sqrt{n_{b,tot}}$ (left y-axis) achieved by stacking 875 LGRBs (equivalent to $\sim$ 5 years of half-sky search) with $\Gamma = 300$, under the assumption that the gamma-ray prompt emission originates from *pn* collisions at subphotospheric radii (inelastic collisional model). The level of signal and background in each detector (indicated in the right y-axis for the median result) is estimated at the trigger level. Results are shown for the following neutrino detectors: (a) KM3NeT/ORCA, (b) DeepCore, (c) KM3NeT/ARCA, (d) IceCube, (e) KM3NeT/ORCA+KM3NeT/ARCA, (f) DeepCore+IceCube. The shaded red and grey regions indicate the uncertainty bands at one and two standard deviations, respectively, obtained with percentiles. Horizontal dashed black lines highlight the levels of significance $n_{s,tot}/\sqrt{n_{b,tot}}$=3 and $n_{s,tot}/\sqrt{n_{b,tot}}$=5.

4 ESTIMATING THE GRB CONTRIBUTION TO THE COSMIC DIFFUSE NEUTRINO FLUX WITH ANTARES DATA

In the previous chapters, we have pointed out that searching for coincidences among GRB photons and high-energy neutrinos is crucial to safely identify this kind of sources as hadronic factories and, consequently, to define their contribution to the observed flux of UHECRs, the most energetic particles observed to date (see Chapter 1). Furthermore, this would also help in shedding light on the composition of their jets and discriminating between the several physical mechanisms that could be responsible for the GRB prompt emission through the energy of detected neutrinos.

After the investigation, in Chapter 3, of the inelastic collisional model (subphotospheric scenario) and the subsequent prediction of the possibility for KM3NeT and IceCube to test it through the detection of neutrinos with sub-TeV energies, we consider in the following the alternative internal shock scenario (the reader can refer to Sect. 3.2.2 for a comparison between the two), by using an experimental approach. A search for neutrino signals coincident with GRBs in time and direction, by using almost 10 years of data (between 2007 and 2017) collected by the ANTARES neutrino telescope is presented. This analysis differs from previously analogous published results both by IceCube [328–330] and ANTARES itself [331–333], since it improves the predictions on the expected neutrino fluences from GRBs: for the first time in this kind of study, the uncertainties on intrinsic parameters of the IS model are considered, by including the wealth of information accumulated over the years thanks to the many astronomical observations, rather than assuming some fixed standard values that do not correctly reproduce GRB properties. Contextually, the different uncertainties due to the poor knowledge of the source dynamics are taken into account and propagated in the evaluation of the prediction of the produced neutrino spectrum, with the aim of providing a clear understanding of the assumptions and limitations behind the upper limits that are set after the lack of detection.

In the following, the analysis is described in detail, omitting the description of the ANTARES detector, already treated in Sect. 2.5.1. The chapter starts, in Sect. 4.1, with the selection of the adopted GRB sample. In Sect. 4.2, the neutrino spectra predicted by the IS model are firstly discussed, then a focus on the various uncertainties in neutrino flux computation due to the poor knowledge of some parameters is given. In Sect. 4.3, the resulting cumulative neutrino fluence expected from all GRBs in the selected sample is presented. Sect. 4.4 describes the various steps of the diffuse search performed through the stacking technique on ANTARES data between 2007 and 2017, investigating whether the discovery potential can be improved by limiting the analysis to an optimised sub-sample of bursts. In Sect. 4.5 the results of our analysis about the contribution of GRBs to the high-energy diffuse neutrino flux with ANTARES data are outlined and discussed. Lastly, in Sect. 4.6, the possible systematics affecting our results are investigated.

The content of the present chapter is based on results already published on behalf of the ANTARES Collaboration in *ANTARES Collaboration, 'Constraining the contribution of Gamma-Ray Bursts to the high-energy diffuse neutrino flux with 10 years of ANTARES data', MNRAS **500**, 5614 (2021)* ([314]), of which I am the corresponding author.

4.1 SELECTION OF THE GRB SAMPLE

The GRB parameters needed for the search (time, direction) and the simulation of expected neutrino fluxes (photon spectrum, fluence, redshift) are collected from published results of Swift[1][71], Fermi[2] [338, 339] and Konus-Wind[3] [340]. Starting with a full sample of GRBs that includes 2604 sources, a selection is performed, satisfying the following criteria:

- Short bursts are excluded, as this class is poorly understood in terms of neutrino production during their short prompt phase. In other words, only GRBs with prompt duration $T_{90} \geq 2$ s (LGRBs) are selected;
- The coordinates of the bursts should be measured by at least one satellite. Those GRBs such that the angular uncertainty provided by the satellite is larger than 10° are excluded;
- The gamma-ray spectrum has to be measured. This is typically fitted with a broken power-law, a cut-off power-law or a smoothly broken power-law function. It is also required that the spectral indices satisfy the conditions $\alpha > -4$ and $\beta > -5$, where α and β are respectively the slope below and above the energy break (see Sect. 3.1.3);
- At least one parameter among electromagnetic fluence and redshift has to be measured, since their values are needed for the calculation of the source luminosity, that is primarily affecting the yields in both gamma rays and neutrinos, as it will be emphasized further on;
- Only GRBs that were below the ANTARES horizon at trigger time were selected for the selection of upgoing-only events. The analysis is, indeed, focused on the track-like signals produced by ν_μ CC interactions in water, because of their better angular resolution with respect to shower-like events (the angular resolution of ANTARES for both track and shower events is shown in Fig. 2.11; moreover, for the discussion and

1 Swift catalogue in https://swift.gsfc.nasa.gov/archive/grb_table/
2 Fermi-GBM in https://heasarc.gsfc.nasa.gov/W3Browse/fermi/fermigbrst.html [334–336]. Fermi-LAT in [337].
3 Konus-Wind information is only available through the GCN archive: http://gcn.gsfc.nasa.gov/gcn3_archive.html

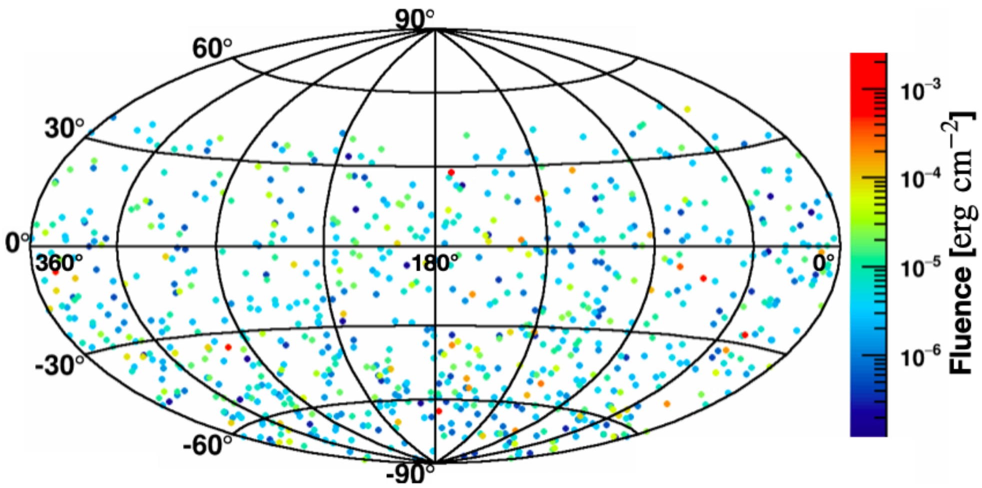

Figure 4.1: Sky distribution and fluence of the selected 784 GRBs in equatorial coordinates.

characterisation of the different event signatures detectable by Cherenkov detectors as ANTARES, see Sect. 2.1.2 and Sect. 2.1.3);

- ANTARES was taking physics data at the GRB trigger time: calibration runs were excluded, as well as runs containing events with an exceptionally high hit multiplicity (indeed, these cannot be considered reliable because some PMTs in the ANTARES detector suffered a high voltage surge). Additionally, only runs with good quality were selected.[4]

When physical parameters of a GRB are measured by different detectors, the adopted criteria are:

- The burst's position is taken from the detector with the smallest angular uncertainty (typically Swift-UVOT, then Swift-XRT, Fermi-LAT, Swift-BAT and finally Fermi-GBM);
- The burst's duration, spectrum and fluence are taken from the satellite reporting measurements in the most extended energy band (typically Konus-Wind $0.02 - 10$ MeV, then Fermi $0.01 - 1$ MeV, and finally Swift $0.015 - 0.15$ MeV).

Following these criteria, 488 GRBs have been added with respect to the ones analysed in [331]. The final sample contains 784 GRBs and their spatial distribution in the equatorial sky is shown in Fig. 4.1. The field of view of the ANTARES detector for upward going events is 2π sr and, due to its geographical location, the sky up to a declination of $47°$ is visible. The statistics of parameters adopted in this analysis from the several instruments about the source positioning and spectral modeling is specified in Tab. 4.1. Note that in some cases some parameters have not been measured, e. g. in many cases the information on the energy break is missing, as well as the spectral slope above it. In such a situation, default values are assumed: the peak energy of the burst is set at 200 keV when unknown (33% of the cases) and $\beta = \alpha - 1$ when only α is available from catalogs (1.4%

4 Quality Basic (QB)≥ 1 was the minimum request. The parameter QB quantifies the run quality according to some properties, as the bioluminescence optical noise or the number of active PMTs.

Source	Position	Spectrum
Swift	29.9%	16.7%
Swift-BAT	9.3%	
Swift-UVOT	3.4%	
Swift-XRT	17.2%	
Fermi	68.8%	71.6%
other (e. g. Konus-Wind)	1.3%	11.7%

Table 4.1: Percentage contributions of the different satellite catalogues to the determination of GRB position and spectrum. The position of the burst is taken from the detector with the smallest angular error. The spectrum is taken from the satellite with the most extended energy band. The total sample is made up of 784 GRBs.

of the cases). Moreover, the host galaxy of the GRB can fail to be identified by the multi-wavelength follow-up and so the redshift remains unknown. With respect to the redshift, former analyses have been adopting the default value $z = 2.15$ in case this information was not available. In addition, for the minimum variability timescale t_v of the bursts, which can be determined by the width of the peaks in the light curve, a default value of $t_v = 10$ ms (derived from theoretical consideration put forward in [341]), has been used so far in all neutrino searches. However, since these parameters affect crucially the GRB-neutrino fluence estimation, a different strategy has been here adopted, as explained in Sect. 4.2.2.

4.2 COMPUTATION OF NEUTRINO FLUXES FROM IS SCENARIO

In this analysis, we computed the expected neutrino fluxes from GRBs in our sample according to the IS framework of the fireball model [268, 342] (see Sect. 3.2.1 and Sect. 3.2.2). The central engine of GRBs produces multiple shells with different speeds: the faster ones catch up with the slower ones and collide. The acceleration mechanism converts part of the jet's kinetic energy into internal energy and a fraction of this energy is expected to be transferred to non-thermal particles, achieving relativistic speeds. Accelerated electrons subsequently loose their energy through synchrotron and inverse Compton processes. The intense emitted radiation field constitutes the target for the photo-hadronic interactions of protons accelerated at shock fronts: from these collisions, mesons are produced, which then decay, generating neutrinos and gamma rays. These processes are thought to occur during the prompt phase of the emission. Nonetheless, if GRBs were purely leptonic sources [343], the observed radiation would be completely ascribed to processes involving primary electrons, such that there would be no possibility to produce neutrinos in these sources. For a more detailed treatment of what we have just explained, the reader can refer to Sect. 1.5.2.

In a simplified one-zone emission model, a single representative collision is realised at the so-called IS radius, located at a distance

$$R_{\mathrm{IS}} \simeq \frac{2\Gamma^2 c t_v}{(1+z)} \simeq 2\times 10^{13}\left(\frac{t_v}{0.01\ \mathrm{s}}\right)\left(\frac{\Gamma}{10^{2.5}}\right)^2\left(\frac{3}{1+z}\right)\ \mathrm{cm}. \tag{4.1}$$

from the central emitter. Note that the IS radius strongly affects the characteristic energy range of emitted neutrinos, while simultaneously scaling the normalisation of the neutrino spectrum [341]. As Eq. (4.1) shows, the Lorentz factor Γ impacts significantly the spectral modeling. In addition, the variability time t_v is expected to be a crucial parameter as well, given its broad range of variation among GRBs. It is also worth mentioning that some models [344, 345] have argued emission radii larger than what indicated by Eq. (4.1), correspondingly predicting a less efficient neutrino production. Interestingly, these models favor the interpretation of GRBs are sources of UHECRs [346, 347], as heavy nuclei would be allowed to survive without being disintegrated. Furthermore, as already widely discussed in the previous Chapter 3, let me recall that neutrino production is thought to be efficiently realised also at radii below the photosphere, namely the location where the optical depth of Thomson scattering along the jet falls to unity, which is expected to be located at $R_{\mathrm{ph}} \sim 10^{12}$ cm. In the photospheric scenario [266, 267, 291, 348–350], because the dissipation radius is located closer to the central engine ($R_{\mathrm{ph}} < R_{\mathrm{IS}}$), the characteristic energy range where photospheric neutrinos are expected to be detected is typically lower than what is expected in the internal shock model.

The neutrino flux expected from GRBs during the prompt phase was first computed analytically in [351] and [352], while refined calculations were performed in the following years [304, 341, 346, 353, 354]. Among such approaches, the numerical method developed in [353] and, later on, in [354] is adopted in the present work. This is described in Sect. 4.2.1, that is followed by the discussion of the uncertainties in neutrino flux calculation and their effect on individual neutrino fluences computed for each GRB of the sample, in Sect. 4.2.2 and Sect. 4.2.3, respectively.

4.2.1 *The numerical modelling with NeuCosmA*

The event generator 'Neutrinos from Cosmic Accelerator' (NeuCosmA) [353, 354], used in this work to compute the expected neutrino fluxes, is based on the assumption that protons are accelerated through first-order Fermi processes [355] (i. e. with a differential energy spectrum $\propto E^{-2}$; see Sect. 1.5.1) in the relativistic ejecta of the burst and interact with the intense jet photon field. The latter is described by an energy distribution in the form of a broken power-law function [234], constrained by observations. The adopted version of NeuCosmA assumes a one-zone collision, namely it simulates average shell properties, such as an average shock speed or Lorentz factor Γ (i. e. the bulk Lorentz factor of the jet). Indeed, it can be considered as approximation that the ejecta coast with constant bulk Γ before decelerating due to the interaction with the external medium [356]. Note that in a more realistic situation, the collisions between plasma shells are different one from the other, each happening under different physical conditions, as the irregular burst light curves demonstrate. The latest release of the NeuCosmA code allows to account for such a multi-collisions scenario [357, 358], by modelling the specific light curve of individual GRBs. However, given the extended sample of sources considered in this work, the one-zone collision approach, that rather relies on the average spectral properties of the bursts, is adopted.

Since the synchrotron-emitted photons constitute the radiation field on which accelerated protons collide, the normalisation of the neutrino fluence depends linearly on the intensity of the photon flux and on the ratio of fireball energy in protons to electrons. This so-called baryonic loading, f_p, is an unknown of the problem, possibly constrained by neutrino observations. From the theoretical point of view, a reasonable value for it could be $f_p \simeq 10$ [354]; such a value will be fixed in the following for each GRB considered. The normalisation of the neutrino fluence depends on other several quantities [354]:

- The total fraction of the energy transferred from protons to pions. Considering the reaction kinematics, approximately 20% of the proton energy is transferred to the produced pion in each interaction (see Sect. 1.5.2);
- The isotropic gamma-ray luminosity of the burst, $L_{\gamma,\text{iso}}$. It is given by $L_{\gamma,\text{iso}} = 4\pi d_L^2 F_\gamma / T_{90}$, where F_γ is the bolometric gamma-ray fluence (1 keV−10 MeV), T_{90} is used as a proxy for the duration of the GRB prompt emission, and d_{L} is the luminosity distance of the source;
- The minimum variability timescale t_v, that is directly connected to the size of the emitting radius R_{IS} through the Eq. (4.1) [341];
- The peak value of the gamma-ray energy spectrum E_{peak}.

4.2.2 *Uncertainties in neutrino flux computation*

Unfortunately, the intrinsic parameters of the emission regions, like the boost Lorentz factor Γ and the variability timescale t_v, cannot reliably be determined on a source-by-source basis and this produces several uncertainties in neutrino fluxes computation.

In particular, the bulk Lorentz factor Γ of the stellar ejecta deserves a particular attention, being a key parameter to understand the physics of GRBs. We have already seen that, in the standard fireball scenario, the temporal evolution of the jet's speed can be approximated as an initial acceleration phase, followed by a period with Γ constant before reaching the external medium and decelerating in it [356]. The bulk Lorentz factor determines the frequency of plasma shell collisions and, consequently, the rate of particle acceleration. For these reasons, it affects the shape of neutrino spectra and in particular the spectral breaks. The first derivations of the energy breaks were performed in [341], where two energy breaks in the neutrino spectra were predicted at the energies

$$\epsilon_{\nu,1} \propto (1+z)^{-2}\, \Gamma_{2.5}^2\, \epsilon_{\gamma,\text{MeV}}^{-1} \tag{4.2}$$

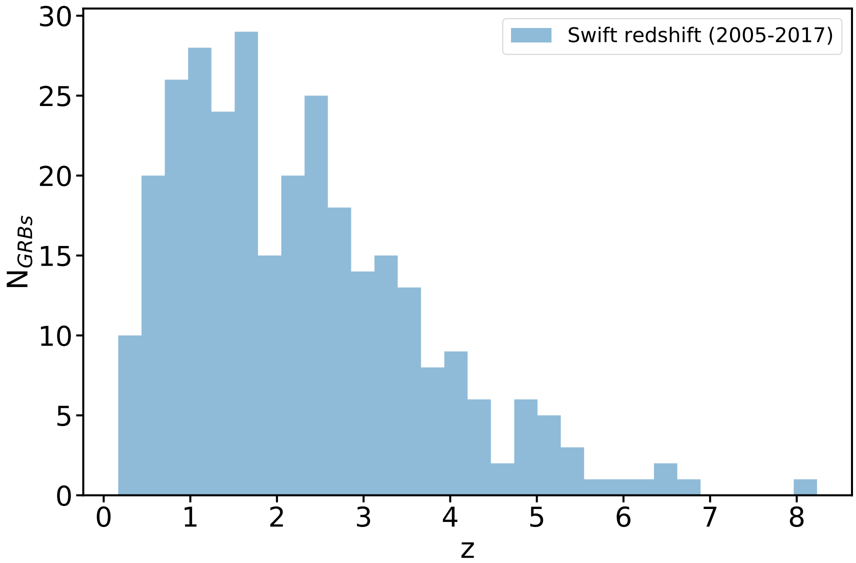

Figure 4.2: Swift redshift distribution for GRBs detected from 2005 to 2017 (data is available in https://swift.gsfc.nasa.gov/archive/grb_table/).

and

$$\epsilon_{\nu,2} \propto (1+z)^{-1}\, \Gamma_{2.5}^{2}\, R_{\rm IS}\, L_{\gamma,52}\, \epsilon_B^{-1/2}, \tag{4.3}$$

where $\Gamma_{2.5} = \Gamma/(10^{2.5})$ and $\epsilon_{\gamma,\rm MeV} = \epsilon_\gamma/\rm MeV$ is the photon energy. The first break, in Eq. (4.2), is due to the synchrotron break observed in the photon spectrum and the second one, in Eq. (4.3), comes from the onset of cooling losses in high-energy muons. Within the model implemented in NeuCosmA, a third break is expected in the combined $\nu_\mu + \bar{\nu}_\mu$ spectrum, due to the onset of cooling losses in pions [354].

In spite of the great importance of the bulk Lorentz factor, the stochastic nature of GRBs, in addition with the complex dynamical evolution of the jet, makes it hard to be reliably determined. However, in few cases, the Lorentz factor can be estimated: in the so-called 'afterglow onset method' [359], one can relate the energy break observed in the GRB light curve during the afterglow phase to the jet deceleration time and hence to the initial jet speed. Alternatively, one can use the maximum energy of observed photons [360–364] or the quiescent periods between the prompt emission pulses, in which the signal of external shock is expected below the instrument threshold [365], to infer an average Γ of the jet. The former approach was for instance adopted in [366] for a sample of 38 GRBs, from which the authors could derive the following correlation between the Lorentz factor Γ and the mean isotropic gamma-ray luminosity $L_{\gamma,\rm iso}$:

$$\Gamma \simeq 249 (L_{\gamma,\rm iso,52})^{0.30}, \tag{4.4}$$

where $L_{\gamma,\rm iso,52} \equiv L_{\gamma,\rm iso}/(10^{52}\ \rm erg/s)$. Therefore, by knowing the isotropic luminosity of the burst, it is possible to infer the jet Lorentz factor. Taking advantage of such a correlation, that from the main author's name we will call *Lü correlation* from here on out in the text, in this analysis we determine specific Γ values for each GRB in the sample from their

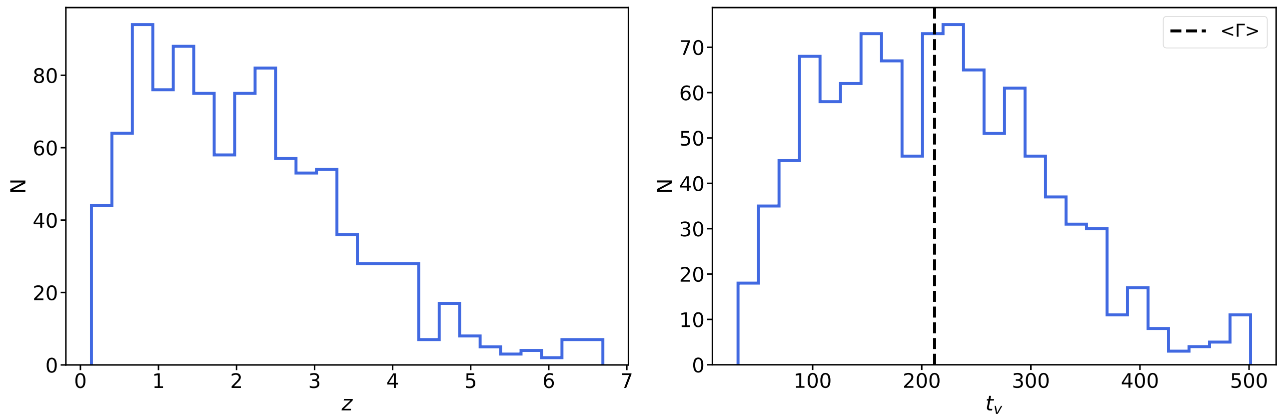

(a) (b)

Figure 4.3: (a) Distributions of the redshift z values randomly extracted for GRB08102853. (b) Corresponding bulk Lorentz factor Γ values obtained by using the correlation in Eq. (4.4) [366]. The black dashed line shows the average Γ of the considered GRB, $\langle\Gamma\rangle \simeq 210$.

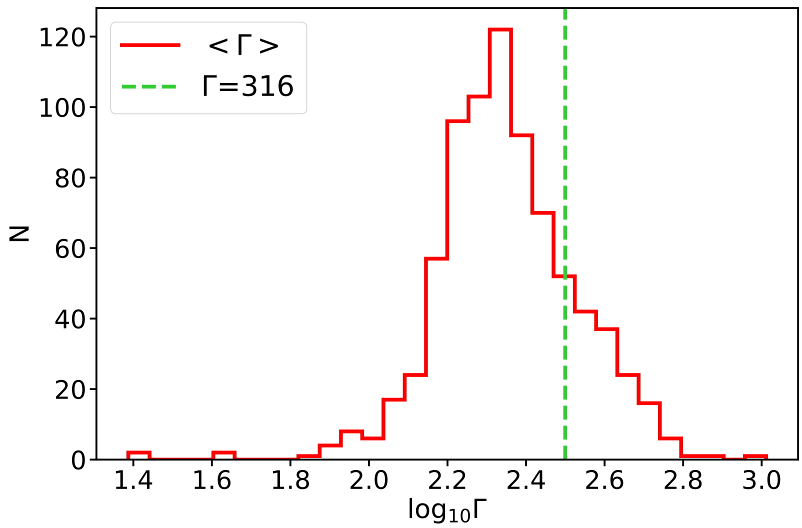

Figure 4.4: Logarithmic distribution of the average bulk Lorentz factor $\langle\Gamma\rangle$ for any burst in the sample (in red), in comparison with default value $\Gamma = 316$ (dashed green line) previously used in [331]. Note that, whenever a measurement of z is missing, $\langle\Gamma\rangle$ is obtained by averaging the 1000 values of redshift extracted for each GRB. On the other hand, for GRBs with measured z, a single contribution of Γ is present in this plot, as given by the *Lü correlation*.

isotropic γ-ray luminosity. Instead, in the previous ANTARES search [331], as well as in several IceCube searches, a default value of $\Gamma = 316$ was used. The application of this method is not free from uncertainties, as the isotropic luminosity is also often unknown. In fact, in order to derive $L_{\gamma,\mathrm{iso}}$, the knowledge of the redshift is required (because of the luminosity distance $d_\mathrm{L} = d_\mathrm{L}(z)$). As redshift is only known in 11% of the cases, a method accounting for the observed redshift distribution of long GRBs was applied in order to estimate sequentially luminosity distance, isotropic gamma-ray luminosity, and bulk Lorentz factor. Specifically, for GRBs with unknown z 1000 random extractions of the z value are performed, according to the redshift distribution of long GRBs, as observed by Swift

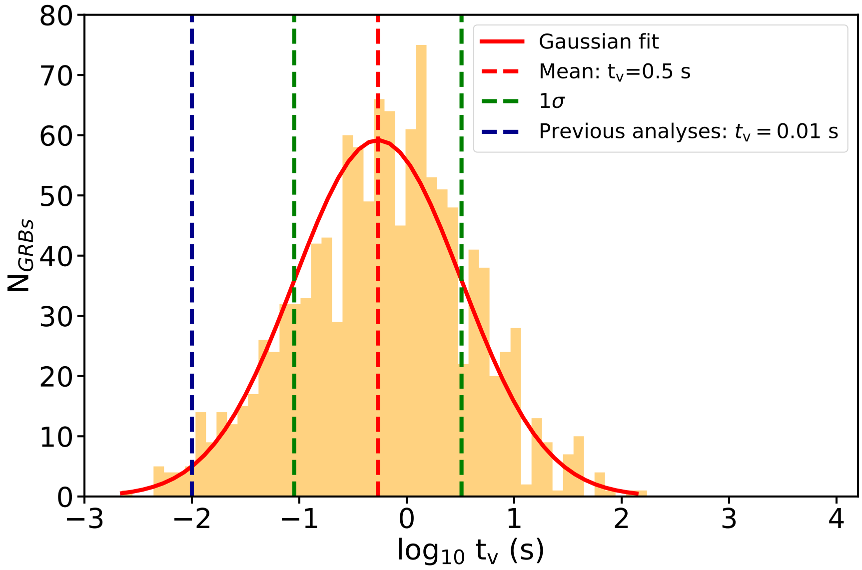

Figure 4.5: Distribution of minimum variability timescales obtained analysing 1213 GRB light curves [367–369]. The solid red line indicates the Gaussian fit of the distribution. The dashed red line is the mean of the distribution, from which a mean value of $t_v = 0.5$ s is obtained. The dashed green lines indicate the 1σ level. The dashed blue indicates the default value $t_v = 10$ ms, previously adopted e. g. in [331] and [330].

since 2005[5] and shown in Fig. 4.2. Therefore, for each GRB whose redshift measurement is missing, each z value assigned allows us to first compute the luminosity distance d_L, then $L_{\gamma,\text{iso}}$ and finally Γ through Eq. (4.4). Note that the resulting value of isotropic luminosity is also required to be between 10^{49} and 10^{54} erg/s since this is the luminosity interval where long GRBs are detected; if such a condition is not satisfied, the z value is extracted again. An example of the procedure we adopted is shown for GRB08102853[6] in Fig. 4.3(a) and Fig. 4.3(b), where the distributions of 1000 values of redshift and Lorentz factor are shown, respectively. Furthermore, Fig. 4.4 shows the comparison between the default value $\Gamma = 316$ previously used in [331] and the average bulk Lorentz factor $\langle\Gamma\rangle$ for any burst in the sample, whose distribution peaks at a value lower than the default one. A similar procedure of random extraction according to a known distribution of values is adopted for the minimum variability timescale t_v, that is known only in the 33% of the cases. For this reason, a distribution of known values of t_v for long GRBs, as obtained from Fourier analyses on burst light curves [367–369], is built as shown in Fig. 4.5. For each GRB with unknown t_v, 1000 values of such parameter are randomly extracted from this distribution. Note that the default value previously adopted in ANTARES GRB search [331] and advocated in [341], $t_v = 10$ ms, is actually located in the tail of the measured distribution, that on the other hand peaks around 0.5 s. From the foregoing, it clearly emerges that the default values assumed so far for intrinsic model parameters, such as Γ and t_v, are

5 The usage in our analysis of the Swift z-distribution does not introduce any bias, as it can be shown that this is representative of the entire sample of long GRBs detected by any instrument from 1997 until today. Nevertheless, the Swift distribution appears very suitable for our purpose, as it can be easily accessed though the satellite's online catalog.

6 The GRB name is given following the Fermi convention, i.e. `GRByymmddfff`, where where `yymmdd` is the date of the burst (`yy`, the year; `mm`, the two-digit month; and `dd`, the two-digit day of the month) and `fff` = fraction of day.

not representative of the different properties of the GRB population. Hence, by using the extracted values of redshift z and variability timescale t_v, 1000 fluxes for each GRB (for which z and/or t_v are unknown) are simulated, in order to estimate the final neutrino fluence by assuming values of the unknown parameters spanning their allowed ranges. The method allows also to investigate how these uncertainties affect the neutrino spectra and to identify the parameter that contributes the most. Therefore, the following procedure is adopted for those sources lacking both z and t_v:

1. Calculate the average neutrino fluence resulting from the 1000 simulations.
2. Use the standard deviation σ of the obtained distribution as uncertainty on the average fluence.
3. Provide the results in terms of $E^2_{\nu_\mu} F_{\nu_\mu} \pm 2\sigma$.

When both z and t_v are known (30 GRBs in the sample), the statistical error around the flux is obtained by propagating the measured parameter uncertainties on $E^2_{\nu_\mu} F_{\nu_\mu}$. In such cases, the uncertainties are so small that the relative difference between $E^2_{\nu_\mu} F_{\nu_\mu}$ and $E^2_{\nu_\mu} F_{\nu_\mu} \pm 2\sigma$ is negligible, of the order of 10^{-1} in the worst cases. However, in a few cases where the uncertainty on redshift was not available from measurements, it has been considered on the last significant digit.

4.2.3 *Effects of parameter uncertanties on individual neutrino fluences*

To investigate which parameter among z, t_v and Γ most affects the neutrino flux computation, we report in Fig. 4.6 some individual neutrino fluence simulations that we obtained, covering all the parameter combinations realised in the selected GRB sample:

- GRB08021273, a source with both z and t_v unknown (Fig. 4.6(a));
- GRB14102845, a source with measured $z = 2.332$ but t_v unknown (Fig. 4.6(b));
- GRB08102853, a source with z unknown and $t_v = 0.35$ s measured (Fig. 4.6(c));
- GRB13042732 (also known as GRB130427A), the brigthest ever detected GRB in gamma rays, for which both $z = 0.34$ and $t_v = 0.04$ s are measured (Fig. 4.6(d)).

For each of these GRBs, 1000 simulations are performed extracting the unknown value of the missing parameter, either the redshift and/or the variability time, from a distribution of the same parameter as obtained from other known GRBs. From these examples, it follows that the minimum variability timescale contributes to the uncertainty on the neutrino fluence expected from GRBs significantly more than redshift. In fact, by comparing the cases (ii) and (iii) in Fig. 4.6(b) and Fig. 4.6(c), respectively, it is possible to note that the uncertainty due to the unknown value of z is contained within $\sim$1 order of magnitude with respect to the mean flux, while it spans over several orders of magnitude when t_v is unknown. On the other hand, when both z and t_v are measured, the error band on the neutrino flux is extremely reduced, as it is only due to the uncertainty in the measurements

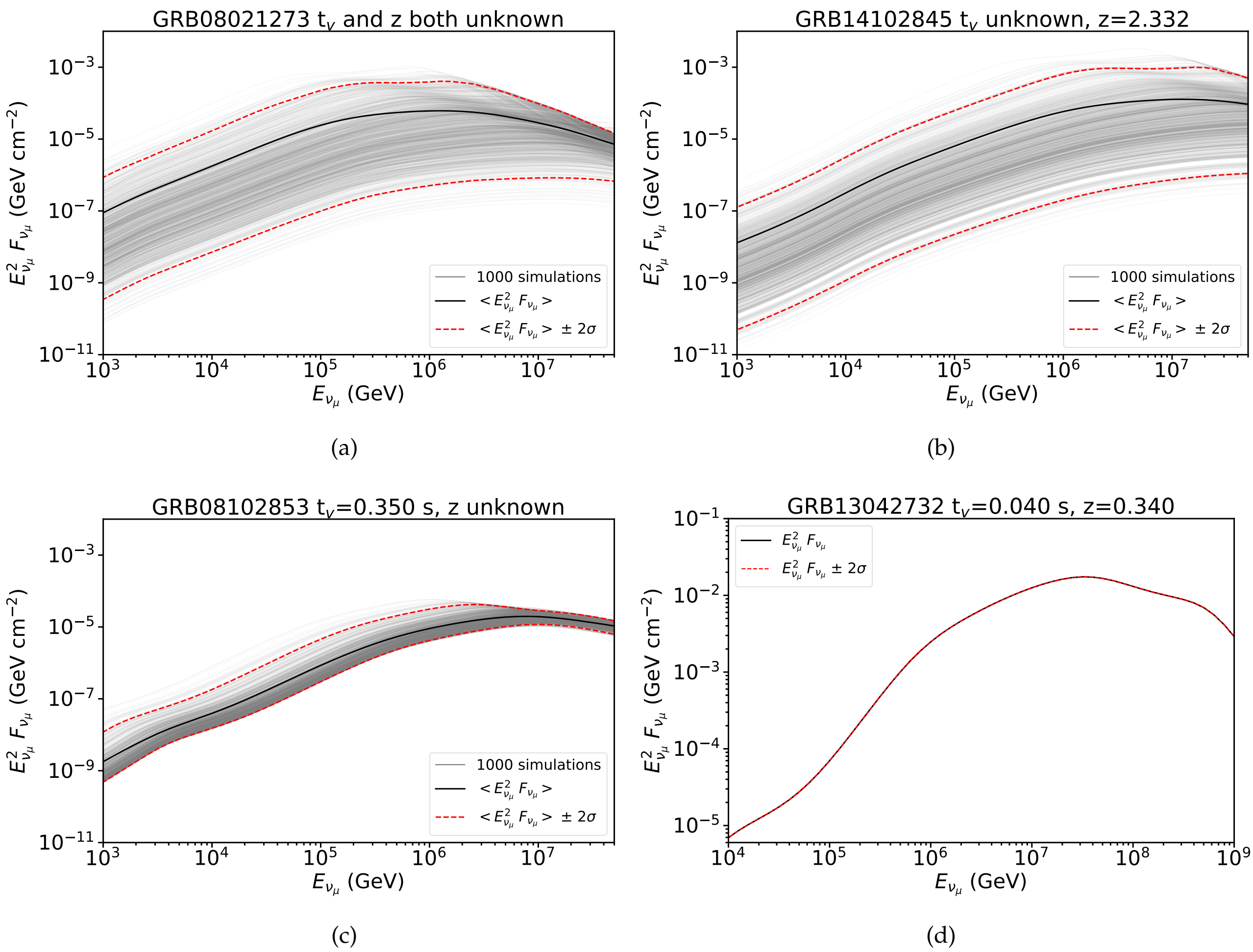

Figure 4.6: Expected neutrino fluence $E^2_{\nu_\mu} F_{\nu_\mu}$ as a function of the neutrino energy E_{ν_μ}. The z and t_v values of each GRB are indicated in the panels, when known: (a) GRB08021273; (b) GRB14102845 [370]; (c) GRB08102853 [368]; (d) GRB13042732 [369, 371]. The grey thin lines indicate the results of 1000 simulations performed with the several randomly extracted values of z and t_v, when at least one of such parameters is unknown. The black thick line shows the mean of all the simulations or, when both z and t_v are known, the resulting neutrino fluence. The red dashed lines delineate the error band around the neutrino fluence. In case both the minimum variability timescale and redshift are fixed, as for the GRB shown in (d), the fluence uncertainty is extremely tiny: in this particular case it is estimated to be $\sim 3\%$.

of spectral parameters. In these cases, it is not possible to distinguish the upper and lower bounds on the neutrino fluence from the mean fluence: an example is shown in Fig. 4.6(d) for GRB13042732. Note that, so far, the uncertainty related to the knowledge on Γ was not considered, as justified by the assumption of the correlation in Eq. (4.4) that allows to infer its value, once the isotropic gamma-ray luminosity of the burst is given. However, several expressions for the Γ estimation exist in the literature, which mainly differ in the observational strategy and physical description of the GRB evolution they rely upon. For instance, a relation between Γ and the peak luminosity $L_{\gamma,\mathrm{peak}}$ was also established some years ago by using a different approach [372], namely by relying on the backwards extrapolation of the self-similar deceleration solution for the shock evolution, as derived by

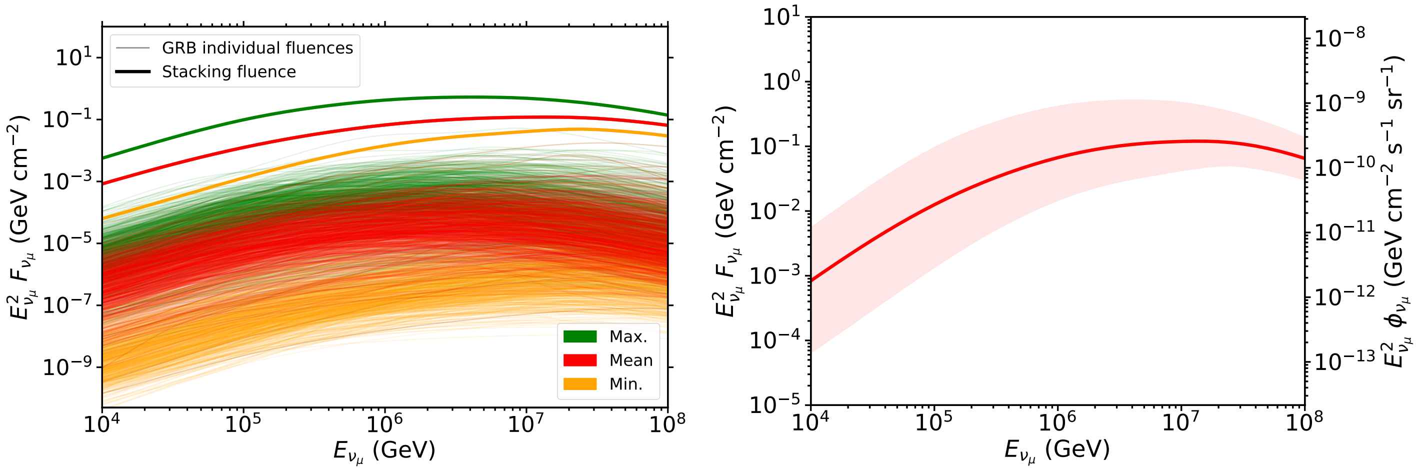

(a) (b)

Figure 4.7: (a) Individual fluences calculated for each GRB of the 784 in the sample (thin lines) and the corresponding stacked fluence (thick line), calculated as in Eq. (4.5). The mean ($E^2_{\nu_\mu} F_{\nu_\mu}$), mininum ($E^2_{\nu_\mu} F_{\nu_\mu} - 2\sigma$) and maximum ($E^2_{\nu_\mu} F_{\nu_\mu} + 2\sigma$) fluences are shown in red, orange and green, respectively. (b) Total neutrino fluence $E^2_{\nu_\mu} F_{\nu_\mu}$ expected from the 784 GRBs in the sample selected in the period 2007-2017 (left-hand axis), as in Eq. (4.5), and corresponding quasi-diffuse neutrino flux $E^2_{\nu_\mu} \phi_{\nu_\mu}$ (right-hand axis), as defined in Eq. (4.6). The shaded region indicates the error band, obtained from the sum of the individual maximum and minimum fluences for each GRB in the sample (see Fig. 4.7(a)).

Blandford and McKee (BM) in [373]. With respect to the method here adopted, this approach comes with two further assumptions: in correspondence of the deceleration stage, the system dynamics has entered the BM self-similar solution, and the intersection of the two asymptotic power-law phases adopted to describe the shock evolution corresponds to the observed peak time of the afterglow light curve. Because of these stringent limitations, in our analysis we adopt the standard *Lü correlation* approach. Clearly, this choice impacts the neutrino flux expectations, in that a significantly different evaluation of the bulk Lorentz factor might lead to a variation in the expected location of the internal shock radius (see Eq. (4.1)). As the neutrino flux is expected to be extremely sensitive to the Lorentz factor [347], a treatment of the additional systematics associated with adopting a different method for deriving Γ will be later on investigated (see Sect. 4.6).

4.3 CUMULATIVE NEUTRINO FLUENCE FROM ALL GRBS IN THE SAMPLE

By summing over all the individual neutrino fluences, the total fluence expected from the cumulative contribution of the selected 784 GRBs in the period 2007-2017 is calculated as:

$$E^2_{\nu_\mu} F_{\nu_\mu} = \sum_{i=1}^{N_{\mathrm{GRB}}=784} (E^2_{\nu_\mu} F_{\nu_\mu})^i. \tag{4.5}$$

In Fig. 4.7(a), the expected minimum, mean and maximum fluences respectively defined as $E^2_{\nu_\mu} F_{\nu_\mu} - 2\sigma$, $E^2_{\nu_\mu} F_{\nu_\mu}$ and $E^2_{\nu_\mu} F_{\nu_\mu} + 2\sigma$ are shown for each GRB and for the whole sample.

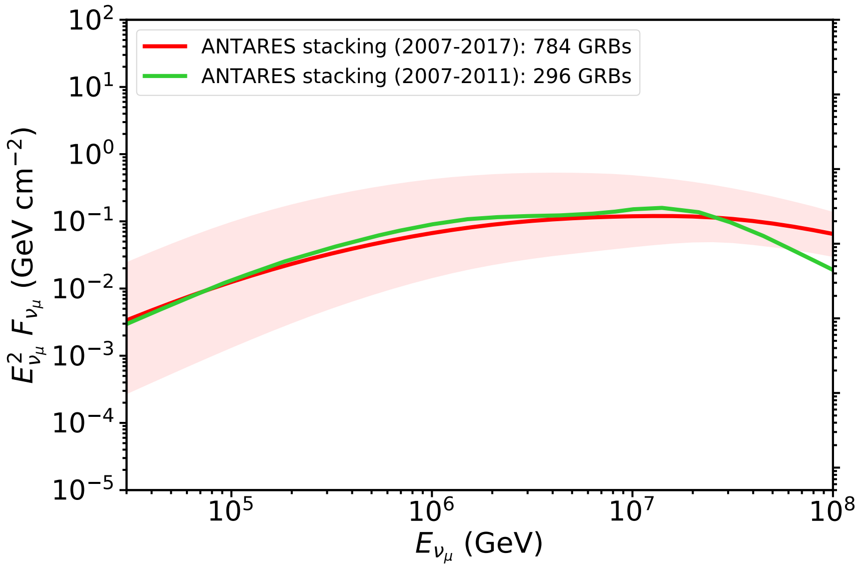

Figure 4.8: Comparison between the cumulative neutrino fluence expected from the stacking of 784 GRBs in the period 2007-2017 (in red) and the cumulative neutrino fluence obtained in [331] from stacking 296 GRBs in the years 2007-2011 (in green) The red shaded region indicates the error band around the neutino fluence estimated in this work, taking into account the several uncertainties affecting the neutrino production in GRBs.

Focusing on the total fluence, note that the maximum and minimum fluences define the calculation uncertainty around the mean one, shown in Fig. 4.7(b). It is possible also to convert the total neutrino fluence of the sample of N_{GRB} into the quasi-diffuse neutrino flux induced by the same sources, by rescaling the total fluence with the average rate of GRBs distributed over the full sky expected per year. Hence, the quasi-diffuse neutrino flux is obtained as

$$E^2_{\nu_\mu} \phi_{\nu_\mu} = \sum_{i=1}^{N_{\mathrm{GRB}}} (E^2_{\nu_\mu} F_{\nu_\mu})^i \frac{1}{4\pi} \frac{1}{N_{\mathrm{GRB}}} 667 \mathrm{yr}^{-1}, \tag{4.6}$$

where an annual rate of long GRBs equal to 667 per year is considered, in agreement with the previous ANTARES analyses [331, 332]. The diffuse neutrino flux computed with this method is indicated in the right-hand axis of Fig. 4.7(b). This quantity is actually more interesting than the total expected fluence, since it allows to compare the neutrino flux produced by the GRBs in the analysis with both the sensitivity of neutrino telescopes and the measurement of the astrophysical diffuse neutrino flux reported by IceCube, in order to constrain the contribution of GRBs to this flux.

For completeness, we compare in Fig. 4.8 the cumulative neutrino fluence estimated in the present work with that of the previous ANTARES analysis [331]. The two are observed at a comparable level, even though the our analysis has more than twice more sources than the previous. This result is, in fact, a consequence of the neutrino modeling adopted: while past predictions tended to overestimate the expected flux by assuming standard values for model parameters, here an accurate modeling is realised by accounting for variations in these parameters reflecting the properties of observed GRBs.

4.4 STATISTICAL ANALYSIS OF 2007-2017 ANTARES DATA

After having described the IS scenario and the related computation of neutrino fluxes expected from each GRB in the sample we built up, we present in this section the analysis chain on data collected by the ANTARES neutrino telescope between 2007 and 2017. The MC simulations of GRB neutrinos events used to provide the detector response to the signal are described in Sect. 4.4.1 (for a more detailed treatment of the MC simulation chain adopted in ANTARES refer to Appendix B). Then, in Sect. 4.4.2, the estimation of the background that characterises ANTARES data is presented. In Sect. 4.4.3, the analysis optimisation is discussed, through the set up of MC pseudo-experiments generated with the aim of obtaining the highest discovery potential for the neutrino flux, by exploiting an extended maximum-likelihood ratio statistical method. In Sect. 4.4.4, the diffuse search performed through the stacking technique, investigating whether the discovery potential can be improved by limiting the analysis to an optimised sub-sample of bursts, is presented.

4.4.1 *Signal simulation: the detector probability density function*

For each source in the sample, a MC simulation of the expected signal is performed in the so-called run-by-run mode (see Sect. B.1.4), i.e. accounting for the specific detector condition at the time that the GRB occurred, as in [331]. In this way, the event generation is able to accurately describe the data taking, calibration and efficiency conditions of the detector during the run in which each GRB happened. Both tracks, resulting from ν_μ CC interactions, and showers, produced at ν_μ NC as well as at ν_e both CC and NC interactions (see Sect. 2.1.2), are included in the simulation and signal events are generated from the specific location of the sky where the GRB was observed by gamma-ray satellites. To take the ANTARES absolute pointing uncertainty into account, the GRB local coordinates used in the MC signal production are shifted of a quantity randomly generated following [374, 375] (see also [376] and [377] for other studies on the ANTARES pointing accuracy). Since only GRBs below the ANTARES horizon at the trigger time are considered in this search to reduce the atmospheric muon background (see Sect. 2.3.2), neutrinos are simulated from the direction of the GRB and passing through the Earth, following the simulation scheme described in Appendix B. Upward going muon tracks are then reconstructed, to compute the acceptance of the detector, with the `AAFit` algorithm described in Sect. B.2.1.1. The quality of the reconstruction is estimated through two parameters: Λ, the track-fit quality parameter, and β, the estimated angular uncertainty on the muon track direction. To improve the signal-to-noise ratio, to ensure a good quality reconstruction and also to limit the atmospheric muon contamination, only tracks with $\beta < 1^\circ$ are considered in the analysis. The search is then optimised through varying a cut on Λ selecting tracks above a given threshold Λ_{cut}, as explained in Sect. 4.4.4. The distribution of the angular distance between the reconstructed track direction (for each Λ_{cut}) and the GRB's coordinates, normalised to the total number of events, defines the signal Probability Density Function (PDF) $S(\alpha) = \mathrm{dN}(\alpha)/\mathrm{d}\Omega$, where α is the angular distance between the simulated GRB position and the reconstructed muon direction and $d\Omega$ is the differential solid angle $d\Omega = 2\pi \sin\alpha d\alpha$. The signal PDF is fitted with a function that is flat for small values of α and by a Rayleigh distribution [378] for larger values, i. e.

$$\log S(\alpha) = \log \frac{dN(\alpha)}{d\Omega} = \begin{cases} A & \alpha \leq \alpha_0 \\ A - B\left(1 - \exp\left(\frac{-(\log\alpha - \log\alpha_0)^2}{2\sigma^2}\right)\right) & \alpha > \alpha_0 \end{cases} \tag{4.7}$$

with the free parameters A, B, α_0, and σ.

The ANTARES MC simulation chain and the software adopted for the signal simulation in this analysis are described in Appendix B. At this level, it was important to check the reliability of MC simulations. Indeed, to trust the GRB signal simulations, I performed data/MC comparison per each run containing GRBs in the sample, examining that all runs were correctly simulated and that none of those exhibited an unusual behavior.

4.4.2 *Background estimation*

The expected number of background events μ_b associated to each GRB, at zenith θ and azimuth ϕ, is evaluated directly from data collected by ANTARES off-source and off-time (between 27th December 2007 and 30th December 2017) as:

$$\mu_b(\theta,\phi)_{\mathrm{GRB}} = 1.5\ T_{\mathrm{s}} \cdot \langle n(\theta_{\mathrm{GRB}},\phi_{\mathrm{GRB}})\rangle \cdot \mathcal{C}, \tag{4.8}$$

where T_{s} is the temporal time window around the GRB occurrence, $\mathcal{C}$ is the detector efficiency in the specific runs where each GRB occurred, and $\langle n(\theta_{\mathrm{GRB}},\phi_{\mathrm{GRB}})\rangle$ is the time-averaged rate of events reconstructed in the GRB direction. In the framework of prompt GRB emission, the temporal search window of the neutrino signal was defined in coincidence with the gamma-ray signal, slightly extended to account for uncertainties due to the gamma-ray duration of the event, to the ANTARES data acquisition system and to the propagation time of particles from the satellite to our detector. The time-averaged rate of events reconstructed in the GRB direction, is here estimated with a sample of 15657 runs, equivalent to 61562.5 hours of livetime ($\sim$2565 days). To be conservative, this average value is compared with the mean of time-averaged rates within a 10° cone around the GRB position, choosing the highest between these two values. This is performed in fact as to account also for the non-uniformity of the background in the vicinity of the GRB position. Finally, in Eq. (4.8) the factor 1.5 is included to conservatively increase the background estimate by 50%. The background PDF, $B(\alpha) = dN(\alpha)/d\Omega$ is assumed to be flat in Ω within the search cone angle, assuming the value as calculated in Eq. (4.8). As a result, the average number of background events expected within a search cone of 10° around a given GRB position is found to be of the order of 10^{-4}.

In Fig. 4.9 the results of the entire analysis chain for GRB111123A (taken as an example) are presented. The figure shows the signal and background PDFs up to a distance of 10° from the simulated GRB position. The signal PDF is obtained by considering all the

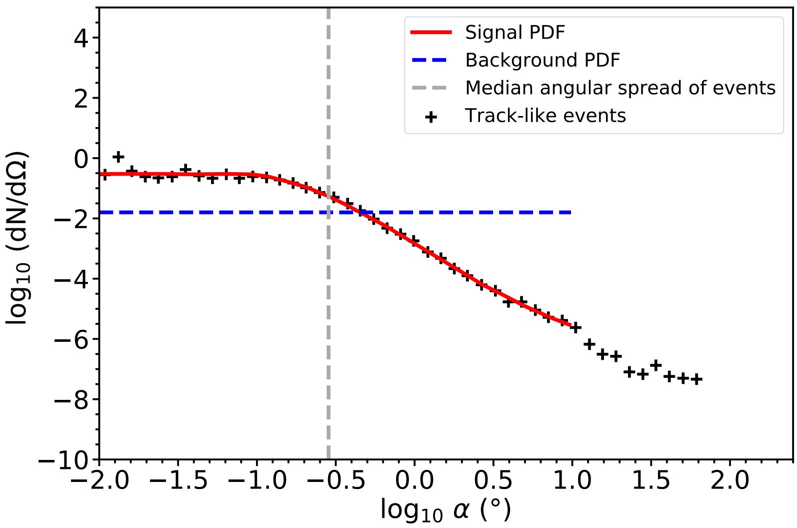

Figure 4.9: GRB111123A: reconstructed events from the MC signal simulation, per solid angle Ω as a function of the logarithm of the space angle α, obtained with tracks from ν_μ CC interactions and tracks from ν_μ NC and ν_e NC+CC interactions (all neutrino channels are shown in black)), with $\beta < 1°$ and $\Lambda_{\text{cut}} = -5.2$. The vertical dashed line (in grey) indicates the median angular spread of events $\langle \alpha \rangle = 0.29°$; the horizontal dashed line (in blue) shows the flat background PDF $B(\alpha)$. The red curve is the signal Point Spread Function (PSF), inside the defined angular window of 10° around the GRB position.

neutrino events simulated that have been reconstructed as tracks with $\Lambda_{\text{cut}} = -5.2$. The median angular spread of events (i. e. the median angular resolution) is also provided.

4.4.3 *Maximum likelihood and pseudo-experiments*

MC pseudo-experiments are simulated individually for each GRB with the aim of constructing an ensemble of independent replications of the data acquisition and computing the significance of the measurement. For each GRB, different sets of simulations are generated by varying Λ_{cut} from -5 to -5.8. For each of these cuts, $\sim 4 \times 10^6$ signal events and $\sim 4 \times 10^{11}$ background events are simulated. A test statistics Q, defined as the ratio between the likelihood in the hypothesis of signal plus background and the likelihood in the background only hypothesis, is evaluated in the form of an 'extended maximum likelihood ratio' [379]:

$$Q = \max_{\mu_s' \in [0, n_{\text{tot}}]} \left(\sum_{i=1}^{n_{\text{tot}}} \log \frac{\mu_s' \cdot S(\alpha_i) + \mu_b \cdot B(\alpha_i)}{\mu_b \cdot B(\alpha_i)} \; - \; \mu_s' \right), \tag{4.9}$$

where α_i is the angular distance between the GRB position and the reconstructed muon direction, $S(\alpha_i)$ and $B(\alpha_i)$ are the corresponding signal and background PDFs, respectively. In practice, with a priori knowledge of the expected number of background events μ_b (as evaluated in Sect. 4.4.2) and with a signal contribution μ_s' scanned between 0 and n_{tot}, the latter being the total number of events, signal and background events i are randomly drawn from the normalised signal and background PDFs corresponding to each considered value of Λ_{cut}, and the test statistic Q is evaluated returning the estimated signal as the one maximising Q. Furthermore, to determine the statistical significance of measurements, the p-value[7] is calculated, i. e. the probability to yield Q-values at least as high as that observed if the background-only hypothesis was true. At the end of this procedure, the optimal cut on the quality parameter, Λ_{cut}, is chosen as the one maximising the MDP, i. e. the probability to observe an excess with a p-value lower than the pre-defined threshold at a given statistical accuracy assuming the signal predicted by the theoretical model (NeuCosmA), as previously described in Sect. 2.4.4. This strategy was already used in other ANTARES analyses related to GRBs, as [331, 333]. However, there is a difference here in the MDP calculation: the systematic uncertainties in the ANTARES acceptance, that translate into a systematic uncertainty on the value of the estimated signal μ_{s}, are considered in this work, consistently with other previous ANTARES analyses on neutrino sources [375, 380].

4.4.4 *Diffuse search optimisation*

The procedure of stacking sources consists into the definition of a GRB sub-sample that includes in the analysis, among the GRBs sample defined in Sect. 4.1, as many candidates in terms of neutrino emission as necessary to obtain the best sensitivity. The progressive inclusion of promising GRBs implies the addition not only of the signal but also of the corresponding background. For this reason, the optimal number of sources to stack is found as a compromise between the statistical reduction and the signal gain due to an increasing number of sources in the final sample. In particular, it corresponds to the value which maximises the probability to make a significant discovery (MDP). The procedure, described in details in [331] the reader can refer to, has been optimised for a 3σ significance level. In Fig. 4.10, it is possible to see how the value of $\text{MDP}_{3\sigma}$ evolves by increasing the number of selected GRBs: the loss in $\text{MDP}_{3\sigma}$ is very limited between the use of the whole sample and of an optimal one. Hence, the stacking is performed on the whole GRB sample (784 GRBs). Though the search is not optimal in terms of cumulative $\text{MDP}_{3\sigma}$, the track quality cut Λ_{cut} is set to optimise the $\text{MDP}_{3\sigma}$ of individual GRBs. In this regards, the most promising 10 GRBs at 3σ are reported in Tab. 4.2, together with the search time window, the optimised cuts, and the corresponding expected number of background and signal events. The results of the stacking of all 784 sources corresponds to an $\text{MDP}_{3\sigma} = 0.027$ (0.009; 0.136), where the values in parenthesis represent the range of $\text{MDP}_{3\sigma}$ values when the model parameters are allowed to vary within 3σ.

4.5 RESULTS OF THE STACKING ANALYSIS

ANTARES data from the end of 2007 to 2017 are analysed according to the cuts identified in the optimisation procedure presented above, searching for neutrino events in spatial and temporal coincidence with the prompt phase of GRBs observed by satellite-based gamma-

7 The two-sided convention is used here, namely $p_{3\sigma} = 2.7 \times 10^{-3}$, $p_{4\sigma} = 6.3 \times 10^{-5}$, $p_{5\sigma} = 5.7 \times 10^{-7}$.

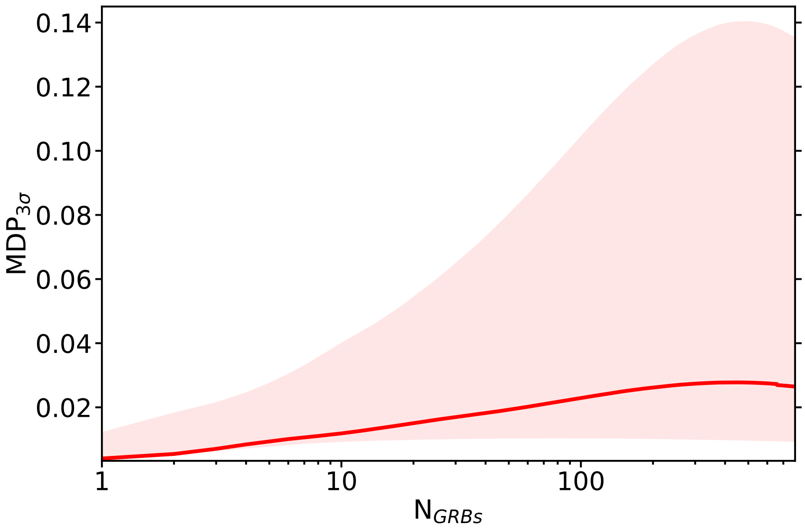

Figure 4.10: Model Discovery Potential at 3σ, $\mathrm{MDP}_{3\sigma}$, as a function of the number of stacked GRBs, $\mathrm{N}_{\mathrm{GRB_s}}$. The thick red line indicates the $\mathrm{MDP}_{3\sigma}$ obtained with the mean neutrino fluence, while the shaded region is the uncertainty on $\mathrm{MDP}_{3\sigma}$ obtained by considering the minimum and maximum fluences (see Fig. 4.7(a)).

GRB	Λ_{cut}	μ_b (events)	μ_s (events)	$\mathrm{T_s}$ (s)	$\mathrm{MDP}_{3\sigma}$
13042732	−5.5	5.3×10^{-5}	2.2×10^{-3}	33.9	2.1×10^{-3}
10072809	−5.5	9.7×10^{-5}	1.1×10^{-3}	268.6	9.8×10^{-4}
17101079	−5.3	1.0×10^{-4}	1.0×10^{-3}	252.0	9.4×10^{-4}
09072071	−5.4	1.8×10^{-5}	7.8×10^{-4}	21.2	6.7×10^{-4}
11092889	−5.4	4.4×10^{-4}	5.1×10^{-4}	115.0	4.3×10^{-4}
14041606	−5.4	5.5×10^{-5}	4.2×10^{-4}	36.8	4.0×10^{-4}
12070780	−5.5	7.9×10^{-5}	4.1×10^{-4}	69.5	3.8×10^{-4}
11122865	−5.5	4.0×10^{-4}	4.4×10^{-4}	163.7	3.6×10^{-4}
14081078	−5.4	7.6×10^{-5}	3.7×10^{-4}	97.7	3.6×10^{-4}
10091081	−5.3	5.4×10^{-5}	3.4×10^{-4}	27.3	3.2×10^{-4}
all GRBs:					
mean	−5.3	9.4×10^{-5}	3.8×10^{-5}	86.9	3.4×10^{-5}
sum		7.3×10^{-2}	3.0×10^{-2}	6.8×10^{4}	2.7×10^{-2}

Table 4.2: Optimisation results obtained with mean fluences: the first ten GRBs with the highest $\mathrm{MDP}_{3\sigma}$ are shown, with the corresponding optimised Λ_{cut} value, the expected number of background μ_b and signal μ_s events at 3σ and the $\mathrm{T_s}$. In the last rows, the sum and mean of the values for all 784 GRBs at 3σ is given. The naming convention of the GRBs is as the same as used by Fermi.

ray instruments. No neutrino events have passed the selection criteria defined through the optimisation procedure and, thus, no neutrino events are found in spatial and temporal coincidence with the GRB sample, for an equivalent livetime of the search of 18.9 hours. The corresponding 90% C.L. upper limit on the computed neutrino signal ϕ_{ν_μ} is calculated as in Eq. (2.16), i.e.,

$$\phi^{90\%}_{\nu_\mu} = \phi_{\nu_\mu} \frac{\mu_s^{90\%}}{n_s} = \phi_{\nu_\mu} \frac{2.3}{n_s} = \phi_{\nu_\mu} \cdot 77^{+226}_{-64}, \tag{4.10}$$

where the expected number of signal events from the total sample, n_s, is estimated to be

$$n_s(N_{\text{GRB}} = 784) = 0.03^{+0.14}_{-0.02}. \tag{4.11}$$

The factor 2.3 in Eq. (4.10) is the 90% CL upper limit of the mean of a Poisson process and the value in Eq. (4.11) is a result of the optimisation procedure applied on minimum, mean and maximum fluences, as explained in Sect. 4.4.4. Note that the relative uncertainty on the expected number of signal events is smaller than the one estimated on the MDP; in other words, the neutrino flux uncertainty due to unknown model parameters is quite limited in the energy range that is relevant for our search. Still, the uncertainty here presented is only partial, as it does not account for the systematics associated with having fixed the correlation in Eq. (4.4) to derive the bulk Lorentz factor, which is the parameter expected to most affect the neutrino flux [347]. In Sect. 4.6 such a contribution is also evaluated.

The absence of neutrinos associated to GRBs in ANTARES data allows us to put constraints the IS model. For the cumulative fluence of Eq. (4.5), this limit reads as $1.3^{+4.1}_{-0.8} \times 10^{-2} < E^2_{\nu_\mu} F_{\nu_\mu} < 0.8^{+5.2}_{-0.7} \times 10^{-1}$ GeV cm^{-2}, in the energy range extending from 6.3×10^4 GeV to 1.3×10^7 GeV, which is the region where 90% of the mean fluence is expected to be detected by ANTARES. The fluence limit translates into $1.3^{+0.4}_{-0.8} \times 10^{-9} < E^2_{\nu_\mu} \phi_{\nu_\mu} < 1.0^{+0.9}_{-0.5} \times 10^{-8}$ GeV cm^{-2} s^{-1} sr^{-1} in terms of quasi-diffuse flux (cfr Eq. (4.6)). The quasi-diffuse expected flux and corresponding upper limit, as calculated from the mean expected fluence, are shown in Fig. 4.11(a) and compared to previous ANTARES limits [331]. A reduction of a factor ~ 2 on the 90% CL upper limit can be observed, due to the increased sample statistics, jointly with having here adopted a more realistic model for neutrino predictions including a detailed study on the model parameters. The results are also compared with the latest IceCube all-sky search [330], where no statistically significant signal was found by combining both track and shower events for 1172 GRBs. From this comparison, it is possible to appreciate that the GRB-neutrino flux expected by IceCube is consistent with the one presented in this work over the entire energy range 10^4-10^8 GeV, the former being on average higher than the latter due to the larger sample size. The same spectral trend is reflected in individual upper limits.

It is worth keeping in mind that when comparing results from different analyses, one should consider that the spectral and limit shapes depend on the selected sample, the measured parameters of each burst and their uncertainty, namely the set of parameters that are introduced in the chosen model. Here, for the first time, no default value for the model parameters are used and more physical and realistic values are considered (see Sec 4.2.2).

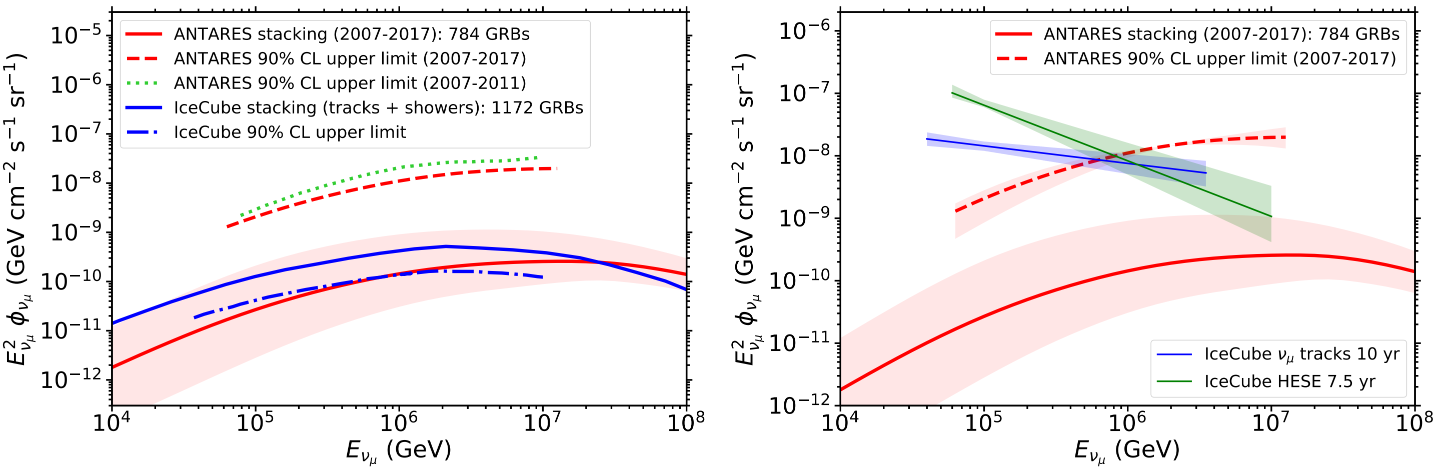

(a) (b)

Figure 4.11: (a) Comparison between the 90% CL upper limit (red dashed line) with respect to the ANTARES expected quasi-diffuse flux for 784 GRBs (red solid line), in Eq. (4.6), and the previous ANTARES 90% CL upper limit (green dashed line) [331]. The solid blue line represents the quasi-diffuse flux expected by IceCube for 1172 GRBs and the corresponding dash-dotted blue line shows the corresponding 90% CL upper limit [330]. (b) GRB ANTARES quasi-diffuse flux for 784 GRBs, in Eq. (4.6), (red solid line) and the corresponding 90% CL upper limit (dashed red line). The red shaded regions show the uncertainty around the GRB quasi-diffuse flux, as in Fig. 4.7(b), and also around the computed upper limit, derived as explained in Sect. 4.4.4. IceCube best fits for ν_μ tracks in 10 years [118] and for HESE events in 7.5 years of collected data [381] are shown in blue and green, respectively.

Finally, the expected quasi-diffuse neutrino flux from the selected 784 GRBs and the corresponding upper limit can be compared with the diffuse astrophysical flux observed by IceCube. To this extent, Fig. 4.11(b), provides the IceCube best fits of the neutrino flux, in both the 10 years ν_μ track data sample [118], and the 7.5 years High-Energy Starting Events (HESE)[8] sample [381]. To allow a more significant comparison, the upper limit derived from this search is reported with its error band (see Eq. (4.10)). By comparing the ANTARES upper limit with the diffuse astrophysical neutrino flux observed by IceCube, it is possible to conclude that GRBs are not the main contributors to the observed flux below $E_\nu \sim 1$ PeV, within the NeucosmA model framework set with benchmark baryonic loading ($f_p = 10$). This result confirms previous searches performed by IceCube [328–330]. In particular, in the energy region where ANTARES is most sensitive, i. e. below ~ 100 TeV, GRBs do not contribute by more than 10%. Consequently, the parameter space still allowed to the internal shock model is characterised by sizeably smaller baryonic loading of GRB jets.

It is worth highlighting that this analysis accounts for the contribution to the observed diffuse astrophysical neutrino flux of long resolved GRBs (i. e. triggered). A potentially interesting contribution is constituted by the many GRBs that elude detection (due to their low photon flux) and which is here left unconstrained. As estimated e. g. , in [382], the neutrino flux from such unresolved GRBs might even be larger than the one due to

8 The neutrino interaction vertex is located inside the detector and its energy is larger than 20 TeV.

resolved ones. In addition to this, other interesting classes of sources possibly contributing to the diffuse astrophysical neutrino flux detected by IceCube are: (i) low-luminous GRBs (LLGRBs) (e. g. , [304, 383]), namely GRBs characterised by a luminosity $\lesssim 10^{49}$ erg s^{-1}; (ii) choked GRBs, which being opaque to radiation in the GeV–TeV band might show up as neutrino sources hidden with respect to gamma-ray observations (e. g. , [384–387]).

4.6 EVALUATING SYSTEMATICS ON ANALYSIS RESULTS

In addition to the parameter uncertainties considered so far, namely those due to the poor knowledge of redshift and minimum variability timescale, a further major source of uncertainty is related to the systematics on the treatment of the Lorentz factor, which could significantly affect the neutrino expectation from GRBs [347]. In fact, the present analysis relies upon the *Lü correlation* between the isotropic gamma-ray luminosity $L_{\gamma,\mathrm{iso}}$ and Γ, that has allowed the values of bulk Lorentz factor for each GRB in the sample to be determined by using Eq. (4.4). In order to evaluate the impact of such a method on neutrino expectations, another correlation present in the literature was also tested, that we call *Ghirlanda correlation* [372]. The latter one actually relates Γ to the peak gamma-ray luminosity $L_{\gamma,\mathrm{peak}}$. Hence, as an intermediate step, the *Ghirlanda correlation* data sample was re-analysed, to obtain the corresponding relation between Γ and isotropic gamma-ray luminosity $L_{\gamma,\mathrm{iso}}$, similarly to that in Eq. (4.4). Common GRBs between the two samples in [372] and [366] were selected in order to consider the Γ estimation from [372] and the corresponding $L_{\gamma,\mathrm{iso}}$ from [366]. From this combined sample, we found the following correlation:

$$\Gamma_G \simeq 146 L_{\gamma,\mathrm{iso},52}^{0.30}. \tag{4.12}$$

The comparison among the *revised Ghirlanda correlation* in Eq. (4.12) and the *Lü correlation* in Eq. (4.4) is shown in Fig. 4.12(a). As visible, the Lorentz factor values obtained through the *revised Ghirlanda correlation* are systematically lower by a factor of $\sim$2 with respect to the values obtained through the *Lü correlation*. To quantify the impact of considering a reduced Lorentz factor on the expected number of neutrino events, the same method described in Sect. 4.2.2 was applied to the computation of neutrino spectra: for each GRB in the sample 1000 spectral simulations were performed with NeuCosmA, by extracting Γ according to Eq. (4.12); then, by summing over all 784 GRBs, a revised stacking flux was obtained, as shown in Fig. 4.12(b). The spectral normalisation appears now significantly higher with respect to the scenario described in Sect. 4.3, while the peak energy of the neutrino spectrum is shifted towards lower energies. This leads to a larger number of expected neutrino events in ANTARES with respect to the computation derived in Sect. 4.5 for the *Lü correlation*; in particular, this is estimated to be $n_{\mathrm{s}} \simeq 0.36$, which is more than a factor 10 above the estimate presented in Eq. (4.11). With the novel neutrino spectrum obtained, we re-run the data analysis chain, by optimising the track-quality cut Λ_{cut} consistently with the procedure described in Sect. 4.4.4. Interestingly, the resulting cuts are found to remain almost unaltered for most of the GRB sample. As a consequence of the absence of

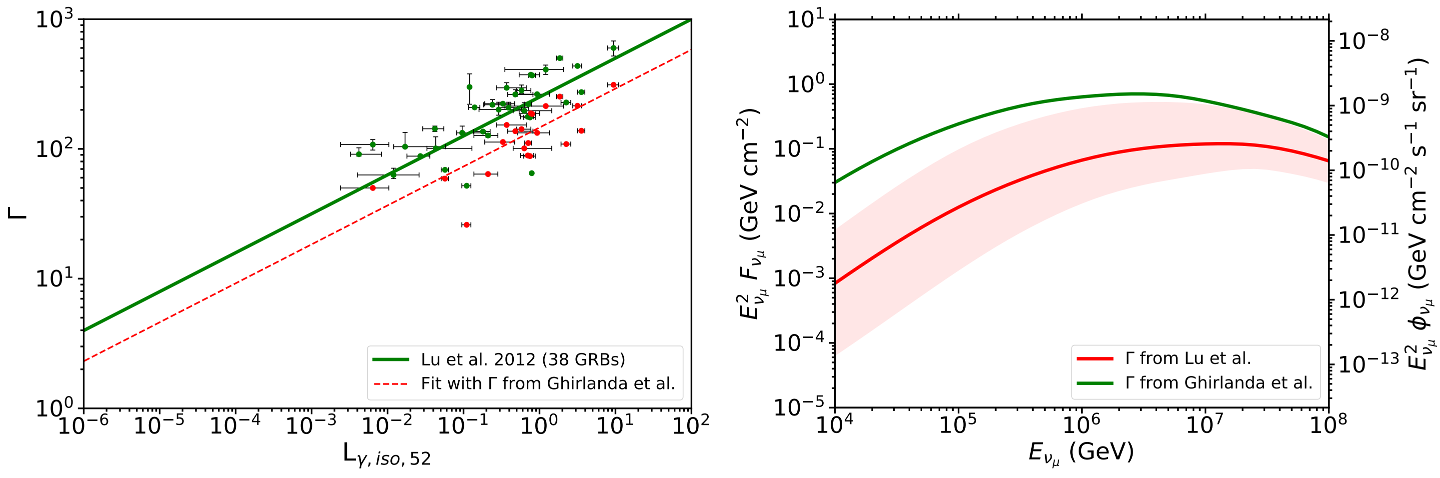

(a) (b)

Figure 4.12: (a) The bulk Lorentz factor Γ as a function of the isotropic equivalent gamma-ray luminosity $L_{\gamma,\text{iso}}$. The green points represents GRBs in the sample studied in [366]. The red points, instead, are a subsample of the sample in [372], containing only those GRBs in common with [366], such that the values of Γ come from [372], while the corresponding values of $L_{\gamma,\text{iso}}$ are from [366]. The green solid and dashed red lines represent the best fits of each sample. (b) Total neutrino fluence $E^2_{\nu_\mu} F_{\nu_\mu}$ expected from the 784 GRBs in the ANTARES 2007-2017 sample (left-hand axis) and corresponding quasi-diffuse neutrino flux $E^2_{\nu_\mu}\phi_{\nu_\mu}$ (right-hand axis). The red and green lines show the different results obtained by either assuming a Γ-distribution according to [366] (see Eq. (4.4)) or according to [372] (see Eq. (4.12)), respectively. The red shaded region indicates the error band around the stacking flux expected from [366], as estimated in Sect. 4.3.

neutrinos associated to GRBs in ANTARES data, we obtain new 90% CL upper limits, that are found to lay at a comparable level than that in Eq. (2.16). From the comparison with the estimated uncertainty due to missing information on redshift and variability timescale, which is contained within a factor of ~ 5 (2σ), it is possible to conclude that the leading source of uncertainty in neutrino spectral modeling is represented by the indirect knowledge of the bulk Lorentz factor of GRB jets. This conclusion is also supported by recent studies from [347].

5 ENABLING NOVEL REAL-TIME MULTIMESSENGER STUDIES WITH KM3NET/ARCA NEUTRINO TELESCOPE

The multipurpose neutrino observatory KM3NeT, currently being constructed in the Mediterranean Sea (see Sect. 2.5.2), is involved in a global multimessenger programme, described in Sect. 1.6.2, which includes sending public/private neutrino alerts in real time to the astronomy community to trigger electromagnetic follow-up observations of interesting events, as well as searching for neutrinos in spatial and temporal coincidence with promising transient astrophysical sources seen in GWs, X rays, γ rays, and other wavelengths. In this context, real-time event reconstruction must be performed quickly so that they feed into an online analysis framework which, for specific criteria of the reconstruction (e.g., quality, direction, energy, etc.), triggers an alert-sending system. It is worth mentioning that neutrino data provide improved power to detect high-energy transient sources. Indeed, contrary to traditional telescopes, Cherenkov-based neutrino detectors have a field of view comprising the whole sky, thus they are ideally suited to detect and inform in very short time other telescopes about interesting events. The real-time multimessenger analysis framework is currently being implemented in KM3NeT. Among the activities performed during this thesis, the development of the online processing framework for the KM3NeT/ARCA detector, devoted to the detection of high-energy neutrinos (1 TeV-10 PeV) produced in astrophysical phenomena during UHECR acceleration, is included. Specifically, I was involved in the track-like events reconstruction both in direction and energy (refer to Sect. 2.1.2 for the explanation of the different event signatures detectable by high-energy neutrino telescopes).

In this chapter, the DAQ system of the KM3NeT detector, within which the online software is implemented, is first described, in Sect. 5.1. Then, Sect. 5.2 outlines the characteristics of the online analysis platform developed for the KM3NeT detector, giving a focus on the framework currently in place to reconstruct events in real time for KM3NeT/ARCA, on which this thesis is focussed. In Sect. 5.3, the validation of the online reconstruction system is shown, either through the real-time data collected by the current detector configuration (KM3NeT/ARCA 21 strings) and via MC simulations of cosmic PeV neutrinos acquired by the future detector KM3NeT/ARCA 115 strings. Finally, the results of the first quasi-real-time analysis performed on a peculiar gamma-ray burst (GRB 221009A) are shown in Sect. 5.4. Indeed, this burst drew the attention of all the astrophysics and astroparticle community for its spectacular characteristics. GRB 221009A was particularly energetic and close to us, and this makes it the brightest ever GRB observed. Despite its position was not favourable for KM3NeT, the explosion having occurred above the detector horizon (i.e., in the downgoing sky for KM3NeT, from which the atmospheric muon background is unavoidable), it was however decided to analyse this GRB because of its exceptionality. This analysis was performed as of events reconstructed in real-time with the online pipeline described in this chapter, and can be taken as reference example for the real-time analyses are currently performed within the online framework of KM3NeT.

5.1 DATA ACQUISITION SYSTEM

The online software is implemented in the DAQ system, described here. As already pointed out in Chapter 2, the neutrino detection principle exploits the Cherenkov light from relativistic particles outgoing high-energy neutrino interaction within a fiducial volume around the telescope. The arrival time and charge of the light is recorded by an array of photosensors; this data is then used to infer the energy and direction of the particles. The main elements of KM3NeT are PMTs, housed inside pressure-resistant glass spheres called DOMs [388]. KM3NeT is made up of an array of multiple lines, called DUs, supplied by 18 DOMs each. Within the DOM, the main electronics board is the Central Logic Board (CLB) [389], which processes data arriving on PMTs and acquires timing and amplitude information of these signals, by means of Time-to-Digital-Converters (TDCs)[1] [390]. The start time is defined as the time at which the pulse passes beyond a 0.3 photo-electron equivalent (p.e.) threshold, and its duration is given by the time the pulse remains above this threshold, namely the pulse width, usually called Time-Over-Threshold (ToT). Both these quantities, recorded with nanosecond precision by the front-end electronics enclosed in the DOM [391, 392], characterise a PMT *hit*.

Because of the high optical background due to β-decay processes of ^{40}K and the bioluminescence phenomena in seawater (see Sect. 2.2.3), an online trigger system is needed; otherwise, storing the corresponding throughput (ranging up to 30 Gbps) would not be a sustainable solution. Data need to be filtered and reduced before being permanently stored, requiring the usage of the *Trigger and Data Acquisition System* (TriDAS), described in detail, e.g., in [393]; this is a computing system devoted to the read-out, aggregation, and filtering of the continuous data flow detected by KM3NeT. The DAQ is driven by the Control Unit (CU) software [394], which represents the detector user interface, that aims at coordinating TriDAS and running DOMs through a dedicated protocol. The logic of the DAQ system of KM3NeT is in the following Sect. 5.1.1 described.

5.1.1 *Data handling and triggers*

To minimise the complexity of underwater electronics, the KM3NeT DAQ does not use any offshore hardware trigger, but follows the *all-data-to-shore* approach, as in ANTARES: via a

1 In electronic instrumentation, a TDC is a device for recognising events and providing a digital representation of the time they occurred. For example, a TDC might output the arrival time for each incoming pulse.

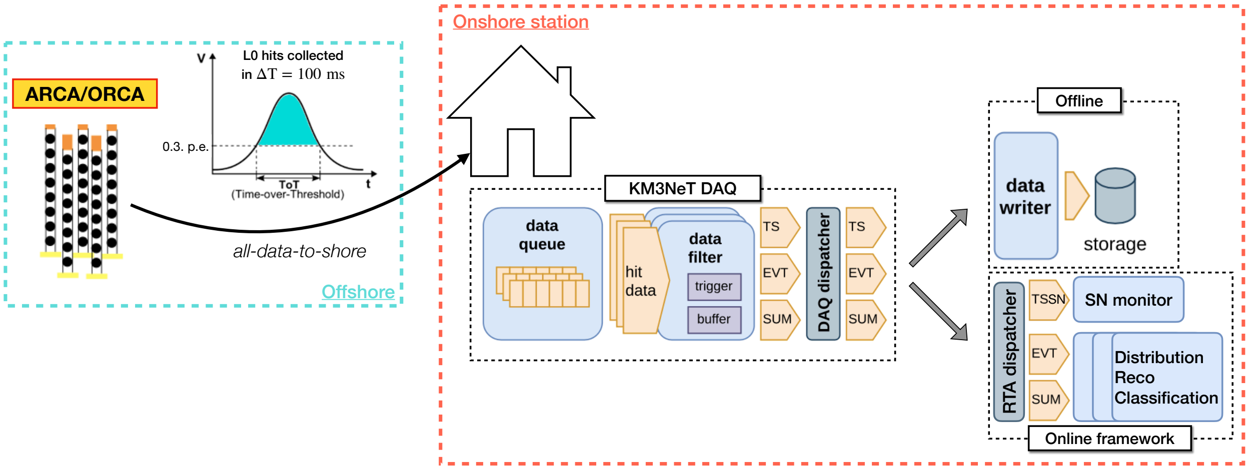

Figure 5.1: Logic diagram of the data acquisition system of KM3NeT detectors. Timeslices, triggered events and summaryslices (different data streams) are indicated as `TS`, `EVT`, and `SUM`, respectively.

dedicated fibre-optic data transmission system, all signals above 0.3 p.e. are collected and sent onshore in segments of 100 ms, where a 10 Gigabit Ethernet (GbE) bandwidth network infrastructure routes the incoming traffic to the computing farm. All hits with a signal above the PMT threshold of 0.3 p.e. are denoted as *level-zero* (L0) hits. This constitutes the most basic trigger and is the only trigger that refers to uncalibrated and unfiltered hits as detected offshore by DOMs.

The logic of the KM3NeT DAQ is presented in Fig. 5.1. In the offshore computing farm, the first stage of data processing consists of collecting unfiltered data through a software named *DataQueue* (DQ). Then, these data are distributed to the *DataFilter* (DF) software, which applies different trigger algorithms to identify candidate events due to high-energy neutrino interactions occurring inside or in the vicinity of the detector. Different levels of trigger are implemented:

- *Level-one* trigger (L1) refers to a collection of two or more L0 hits from different PMTs on the same DOM, within a fixed time window centred around the first triggered hit (the typical configuration uses $\Delta t = 25$ ns). The spread of Δt is determined by the possible delays occurring in the photon propagation in water, caused for example by scattering (see Sect. 2.2.2), giving typically time delays of about 10 ns. This trigger limits the accidental correlations of hits and reduces the background due to bioluminescence and ^{40}K decays (see Sect. 2.2.3).

- *Level-two* trigger (L2) is the combination of more complex conditions on L1 hits from different DOMs, taking advantage of the knowledge of the orientation of the PMTs within the DOM itself, reducing the data rate by a factor of two.

The idea behind the trigger algorithms is that events produce cluster of hits separated in time by light propagation in water, while background is uncorrelated. Hits related to the same cluster have to satisfy the following condition:

$$|\Delta t| < \frac{|\Delta r|}{c/n} + T_{\text{extra}}, \tag{5.1}$$

where Δt and Δr are the time and distance differences, respectively, between two hits within a possible cluster, the factor c/n is the speed of the light in water, and T_{extra} is the additional factor that accounts for the time delay, above mentioned, related to uncertainties on photon propagation. The condition in Eq. (5.1) can be applied also on DOMs to have an idea of the propagation time of the light produced by an ultrarelativic muon in our detector: by considering the vertical spacing of the DOMs in KM3NeT/ARCA of 36 m and $T_{\text{extra}} = 10$ ns, one finds $\Delta t \lesssim 170$ ns for adjacent DOMs and $\Delta t \lesssim 330$ ns for next-to-adjacent DOMs. It is worth also noticing that an ultrarelativistic muon is able to traverse the whole detector volume: the muon track length is about 4 km if the neutrino that generates it via CC interaction in seawater is characterised by an energy of 1 TeV. To pass through the instrumented detector volume, it takes $\sim 4(6)$ μs for KM3NeT/ARCA21(1BB). Trigger requirements need to be adapted to such statements. Refer to Sect. 2.1.3 for the treatment of the particle propagation in seawater, in particular that of muons.

Each L0 hit that satisfies one of the L1 trigger conditions is marked as *triggered hit*. Starting from these definitions, three main types of data are produced as output of DF:

- *Triggered events* (`EVT` or `IO_EVT`): a triggered event contains information on the set of causally connected triggered hits. The triggered hits are stored in a so-called *snapshot* together with all background hits recorded in a certain time interval that extends before and after the triggered hits.

- *Timeslice data* (`TS` or `IO_TS`): hit data collected from all DOMs in a time interval of 100 ms and selected according to coincidence criteria based on hit time difference, number of PMTs participating in coincidence (*multiplicity*), and angular separation between PMTs. Several types of timeslice are produced according to difference selections, each dedicated to specific analysis purposes. For example, the supernova timeslices (`IO_TSSN`), characterised by at least four hit PMTs in a DOM whose axes are within 90 degrees in a time window of 15 ns, are dedicated to supernova searches; L1 timeslices (`IO_TSL1`) contain all hits in coincidence within 25 ns time windows and are produced for detector calibration[2].

- *Summaryslice data* (`SUM` or `IO_SUM`): individual PMT rates, derived from the raw hit data and averaged over the corresponding 100 ms of a timeslice, and status information for each PMT channels. These are generally used to monitor the quality of the data and are auxiliary to calibration.

Specific muon track and shower triggers also exist to identify different physical signatures:

2 L1 timeslices can also be used for astrophysical follow-ups; those are temporarily stored on a local storage space and dumped on request (see [395] for more details).

- **3DShower**: cascade trigger that assumes that all light is emitted isotropically from the neutrino interaction vertex and looks for causally connected L1s on DOMs separated by a maximum distance (e.g., for KM3NeT/ARCA21, 5 L1s on 5 different DOMs within a sphere of diameter of 250 m are set);

- **3DMuon**: muon track trigger consisting of a scan around the visible sky, which is combined with an assumed directional filter for the muon track. In this case, only PMTs within distances from the track that are smaller than a few times the absorption length of the water are taken into account (e.g., for KM3NeT/ARCA21, at least 5 L1 hits on 5 DOMs with a maximum distance of ~ 820 m and within a cylinder with radius of 120 m and centered on the track direction). In this filter, scans over 200 uniformly distributed track directions are performed, each time in a portion of the sky of $10°$;

- **MXShower**: trigger that uses a mixture of L0 and L1, in order to lower the threshold and include events that do not feature the minimum of causally connected L1 hits required by the cascade trigger.

The parameters used by the different triggers can be adapted to cope with varying ambient conditions and detector configurations. After filtering and triggering operations, the DFs send their output to the DAQ dispatcher. At this point, there are different possibilities: for offline analyses, the received data is sent to the *DataWriter* (DW) application and written on disk; meanwhile, for online purposes, the outputs of DF are directly taken and managed, namely these are sent as input to the real-time reconstruction and classification software framework, presented in the next Sect. 5.2.

5.2 REAL-TIME ANALYSIS FRAMEWORK

Real-time multimessenger and multiwavelength campaigns, through which information coming from different instruments are combined (from radio to γ-rays, GWs, and neutrinos) could prove crucial in unveiling the sources of the most energetic particles and the acceleration mechanisms at work. In particular, as widely discussed in this thesis, neutrinos would provide insight into the physics of stellar explosions, compact object mergers, and relativistic jets, as well as particle acceleration processes. The main requirement for these multimessenger studies is the quasi-online communication of potentially interesting observations to partner instruments through the so-called *alerts*, with latencies of a few minutes, at most. Such alerts are the only way to achieve simultaneous observations of transient phenomena by pointing instruments (see Sect. 1.6.2 for an introductory description of the real-time observational strategy between different observatories).

The KM3NeT Collaboration aims at becoming a pioneer in this kind of activities and is developing a complex analysis framework for real-time multimessenger studies. In the following, I first describe the general architecture in place for the KM3NeT online system (see Sect. 5.2.1), and then I focus on the real-time processing pipeline used to manage KM3NeT/ARCA DAQ events (see Sect. 5.2.2).

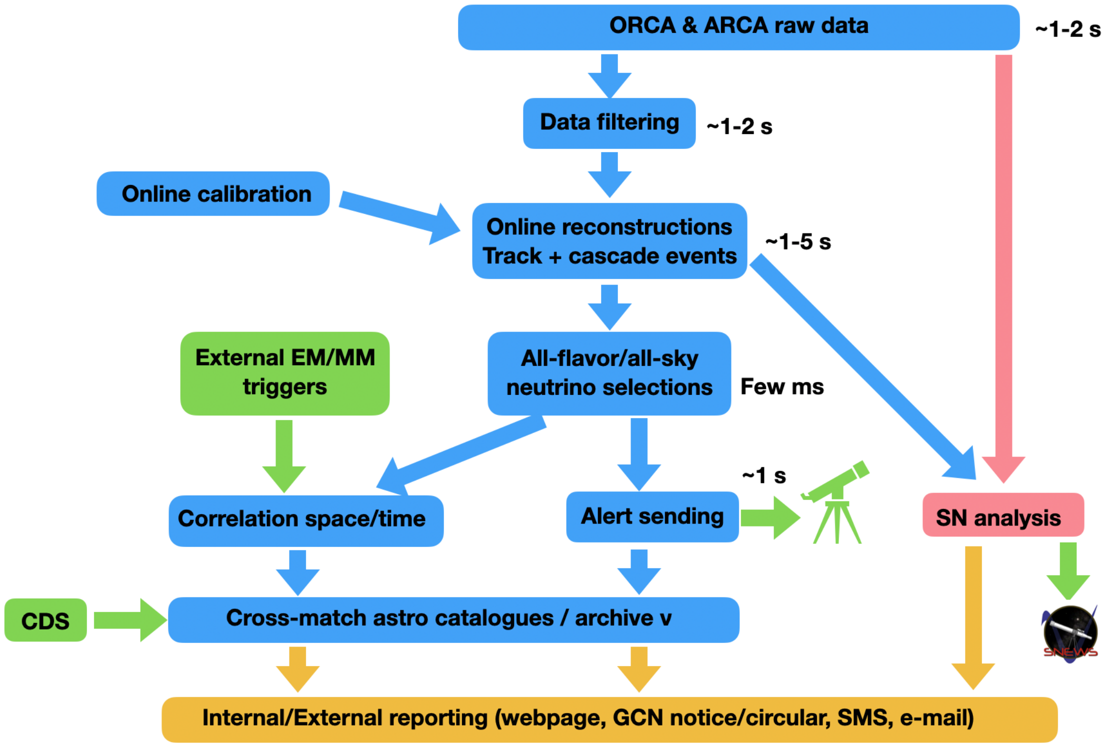

Figure 5.2: Main components of the KM3NeT real-time analysis framework. Triggered events are reconstructed and classified as muon/neutrino and track/shower. Afterwards, if interesting neutrino candidates are selected and identified, neutrino alerts are sent to external communities for subsequent follow-ups. On the other hand, also follow-ups of external electromagnetic/multimessenger triggers are performed, as well as time/-space correlation searches with catalogs of the astronomical objects outside the solar system, available through the Strasbourg astronomical Data Center (CDS) [396]. Internal or external (for private and public alerts) reporting tools are used, mainly the Gamma-ray Coordinate Network (GCN, `https://gcn.gsfc.nasa.gov`) and the Astronomer TELegram (ATEL, `https://astronomerstelegram.org`). The SN quasi-online astronomy analysis is in place and KM3NeT is integrated into the SNEWS 2.0 global alert systems (`https://snews.bnl.gov`) [397, 398]. The maximum times we consider acceptable to allow a fast online data processing are also indicated for each step from the DAQ level to the alert sending.

5.2.1 *Online architecture overview*

The logical structure of this online system is outlined in Fig. 5.2: raw data from the DAQ are analysed, following the flow already described in Fig. 5.1, and different packages of data (see Sect. 5.1.1) are propagated into the multimessenger system that aims to

- Process triggered events with the track and cascade reconstruction algorithms (these are described in Appendix A);
- Select in real time a sample of particularly interesting neutrino candidates out of the large background of atmospheric muons (and bundles of muons) to send rapid public/private alerts to external telescopes for the most interesting ones in order to allow subsequent real-time follow-ups of high-energy neutrino alerts;

- At the same time, receive and filter triggers from the external community (LIGO/VIRGO gravitational alerts, IceCube neutrino triggers, others X-ray/gamma-ray transients), quickly search for temporal and spatial coincidences between high-energy neutrinos and these alerts, and finally provide the results;

- Perform offline time/space correlation searches with archival astrophysical catalogues for several sources such as GRBs, AGNs, SNe, etc.

Several methods for reporting the analysis results and advertising the astronomy community in case of interesting neutrino events occurring in our detector are adopted: for public alerts, the most widely used are the Gamma-ray Coordinate Network (GCN, https://gcn.gsfc.nasa.gov) and the Astronomer Telegram (ATel, https://astronomerstelegram.org); on the other hand, for private alerts, specifics programmes are also established with external collaborations. Note that, at the time of writing, the event reconstruction and the analysis of external alerts are in quite advanced status, whereas the neutrino selections and the online alert distributions are still being defined. In addition, the online analysis uses an ideal static detector for the event reconstruction; in other words, it does not include the knowledge of the dynamical positioning and the precise charge and time calibration sets, which are typically made available a few weeks later for the offline analysis. However, it is well known that in periods of high sea current, the detector angular resolution and the overall performances degrade. Since a real-time positioning of the detector strings could solve this problem, an important task for the future is to use in quasi-real time a calibration set with compatible precision to the one computed offline (especially for time and positioning calibrations).

Another pillar activity carried out within the framework of the KM3NeT online system consists of the real time Core-Collapse SuperNovae (CCSN) analysis. Although KM3NeT detectors are mainly designed for high-energy neutrino detection, KM3NeT is capable of detecting the neutrino burst from a Galactic or near-Galactic Core-Collapse SuperNova (CCSN) thanks to the multi-PMTs design of DOMs: in particular, the MeV-scale neutrino signal from a CCSN can be identified as a simultaneous increase of the counting rate in the PMTs of the detector. The real-time implementation of the supernova neutrino search operates on the two KM3NeT detectors since the first months of 2019; a quasi-online astronomy analysis is performed to study the time profile of the detected neutrinos for especially significant events. The mechanism for generating and distributing alerts is in place and, additionally, KM3NeT is integrated into the global SuperNova Early Warning System (SNEWS) [397, 398][3].

To summarise, thanks to the combination of the KM3NeT/ORCA and KM3NeT/ARCA detectors, the online system of KM3NeT aims to catch neutrinos in real time in an extended

3 The SNEWS project involves an international collaboration between several current supernova-neutrino-sensitive detectors. The goal of SNEWS is to provide the astronomical community with a prompt alert of the occurrence of a Galactic core-collapse event: if several detectors report a potential supernova within a small time window, SNEWS will issue an alert to its subscribers. No nearby core collapses have occurred since SNEWS started running in 2005, but the system is ready for the next one. This argument is beyond the scope of this thesis; the reader can refer to, e.g., [395], for a detailed description of both the implementation and first results of the KM3NeT real-time CCSN neutrino search.

energy range, i.e. from the MeV-scale (neutrinos from CCSNe) to astrophysical neutrinos up to a few PeV.

5.2.2 *KM3NeT/ARCA software architecture*

The software architecture developed to manage the data flow in the KM3NeT/ARCA detector and to reconstruct in real time each of the triggered events is presented here. The first stage of the pipeline is the so-called *Real Time Analysis* (RTA) framework located at the detector shore station, directly connected to the corresponding DAQ system. At this level, the aim is to reconstruct each triggered event (`IO_EVT`) either as a track or as a shower and, thereafter, to estimate which of the two is the event topology that most likely describes the event. This thesis deals with online track reconstruction algorithms, as the shower reconstruction step and the classification process as track/shower and signal/background are both currently work in progress at the time of writing. Therefore, their description is not included here.

After being developed and installed at the KM3NeT/ARCA shore station, the set of software currently in place was made operational on real data in December 2020, when only 6 DUs were taking data. From then on, the real-time reconstruction of events has been continuously working and has been adapted every once new DUs were deployed and the detector size has increased. At the time of writing, KM3NeT/ARCA is taking data with 21 DUs (the footprint and three-dimensional view of the current detector are shown in Fig. 5.3). Note that for KM3NeT/ORCA, which is not the subject of this thesis, the online software framework is characterised by the same steps as in KM3NeT/ARCA, even if they are implemented with a different approach: indeed, for the high-energy detector KM3NeT/ARCA, the Docker architecture[4] is used [399].

As first step, DAQ events are collected from the DAQ dispatcher and sent to a multitasking operative system, dedicated exclusively to online activities, and placed at the KM3NeT/ARCA shore station (namely, the RTA dispatcher). In fact, to avoid perturbing the standard DAQ system, the online pipeline is installed on a different computer. Then, these events are given as input to the reconstruction software that, under the hypothesis that each `IO_EVT` come from a muon track generated by a neutrino interaction with quarks in seawater, estimate the direction and the energy of each events in fractions of a second.

4 Docker is an open source software development platform that allows one to package applications inside *containers*, which are lightweight, standalone, executable software packages that include all what is needed to run an application: code, runtime, system tools, system libraries, and settings. An important advantage given by the usage of docker containers is the easy reproducibility and scalability to other computer machines. Docker containers can be run and transported in any environment without changes. Once configured for the first time, they are fastly ready-to-use. This constitutes a very efficient, easy, and fast way of working with various applications. The Docker architecture is quite simple. The developer can build a container *image* writing a so-called Dockerfile, with all the instructions for the installation of the software needed to execute a given command in that container. Several containers related to each other can be run together, as needed in the case here described, through the Docker Compose tool is used, which allows us to create a multi-container workflow. Without the usage of Docker containers and the Docker Compose tool, the installation of all the software needed for online data processing on the KM3NeT/ARCA shore station would be rather cumbersome, particularly for what concerns the scalability of the system, constantly increasing in DUs and data outputs.

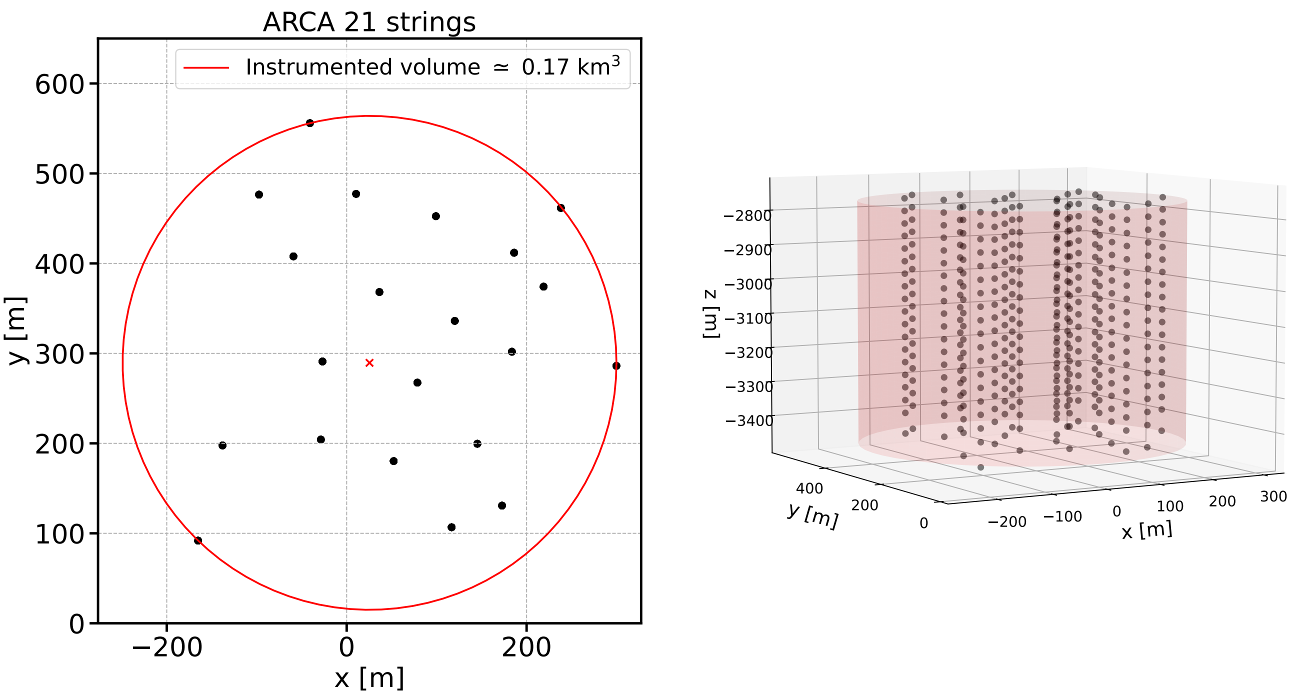

Figure 5.3: Footprint showing the DU positions (black circles) of the KM3NeT/ARCA detector at the time of writing (21 DUs operational). The panels at left and right shows the top- and the three-dimensional view of the detector, respectively, where the instrumented volume, amounting to $0.17 km^3$, is outlined by the red circle and cylinder.

Moreover, the reconstruction algorithm returns a certain quality of the reconstruction that help us in recognising reliable muon tracks that can be used at analysis level, as it will be shown further. In view of a real-time event reconstruction and a forthcoming triggering of the alert-sending system in the case of an interesting event (astrophysical origin), these steps have to be performed as fast as possible, avoiding the accumulation of delays between the trigger time and the moment their reconstruction starts. For this reason, even the reconstruction itself is executed through multi-processes, to handle the incoming rate of events into the detector; otherwise, `IO_EVT` would get stacked in queue for a long time waiting for being reconstructed. This is crucial for fastly sending alerts to the whole multiwavelength/multimessenger community and allows observations by different detectors. The schematic diagram of the online system is provided in Fig. 5.4, in which the several software currently in use is called upon. These are presented in the following:

- `Jpp`: a Java inspired set of C++ interfaces, classes and methods developed within the KM3NeT project and extensively adopted for several purposes, e.g., in the data acquisition system, offline triggering, calibration of the data sent to shore, and event reconstruction. Each `Jpp` application is indicated by the letter 'J' at the beginning of its name;
- `Harmonia`: dispatcher for online processing of events developed within the KM3NeT project;

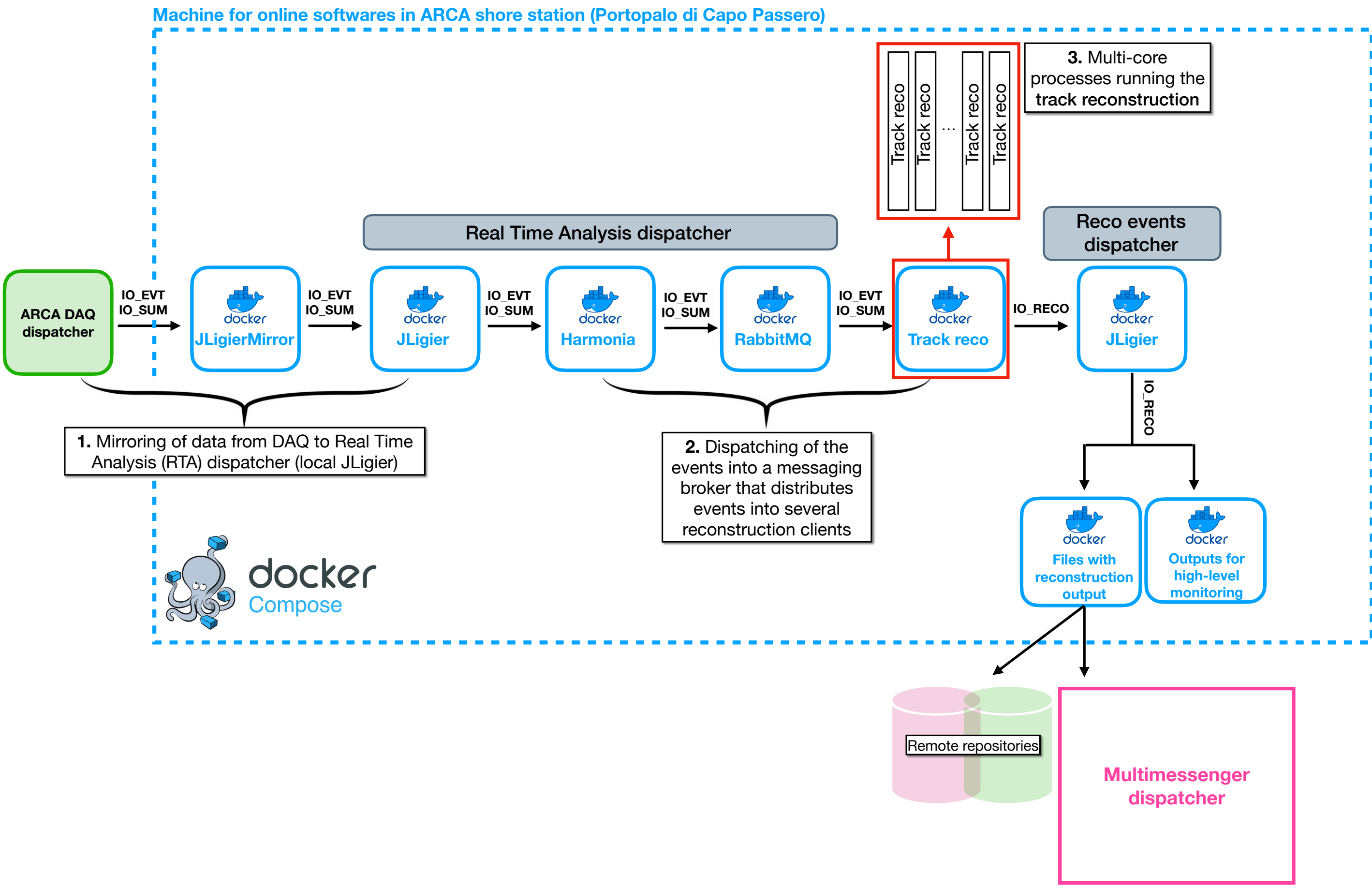

Figure 5.4: Real-time analysis framework in place in ARCA shore station. Multi-container applications (each Docker container is represented by a cyan box), are run simultaneously through the Docker Compose tool. `IO_EVT`, `IO_SUM` and `IO_RECO` tags indicate triggered events, summaryslices and events reconstructed as tracks by the reconstruction software, respectively.

- `RabbitMQ`: open source messaging broker [400]. It manages the communication with `Harmonia`, from which online events are received, and distributes them to a certain number of C++ clients where the reconstruction algorithms run.

In addition to some ready-to-use software, such as those mentioned above, specific C++ and Python applications have been developed in the online framework, being devoted to produce different reconstruction outputs.

Taking as reference Fig. 5.4, events (with tags `IO_EVT` and `IO_SUM`) are mirrored (through the `JLigierMirror` application) by the DAQ dispatcher to the RTA dispatcher, namely, a local `JLigier`. The messages received by the `JLigier` are then distributed by the `Harmonia` software to a messaging broker (`RabbitMQ`) that correctly manages the rate of incoming events and allocates them into a number N of reconstruction clients running inside a specific Docker container. After being reconstructed, the events are characterised by the tag `IO_RECO`[5] and are sent to another local dispatcher (`JLigier`), which works at this level

5 Tags `IO_SCORE`$_1$ and `IO_SCORE`$_2$ will identify events after the further processing through online classification algorithms (discriminating between track/shower-like events, and muons/neutrinos.).

as a listener of the reconstruction clients. The reconstructed events are then transferred to containers aimed at producing different types of output (i.e. files in root/json formats and plots) for storage and monitoring purposes. Temporary storage occurs in the common Multi-Messenger (MM) dispatcher, while permanent storage is realised in back copies to CC-Lyon[6] and CNAF-Bologna[7] computing centers. These output files are used, indeed, by different tools, either the ones hosted there to monitor the online event reconstruction processes, as well as to run analysis pipelines to automatically analyse events in case of interesting neutrino-induced events in our detector and/or external triggers by the multimessenger community. The common dispatcher hosts also other services (event storage, internal/external reporting), the SN final processes [395] (SN trigger, SN alert and SNEWS sender [397]), and the neutrino alert sending module, the latter being under development and not yet ready to be used.

5.2.3 *Online track event reconstruction*

The extensive set of available Jpp applications is used for fast track reconstruction of events in real time. The same reconstruction algorithms as those adopted in offline analyses are used here, which are based on maximum-likelihood methods. However, the code design for these algorithms has been modified in order to be compliant with the event-by-event analysis required by the online system. In particular, the online reconstruction of the neutrino interaction vertex position and energy values for track events has been developed for the first time in the context of this thesis. The results of such reconstruction steps will be shown in Sect. 5.3.1.

The muon direction is reconstructed from the sequence of Cherenkov photon hits on the PMTs, profiting from the fact that photons are emitted along the particle track at a Cherenkov angle of about 42° (see Sect. 2.1.1). A suitable set of start values for the trajectory fit is obtained with a pre-fit scanning the full solid angle. For each prefit, the track is then reconstructed by maximising a likelihood derived from a probability density function depending on the position and orientation of the PMTs with respect to the muon trajectory and on the hit times. Among these intermediate tracks, the one with the best reconstruction quality is chosen, the latter being expressed through a parameter called *lik*. The energy is reconstructed from the spatial distribution of hit and non-hit likelihood for all PMTs in a cylindrical volume surrounding the track hypothesis. More details about the track reconstruction algorithms adopted are provided in Appendix B.

5.3 VALIDATION OF THE ONLINE RECONSTRUCTION PIPELINE

In this section, the performances of the event track reconstruction system are outlined. This is shown both for events reconstructed in real time with the detector configuration active at the moment of writing (Sect. 5.3.1), and for the future KM3NeT/ARCA 1BB (namely,

6 https://cc.in2p3.fr/en/.
7 https://www.cnaf.infn.it/en/.

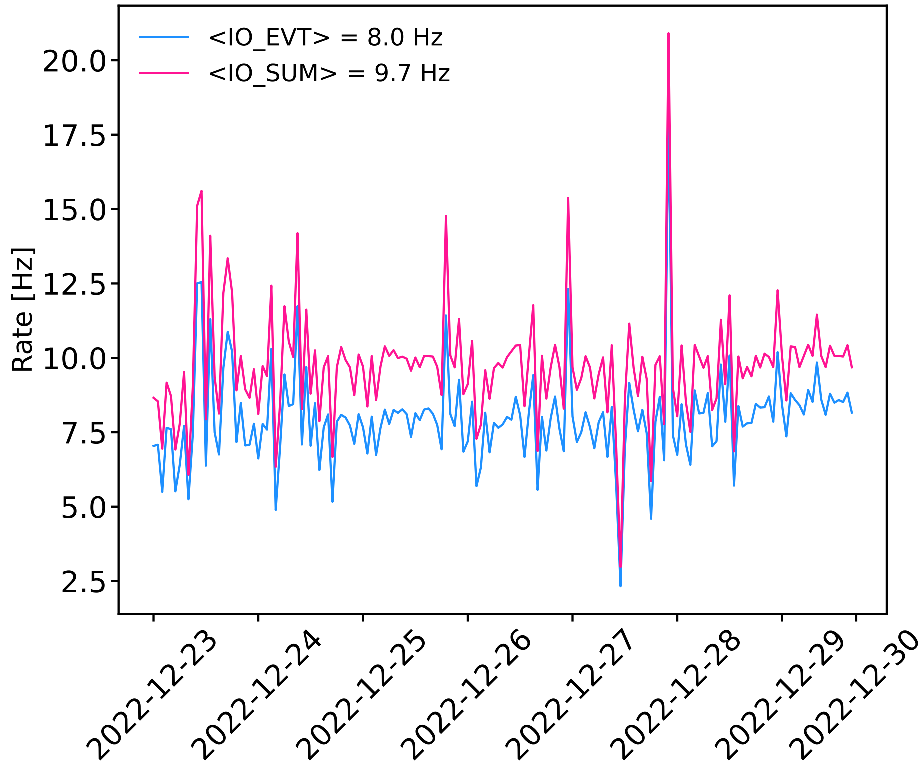

Figure 5.5: Rate of triggered events (IO_EVT) and summaryslices (IO_SUM) incoming into the KM3NeT/ARCA RTA dispatcher over seven days of continous data taking, between the last 23rd and the 30th of December. Data is showed considering average values in time windows of 3 hours. The visible fluctuations are related to some trigger instabilities occasionally affecting the detector (e.g., at the run stop and start, or during changes or tests of the DAQ trigger system).

115 active DUs), in the latter case simulating a flow of PeV neutrino events to study the response of the detector at the occurrence of such very-high-energy events (Sect. 5.3.2). In such a way, it is possible to investigate the time taken by the online pipeline to reconstruct events induced by PeV neutrinos. This information is crucial to ensure a proper working of the online system and a smooth prosecution of its activity even in the presence of extremely energetic events.

5.3.1 *Analysis of real-time events from KM3NeT/ARCA 21 strings configuration*

At the time of writing, 21 strings are in data taking at the ARCA site; as such, an average rate of triggered events (IO_EVT) and summaryslices (IO_SUM) of about 8 Hz and 10 Hz, respectively, is observed to income in the online system of KM3NeT/ARCA (see Fig. 5.5). This rate of IO_EVT is distributed to 30 C++ reconstruction clients; this number is at present sufficient to guarantee fast event processing avoiding overloading the computing infrastructure. Still, resources at the shore station would allow us to increase the number of operating clients, when for example the incoming event rates will grow because of the future detector deployments or if algorithms for shower reconstruction will require running in parallel to the track reconstruction. The total rate of IO_SUM is sent

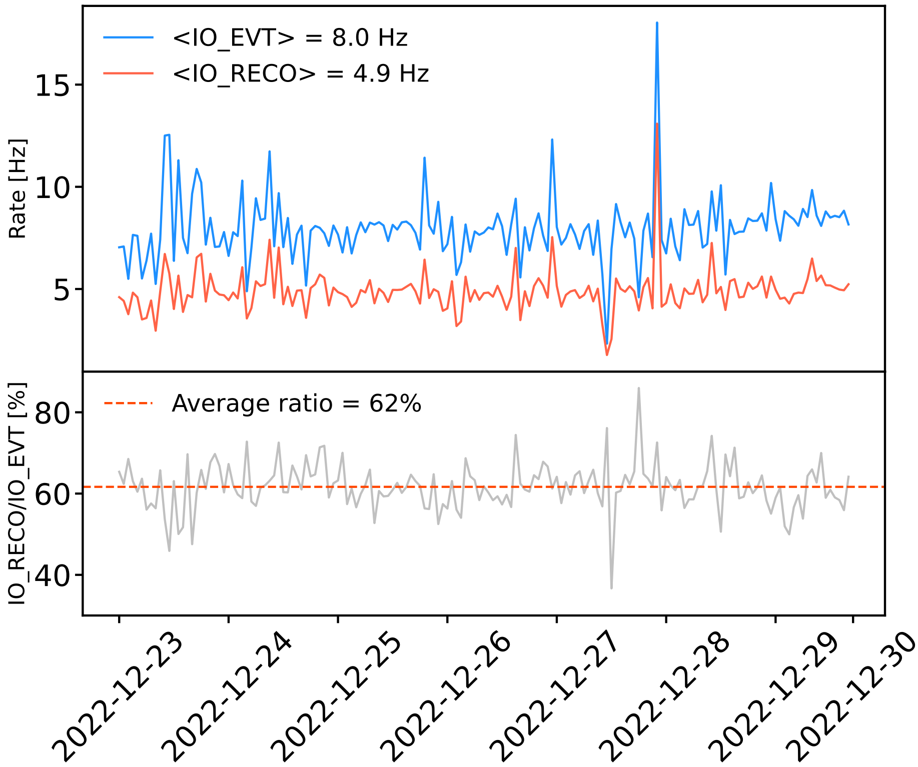

Figure 5.6: Upper panel: rate of triggered events (IO_EVT) incoming into the KM3NeT/ARCA RTA dispatcher and corresponding reconstructed event (IO_RECO) rate. Lower panel: Ratio between IO_EVT and IO_RECO. These data refer to the same data stream and time window as the one shown in Fig. 5.6.

to each reconstruction process. In fact, before performing the track reconstruction of an event, the system tries to find the corresponding summaryslice, as to use tailored information about the detector at the time of the event; in fact, since IO_SUM contain individual PMT rates and status information for each PMT channel, they may, in principle, improve the quality of the reconstruction. However, by investigating the reconstruction output in KM3NeT/ARCA for the same IO_EVT reconstructed either with or without the corresponding IO_SUM, it has been found that the usage of information from summaryslices does not induce any significant improvement in the quality of the reconstruction, neither in direction nor in energy. Despite this fact, the online data flow is still implemented to distribute the IO_SUM to individual reconstruction clients, mostly because summaryslices contain useful information for a real-time monitoring of the event data quality; in addition, the search for the association between IO_EVT and IO_SUM is not particularly time consuming, as will be shown further in the section.

For each reconstructed IO_EVT, only events with quality returned by the reconstruction algorithms (*lik*) greater than 0 (i.e., physically meaning events) are tagged as IO_RECO and transferred to subsequent steps in the online data flow represented in Fig. 5.4. These events constitute $\sim 60\%$ of the total rate of incoming triggered events (see Fig. 5.6). For the reasons already explained, it is crucial that the total amount of IO_RECO arrive at the final process in the shortest possible time, to be able to send alerts to the whole multimessenger community as fast as possible, allowing a prompt reaction by CR, GW, and γ-ray instru-

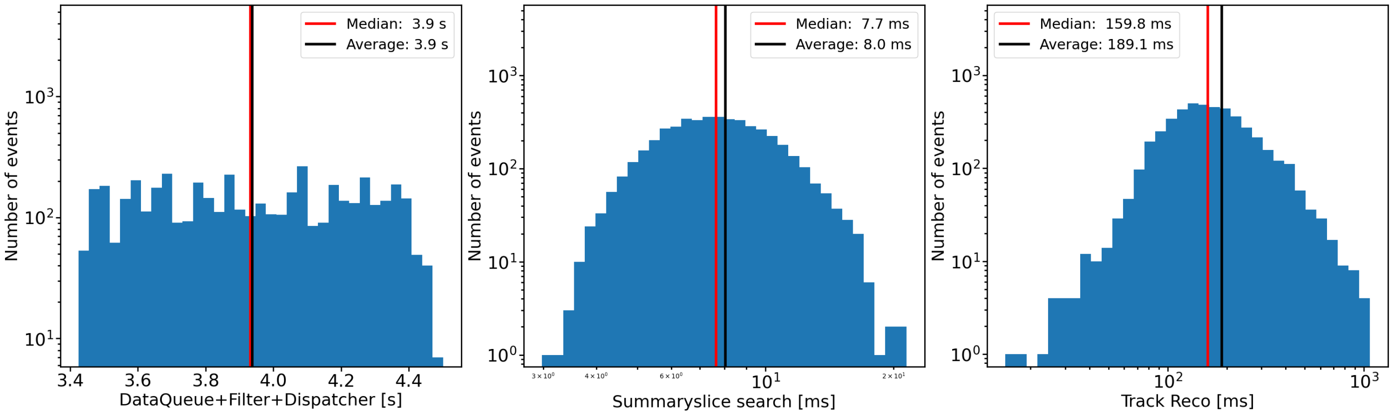

Figure 5.7: Distribution of online processing time values for events collected in 15 minutes of KM3NeT/ARCA data taking with 21 strings. From left to right are shown: (i) the time for an `IO_EVT` to be processed in DQ, filtered through DF and finally sent to DAQ dispatcher; (ii) the time needed for searching the `IO_SUM` corresponding to each `IO_EVT`; and (iii) the track reconstruction time for each `IO_EVT`. The median and average values are indicated by the red and black lines, respectively.

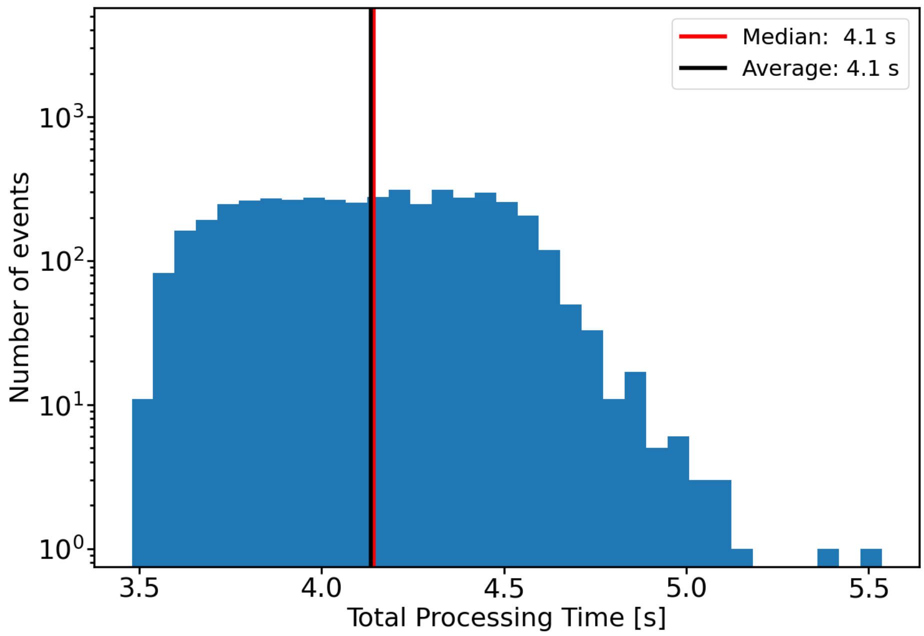

Figure 5.8: Distribution of the total online processing time values for events collected in 15 minutes of KM3NeT/ARCA data taking with 21 strings. This distribution refers to the same events as those in Fig. 5.7 The median and average values are indicated by the red and black lines, respectively.

ments, as well as other operative neutrino facilities. In addition to the time taken by the reconstruction process, there is also an internal timeout in the DQ and DF processes, that is not in our side, but that is constantly monitored. In fact, the DQ has an internal timeout (now set to 4 seconds for KM3NeT/ARCA) during which it waits for the data packets coming from all the DOMs; once this timeout is reached, it sends the frames to the DF. So, when `IO_EVT` and `IO_SUM` are mirrored from the DAQ to the RTA dispatcher, essentially frames containing data triggered during the 4 seconds before are mirrored. In light of this, if the online system is properly working and no trigger instabilities are affecting the detec-

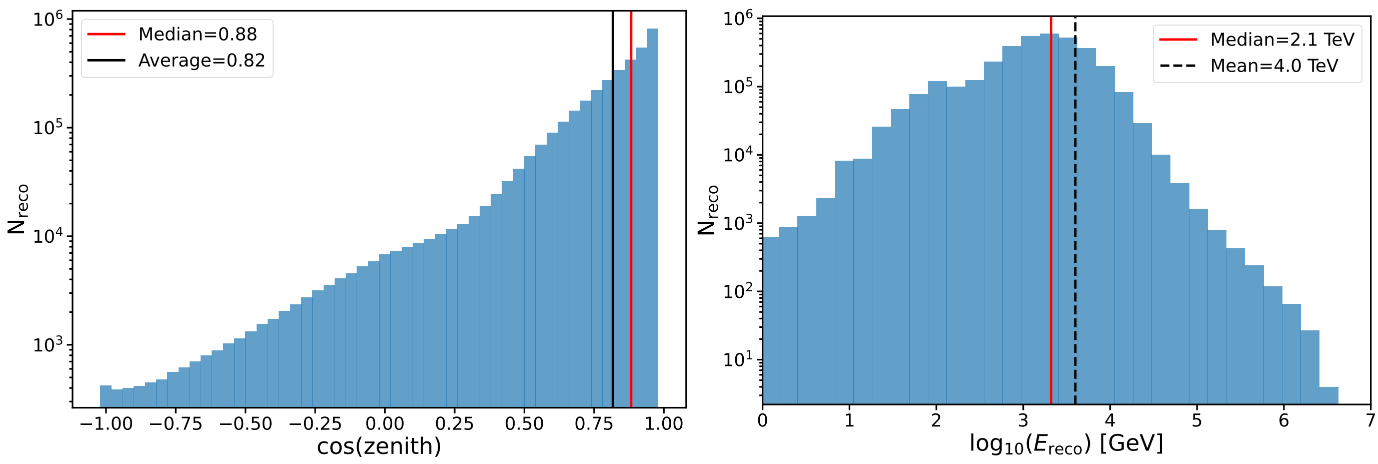

(a) (b)

Figure 5.9: Distribution of the cosine of the zenith angle (a) and energy (b) for $N_{reco} \simeq 3.5 \times 10^6$ events reconstructed in ~ 8.5 days of stable data acquisition. The median and average values are indicated by the red and black lines, respectively.

tor, on average each event is ready to be reconstructed after ∼4 seconds. The total online processing time for events reconstructed in real-time include:

1. The time for an `IO_EVT` to be processed in DQ, filtered through DF and finally sent to the DAQ dispatcher;
2. The time needed to find `IO_SUM` corresponding to each `IO_EVT`;
3. The reconstruction time for each `IO_EVT` (track direction and energy).

These are singularly shown, from left to right, in Fig. 5.7, and are characterised by median values of 3.9 s, ∼8 ms, and ∼160 ms[8], respectively. By summing the contribution of all these times, the corresponding total online processing time is shown in Fig. 5.8. In other words, the current KM3NeT/ARCA detector is able to provide the evaluation of both direction and energy of each reconstructed event on average after 4 seconds from its detection.

Most of the events reconstructed in real-time are downgoing ($\sim 99\%$) and their energy is evaluated to have a median(average) value of $\sim 2(4)$ TeV, as shown in Fig. 5.9(a) and Fig. 5.9(b), representing, respectively, the distribution of the cosine of the zenith angle and of the energy values for 3.5×10^6 `IO_EVT` reconstructed as tracks by the online algorithms (the number of entries corresponds to about ~ 8.5 days of data taking). Regarding the energy, it is important to clarify that, as discussed in Appendix C for the KM3NeT/ARCA detector in the 6 strings configuration, the reconstruction algorithms typically overestimate(underestimate) the energy of the initial muon(neutrino) interacting in water and that produces the observed track. It is therefore expected that the energy values returned by our reconstruction algorithms, E_{reco}, deviate from the true values; in principle, E_{reco} should be shifted by a factor that is both particle- and detector-dependent and that, for these reasons, is obtained as a result of a dedicated study. At the time of writing, the energy correction is

8 ∼100 ms to reconstruct the track direction and ∼50 ms for the energy reconstruction.

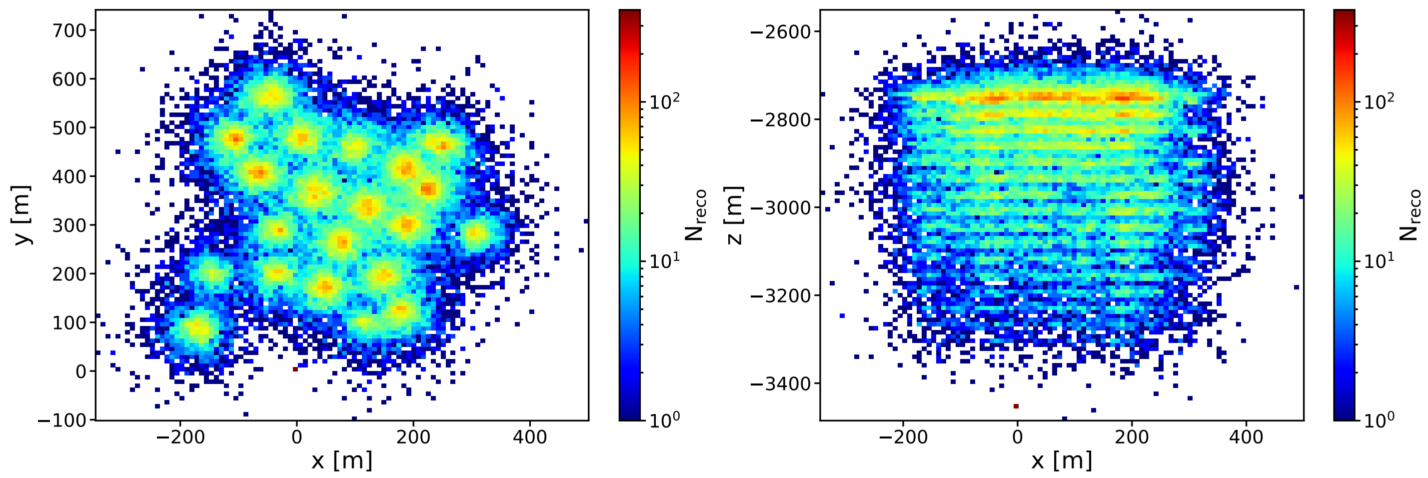

(a)

(b)

Figure 5.10: Two-dimensional histograms showing in the y-x plane (a) and z-x plane (b) the coordinates of vertices reconstructed by the online pipeline for $\sim 5 \times 10^4$ `IO_EVT` in one run of data acquisition (lasting 3 hours).

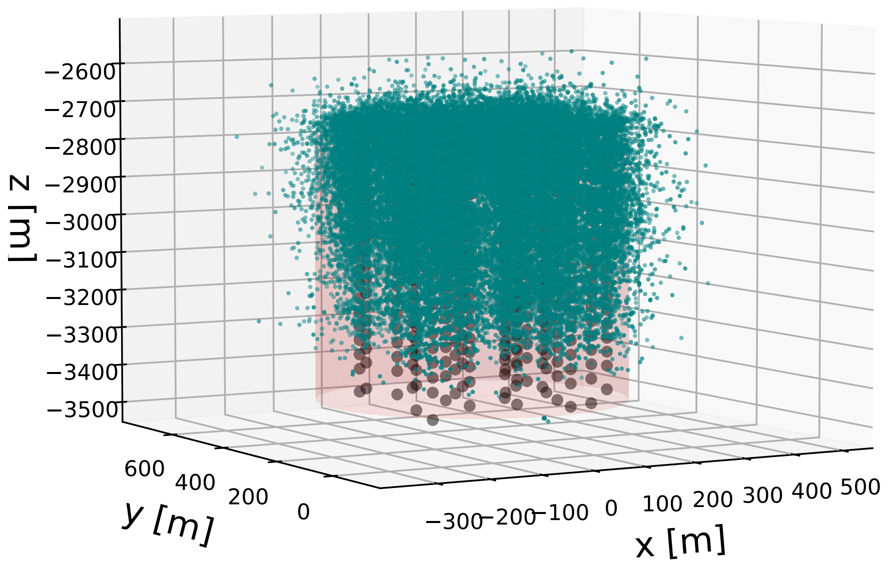

Figure 5.11: Three-dimensional plot with the footprint of the KM3NeT/ARCA21 detector (the same as that of Fig. 5.3) overlapped with the coordinates of vertices (teal points) reconstructed for the same sample as that of Fig. 5.10.

not taken into account in online reconstructions; instead, it is possibly included in offline analyses dedicated to follow-up studies (e.g., this is the case of the KM3NeT search for neutrinos in coincidence with the blazar PKS 0735+17; see Sect. C.3) and/or to interesting neutrino events identified in our detector. The dominance of events coming from the downgoing sky is also evident in Fig. 5.10, which shows the vertex positions returned by online algorithms for $\sim 5 \times 10^4$ events reconstructed as tracks in ~ 3 hours of data taking (corresponding to one run of data taking): most of the muon track vertices accumulate at the top of the strings, namely in the upper part of the detector. The same vertices are also shown in Fig. 5.11, where these are overlapped with the three-dimensional footprint of the

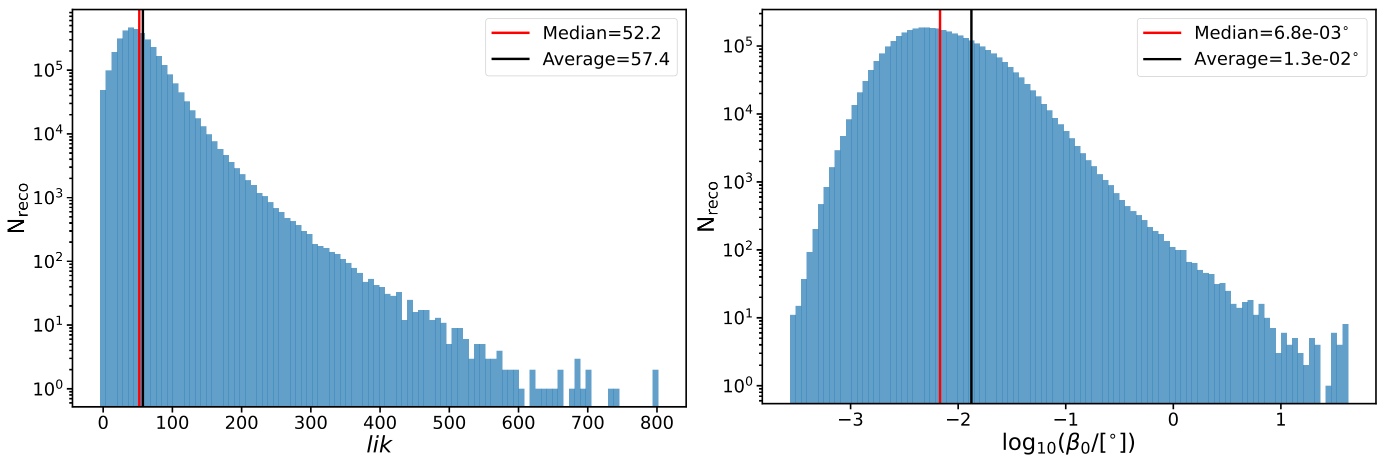

Figure 5.12: *lik* (a) and $\log_{10}(\beta_0)$ (b) distributions for $N_{\text{reco}} \simeq 3.5 \times 10^6$ events reconstructed in ~ 8.5 days of stable data acquisition. The median and average values are indicated by the red and black lines, respectively.

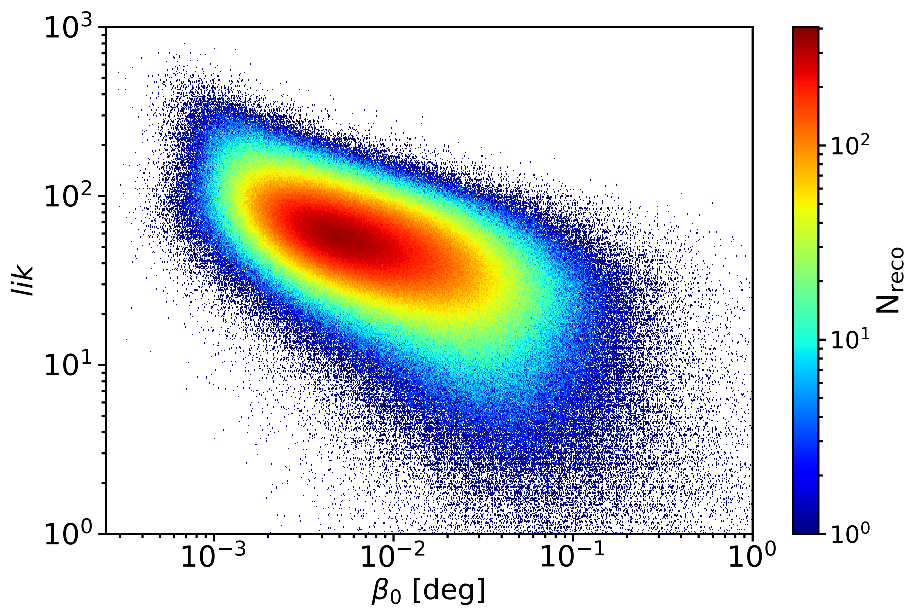

Figure 5.13: Two-dimensional histogram showing the relationship between *lik* and β_0. The colorbar shows the number of reconstructed events in the sample considered, namely $\sim 3.5 \times 10^6$ `IO_EVT` in ∼8.5 days of data taking (the same sample as in Fig. 5.12).

KM3NeT/ARCA21 detector. A considerable fraction of such reconstructed events in real time come from atmospheric muons and neutrinos, characterised by event rates several orders of magnitude higher than astrophysical neutrino events. Indeed, theoretical expectations on neutrino fluxes from astrophysical sources combined with neutrino cross sections and interaction probabilities, suggest that with a detection area of ~ 1 km^2 the number of astrophysical neutrino events is of the order of some events per year. On the other hand, as regards the atmospheric background, even at the depth in which KM3NeT/ARCA is located, the atmospheric muon flux is about 10^6 times larger than that of muons induced by atmospheric neutrinos. Thereby, it is important to identify some cuts in reconstruction outputs that help to reduce atmospheric background contamination, such to allow the tiny signal of astrophysical neutrinos to emerge. For example, only upgoing events (i.e., negative values for the cosine of the zenith angle) can be selected to remove the atmospheric muon contamination (muons are absorbed within a path of about 50 km of water, and they are not able to travese the entire Earth diameter). However, even upgoing events suffer from background due to misreconstructed downgoing events; to account for this effect, the selection on only well-reconstructed tracks is usually applied.

As already anticipated in Sect. 5.2.3 and better explained in Sect. B.2, the reconstruction algorithms return the best fit among several track hypothesis, through a minimisation procedure of a maximum-likelihood test statistic. The quality of such a reconstruction is identified by the *lik* parameter: the higher the lik, the better the track fit. Fig. 5.12(a) shows the *lik* distribution for the sample considered, peaking at $lik \sim 50$. Another important parameter for the directional reconstruction is the uncertainty on the direction provided, β_0, whose distribution is shown in Fig. 5.12(b): the online reconstruction algorithm currently in place estimates the direction of muon tracks in median(average) with an uncertainty of $\sim 7 \times 10^{-3}(\sim 1 \times 10^{-2})$ degrees. Furthermore, the smaller β_0, the better the quality of the reconstruction (see Fig. 5.13).

Fig. 5.14 shows information at trigger level about the sample considered here. Without any selection (namely, if no cuts are applied on reconstruction output variables), the majority of the events triggers 21 PMTs, 6 DOMs and 2 DUs (see Fig. 5.14(a), Fig. 5.14(c) and Fig. 5.14(e), respectively). However, despite discarding events with negative *lik* from the final sample of `IO_RECO` (let remember that this occurs in the $\sim 40\%$ of the cases; see Fig. 5.6), part of the sample of `IO_RECO` is polluted by events characterised by other reconstructed parameters without physical meaning, i.e., null track length L_μ. The latter case constitutes $\sim 1.6\%$ of the events and, in median, ~ 20 hits are triggered on PMTs. I found that when the length of the track is not estimated, the number of triggered hits and DOMs used for reconstruction is at most ~ 100 and ~ 40, respectively, resulting in poor quality of the directional reconstruction ($lik < 100$). This is the reason why, in Fig. 5.14(b), Fig. 5.14(d) and Fig. 5.14(f), the number of triggered hits, DOMs and DUs at trigger level is shown in comparison with those resulting from the selection of only events with $lik > 100$ (the sample is reduced to to the twelfth part of the original one).If the quality cut $lik > 100$ is applied, on average a higher number of triggered hits, DOMs, and DUs is observed with respect to the case without cuts: more PMTs are triggered, more information is used by reconstruction algorithms, and better the reconstruction quality, as also highlighted in Fig. 5.15. Consequently, since the higher the number of triggered hits and more time consuming the reconstruction, as evident in Fig. 5.16(a), tracks reconstructed with better quality require more time to be fitted by the algorithm (see Fig. 5.16(b)). This means that, in case particularly energetic neutrino events occur in our detector producing long and well-defined muon tracks, these should be characterised by longer online processing times with respect to nominal events. Note that the variation of total online processing time is basically affected by the time taken by the reconstruction software to run and not by the dispatching

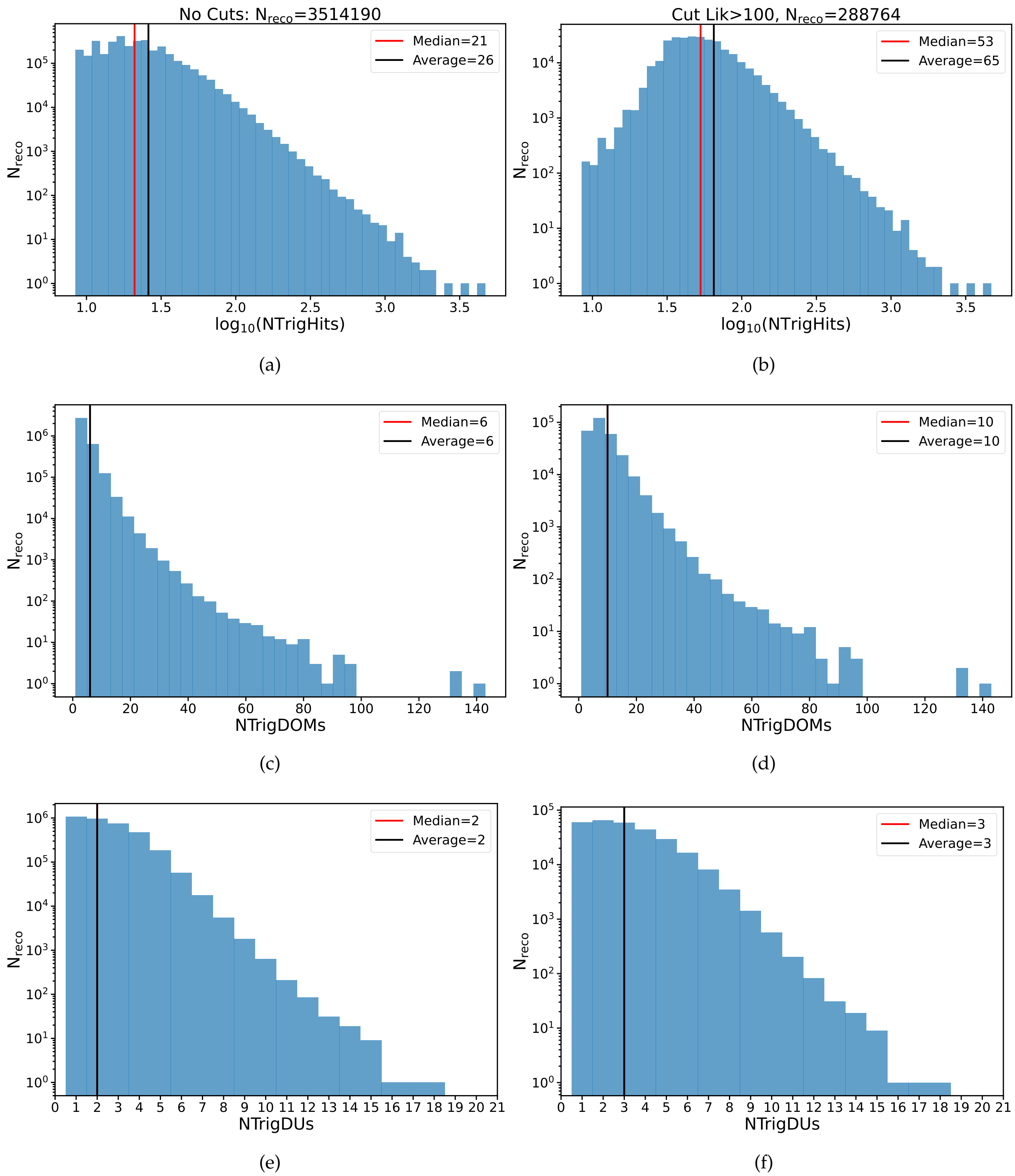

Figure 5.14: Distribution of number of triggered hits (in logarithm values), DOMs and DUs: (a), (c), and (e) refer to $N_{\text{reco}} = 3514190$ events reconstructed in 8.5 days of data taking and without cutting of the reconstruction output applied; (b), (d) and (f) show the same distributions but only for events characterised by the quality of the directional reconstruction (*lik*) greater than 100 ($\sim 8\%$ out of the total sample). The median and average values are indicated by the red and black lines, respectively.

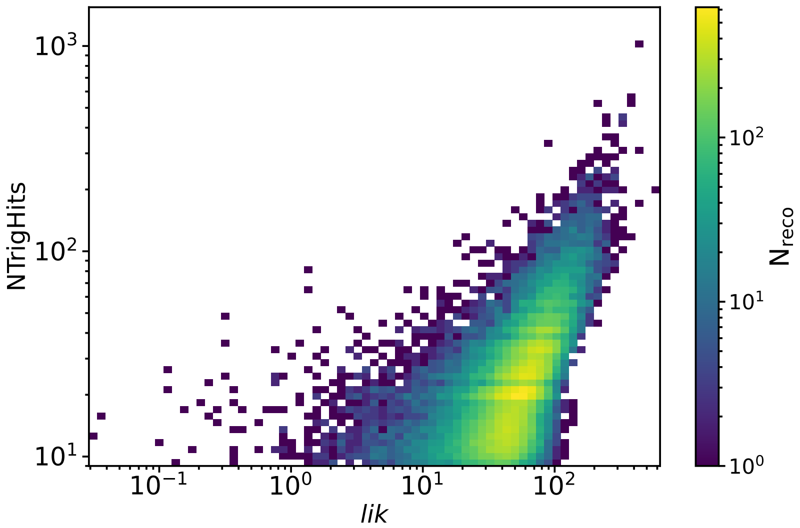

Figure 5.15: Two-dimensional distribution showing the relation between the number of triggered hits and the *lik* parameter for $\sim 5 \times 10^4$ `IO_EVT` reconstructed in one run of data taking (lasting three hours). The colorbar shows the number of reconstructed events in the sample considered.

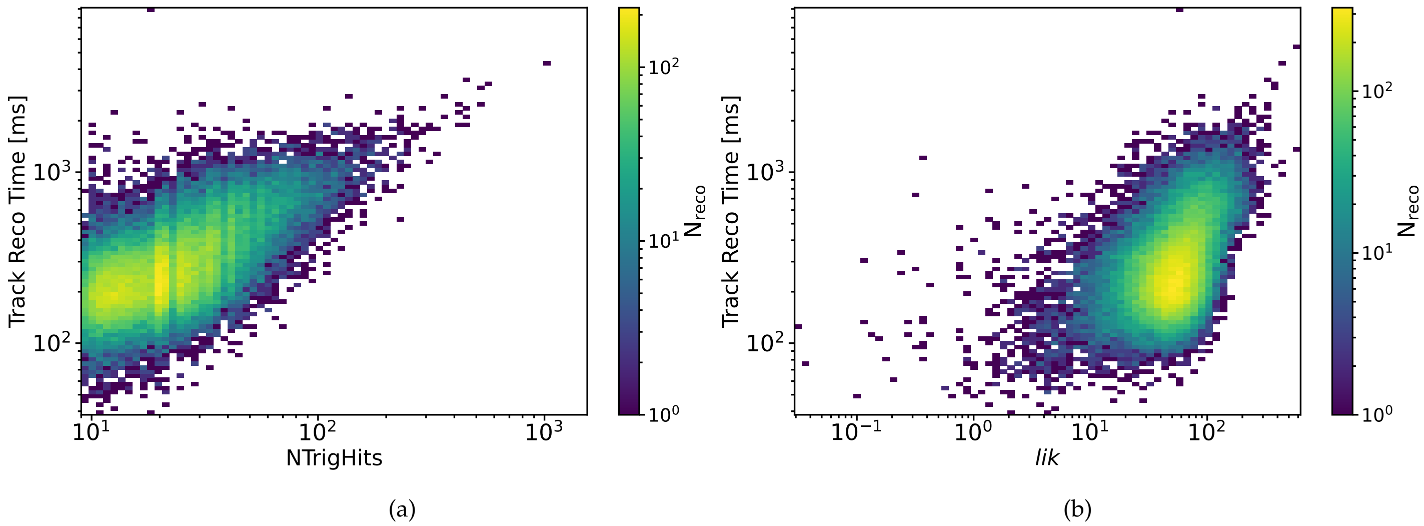

Figure 5.16: Two-dimensional distributions showing the relation between the time used by our algorithms to reconstruct `IO_EVT` as a function of the number of triggered hits (a) and the quality of the directional reconstruction (b). The colorbar shows the number of reconstructed events in the sample considered (same sample as in Fig. 5.15).

and filtering time, which is instead independent of the triggered event properties. Note that the effect of the selection $lik > 100$ is the same as NTrigHits > 20, as demonstrated by the distribution in Fig. 5.17, where the *lik* values are shown for events that have triggered at least 20 PMTs: Indeed, the minimum value *lik* in the distribution is 100. The rate of `IO_RECO` with such characteristics in KM3NeT/ARCA21 is ~ 2.6 Hz. If also the upgoing selection is applied ($\cos(\text{zenith}_{\text{reco}}) < 0.1$), the rate of reconstructed events is reduced to $\sim 2 \times 10^{-2}$ Hz.

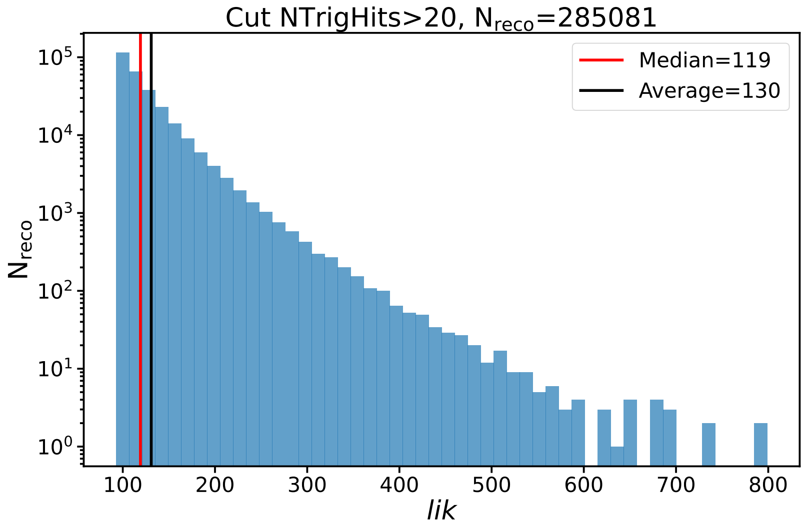

Figure 5.17: Distribution of *lik* values for `IO_RECO` with number of triggered hits > 20. The same sample as that in Fig. 5.12 is considered. The median and average values are indicated by the red and black lines, respectively.

Finally, an analogous comparison as that of Fig. 5.14 is outlined for the quantities used at the reconstruction level in Fig. 5.18.

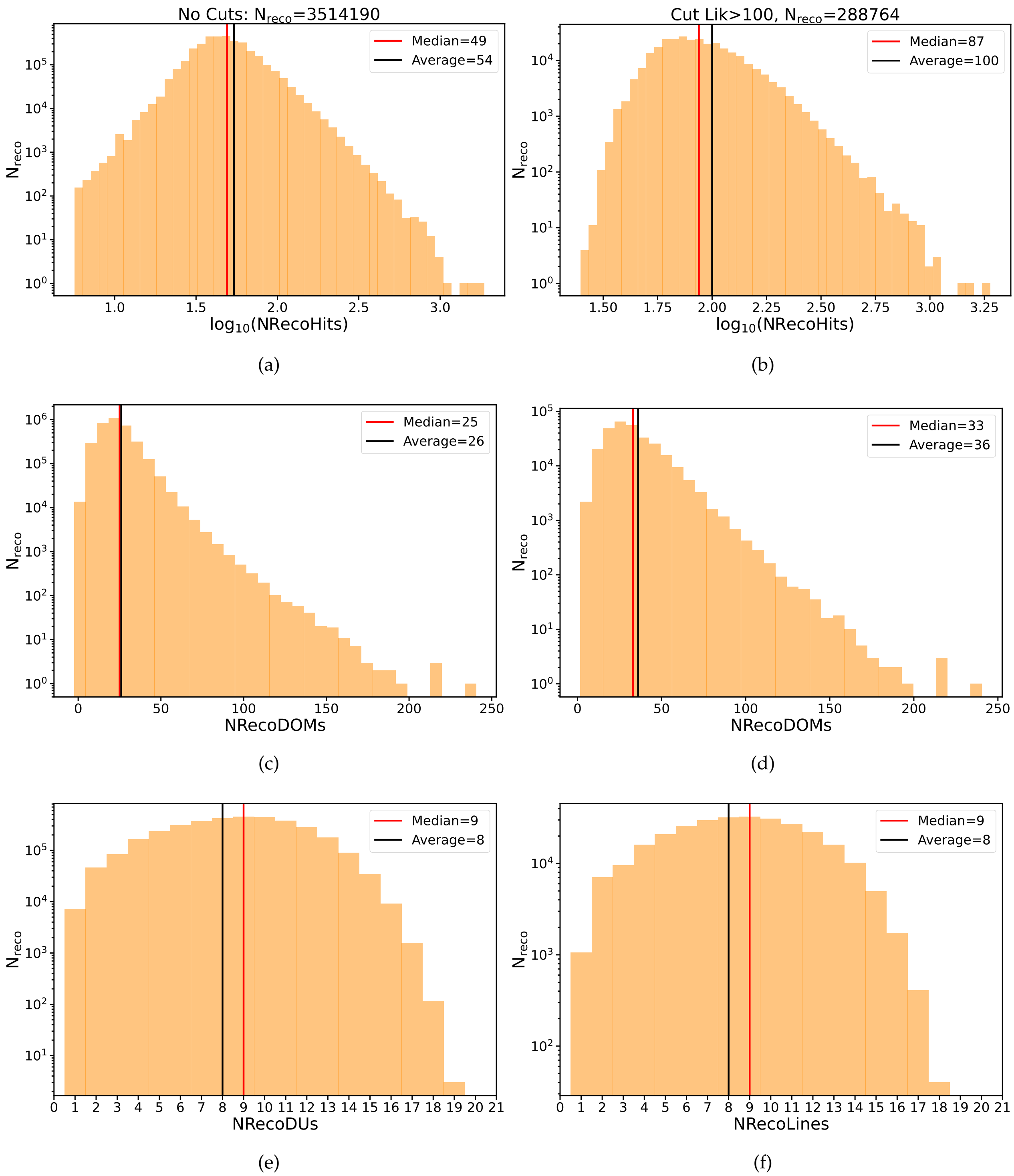

Figure 5.18: Distribution of the number of hits (in logarithm values), DOMs and DUs used for the `IO_EVT` reconstruction: (a), (c) and (e) refer to $N_{\text{reco}} = 3514190$ events reconstructed in 8.5 days of data taking and with no cuts on reconstruction outputs applied; (b), (d) and (f) show the same distributions, but only for events characterised by the quality of the directional reconstruction (*lik*) greater than 100 ($\sim 8\%$ out of the total sample). The median and average values are indicated by the red and black lines, respectively.

5.3.2 *Analysis of simulated astrophysical neutrinos of PeV energy in KM3NeT/ARCA 1BB*

Among the huge flux of atmospheric muons and neutrinos coming into our detector, it is crucial to identify and recognise events of astrophysical nature when they are detected and then reconstructed by the automatic real-time pipeline developed in this work. The purpose of this section is to test its performance in the future configuration of KM3NeT/ARCA with 1BB[9] taking data. For this purpose, I simulated both a downgoing and diffuse flux of ν_μ events with different energies (50 TeV, 100 TeV, 1 PeV, 5 PeV, and 10 PeV) using specific software developed within the KM3NeT Collaboration. In particular, following the neutrino simulation chain described in Appendix B, neutrinos and light were simulated with `gSeaGen` and `JSirene`, respectively; later, the events triggered in the detector were simulated with `JTriggerEfficiency`. Such simulations were performed for an ideal detector with 115 strings (maximum efficiency for all PMTs, standard trigger parameters and nominal position for all DUs), whose geometry is represented in Fig. 5.19. The instrumented volume ($\sim$ 0.55 km^3) has been extended by a factor of 350 m of distance around each dimension, for a final effective volume of $\sim$ 2.55 km^3, being the latter the volume within

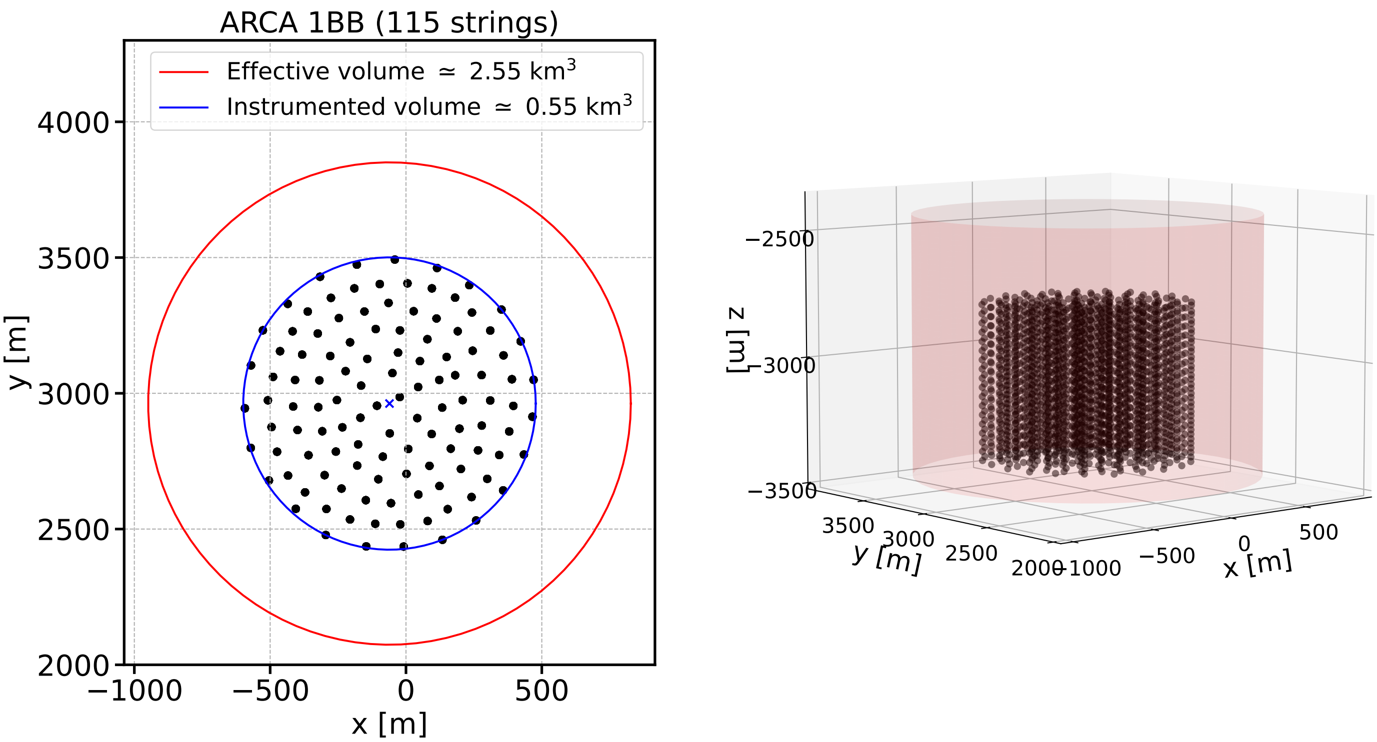

Figure 5.19: Footprint showing the DU positions (black circles) for the future detector KM3NeT/ARCA 1BB. The panels at left and right shows the top- and the three-dimensional view of the detector, respectively. The instrumented volume ($\simeq$ 0.55km^3) and the effective volume used in the neutrino MC simulations ($\simeq$ 2.55km^3) are indicated by the blue and red circles, respectively. In the right panel, only the effective volume is shown (red cylinder).

9 The plan is to build KM3NeT/ARCA with 2 BB, namely 230 strings (see Sect. 2.5.2). Here, the detector configuration with 1BB is considered since at the time of writing, 1BB was already fully funded.

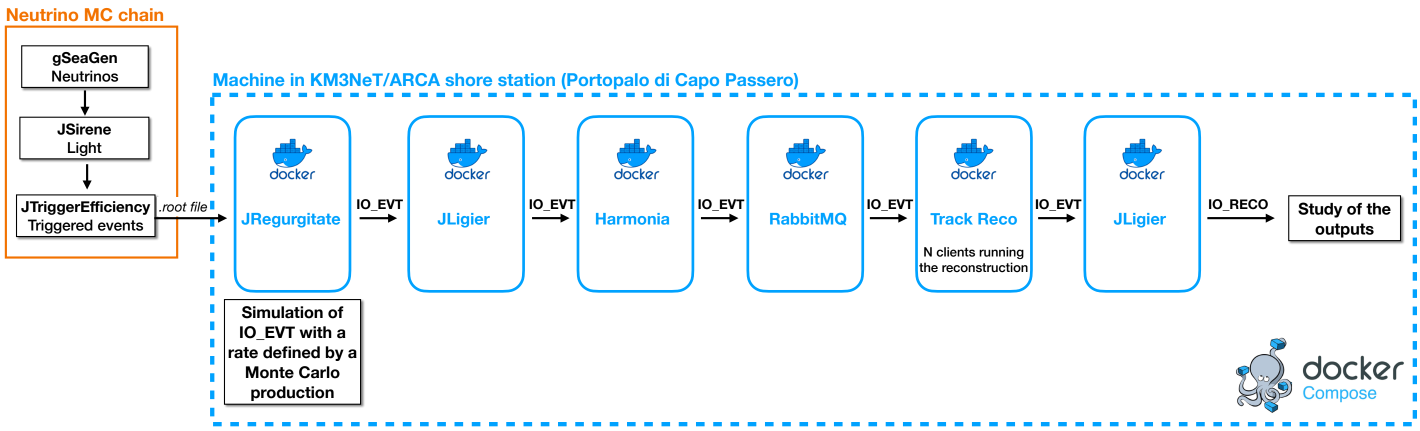

Figure 5.20: Scheme showing the procedure adopted to simulate a flow of IO_EVT coming from ν_μ of PeV energy into the online reconstruction pipeline developed for KM3NeT/ARCA. The orange box shows the neutrino MC chain adopted (it is detailed in Appendix B). Then, in the KM3NeT/ARCA shore station, multi-container applications (each Docker container is represented by a cyan box), are run simultaneously through the Docker Compose tool. The procedure and software are similar to that in Fig. 5.4, with the difference that here triggered events are not real events taken from the DAQ dispatcher, but simulated ones through the `JRegurgitate` application.

which the detector is still able to detect neutrino signatures through the emitted Cherenkov photons on PMTs, even if their interaction point is located outside the geometrical volume.

Indeed, dedicated studies performed inside the KM3NeT Collaboration and based on the comparison of neutrino effective areas, have shown that this extension, corresponding to about 5 times the absorption length in seawater (the effect of the photon absorption is explained in Sect. 2.2.1), increases the ν_μ effective area up to $\sim$10% for PeV energies.[10] The output of this MC neutrino simulation chain (up to the generation of triggered events in the detector, hence before reconstruction, can be used as input to the online reconstruction pipeline by taking advantage of the `JRegurgitate` application, which is capable of generating from the output of `JTriggerEfficiency` (a root file) different types of DAQ events. These can be transferred into the KM3NeT/ARCA online reconstruction pipeline data flow, to test its response to PeV neutrinos (of astrophysical origin), as shown by the scheme in Fig. 5.20. Apart from the simulation of IO_EVT, that substitutes the mirroring of real data from the DAQ to our dispatcher, everything else is analogous to what already discussed (i.e., software used and multi-processes to reconstruct events). Note that IO_SUM are not included at this level, since the `JRegurgitate` application does not allow to simulate more than one type of event at the same time. However, this does not affect the study here discussed for two reasons: the reconstruction quality seems to be independent of the usage of information contained in summaryslices, and the time taken by the online processing to associate IO_EVT to its corresponding IO_SUM is negligible with respect to the total processing time. Both these effects have been previously discussed in this chapter (see Sect. 5.3.1).

10 For ν_e effective area, an increasing up to about 60% has been predicted.

For the following study, a flow of `IO_EVT` resulting from CC interactions of PeV ν_μ coming from both a point-source and isotropic sky directions, in order to mimic a diffuse flux, was simulated. In particular, I consider here a point-source located above the sky of KM3NeT (Dec=+45°)[11]. Incoming ν_μ were simulated with energy E_{ν_μ} between 50 TeV and 10 PeV. For each direction and energy of generated ν_μ, I monitored the time necessary to reconstruct the resulting events (a sample of 10^5 `IO_RECO` was considered). Note that, to avoid perturbing the real time reconstruction, these tests were carried out on a different machine with respect to that where the real-time reconstruction is currently running.

The reconstruction time of the simulated events from the track algorithm was observed to increase with the energy of the incoming neutrino: the more energetic the event induced by the neutrino interaction, the higher the number of hits triggered on PMTs. In particular, for the downgoing flux of ν_μ from a point-source, the reconstruction time varies from ~ 1.5 s at $E_{\nu_\mu} = 50$ TeV to ~ 4.8 s at $E_{\nu_\mu} = 10$ PeV. A similar trend is obtained in the study of neutrinos from any direction in the sky. Overall, these results suggest that, if events induced by CC interactions of PeV ν_μ will arrive into the KM3NeT/ARCA 1BB volume producing a detectable signal, the current online software framework in place would be able to reconstruct the direction and energy[12] of such events (in the track-like hypothesis) within 5 seconds on average.

5.4 REAL-TIME SEARCH FOR ν_μ FROM GRB 221009A USING ONLINE RECONSTRUCTED DATA

An important step of the online analysis is to look for time and space correlations between events reconstructed in real-time by the online pipeline described in this chapter and external triggers. The KM3NeT detector daily receives alerts by the external electromagnetic community; consequently, an automatic software in place at the MM dispatcher checks the position of the source and, if this is located in the upgoing sky, the online pipeline automatically runs a fast analysis implemented to get quick results. This is based on a counting analysis, that looks for a signal excess in predefined search angular and time windows. The background is directly extracted in the data using an off-time window around the signal time window. Starting from the following Sect. 5.4.1, I present the first-quasi-real time analysis performed with this approach on an astrophysical source, i.e., GRB 221009A, within KM3NeT. Sect. 5.4.2 describes the analysis method adopted for performing this fast and simple analysis. In Sect. 5.4.3, the selection of events reconstructed in real time and the check of quality data before performing the analysis are both presented. Finally, Sect. 5.4.4 highligts the results obtained.

11 Negative declinations are not considered to avoid the Earth absorption effect on upgoing neutrinos that otherwise would influence our results.

12 Note that the reconstructed energy can be overestimated or underestimated with respect to the original one. See, e.g., Appendix C, where this effect is investigated for KM3NeT/ARCA in 6 strings configuration.

5.4.1 *GRB 221009A*

The 9th of October 2022, at 14:10:17 UT, the Swift-BAT telescope triggered a spectacular transient event located at right ascension RA = 288.263° and declination Dec=+19.803° (J2000 degrees[13]) [401]. From about the same direction of the sky (RA = 290.4° and Dec=+22.3° with 1° statistical uncertainty), *Fermi*-GBM reported the observation, ~ 1 hour before (13:16:59 UT), of an extraordinarily bright GRB, the brightest among all GBM detected GRBs [402], called GRB 221009A. After a first isolated emission mechanism (pulse of ~ 10 s), its γ-ray light curve shows an extremely bright, multi-pulsed emission episode with a duration longer than 300 s and characterised by a γ-ray fluence $F_\gamma \sim 3 \times 10^{-2}$ erg cm^{-2} (10-1000) keV. The latter constitutes the main burst and began at ~ 180 s after the GBM trigger time T_0. The detection of high-energy gamma rays at $\sim$ 200-600 s after T_0 was also reported by *Fermi*-LAT [403]: the highest energy photon (~ 99 GeV) was detected at 240 s after the trigger, classified as the most energetic photon ever reported by LAT so far. Later, LHAASO announced the observation of photons from this GRB with energy up to 18 TeV [404]. This is clearly astonishing, representing the first detection of photons above TeV from GRBs. The observation of the afterglow emission from this event located GRB 221009A at $z \simeq 0.151$ [405], corresponding to an equivalent isotropic γ-ray energy of $E_\gamma^{\rm iso} \sim 3 \times 10^{54}$ erg. This has challenged our knowledge of photon propagation into the EBL (see Sect. 1.2.2); indeed, the detection of photons above 10 TeV is not expected from bursts beyond $z \gtrsim 0.1$ due to their attenuation with the EBL (see Sect. 1.2.2). Hence, huge ferment was triggered in the scientific community, leading in only a few weeks to several works trying to interpret this observation in the light of our current knowledge and invoking new physics. The description of such interpretations go beyond the scope of this thesis and is not treated here (see e.g., [406]). Given the exceptionality of GRB 221009A, follow-ups were encouraged by γ-ray instruments. More than forty GCN entries related to this GRB have been published by many facilities in the 3 days after the event, reporting detections or upper limits. As regards neutrino searches, IceCube promptly reacted reporting zero track-like events in coincident with the position of the GRB in a time window around the Fermi-GBM event extended between 1 hour before and 2 hours later [407].

Unfortunately, for the KM3NeT detector, the GRB 221009A direction was downgoing at the time of the event. However, given its importance and exceptionality, it wad decided to manually start the follow-up analysis following an analogous procedure to the one adopted in the automatic analysis pipeline. Within the KM3NeT Collaboration, three different analyses were performed:

- A low-energy analysis (MeV range) based on the search for the maximum number of 10 ns coincidences between PMTs in a single DOM during 500 ms, computed every 100 ms. A post-trial p-value of 0.9 was obtained, consistent with background expectations.

13 The current standard epoch of equatorial coordinates. J2000 refers to the RA and Dec of an object on the noon time UT on January 1, 2000. This is a Julian epoch, denoted by the "J", since it is 100×365.25 days since the standard epoch J1900.

- Two high-energy analyses (one for ORCA and one for ARCA) based on the ON/OFF technique (see Sect. 5.4.2). In both detectors, zero events were observed in the search window, while ~ 0.1 were expected from the background. In Sect. 5.4.3, the details of the analysis performed for the KM3NeT/ARCA detector, in which I participated, is described.

5.4.2 *ON/OFF technique*

The search method adopted is based on an ON/OFF technique, described below:

- The **ON region**, where the signal is expected to dominate over the background, is defined as the region where the angular distance to the source position is lower than the radius of a defined Region of Interest (RoI), which is adapted on the detector;
- The **OFF region** is characterised by an area compatible with the ON region, while not including the source under investigation from where only background is expected.

For the KM3NeT/ARCA analysis, an ON region defined by a radius $\mathrm{RoI} = 2^\circ$ is defined. The signal search covers the time range of $[T_0 - 50\ \mathrm{s}, T_0 + 5000\ \mathrm{s}]$, with $T_0 = 13:16:59$ UT being the trigger time reported by *Fermi*-GBM. This time search window was set after the ground-based Cherenkov detector Carpet-2 at Baksan Neutrino Observatory reported the detection of an air shower originating from a 251 TeV photon at $T_0 + 4536$ s from the direction of GRB 221009A [408]. However, it is important to mention that after the KM3NeT analysis was performed, this event was associated with a Galactic source seen by HAWC [409], whose location is consistent with the ~ 250 TeV photon within the 90% uncertainty. As coordinates for the event, those given by Swift-BAT (RA = 288.263° and declination Dec=+19.803°) were used. On the other hand, for background estimation, the OFF region considered was a band following the elevation $h(t)$ of the source in a time window extended 1.5 hours more than that of the signal, to ensure us of good statistics, i.e. $[T_0 - 50\ \mathrm{s} - 1.5\ \mathrm{h}, T_0 - 50\ \mathrm{s}]\&[T_0 + 5000\ \mathrm{s}, T_0 + 5000\ \mathrm{s} + 1.5\ \mathrm{h}]$. To adapt the OFF region to the same area as that in the ON region and to have a correct estimation of the signal and background events expected in the search, a rescaling factor of the solid angle was used, as:

$$\frac{\Omega_{\mathrm{ON}}}{\Omega_{\mathrm{OFF}}} = \frac{2\pi[1 - \cos(\mathrm{RoI})]}{2\pi[\sin(\max(h(t)) + \mathrm{RoI}) - \sin(\min(h(t)) - \mathrm{RoI})]}. \tag{5.2}$$

Additionally, the number of events was also rescaled by a factor accounting for the difference between T_{ON} and T_{OFF}, namely the time windows considered for the signal and background estimation, respectively:

$$\frac{T_{\mathrm{ON}}}{T_{\mathrm{OFF}}} = \frac{5050\ \mathrm{s}}{10800\ \mathrm{s}}. \tag{5.3}$$

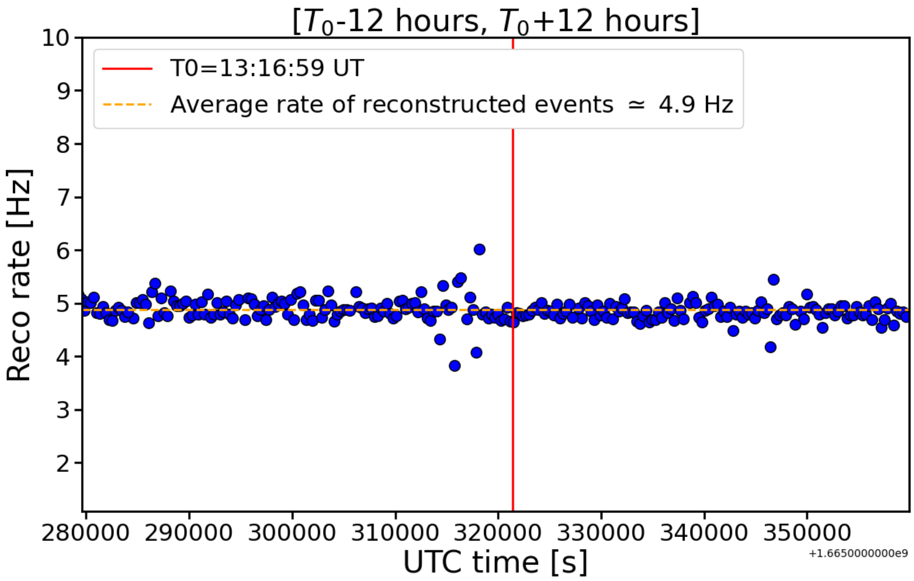

Figure 5.21: Rate of reconstructed events by the online pipeline of KM3NeT/ARCA in ±12 hours around the GRB 221009A trigger time $T_0 = 13:16:59$ UT, indicated by the vertical line. At time, KM3NeT/ARCA was taking data with 21 strings. The blue circles indicate the rate of `IO_RECO` averaged over five minutes of data taking. The horizontal dashed line shows the average rate of `IO_RECO` in $[T_0 - 12 \text{ hours}, T_0 + 12 \text{ hours}]$, amounting to $\simeq 4.9$ Hz.

5.4.3 *Sample selection*

Using the data reconstructed from the online fast processing chain implemented in KM3NeT/ARCA (namely `IO_RECO`), a dedicated search for track-like muon neutrino events compatible with the direction of GRB 221009A was performed. At the time of the GRB, KM3NeT/ARCA was equipped with 21 strings and the detector was collecting good quality data. Before proceeding with the analysis, checked the stability of the real-time reconstruction over ~12 hours around T_0 was checked. The results are shown in Fig. 5.21, where the stable conditions of the online pipeline reconstruction are visible: the mean rate of events reconstructed as a track in real time was ~ 4.9 Hz. However, the GRB location was above the KM3NeT horizon (mean elevation of approximately $\sim 48°$) during the search time window, as shown in Fig. 5.22, significantly reducing the point-like source sensitivity. The expected atmospheric background from the direction of the sky coincident with the GRB 221009A position is high because of atmospheric muons. In fact, by counting the events in the zenith band in the OFF time window and rescaling them for the time window and the solid angle of this analysis (as indicated in Eq. (5.2) and Eq. (5.3), respectively), the expected background amounts to ~ 3.7 events in the time and angular search, dominated by atmospheric muons. To reduce the muon contribution, some basic cuts were first applied in order to select only events with positive track length and reconstructed energy greater than 1 TeV (as a result of these cuts, the sample reduces by a factor of $\sim 3\%$); a cut in *lik* was also used to select only tracks reconstructed with good quality; in particular, $lik > 155$ was adopted, as it allowed to achieve an expected number of background events in our time and angular window search of $(8.4 \pm 0.9) \times 10^{-2}$ (only the $\sim 0.8\%$ out

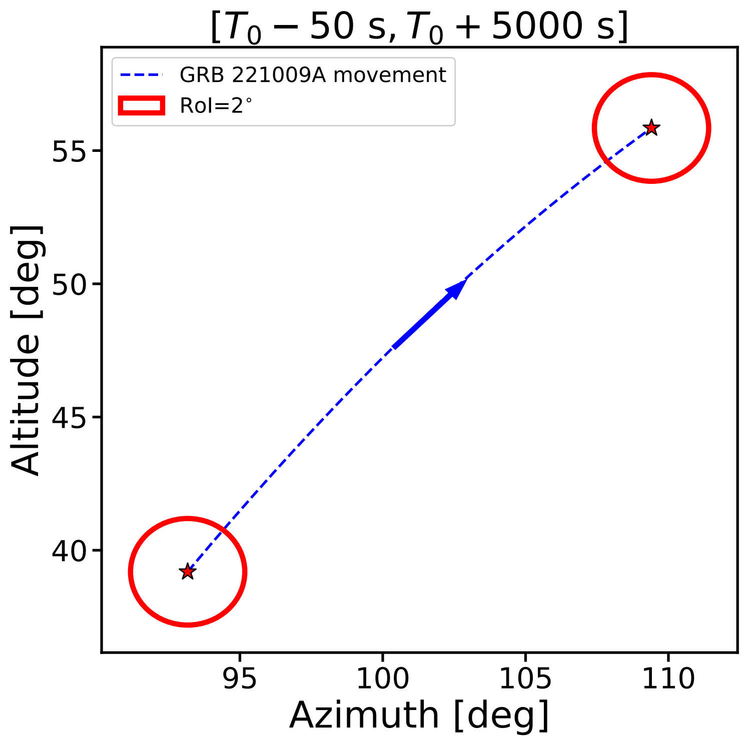

Figure 5.22: Movement in local coordinates (blue line) of the GRB 220910A position in the search time window $[T_0 - 50\text{ s}, T_0 + 5000\text{ s}]$ used in the analysis. The red circles represent the RoI$= 2°$ at $T_0 - 50$ s and $T_0 + 5000$ s.

of the original sample survive). As a comparison with Fig. 5.21, Fig. 5.23 shows the rate of `IO_RECO` in the KM3NeT/ARCA21 detector surviving the cuts set in this analysis for the 12 hours around the GRB 221009A trigger time: only $\sim 4 \times 10^{-2}$ events, out of the ~ 5 events per second reconstructed by the online pipeline of KM3NeT/ARCA, satisfy the conditions required.

5.4.4 *Analysis results*

By exploiting reconstructed data selected as explained in the previous Sect. 5.4.3, KM3NeT/ARCA data were unblinded, looking for possible neutrino events exceeding the background level in the ON region defined by the RoI and the source movement of Fig. 5.22. The results of our follow-up are shown in Fig. 5.24: in the search time window between $T_0 - 50$ s and $T_0 + 5000$ s, no event was found to satisfy the selection criteria in the signal region, while one outside the RoI survived the cuts defined by the analysis (indicated by the blue point). Note that the online fast processing uses preliminary calibrations and detector alignment, which will be superseded in a future more elaborated offline analysis. The results discussed here have been communicated to the external multimessenger community just three days after the first GRB 221009A trigger alert through the GCN in [410].

This analysis can be considered as the start of the intense KM3NeT real-time observational strategy activity that we plan to perform in the coming future in the field of multi-

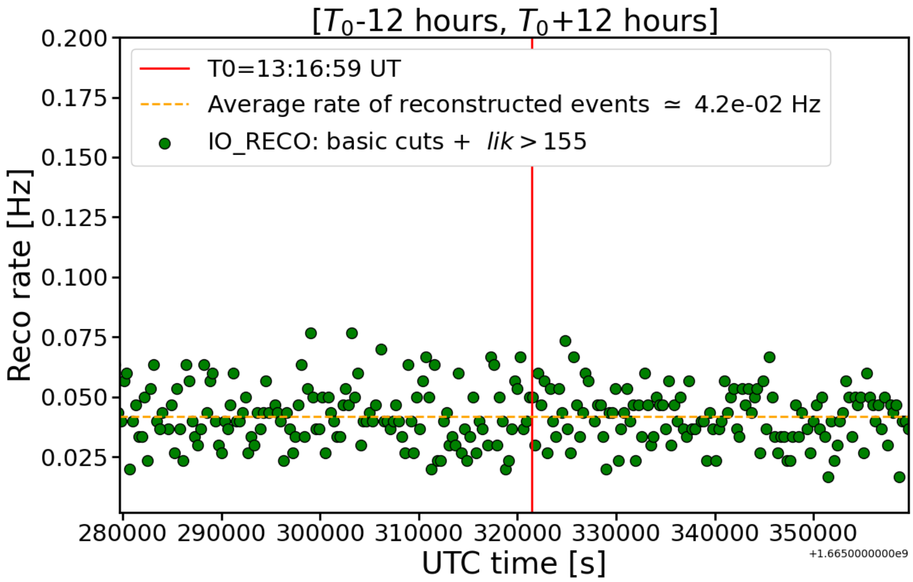

Figure 5.23: Rate of reconstructed events with $E_{reco} > 1$ TeV and $L_\mu > 0$ (basic cuts), and $lik > 155$ by the online pipeline of KM3NeT/ARCA in ± 12 hours around the GRB 221009A trigger time $T_0 = 13:16:59$ UT, indicated by the vertical line. At time, KM3NeT/ARCA wastaking data with 21 strings. The green circles indicate the rate of `IO_RECO` surviving the cuts averaged over five minutes of data taking. The horizontal dashed line shows the average rate of `IO_RECO` in $[T_0 - 12 \text{ hours}, T_0 + 12 \text{ hours}]$, amounting to $\simeq 4.2 \times 10^{-2}$ Hz.

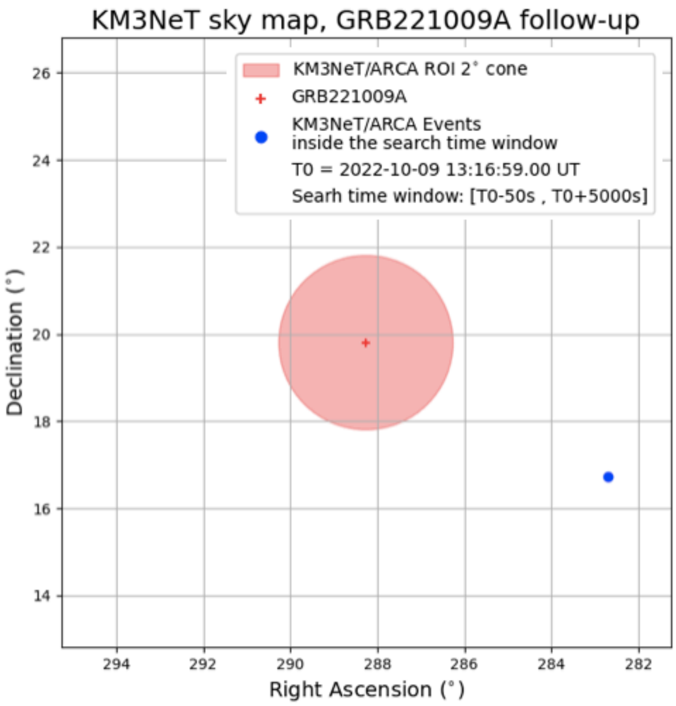

Figure 5.24: Sky map showing the results of the search, performed with the KM3NeT/ARCA21 data, for neutrinos unblinded in spatial and temporal coincidence with GRB 221009A. A RoI of 2° (red circle) was opened around the GRB position (red cross), and a temporal window $[T_0 - 50 \text{ s}, T_0 + 5000 \text{ s}]$ was considered. The only event surviving the selection criteria, i.e. $E_{reco} > 1$ TeV, $L_\mu > 0$, and $lik > 155$, is found outside for the ON signal region (blue point).

messenger astronomy. As anticipated, an automatic analysis pipeline is already in place at the MM dispatcher, promptly reacting in case of external alerts received from instruments detecting several visible messengers (e.g., νs and γ-rays), if these occur in the upgoing sky of the detector. In addition, dedicated pipelines for specific classes of sources have being developed withing the KM3NeT Collaboration, i.e., GRBs (already operative), and GWs (work in progress).

The tools implemented within the context of the present work demonstrates that KM3NeT/ARCA is capable of reconstructing events in real-time, collect the results of such reconstruction, and analyse them. Once the implementation of the alert-sending framework will be finalised as well, KM3NeT will be fully integrated into the global multimessenger worldwide network. However, the analysis currently implemented is very simple and is useful to get quick results. Indeed, as previously discussed, it is based on a counting analysis looking for a signal excess in predefined search angular and time windows, and where the background is directly extracted in the data using an off-time window around the signal time window. More sophisticated analysis methods, based on maximum likelihood ratio, will be implemented in the future.

6 SUMMARY AND CONCLUSIONS

This thesis concerns astrophysical neutrinos, which are thought to come from several classes of high-energy transient sources as a result of Cosmic Ray (CR) hadronuclear and photohadronic interactions with matter and photon fields, respectively. While gamma (γ) rays are also emitted in purely leptonic processes such as synchrotron, inverse Compton scattering, and bremsstrahlung, neutrinos constitute the smoking gun signature for hadron acceleration. An advantage of considering astrophysical neutrinos is the fact that they can reach the Earth without any absorption and deflection by magnetic field effects, unlike γ rays and CRs. This means that neutrinos preserve the directional information of the sources originating them. In light of this, cosmic neutrinos provide a unique probe for the discovery of astrophysical sources accelerating Ultra-High-Energy CRs (UHECRs), i.e. CRs detected with energies greater than 10^{18} eV, whose extragalactic origin remains still today deprived of any firm association with known sources, despite the recent mild correlation (4.2σ) with observed starburst galaxies. However, as neutrino interactions are mediated by the weak force, their tiny cross section makes detection of high-energy cosmic neutrino sources challenging; huge particle detectors are instrumented within large volumes of natural target in order to collect cosmic neutrinos in statistically significant numbers. Great efforts have been concentrated over the years to the installations of large detectors deep in water and ice capable of collecting Cherenkov light induced by secondary particles resulting from neutrino interactions with nuclei in the detector volume. These efforts have led towards the construction of bigger and bigger detectors all over the world, such as the IceCube neutrino telescope at the South Pole, Baikal-GVD below the surface of Lake Baikal in Russia, and two detectors in the depths of the Mediterranean Sea, that this thesis describes in details: ANTARES, that operated from the end of 2007 to 2022, and the next generation cubic-kilometre neutrino telescope KM3NeT (currently under construction and already taking data).

The first detection of astrophysical neutrinos dates back to 2013, when IceCube reported the discovery of a diffuse flux of PeV neutrinos. This discovery opened a new window to the high-energy Universe, proving further evidence for the existence of extreme CR accelerators, most likely of extragalactic origin, though still unassociated with any specific source population. However, correlation studies among neutrino events and different catalogs of known astrophysical sources have resulted into lack of significant associations, such that still today no dominant source contribution has emerged. Neutrino data can tell us when and where to look for an electromagnetic counterpart, providing improved power to discriminate between proposed source models. Contrary to traditional telescopes, Cherenkov-based neutrino detectors have a field of view comprising the whole sky, thus they are ideally suited to detect and inform in very short time other telescopes about interesting events. These low-latency real-time alerts prompt follow-up multimessenger and multiwavelength observations, especially fostering the detection of transient and variable sources. This approach allowed to achieve another major step in the field of neutrino astronomy: on September 2017, IceCube triggered a high-energy neutrino of about 300 TeV (IC-170922A) that, thanks to the extensive follow-up activities by γ-ray observatories (first of all, the *Fermi*-LAT satellite), was spatially and temporally associated with a significance of about 3σ to the blazar TXS0506+056 in active state. After this detection, archival analyses of IceCube data prior to the IC-170922A event revealed a potential flare in neutrinos, between September 2014 and March 2015, with statistical significance of 3.5σ and independent of the 2017 neutrino alert. IC-070922A, together with the association occurred just one month earlier between the short-duration Gamma-Ray Burst (GRB) GRB 170817A and the Gravitational Wave (GW) GW170817 (from the merger of two neutron stars) detected by the LIGO and Virgo interferometers, marked the birth of the so-called *multimessenger astronomy* at extragalactic scales.

Multimessenger astronomy is a novel field rapidly becoming a major avenue to explore the Universe: a deeper understanding of the physical processes governing individual cosmic sources, can arise from the complementary information carried by γ rays, gravitational waves, neutrinos, and CRs. Growing synergies between different instruments and satellites currently operating are opening new frontiers that promise profound insights into several astrophysical aspects (e.g., for the identification of the astrophysical sources responsible for the cosmic diffuse neutrino flux, the definition of the physical mechanisms acting in such sources, their particle composition, etc.). In these regards, it is also interesting to point out that, from the comparison of the IceCube diffuse cosmic neutrino flux measurements with the isotropic extragalactic γ-ray background observed by Fermi and with UHECRs data collected by the Pierre Auger Observatory, comparable energy densities result. This consideration suggests that the three particle populations might be connected and originated from the same source class.

Among several possibilities, GRBs have been proposed quite naturally as responsible for the UHECR flux, hence for the secondary emission resulting from their interactions inside the GRB jets. With an isotropic-equivalent energy of up to 10^{54} erg and powered by the core-collapse of a very massive star or the merger of two compact objects, GRBs constitute the brightest explosions known to date in the Universe. The broad-band non-thermal γ-ray spectrum likely results from a combination of leptonic and hadronic radiation mechanisms. GRBs would be also sources of high-energy neutrinos and UHECRs. Their transient nature additionally offers one of the most promising perspectives for the coincident detection of cosmic neutrinos, allowing an almost background-free search. So far, neutrinos have not been observed in coincidences with GRBs; however, for several years, searches for ν-GRB associations have focused primarily at TeV-PeV energies, limiting the results to a partial class of hadronic models among the several ones proposed. I studied, in Chapter 3, the possibility to investigate with current and future neutrino telescopes an alternative scenario for the prompt origin and related neutrino emission from GRBs. In particular, I considered GRB jets consisting of protons and neutrons, where a fraction of the outflow kinetic energy is converted to thermal energy and radiation via inelastic nuclear collisions occurring in the photosphere. In the photospheric scenario, a thermal spectrum is released near the photosphere and this is then modified by a dissipation mechanism related to the above mentioned *pn* collisions. Such collisionally heated GRBs could produce multi-GeV neutrinos. The existence of complementary detectors of IceCube and KM3NeT, i.e., DeepCore and ORCA, respectively, that are optimised for GeV studies, allows to test this scenario. In the interested energy range, the atmospheric neutrino background is very strong, therefore, detecting these νs from GRBs is very challenging. However, as a result of my investigation, I found that these detectors are able to explore the occurrence of inelastic collisions in GRB jets by means of a stacking analysis of upgoing tracks with data collected in coincidence with $\sim$900 Long GRBs (LGRBs), i.e. with prompt γ-ray emission lasting for more than 2 seconds. As previous experimental studies conducted with neutrino data indicate, it is likely that such a number of LGRBs are included in experimental analyses after about 10 years of data taking; however, we expect that more sensitive future gamma-ray facilities will provide the same statistics on shorter timescales. The search for upgoing events requires detectors in different hemispheres to probe the entire population of GRBs, as to guarantee full sky coverage. According to these results, short GRBs alone, namely those with duration of the prompt γ-ray emission shorter than 2 seconds, do not provide enough signal. Concerning individual sources, only nearby and very energetic GRBs with γ-ray fluence $F_\gamma \geq 10^{-2}$ erg cm^{-2} (rare events) appear to produce, according to this model, at least one signal event in the available detectors. The key role of neutrinos in assessing the origin of the prompt radiation emerging from GRBs demonstrates the importance of dedicated searches in the multi-GeV domain, that are therefore encouraged to start, by combining data collected both by low and high-energy detectors (DeepCore+IceCube and KM3NeT/ORCA+KM3NeT/ARCA). A detection of such a neutrino emission would allow to establish the baryonic nature of GRB jets, although within the context of a model that does not directly involve particle acceleration. In fact, so far, the lack of a correlation among γ-ray signals from GRBs and neutrinos did not allow to distinguish among the leptonic or hadronic nature of radiation from GRB jets. Furthermore, the detection of multi-GeV neutrinos in coincidence with GRBs would provide information on the occurrence of photospheric dissipation, as well as on the jet composition.

The lack of association between GRBs and TeV-PeV neutrinos is furthermore critically assessed in this thesis. Indeed, in Chapter 4, I discuss the analysis performed within the ANTARES Collaboration, considering a standard model explaining the GRB observed radiation through particles accelerated at internal shocks in the optically thin region of the jet. Extending previous existing ANTARES studies, I used data from the end of 2007 to 2017. I performed a search for upward going muon neutrinos and anti-neutrinos in spatial and temporal coincidence with 784 GRBs. Through a numerical computation, I estimated the expected neutrino flux from each burst individually, in the context of the one-zone internal shock model. A novel aspect of the search I present is the inclusion in the data analysis chain of the uncertainty that possible unknown parameters, related to the characteristic activity of the central engine, can introduce in the neutrino flux evaluation. This is crucial in order to correctly interpret the validity of model-dependent results, in terms of upper limits set by non-detections of neutrinos in coincidence with GRBs. These parameters have been identified in the bulk Lorentz factor, variability timescale and source redshift, all of which are affecting the so-called dissipation radius, where shell collisions are realised. Among these parameters, the former was shown to impact the most GRB-ν flux predictions. At the same time, it is also possible to marginalise the uncertainty related to it by including in the modelling its observed correlation with the source isotropic γ-ray luminosity. As a result of such procedure, I found that the minimum variability timescale contributes more than redshift to the uncertainty of the neutrino flux predictions from GRBs. Thanks to this investigation approach, the expected ν-fluxes are provided for the very first time with an uncertainty band. Analogously to previous ANTARES searches, I performed Monte Carlo (MC) simulations of the predicted signal, while I estimated the respective background directly from off-source data collected by ANTARES. I selected only track-like events reconstructed within 10° in radius from the expected GRB position, and in temporal correlation with the prompt γ-ray emission. This analysis was optimised on a burst-per-burst basis in order to maximise the discovery potential of the search, thus enabling the identification of the most promising sample of GRBs for ANTARES. However, because a negligible reduction of the model discovery potential would be obtained when stacking the entire catalog, the Collaboration dediced for investigating the flux from the whole sample of 784 GRBs. After unblinding ANTARES data occurred in space and time correlation with GRBs, no event was found to pass the selection criteria, and so I derived upper limits on the contribution of the detected GRB population to the cosmic neutrino flux, ranging between $1.3^{+0.4}_{-0.8} \times 10^{-9}$ GeV cm^{-2} s^{-1} sr^{-1} and $1.0^{+0.9}_{-0.5} \times 10^{-8}$ GeV cm^{-2} s^{-1} sr^{-1} in the energy range from ~ 60 TeV to ~ 10 PeV. In particular, within standard assumptions of energy partition among accelerated hadrons, leptons and magnetic fields (baryonic loading equal to 10), GRBs are found to not be the main sources of the astrophysical neutrino flux, possibly contributing for less than 10% at energies around 100 TeV. This result represents a further independent constraint with respect to the IceCube limits, fully compatible with the latter.

Finally, in Chapter 5, the thesis focusses on the multimessenger frontier, within the context of the KM3NeT Collaboration. The work is related to the high-energy detector KM3NeT/ARCA, devoted to the detection of high-energy neutrinos (1 TeV-10 PeV) produced in astrophysical phenomena during CR acceleration. I contributed to the development of the online pipeline that is currently in place to reconstruct both the direction and energy of track-like events in real time. The software framework implemented for the reconstruction was already operative for processing real data in December 2020; from then on, the real-time reconstruction of events has been continuously working and has been adapted every once the detector size has increased. In the current 21-strings configuration of KM3NeT/ARCA, we are able to collect each event from the data acquisition system of the detector and reconstruct it, under the hypothesis of a track signature, within about on average 4 seconds, of which the reconstruction process takes just 160 ms. The average properties of reconstructed events showed consistent results with offline algorithms, and a correlation between the number of Cherenkov photons released into the detector volume and the quality of the reconstruction was observed, as well as with the duration of the whole reconstruction process. In addition to the data characterisation, the online pipeline was validated through MC simulations of cosmic PeV neutrinos acquired by a fully funded detector configuration (with a volume more than a factor 4 larger than the current one). I found that, in case such energetic neutrinos will be detected through their interaction products, we would be able to reconstruct such events, with the current online software framework in place (direction and energy of a muon track), within 5 seconds on average. This result proves that, just few seconds after the detection of a high-energy cosmic ν, KM3NeT would be ready to send an alert to the external multimessenger community. I also contributed to the first quasi-real-time analysis performed with data reconstructed by the online pipeline relatively to GRB 221009A, the brighest GRB to date. Following a fast analysis aiming at looking for neutrinos emerging over the background level in a signal region defined around the GRB and without any particular assumption on the neutrino flux shape, no neutrino events were found in spatial and temporal association with GRB 221009A. However, this analysis can be considered for the KM3NeT detector as the start of the intense real-time observational strategy activity that will be performed in the coming future in the field of multimessenger astronomy. Indeed, KM3NeT is progressively becoming fully integrated into the global multimessenger worldwide network.

A

CALIBRATION OF DETECTOR STRINGS FOR THE KM3NET/ARCA NEUTRINO TELESCOPE

In this appendix, I briefly summarise the activity related to calibration tests performed on DUs of the KM3NeT/ARCA detector and carried out at the CAPACITY laboratory (Campania AstroPArtiCle Infrastructure FacilitY), in Caserta (Italy). First, the CAPACITY laboratory is described in Sect. A.1, as well as its purposes and goals. Then, after a brief description of the DU integration processes, the main elements of the calibration procedure are discussed in Sec. A.2. Test results, in particular with respect to time calibration, acoustic check, and led beacon runs, are presented in Sect. A.3, Sect. A.4, and Sect. A.5, respectively. The work here described is based on *S. Mastroianni, W. Idrissi Ibnsalih and* ***A. Zegarelli****, "Calibration Facility for Detector Strings for the KM3NeT/ARCA Neutrino Telescope at the CAPACITY Laboratory," in IEEE Transactions on Nuclear Science, doi: 10.1109/TNS.2023.3250483*.

For a better understanding of the topics here treated, the reader is invited to look through this appendix in association with Sect. 2.5.2, where the characteristics of the KM3NeT detector are presented, Sect. 2.6, which contains information about the procedures adopted to calibrate underwater Cherenkov neutrino telescopes, and Sect. 5.1, focused on the KM3NeT DAQ system.

A.1 THE CAPACITY LABORATORY

The realisation of the KM3NeT infrastructure is now proceeding toward the mass construction of DUs. In particular, the building activities of the KM3NeT/ARCA detector started in 2015 and has continued until leading to the current detector status, i.e. 21 DUs in data taking. In the coming 3 years, 114 additional DUs (already funded) are planned to be deployed. To sustain such an increase in the DU production rate, a collective effort is needed by the Collaboration. Several laboratories are involved in the construction of the KM3NeT/ARCA detector and, among those, the CAPACITY laboratory in Caserta (Italy) has quite recently started to actively participate. It has been fully operative since September 2020 and its primary goal is to integrate, test, and calibrate the DUs for the KM3NeT/ARCA detector before their deployment. To date, this laboratory has provided a very important contribution to the DU construction and integration for the last successful deployments during the sea campaigns in 2021 and 2022.

The facility mainly hosts several measurement instrumentations for photosensor characterisation and qualification, a hyperbaric chamber for DOM tests, a small water pool for photodetector studies, a few dark boxes for photosensor measurements and calibration, and finally also a test bench specifically dedicated to the DU data readout and online server for data processing and checks. Here, starting from the following Sect. A.2, we focus on the calibration activities performed on DUs in such a laboratory during the pre-deployment phase.

A.2 DU CALIBRATION IN DARK BOX

The construction and integration of DUs involve several challenging steps that take place at different sites of the KM3NeT Collaboration. Once the DOMs of a DU are produced and all the measurements and validation tests have been performed, the DU integration process starts. Firstly, the DOMs are electrically and optically connected to the VEOC such that each DOM has an assigned position within the DU. Then, the BM already integrated and closed in a titanium base container is connected to the VEOC. At this point, the DU is in principle in its final configuration, ready for the data taking. However, before continuing with the last procedure, that consists of rolling the DU on the Launching vehicle of Optical Modules (LOM)[1], the string needs to be tested and calibrated in a dedicated dark box. After the integration of the BM to the VEOC and a few days of darkening time, electrical power measurements are performed according to a well-defined sequence of operating conditions (DOM off/on/running) and various attached devices (hydrophone and beacon connected and turned on). Measurements are carried out by a microcontroller housed on the BM Central Logic Board (CLB), which reads the sensors on the power supply board. Several functional tests are then needed to verify that the embedded modules/devices work properly in each DOM, as, for example, the acoustic receives and LED becons, and the correct data transfer for compasses/tilmeters. The detector operation and data readout are managed by a testing station computer resource implementing all the hardware/software components and the optical connections to the DOMs. A full DAQ chain, consisting of on-shore/off-shore elements, network connection, and timing synchronisation components, is used to validate the data readout and the monitor information of all the DOMs under real conditions. The calibration operations take advantage of the use of the Control Unit (CU), a flexible instrument that allows the control of each part of the detector and triggering/processing programs. The CU is a gateway to access the central database of the Collaboration both for reading the detector definition and operating parameters and logging the readout parameters (i.e. temperature, humidity, compass, tiltmeter, current, link signal strength etc.). A fast analysis and an online monitoring can be performed on a subset of the selected data showing the status of the data taking (PMT and trigger rate, calibration checks, etc.).
After a careful setup and configuration, the exact synchronisation of all the DU CLBs must be strictly checked to guarantee the proper merging of the UTC time information with the acquired data and, then, the correct resolution by the onshore data acquisition system. Moreover, to provide subnanosecond synchronisation between the DOMs, the White Rab-

1 The string, during the deployment phase, after arrival at the seabed is unrolled to its full length.

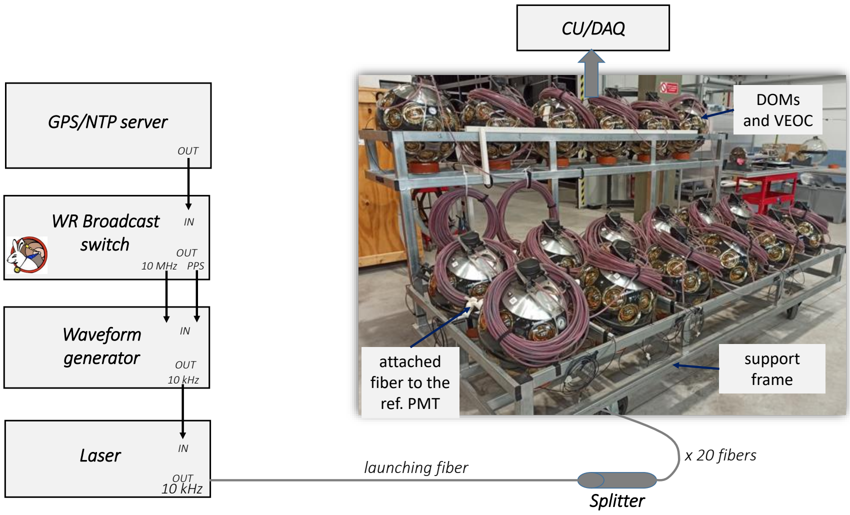

Figure A.1: Laser calibration system in the dark box for DU time measurements. 18 DOMs connected to the VEOC are arranged on a metallic frame which can be easily handled. This setup provides the inter-DOM calibration.

bit (WR) Precision Time Protocol (PTP) [411] is used in KM3NeT. Once the fast data are sent to the online data queues, the detector monitor operation and the data quality check can be run. After these data readout checks and preliminary measurements, the detector fine-tuning can be performed according to the procedure described in the following.

The PMT data frame, constituted by the information left by hits on PMTs, includes the arrival time and the ToT, which is the time the PMT signal is above a threshold of 0.3 p.e. During the pre-deployment calibration phase, the ToT distribution (typically peaked around 25 ns) is produced and checked for each PMT of all the DOMs. The channels with a unusual behaviour in this distribution are deeply investigated and eventually excluded in the following steps of the calibration procedure. Additionally, a counting rate obtained from the ToT distribution allows the exclusion of PMTs with extreme low and high counting rates, i.e. < 100 Hz or > 10 kHz, respectively

The High-Voltage (HV) tuning is defined by a desired gain of 3×10^6, that corresponds to a single detected photon ToT of about 26.4 ns. For each PMT of a DOM, all hits detected during a given run are read. The tuning procedure can be accomplished with a 8V HV scan ranging the interval between -56V and 56V centered around the vendor value (typically we take a few minutes run each step). By fitting multiple single photoelectron ToT distributions taken at different HV settings as a function of the PMT gain, the HV value that gives rise to a nominal gain can be estimated. More details can be found in [412] and [413]. The final HV tuned value can be estimated from a linear behaviour of ToT values versus HVs. The results of all the tests and measurements of DU calibration are stored in the main database allowing the final in-situ detector operation.

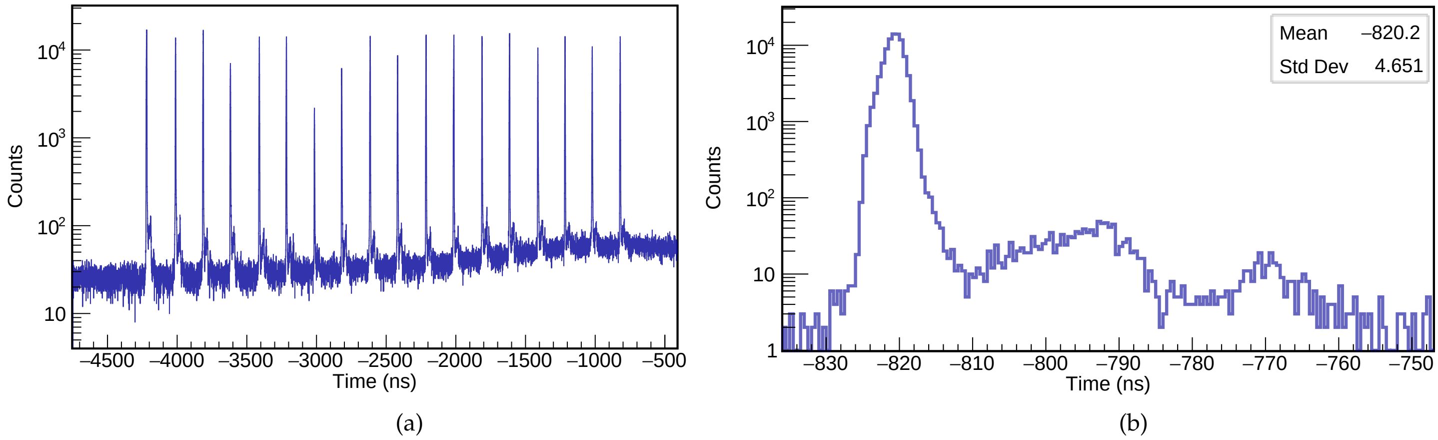

Figure A.2: Left: laser peaks for all the 18 DOMs of one of the ARCA DUs calibrated at the CAPACITY laboratory in Caserta. From right to left, the results from the first DOM (the closest to the seabed) to the last one (at the top of the string) are shown. Right: the zoom in on the laser peak observed on the first DOM of the DU is shown. The correction offset is calculated by the mean value of the Gaussian fit to the first peak of the distribution.

A.3 TIME CALIBRATION

The time synchronisation between several thousands of optical modules in a sparse array located in deep sea, such as KM3NeT, is mandatory to properly reconstruct the event signature and with this the event properties like direction and energy. The sub-nanosecond time synchronisation among the DOMs is the main goal of the DU timing calibration. It is obtained by a combination of several calibration procedures, consisting of the determination of the relative time offsets 1) between the PMTs in the DOM (intra-DOM); 2) between DOMs in the DU (inter-DOM); 3) and between different DUs (inter-DU). The intra-DOM offsets are mainly due to intrinsic time uncertainties of the individual PMTs (i.e., TTS). It is typically calibrated with signal from radioactive potassium decay in sea water (see Sect. 2.6), when the DU has already been deployed. The inter-DU offset depends on the propagation of the clock signals from shore to the base of each DU. An accurate measurement of the delay of the laser signal allows the evaluation of different contributions of latencies and asymmetries in the WR technology and then to the final correction. In CAPACITY, our main interest is focused on the inter-DOM time calibration that is performed in the dark box during the DU calibration. The details of the measurements are discussed below.

A.3.1 *Inter-DOM calibration in dark box*

The time delays between DOMs of a single DU are mainly determined by the different propagation time of the clock signal from the shore to the CLB boards. The DOMs are separated by a fiber length of about 36 m that corresponds to a time delay of about 180 ns, and the lower DOM receives the signals earlier than the upper one. The measurements of the

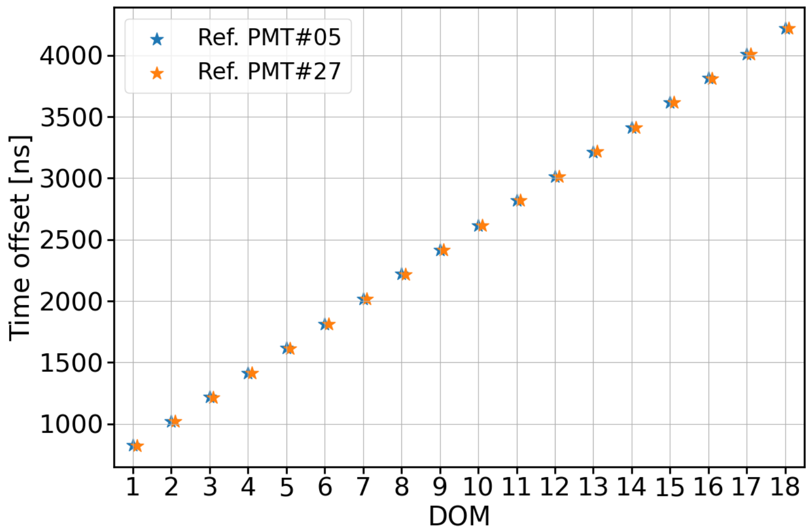

Figure A.3: Laser calibration result for one of the ARCA DUs calibrated at the CAPACITY laboratory in Caserta. The plot shows the time offsets for the reference PMTs as a function of the DOM position, numbered from bottom to top. Note that the results for reference PMT27 (bottom hemisphere) are slightly shifted with respect to the ones for PMT05 (top hemisphere) to allow to distinguish them.

time offset of each DOM in the string can be performed in the dark box by means of a laser source and a light distribution system that provides laser pulses directly and simultaneously to two reference PMTs chosen for all the DOMs. These light pulses are timestamped with respect to the reconstructed clock signal with the WRPTP, and the correction offset to be added to each DOM (with respect to the DU BM) can be calculated. The laser calibration system for time measurements is shown in Fig. A.1. A 10kHz laser pulse generation at a wavelength of 406 nm is synchronized with a pulse per second (PPS) signal from WR broadcast and the output feeds fibers illuminating 18 PMTs through a 1/20 optical splitter, one on each DOM. The resulting 18 laser peaks from the inter-DOM calibration, performed on an ARCA DU at CAPACITY laboratory, are shown in Fig. A.2(a). In particular, while the peak of the DOM closest to the seabed, namely DOM01, corresponds to the biggest values of the time axis, the one of the DOM at the top of the string, namely DOM18, has the smallest values. As regards the negative time measurements, it is worth mentioning that the CLB timeslice start signals synchronized with the WR master switch arrive later than the laser pulses. Fig. A.2(b) shows the arrival time distribution of first hits on PMTs in DOM01. The main peak of the distribution corresponds to the PMT Transit Time (TT). A Gaussian fit of the TT distribution provides the offset value (i.e. for DOM1, as shown in the figure, the mean value of the first peak is -820.2 ns). Note that such PMT TT distributions obtained during the calibration in the dark box are also used in Monte Carlo simulations and modelling. As the DOM readout electronics are segmented into two hemispheres, 2 PMTs of each DOM (one located in the upper and the other one in the lower hemisphere) are used for time calibration. These double-time measurements for each DOM allow an essential redundancy in case of an issue of one PMT or readout electronics. The behaviour of the time offsets (positive defined) for the two reference PMTs versus the DOM number is displayed in Fig. A.3. The linear increase of the time offset values, that starts from the

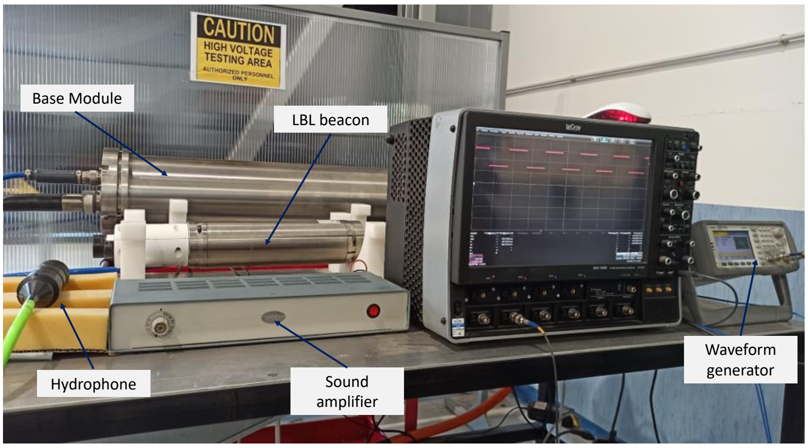

Figure A.4: Setup of the acoustic check validation. The BM is connected to the hydrophone and LBL beacon under test. A waveform generator, synchronised with WR system, outputs a sinusoidal wave to an acoustic amplifier to test the acoustic receiver functionality.

lower DOM to the one placed in the upper part of the string, is evident. When the time offsets are compared between the upper and lower hemispheres of the DOM, a mean/median time offset difference of the order of a few ns is observed, and this is expected as the PMTs have different TTs.

A.4 ACOUSTIC CHECK VALIDATION

During the DU calibration, we fully check the functionality of all the acoustic devices used for the positioning system. As previously explained, to determine the event reconstruction with good accuracy, the position of detector elements needs to be known with high accuracy (within 10 cm) and continuously monitored to overcome the effect of the sea currents. To validate the acoustic devices in each string, several careful checks are performed during the DU calibration. Firstly, communication tests and power consumption measurements are done. Then, the acoustic receiver functionality of the hydrophone and piezo-electric devices can be tested. For this purpose, the setup consists of a waveform generator, a sound amplifier-and-splitter (1/20) coupled with acoustic piezoelectric emitters (positioned at about 10 cm from the DOM south pole, near the piezo receiver). A sinusoidal wave emission at 30 kHz frequency and an amplitude of 2 V_{pp} is set. The acoustic emission is synchronised with WR system, and the generation is triggered by PPS signal. The acoustic data frames, thanks to a dedicated data filter on the online processing server, are quickly available on the DB and the correct detection of acoustic signals is checked through an analysis of ToA (Time of Arrival) of the emitters signals and their synchronicity with respect to the DU master clock.

A.5 LED BEACON AND OTHER RUNS

A crosscheck of the inter-DOM time calibration performed in the dark box can be carried out in-situ after the DU deployment through the Light Emission Diode beacon, also called NanoBeacon (NB) [226], installed in the upper part of each DOM. A short light pulse at a fixed wavelength of 470 nm with the possibility to configure the intensity and frequency of flashing is controlled by the CLB logic. Measurements of time differences between pairs of DOMs allow calibration of the surrounding DOMs with respect to the one emitting light. The NB functionality tests are performed in the dark box by checking the hits released on the PMTs closest to the emitting NB. Dedicated runs are taken with a bias voltage scan for each DOM NB.

Another special run characterised by a long duration (several hours), with a trigger that require at least 2 PMTs in coincidence on the same DOM, is collected to perform efficiency studies and long-monitor checks.

B

MONTE CARLO SIMULATIONS AND EVENT RECONSTRUCTION CHAIN IN ANTARES AND KM3NET/ARCA

In high-energy physics experiments, Monte Carlo (MC) simulations are typically used to understand the behaviour of the detector and its physics potential. Here, the MC chain developed for the ANTARES and KM3NeT/ARCA experiments (Sect. B.1) together with the reconstruction algorithms (Sect. B.2) are presented. In this regard, the software tools used within both experiments are briefly discussed. Some of the tools are common between the two; others will be specified for each of them.

Both the ANTARES and KM3NeT/ARCA simulation and reconstruction chains were used by the author of this thesis, within the context of works presented in Chapters 4 and 5, respectively.

B.1 MONTE CARLO SIMULATIONS CHAIN

The MC simulation chain provides the following steps:

1. Event generation;
2. Particles and light propagation;
3. Detector response simulation.

Physical events induced by neutrinos and atmospheric muons and capable of leaving a signature in a neutrino telescope are generated in the proximity of the detector and then propagated through the medium (i.e., for our detectors, in seawater); the emitted Cherenkov light is reproduced and photons are propagated to the OMs, taking into account also the PMT response. Finally, the data stream is simulated, also adding the optical background, together with the DAQ electronics and triggers. Triggered events resulting from the MC simulations are then reconstructed by specific algorithms as track- and/or shower-like events, as further explained in Sect. B.2. The complete analysis chain, i.e., the MC simulation steps together with the reconstruction typically implemented in the ANTARES and KM3NeT/ARCA detectors are summarised in Fig. B.1(a) and Fig. B.1(b), respectively. More details about the software tools adopted are provided below.

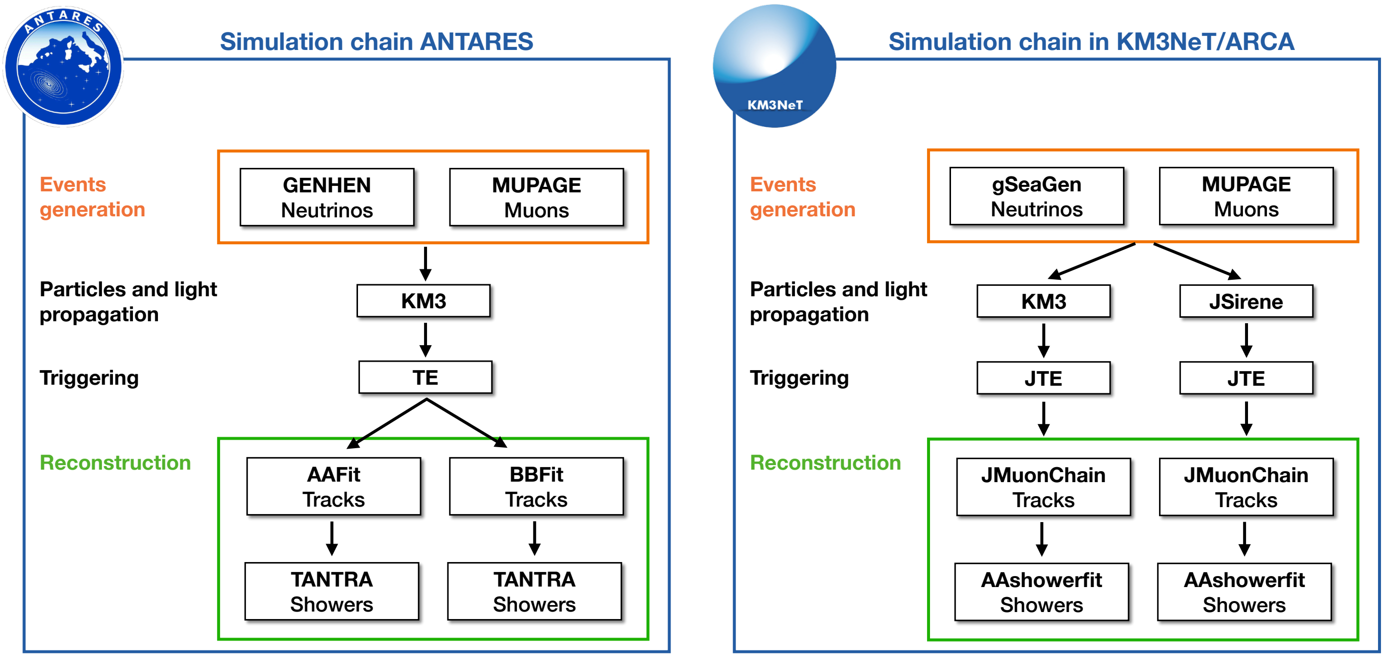

(a) (b)

Figure B.1: Analysis simulation chain implemented in ANTARES (a) and KM3NeT/ARCA (b) neutrino telescopes.

B.1.1 *Event generation*

As first step of the MC simulation chain, neutrino and atmospheric muon interactions are reproduced in seawater inside the so-called detector *can*, which is a cylinder representing the active volume of the detector surrounding the instrumented one (see Eq. (2.13) for its definition). Typically the can is built by enlarging the instrumented volume by a factor n times the light absorption length (see Sect. 2.2.1)[1], being n chosen in order to optimise the detector performances[2]. In practise, the can represents the volume surrounding the detector in which interactions can produce detectable particles, taking into account the density and composition of the media surrounding the detector: all events leading to Cherenkov radiation in the can, i.e. events interacting inside the can or producing a signal reaching the can surface, are included in the MC simulation chain.

For neutrinos, two different codes generating neutrino-induced events detectable in a neutrino telescope are available within the ANTARES and KM3NeT Collaborations. These are able to generate events induced by all neutrino flavours, considering topological differences between track-type and shower-like events. Both codes can simulate neutrinos coming from diffuse sources (e.g. atmospheric neutrinos) and from point-like or extended astrophysical sources, according to several interacting neutrino spectra (a power law $E^{-\gamma}$

1 Except from below, where the instrumented volume is bounded by the seabed, from which Cherenkov light cannot emerge.
2 For example, in KM3NeT/ARCA115 simulations used in Chapter 5, the effective volume, namely the detector can, is enlarged of a factor of 350 m with respect to the instrumented volume.

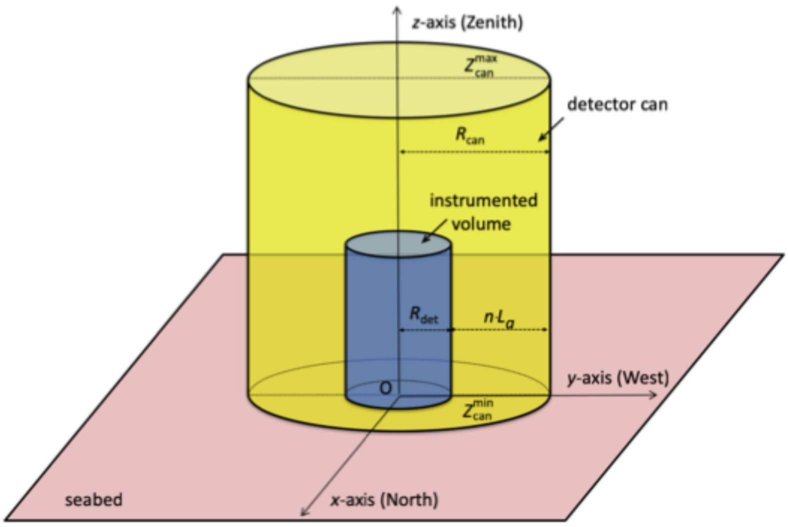

Figure B.2: Definition of the detector can. The instrumented volume (in blue) is surrounded by the *can* (in yellow), whose dimension is n times the light absorption length L_a. Credit image: [414].

is chosen for the generation spectrum of neutrino interactions, with γ as input of the simulation). More details about these codes are provided below:

- **GENHEN** (GENerator of High Energy Neutrinos) [415]: package (written in FORTRAN) developed inside the ANTARES Collaboration for MC neutrino simulations over the full range of energy for neutrino studies in ANTARES; the majority of detected neutrinos are in a range of energies from tens of GeV, limited by the energy threshold of muon detection at around 10 GeV, to multi-PeV, where the absorption of neutrinos in the Earth strongly attenuates the upward neutrino flux. Being not optimised at energies below $\sim$100 GeV, GENHEN cannot be used to simulate interactions below 10 GeV. This represents a clear limitation for studies at lower energies, i.e. those regarding atmospheric neutrino oscillation parameters. For this reason, the KM3NeT Collaboration has developed another code (described below) well representing also such low energies, these being of interest for the KM3NeT/ORCA detector, aiming at measuring the neutrino mass hierarchy and studying neutrino oscillations;

- **gSeaGen** [414]: C++ code based on GENIE (Generates Events for Neutrino Interaction Experiments) [416] and written within the KM3NeT Collaboration. Originally suited for the simulation of neutrino interaction up to 5 TeV, the new versions of this code are now able to cover the huge energy range from a few MeV to EeV, profiting from recent GENIE extensions. For this reason, gSeaGen is currently considered the official MC neutrino simulator for both the KM3NeT/ORCA and KM3NeT/ARCA detectors, and it has been recently extended to some simulations for ANTARES analyses. The last software release at the time of writing is available at [417].

Regarding the present thesis, GENHEN has been adopted for simulating neutrino events inside the ANTARES detector in the context of the analysis discussed in Chapter 4 (in particular, see Sect. 4.4.1); gSeaGen, in turn, for MC simulations of neutrino-induced events in KM3NeT/ARCA used to obtain the results discussed in Chapter 5 (Sect. 5.3.2).

For atmospheric muons, **MUPAGE** (MUon GEnerator from PArametric formulas) [418] is used both in ANTARES and KM3NeT. This code was developed for the production of atmospheric muon bundles on underwater detector can surface and is based on the usage of a parameterisation that describes the multiplicity of each muon bundle, the distance of each muon from the shower axis, and the energy spectrum within each event [198]. This has been built using a complete simulation, performed with the HEMAS software [419], using the angular distribution and the energy spectrum of underground muon measurements. MUPAGE allows the production of atmospheric muons between 0° and 85° in zenith angle and covers the entire range of energies relevant for a neutrino telescope.

B.1.2 *Particle and light propagation*

All long-lived particles produced in neutrino interactions are tracked through the can volume; namely, after the generation they are followed during their propagation until they interact or decay, inferring the Cherenkov radiation that is produced. Light is also propagated until it is absorbed or detected by PMTs. The main codes used in ANTARES and KM3NeT studies for particle and light propagation have been developed by the Collaborations themselves and are described in the following:

- **KM3**: GEANT-based software simulating all particle propagation inside the can and the light that reaches the OMs. All physical relevant processes such as energy losses, hadronic interactions, light emission, and multiple scattering are considered (see Sect. 2.1.3). The emission of Cherenkov light is performed on a statistical basis, i.e. using the probability of a photon to produce a hit on a PMT. The computation of such probability is taken from tables which include the probability distributions of the number of hits and the arrival times of the hits for photons originating from different positions and with different orientations with respect to the OM. The effect of the OM angular acceptance and efficiency is included. Note that KM3 uses the *multi-particle approximation*, namely all particles that are not electrons or muons are simulated as equivalent electrons with the appropriate light yield. This collective approximation of the hadronic cascade makes KM3 unsuited for the simulation of low-energy neutrino events in KM3NeT/ORCA, where the individual hadronic cascade topology plays a role in event reconstruction; the same approach is not problematic for KM3NeT/ARCA and ANTARES, given the larger spacing between OMs and the higher energy threshold.

- **JSirene**: framework for the light propagation developed within the Jpp project, already presented in Chapter 5. It is analogous to the previous software, but, instead of using tables as KM3, JSirene takes analytical PDFs that give the users the probability for a photon, produced at a certain distance with a given energy and a certain angle with respect to the light sensor, to arrive to a PMT and to be converted into a photoelectron. The distance and angle to generate the PDFs are computed from the interaction vertex for tracks and from the maximum of electron emission in the case of a shower.

B.1.3 *Detector response simulation and trigger*

Estimating the trigger efficiency is a crucial step in each analysis. The detector response is simulated in ANTARES and KM3NeT with two different programmes with the same functionalities, called **TriggerEfficiency** (TE) and **JTriggerEfficiency** (JTE), respectively. These simulate the PMT response including electronics and accounting for the individual PMT efficiencies and the detector calibration. E.g., for the KM3NeT detector, JTE is responsible for the application of triggers defined in Sect. 5.1.1. By default, only events that survive at least one trigger are kept for physics data analysis.

After the simulation of light propagation, the Transit-Time Spread (TTS)[3] of the PMTs is simulated. In the KM3NeT software, a Gaussian smearing is applied to the hit arrival times to simulate the TTS. In ANTARES, it is simulated directly from its measured values. Coincident hits on the same PMT are also merged into a single pulse with an increase in ToT. In addition to the detector response to individual hits, the background due to environmental conditions can also be directly simulated at this step, including the ^{40}K contribution at each multiplicity and the total baseline rates. However, note that the programme does not provide the possibility of simulating time/space correlations from bioluminescence.

B.1.4 *Run-by-run strategy*

The MC simulation strategy provides the possibility to simulate the detector response in a *Run-By-Run* (RBR) mode: for every physics run, a specific MC is produced through a TE/JTE option that takes information from data and uses it in processing the physics output of the MC chain. This approach is used to take into account the variability of conditions in a marine environment and their effect on data acquisition. In this way, a temporary or permanent malfunction of a PMT is also considered. Finally, only the triggers active during a specific data acquisition run considered in the simulation.

In this thesis, the RBR strategy was used in the stacking analysis aimed at looking for ν-GRB coincidences using ANTARES data and is described in Chapter 4. In particular, it was used to simulate inside the ANTARES detector the expected neutrino signal coming from a temporal and spatial window selected around each GRB of the used sample, taking into account the specifics of the data acquisition run during which each burst occurred.

3 The TTS of a PMT refers to the transit time jitter of a single photoelectron output pulse generated by the amplitude of the light pulse irradiating the photocathode surface, which is an important indicator to measure the time characteristic of the PMT. Generally, the full width at half maximum of the statistically obtained electron transit time spread is called the TTS.

B.2 EVENT RECONSTRUCTION

The reconstruction of triggered events is a fundamental step in the analysis chain with neutrino telescopes, where an event is basically a set of triggered hits detected by the PMTs, associated with a position, a time, and a charge related to the number of photoelectrons that is detected. In this view, the patterns of the hit time, hit amplitude, and hit position over the strings are used to trace back the trajectory of the particle inducing the Cherenkov light, and hence to infer the interaction vertex, the direction of the outgoing lepton and its energy, the latter quantities being a proxy of the parent neutrino energy and the direction of the parent interacting neutrino. Different approaches are followed according to the detector configuration and the event topology (tracks and showers).

Algorithms that perform the event reconstruction for ANTARES and KM3NeT are described below. Note that their performances, previously discussed in Sect. 2.5.3, depend on the precision of reconstruction software, because they determine the detector capability to infer the direction of incoming neutrinos through their interaction products (angular resolution), as well as their energy (energy resolution).

B.2.1 *Track reconstruction*

In this thesis, two track event reconstruction algorithms have been used, one for ANTARES (in Chapter 4) and the other for KM3NeT (in Chapter 5). A brief description of the two and the quantities specifically used in this work are reported in the following.

B.2.1.1 *ANTARES*

DIRECTION RECONSTRUCTION **AAFit** [420] is a high performance algorithm developed by the ANTARES Collaboration to reconstruct track-like events and used in the present thesis for the analysis in Chapter 4. It is based on a likelihood fit, which is recursively performed through several steps with an increasing sophistication, up to provide the starting point for the last likelihood fit: a linear prefit (χ^2 minimiser), a M-estimator fit (also a minimiser) and a maximum likelihood fit with a simplified PDF. Based on causality criteria, a pre-selection of hits is applied to feed the reconstruction algorithm and discard pure-noise hits. After these three steps, a final maximum likelihood fit is performed, which gives the direction of the reconstructed track. To this aim, a maximum likelihood function $\mathcal{L}$, which includes hits with small time residuals with respect to the PDF used in the first step, is used. A final PDF of the observed hit time residuals as a function of track parameters is thus obtained.

The quality of the track reconstruction Λ is estimated as

$$\Lambda = \frac{\log \mathcal{L}}{N_{\mathrm{DOF}}} + 0.1(N_{\mathrm{comp}} - 1), \tag{B.1}$$

where the number of Degrees Of Freedom (DOF) of the track is given by $N_{\mathrm{DOF}} = N_{\mathrm{hits}} - 5$ and N_{comp} represents the number of solutions found by the reconstruction algorithm compatible with the preferred result. N_{comp} is also an indicator for rejection of misreconstructed tracks: for badly reconstructed events, $N_{\text{comp}} = 1$ on average, and can reach values up to 9 for well-reconstructed events (i.e., all the solutions have resulted in the same track). So, higher values of Λ, better quality of the track reconstruction.

Another important parameter returned by AAFit is the angular uncertainty β on the reconstructed muon track:

$$\beta = \sqrt{\sigma_{\phi^2} \sin^2(\theta_{\text{rec}}) + \sigma^2_{\theta^2}}, \tag{B.2}$$

where θ_{rec} is the reconstructed zenith angle of the track, and σ_θ and σ_ϕ are the uncertainties in the reconstructed zenith and azimuth angles, respectively.

Typically, event selection criteria based on Λ and β parameters, in Eq. (B.1) and Eq. (B.2), respectively, are used to improve the signal-to-noise ratio, as also done in Chapter 4: to ensure solid directional reconstruction of the selected neutrino candidates, $\beta < 1°$ is required; additionally, selecting simulated tracks with high reconstruction quality, allows us to reject most of the so-called misreconstructed events, namely atmospheric muons falsely reconstructed as up-going.

Note that another direction reconstruction algorithm, called BBFit [421], was developed for ANTARES. This constitutes an alternative strategy (χ^2 based) mainly used in analyses focused on sub-TeV energies (e.g., dark matter), for which the algorithm is optimised. For TeV-PeV energies, the better performant AAFit algorithm is preferred. However, BBFit has been also adopted by ANTARES in online triggering follow-up observations among other multimessenger studies. Indeed, its performs much faster, improving the computation time with respect to AAFit of a factor of ~ 10, and this is very important for a real-time observational strategy, discussed in Sect. 1.6.2. In fact, BBFit considers only the time and position information of the hits, resulting in a simplified geometry of the detector. Despite the less accuracy, the software is however able to reconstruct the muon direction with good efficiency: its reachable median angular resolution lies between $\sim 1°$ and $\sim 3°$ for multi-line and single-line events, respectively.

ENERGY RECONSTRUCTION For energy reconstruction in ANTARES, several estimators can be used, using various features of the muon energy loss processes, applying different statistical methods and reaching different levels of complexity. Some methods use parameter fitting, such as the timing information of the number of hit repetitions per OM and the charge deposited during the particle propagation; others, instead, are based on PDFs (a machine learning technique and maximum likelihood method are available).

Among them, one of the most used is based on the total muon energy loss mechanism; it is called *dE/dx energy estimator* and is parameterised as in Eq. (2.5). To determine the muon energy loss, the dE/dx estimator uses the total number of photons created by the muon and incident on the PMTs. The total energy loss can be approximated by the quantity ρ as

$$\frac{\mathrm{d}E_\mu}{\mathrm{d}x} \sim \rho = \frac{\sum_{i=1}^{N_{\text{hit}}} a_i}{L_\mu \epsilon}, \tag{B.3}$$

where N_{hit} is the number of hits used for the reconstruction of the track, a_i denotes the charge recorded by a given PMT i, L_μ is the length of the muon path in the detector, and ϵ is a correction factor for the detector efficiency (it is a function of the distances between the active PMTs and the reconstructed muon track and takes into account the angular acceptance of the OMs). The quantity in Eq. (B.3) is then converted to an energy estimation through calibration tables created from MC simulations. For more details on all the energy estimator methods, see [422].

B.2.1.2 *KM3NeT/ARCA*

In KM3NeT/ARCA, `Jpp` applications are used to perform event reconstruction as a muon track, determining its direction and energy in a same simulation chain, as explained in [423]. This is called **JMuonChain** and includes the steps described below. As a coordinate system for the muon trajectory fit, the one shown in Fig. B.3 is considered: given an assumed direction for the muon, it travels along the z-axis crossing the $z = 0$ plane at coordinates (x_0, y_0) at time t_0. In the absence of scattering and dispersion of light, the expected arrival time of Cherenkov photons on a PMT i, can be expressed as

$$t_i = t_0 + \frac{z_i}{c} + \tan(\theta_c)\frac{\rho_i}{c}, \tag{B.4}$$

where θ_c is the characteristic Cherenkov angle, $\rho_i = \sqrt{(x_i - x_0)^2 + (y_i - y_0)^2}$ is the minimum distance of the muon from the PMT and z_i is the distance from the PMT to the $z = 0$ plane.

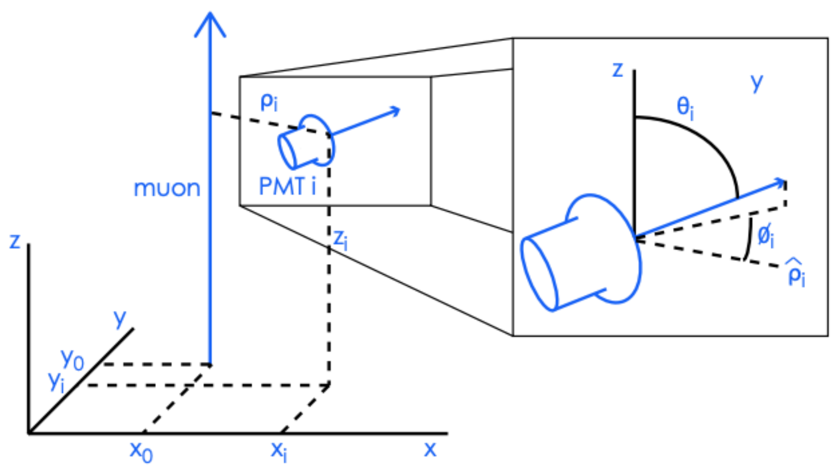

Figure B.3: Coordinate system used in the muon trajectory fit. Credit image: [423].

1. **`JMuonPrefit`**: this step overcomes the difficulty in the directional reconstruction fit arising from the fact that this is originally a nonlinear problem, the muon trajectory being defined by its position and direction at each point in time, for a total of five independent parameters. In fact, the prefit is used to provide a suitable set of start values for the final trajectory fit. By considering all pairs of consecutive hits,

the problem becomes solvable. At this level, hits caused by optical background and strongly scattered photons are excluded by selecting a cluster of causally related hits, on which a linear fit is applied. Possible outliers are removed as long as their contribution to the total χ^2 is greater than 3 standard deviations. This procedure is repeated for a scan of assumed track directions within a specific angle (the default value for KM3NeT/ARCA is 1°). The N best-fit solutions are stored and used in the next reconstruction stage ($N = 12$ used as a default value at the time of writing). The quality of the fit is quantified as[4]

$$Q = \mathrm{DOF} - 0.25\frac{\chi^2}{\mathrm{DOF}}. \tag{B.5}$$

2. **`JMuonSimplex`**: starting from the fit solutions of `JMuonPrefit`, it performs an intermediate χ^2 fit improving the reconstruction accurancy and reducing time residuals.

3. **`JMuonGandalf`**: this code represents the main algorithm of JMuonChain. Starting from the twelve best-fit directions in the prefit, a maximum-likelihood search is performed. By adopting an iterative approach, the following quantity is minimised:

$$\lambda = \frac{\ln \mathcal{L}(dt_1, dt_2, ...dt_M|H_0)}{\ln \mathcal{L}(dt_1, dt_2, ...dt_M|H_1)}, \tag{B.6}$$

that represents the ratio between the logarithm of the likelihoods that a cluster of hits with relative detection times dt_i ($1 \leq i \leq M =$total number of hits in the cluster) was caused by background only (H_0) and a track particle (H_1). The best track is the one with the minimum λ value, found through the Levenberg-Marquardt algorithm [424, 425]. The quality of the fit is then returned by a quantity (called *lik*) which is higher the better is the fit. In the likelihood function, the PMT response is described by a set of PDFs as

$$\mathcal{L} = \prod_{\text{PMT hits}} \frac{\partial P}{\partial t}(\rho_i, \theta_i, \phi_i, \Delta t), \tag{B.7}$$

where θ_i and ϕ_i describe the orientation of the PMT (see Fig. B.3) and Δt is the difference between the expected and measured arrival time of photons on PMTs. PDFs include information about the PMT response as a function of the minimum distance from the muon track to the PMT, the PMT orientation, and the time residual of the hit. These are computed semi-analitically from simulations. In this regard, it is worth mentioning that muon arrival time PDFs are found to be characterised by a very sharp peak that exceeds the expected background rate by many orders of magnitude [423]. This constitutes the key for achieving the optimal performances expected in KM3NeT/ARCA, in particular the unprecedented angular resolution of $\sim 0.1°$ at energies greater than 10 TeV (see Fig. 2.12).

4 Dividing by the number of degrees of freedom is done in order to weight the fit directions with small associated hit statistics with those fit directions with a large number of hits. The division by 4 is chosen to provide sufficient separation between the qualities of the individual fits.

4. **JMuonStart**: this reconstruction step defines the vertex, i.e. the start position, of the muon trajectory. The first emission point along the track, under the Cherenkov angle, exceeding the random background level, is selected as the start position.

5. **JMuonEnergy**: the last step of the chain determines the muon energy through the maximisation of a likelihood that considers, as a function of the muon energy, the spatial distribution of hits/no-hits on PMTs inside a cylindrical volume surrounding the track hypothesis. The probability of a PMT being hit is obtained from the same PDFs as those introduced for the JMuonGandalf step. All PMTs within a predefined road width (200 m by default in KM3NeT/ARCA) around the muon trajectory are used.

The reconstruction chain described above is important for this thesis, as it is adopted for the real-time reconstruction of events in the KM3NeT/ARCA detector (see Chapter 5). In particular, the Jpp modules for estimating the vertex and energy of online events (steps 3. and 4.) have been developed for the first time in the context of the present thesis.

B.2.2 *Shower reconstruction*

TANTRA (Tino's ANTARES shower Reconstruction Algorithm) [426] and **AAshowerfit** [423] are the shower reconstruction algorithms developed in ANTARES and KM3NeT/ARCA, respectively. While for tracks the vertex position is reconstructed, in the case of showers the algorithms fit the position of the maximum of the shower development. In addition, since tracks can start outside the instrumented volume, meanwhile showers are contained events in the detector, in the latter case it is easier to infer the energy, by estimating the energy deposited in the detector. Both TANTRA and AAshowerfit are based on an initial fit of the vertex position followed by a cascade direction fit. A likelihood maximisation is performed, the likelihood being built considering the distribution of PMTs being hit or not.

Since for the purposes of the present thesis these algorithms are not used[5], their details are not provided here. The interested reader can refer to the references previously indicated for a detailed description of all reconstruction steps.

5 At the time of writing, the implementation of real-time shower reconstruction for events detected by the KM3NeT/ARCA detector is under development and test. To this aim, we are adapting AAshowerfit to online purposes, taking DAQ events as input of the algorithm, analogously to the online track reconstruction.

C

RECONSTRUCTED ENERGY CORRECTION FOR KM3NET/ARCA6 MC PRODUCTION

In this appendix, I present a correction derived for reconstructed energies of events detected by the 6 strings configuration for the ARCA detector (KM3NeT/ARCA6). Both neutrinos and muons resulting from dedicated MC simulations (the MC production chain for KM3NeT is described in Appendix B), can be gone through a reconstruction chain able to estimate the direction and the energy of the incoming neutrino and/or muon generating the detected signal with a quality defined by a parameter called *lik*.

By comparing the event direction and energy at generation level and the same quantities returned at the end of the reconstruction chain, it is possible to evaluate the level of accuracy in characterising each event; namely, the angular resolution with which the direction of the original event is reconstructed and the energy resolution, both already discussed during this thesis (in Sect. 2.4.1 and Sect. 2.4.2, respectively). As regards the energy, one should take into account that the reconstruction software returns a value that need to be revised through a specific correction, that is MC dependent; in other words, for a proper evaluation of each event energy, the original reconstructed value is recalculated thanks to a correction derived by comparing the generated and the reconstructed energy values. Note that each correction can be used only for the specific MC production from which it has been derived, namely it refers on a specific detector configuration and MC software version. In addition, different energy corrections need to be applied on neutrinos and atmospheric muons, being these generated in the MC production chain by different software.

In the following Sect. C.1, the characteristics of the KM3NeT detector configuration with 6 strings, for which the energy correction has been derived, are presented. This correction is provided in Sect. C.2, together with the neutrino MC production that has been used to derive it, and is finally applied in an analysis, performed by KM3NeT, searching for neutrinos in association with the blazar PKS 0735+17 in Sect. C.3.

C.1 KM3NET/ARCA6 DETECTOR CONFIGURATION

For deriving the energy correction here discussed, a specific MC simulation for KM3NeT/ARCA at 6 strings was used, that refers to an ideal detector which is not tuned to the exact settings of the true calibrated detector in the seawater. This MC production was,

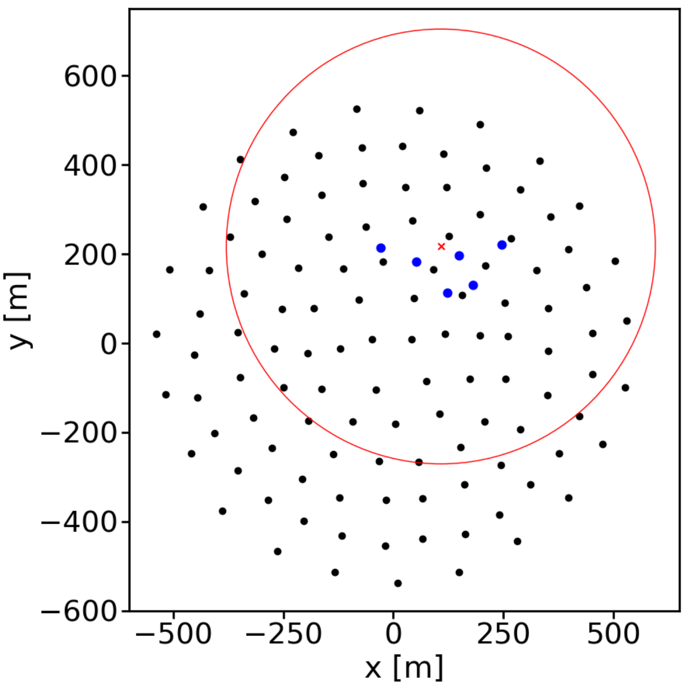

Figure C.1: Footprint of the KM3NeT/ARCA6 ideal detector used for the MC simulation. The 6 strings are shown as blue points, overlayed to the KM3NeT/ARCA115 footprint (black points). The *can* considered in the simulation is indicated as a red circle (whose center is given as a red dot).

indeed, produced to test the performances of KM3NeT/ARCA6 before its deployment (it will be called in the following *ARCA6 test production*).

The footprint of KM3NeT/ARCA6 is shown (in blue) in Fig. C.1, where it is compared with the future detector configuration KM3NeT/ARCA115 (in black). The effective volume (introduced in Eq. (2.13)), within which the detector is supposed to be able to trigger events, is indicated in red.

C.2 NEUTRINO MC PRODUCTION AND ENERGY CORRECTION

To derive the energy correction for neutrino events in the KM3NeT/ARCA6 detector, 200 MC simulations files were used both for ν_μ-CC and $\bar{\nu}_\mu$-CC events, generated between 100 GeV and 100 PeV according to an $E^{-1.4}$ power law[1]. In Fig. C.2, a 2D histogram comparing the simulated MC energy (`mc_trks[0].E`) and its corresponding reconstructed value for the track with the highest value of *lik* parameter (`best_t.fitinf[4]`) is shown. In Fig. C.3, the distribution of all (`best_t.fitinf[4]`) values from entire sample of MC files is reported.

For the estimation of the energy correction, only events with number of triggered hits $N_{\text{hits}} > 20$, $lik > 60$ and angular uncertainty $\beta_0 < 1°$ are considered, as they allow to partially discard noise and badly reconstructed events and obtain a more detailed evaluation

1 It is worth noting that in the used MC files the muon energy is at *can* level. In principle, for this reason, a first correction that evaluates the fitted muon energy at the enter point into the *can* has to be applied. However, as this effect is expected to be small, it is here discarded.

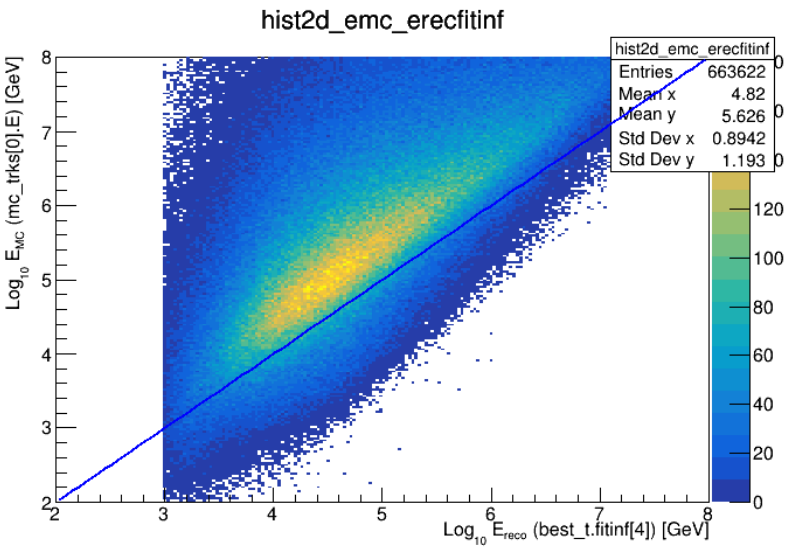

Figure C.2: Logarithm of the true MC energy as a function of the logarithm of the uncorrected reconstructed energy for $\nu_\mu + \bar{\nu_\mu}$ in ARCA6 test production. The blue solid line shows the bisector, where both distributions should peak if the reconstructed energies were as simulated ones.

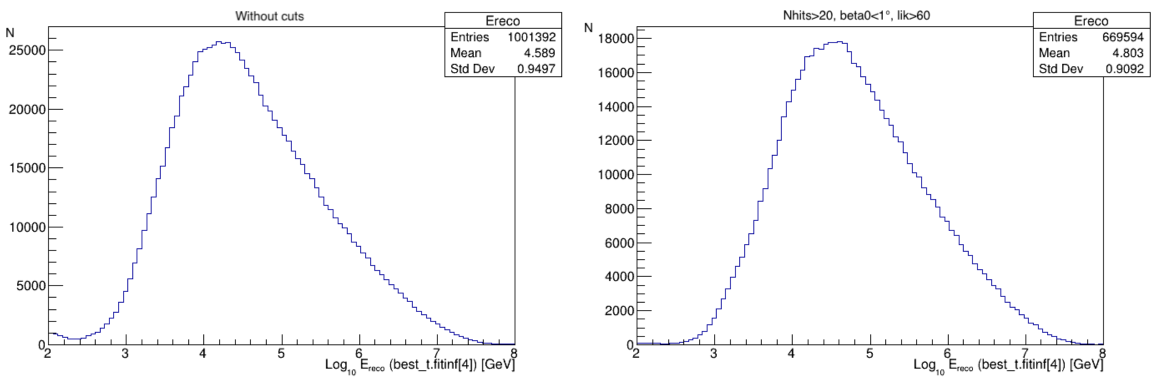

(a) (b)

Figure C.3: Logarithm distribution of the uncorrected reconstructed energy for $\nu_\mu + \bar{\nu}_\mu$ in ARCA6 test production (a) without any cut, and (b) with cuts $N_{\text{hits}} > 20$, $lik > 60$ and $\beta_0 < 1°$.

of the energy correction. From Fig. C.2, it is clear that the reconstruction chain tends to underestimate the real energy of the detected tracks induced by ν_μ and $\bar{\nu}_\mu$ CC interactions in KM3NeT. This demonstrates the importance of evaluating and applying an energy correction for events at the end of the reconstruction procedure.

The method adopted to correct energy values as directly returned by the reconstruction software is:

1. The median of each bin in the 2D-histogram of E_{MC} vs E_{reco} as in Fig. C.2 is evaluated;

2. A fit of those median values as a function of the reconstructed energies is performed;

3. The best-fit found in the previous step is then used as correction of the reconstructed energy.

The results of steps 1. and 2. are shown in Fig. C.4. The median values of the MC versus reconstructed energies for each bin of Fig. C.2 are represented by the grey crosses. The red solid lines show the fits performed on these points for two different energy ranges, namely E_{reco} between 1 TeV and 1 PeV, and E_{reco} >1 PeV. The fit in the energy region between 100 GeV and 1 TeV is discarded, because of the low statistics available with the set of MC simulations used.

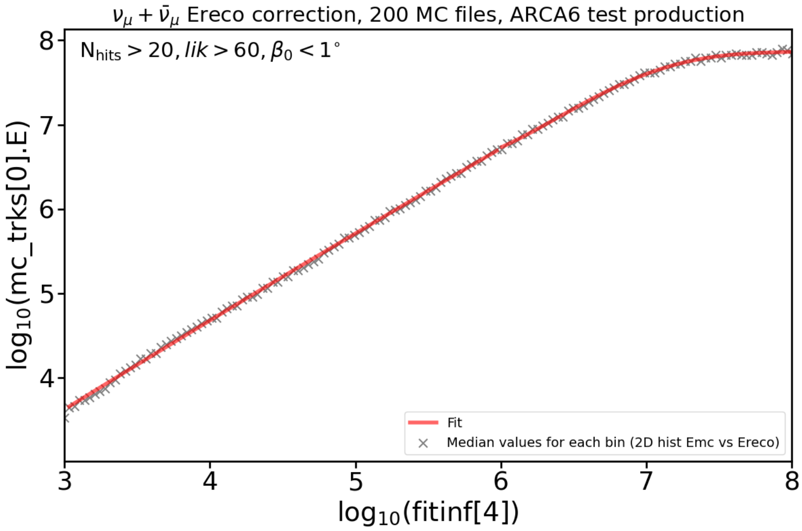

Figure C.4: Median values of $\log_{10}(\mathrm{E_{MC}})$ vs $\log_{10}(\mathrm{E_{reco}})$, where $\mathrm{E_{reco}}$ is stored in fitinf[4].

The functional form of the fitting function shown in Fig. C.4 for E_{reco} between 1 TeV and 1 PeV is given by the following polynomial (goodness of fit: $\chi^2 \simeq 0.01$):

$$\log_{10}(E_{\mathrm{true}}) = 0.320148 + 1.135019\ \log_{10}(E_{\mathrm{reco}}) - 0.011443\ \log_{10}(E_{\mathrm{reco}})^2, \tag{C.1}$$

while for $E_{\mathrm{reco}} > 1$ PeV (goodness of fit: $\chi^2 \simeq 0.002$)

$$\begin{aligned}\log_{10}(E_{\mathrm{true}}) = 316.930828 - 180.943643\ \log_{10}(E_{\mathrm{reco}}) + 38.962374\ \log_{10}(E_{\mathrm{reco}})^2 + \\ -3.674432\ \log_{10}(E_{\mathrm{reco}})^3 + 0.128467\ \log_{10}(E_{\mathrm{reco}})^4.\end{aligned} \tag{C.2}$$

By applying the corrections in Eqs. (C.1) and (C.2) to the energy values returned by the reconstruction chain in the MC neutrino production, the results in Fig. C.5 are obtained, where the true MC energies and the corrected ones are compared. Such plot demonstrates the validity of the correction found on the ARCA6 MC test production (produced in the energy range 100 GeV - 100 PeV) by applying the cuts $N_{\mathrm{hits}} > 20$, $lik > 60$ and $\beta_0 < 1^\circ$.

Note that this correction has been derived by using MC neutrino files where the spectral index at generation level is equal to 1.4. However, neutrino spectra usually considered in analyses searching for neutrinos produced in astrophysical sources, usually consider a spectrum $\phi_\nu \propto E^{-2}$. For this reason, how the difference in neutrino spectrum could affect the energy correction was investigated. Indeed, in Fig. C.6 a 2D histogram of $\log_{10}(E_{\mathrm{reco,corr}}/E_{\mathrm{MC}})$ vs $\log_{10} E_{\mathrm{MC}}$ reweighted by considering the neutrino spectrum with a shape $\propto E^{-2}$ is shown (for the explanation of the computation of event weights, the reader

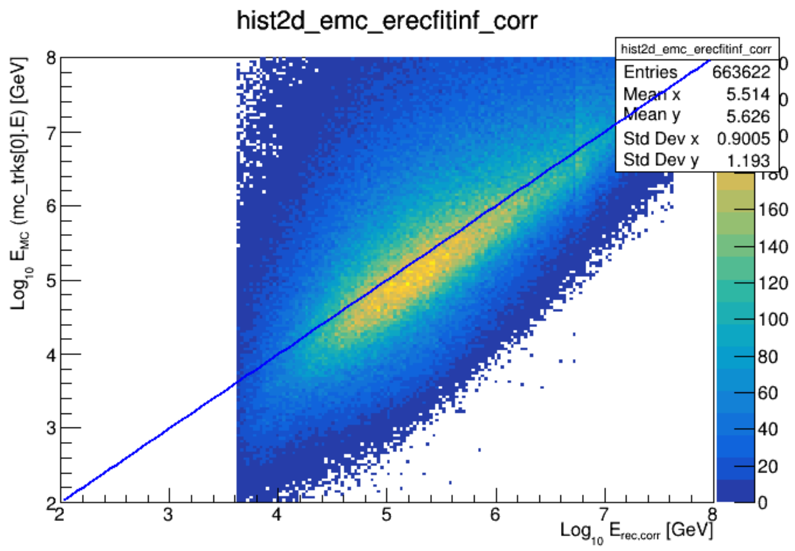

Figure C.5: True MC energy as a function of the corrected reconstructed energy for $\nu_\mu + \bar{\nu}_\mu$ in ARCA6 test production.

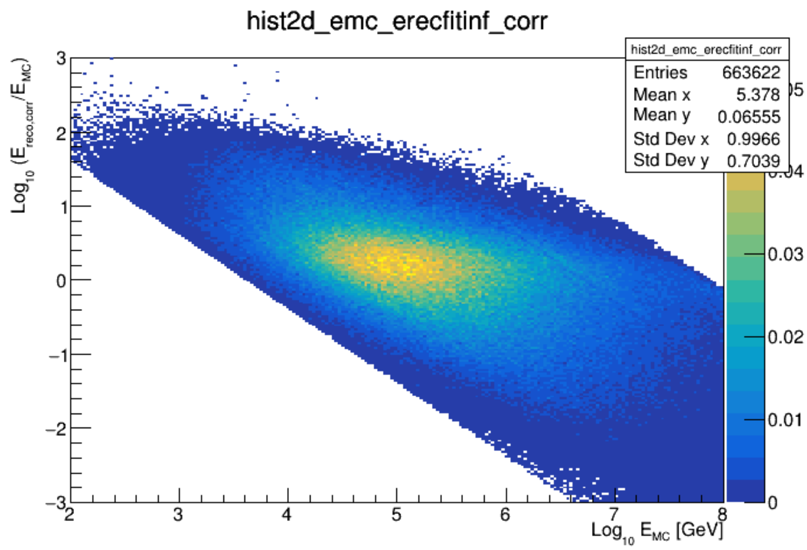

Figure C.6: Comparison among reconstructed and MC neutrino ($\nu_\mu + \bar{\nu}_\mu$) energies in ARCA6 test production by weighting the neutrino spectrum for a signal energy spectrum of $\propto E^{-2}$.

can refer to [414]). It appears that the corrections found in Eq. (C.1) and (C.2) describe well also the spectra weighted with a hard spectrum: after correctly weighting the neutrino spectra, on average $E_{\mathrm{reco,corr}} \simeq 1.2\ E_{\mathrm{MC}}$.

Note that, in turn, atmospheric muons show an opposite behaviour with respect to neutrinos, namely the reconstructed energies generally overestimate the real (simulated) muon energy values. As an example, Fig. C.7 and Fig. C.8 show this behaviour for the most energetic muon of the bundle and for the entire muon bundle (the energies of each muon are summed up), respectively. Such results were obtained through 50 MC files of the ARCA6 test production, each containinf the result of a simulation of 10^7 atmospheric muons.

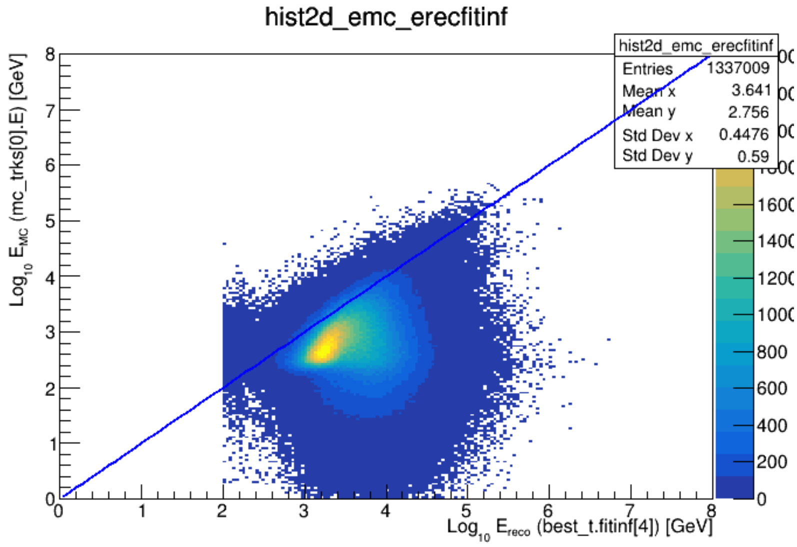

Figure C.7: Logarithm of the true MC energy as a function of the logarithm of the uncorrected reconstructed energy for the most energetic simulated muon among all the muons of each bundle in ARCA6 test production (`MUPAGE` simulations). The blue solid line shows the bisector, where both distributions should peak if the reconstructed energies represent the real ones.

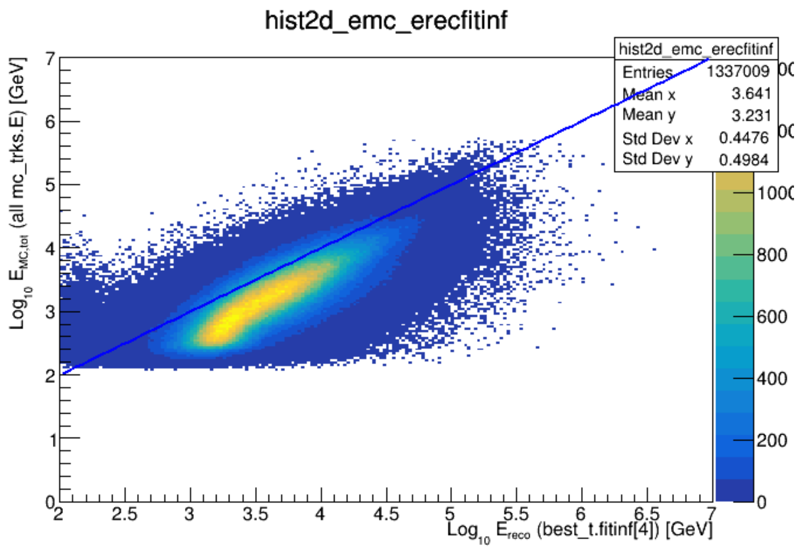

Figure C.8: Logarithm of the true MC energy as a function of the logarithm of the uncorrected reconstructed energy for the simulated muon bundle (the energies of each muon of the bundle are summed up) in ARCA6 test production (`MUPAGE` simulations). The blue solid line shows the bisector, where both distributions should peak if the reconstructed energies represent the real ones.

C.3 ASTROPHYSICAL APPLICATION: SEARCH FOR NEUTRINOS IN ASSOCIATION WITH THE BLAZAR PKS 0735+17

The energy correction here investigated has been applied, for the KM3NeT/ARCA detector, in a specific analysis performed by the KM3NeT Collaboration, whose results can be found in [427].

The 8th of December 2021, the IceCube Collaboration detected a track-like event characterised by a moderate probability of being of astrophysical origin [428], alerting the worldwide multimessenger community and encouraging follow-up by other instruments to help identify a possible astrophysical source for the candidate neutrino. This event was associated with a strong flare of the blazar PKS 0735+17 in γ rays, X rays and radio and, interestingly, also the Baikal-GVD Collaboation reported an observation of a high-energy cascade neutrino in coincidence with this flaring blazar and the IceCube event (IC 211208A) [429]. At that time, the automatic analysis pipeline described in Chapter 5 was not active and it was not possible follow-up KM3NeT data in real-time. However, motivated by the interesting scientific case, in the subsequent weeks KM3NeT looked at data to search for a potential correlation with IC 211208A and the flare of PKS 0735+17, the latter covering the full month of December 2021. During a ± 1 day time-window centered on the IceCube event time, no up-going muon neutrino candidate was recorded by the ARCA detector within an MDP optimized search cone of 1.4° radius centered on the blazar coordinates. During this time window, the source remains 42.3% visible. An additional search over an extended time window covering the full month of December 2021 has yielded one up-going muon neutrino candidate in coincidence in ARCA at Dec 08h51'31.6 from the blazar direction (RA=113.5°, DEC=17.6°, Error (50%) = 1.8°). The energy of this event, under the hypothesis to be induced by a neutrino, was estimated to be $\sim$18 TeV. This evaluation was possible thanks to the energy correction in Eq. (C.1), since the KM3NeT/ARCA detector was taking data at that time with a configuration similar to the one described in Sect. C.1. The p-value of this association is 0.14. The 5-95% neutrino energy range where this search is sensitive is 9 TeV-11 PeV.

BIBLIOGRAPHY

[1] T. Wulf, "Observations on the radiation of high penetration power on the Eiffel tower", *Physikalische Zeitschrschift*, vol. 11, p. 811, 1910.

[2] V. F. Hess, "On the observation of the penetrating radiation in seven free balloon campaigns", *Physikalische Zeitschrschift*, vol. 13, p. 1084, 1912.

[3] D. Pacini, "La radiazione penetrante alla superficie ed in seno alle acque", *Il Nuovo Cimento*, vol. 3, no. 1, pp. 93–100, 1912. DOI: 10.1007/BF02957440. arXiv: 1002.1810 [physics.hist-ph].

[4] W. Kolhörster, "Measurements of the penetrating radiation in a free balloon at high altitudes", *Physikalische Zeitschrschift*, vol. 14, p. 1153, 1913.

[5] T. K. Gaisser, *Cosmic rays and particle physics.* 1990.

[6] C. Evoli, *The CR Spectrum*, 2021. DOI: https://doi.org/10.5281/zenodo.4309926.

[7] L. A. Fisk, "Solar modulation of galactic cosmic rays", in *The Ancient Sun: Fossil Record in the Earth, Moon and Meteorites*, R. O. Pepin, J. A. Eddy, and R. B. Merrill, Eds., 1980, pp. 103–118.

[8] K. A. Firoz, D. V. P. Kumar, and K. S. Cho, "On the relationship of cosmic ray intensity with solar, interplanetary, and geophysical parameters", *Ap&SS*, vol. 325, no. 2, pp. 185–193, 2010. DOI: 10.1007/s10509-009-0181-9.

[9] M. S. Potgieter, "Solar Modulation of Cosmic Rays", *Living Reviews in Solar Physics*, vol. 10, no. 1, 3, p. 3, 2013. DOI: 10.12942/lrsp-2013-3. arXiv: 1306.4421 [physics.space-ph].

[10] B. Peters, "Primary cosmic radiation and extensive air showers", *Il Nuovo Cimento*, vol. 22, no. 4, pp. 800–819, 1961. DOI: 10.1007/BF02783106.

[11] HEGRA Collaboration, "Energy spectrum and chemical composition of cosmic rays between 0.3 and 10 PeV determined from the Cherenkov-light and charged-particle distributions in air showers", *A&A*, vol. 359, pp. 682–694, 2000. arXiv: astro-ph/9908202 [astro-ph].

[12] J. W. Fowler, L. F. Fortson, C. C. H. Jui, D. B. Kieda, R. A. Ong, C. L. Pryke, and P. Sommers, "A measurement of the cosmic ray spectrum and composition at the knee", *Astroparticle Physics*, vol. 15, no. 1, pp. 49–64, 2001. DOI: 10.1016/S0927-6505(00)00139-0. arXiv: astro-ph/0003190 [astro-ph].

[13] M. Aglietta *et al.*, "The cosmic ray primary composition in the knee region through the EAS electromagnetic and muon measurements at EAS-TOP", *Astroparticle Physics*, vol. 21, no. 6, pp. 583–596, 2004. DOI: 10.1016/j.astropartphys.2004.04.005.

[14] J. R. Hörandel, "Cosmic-ray composition and its relation to shock acceleration by supernova remnants", *Advances in Space Research*, vol. 41, no. 3, pp. 442–463, 2008. DOI: 10.1016/j.asr.2007.06.008. arXiv: astro-ph/0702370 [astro-ph].

[15] P. Blasi, "The origin of galactic cosmic rays", *A&A Rev.*, vol. 21, 70, p. 70, 2013. DOI: 10.1007/s00159-013-0070-7. arXiv: 1311.7346 [astro-ph.HE].

[16] S. Gabici, C. Evoli, D. Gaggero, P. Lipari, P. Mertsch, E. Orlando, and A. Strong A.and Vittino, "The origin of Galactic cosmic rays: Challenges to the standard paradigm", *International Journal of Modern Physics D*, vol. 28, no. 15, 1930022-339, pp. 1 930 022–339, 2019. DOI: 10.1142/S0218271819300222. arXiv: 1903.11584 [astro-ph.HE].

[17] KASCADE-Grande Collaboration, "The spectrum of high-energy cosmic rays measured with KASCADE-Grande", *Astroparticle Physics*, vol. 36, no. 1, pp. 183–194, 2012. DOI: 10.1016/j.astropartphys.2012.05.023. arXiv: 1206.3834 [astro-ph.HE].

[18] IceCube Collaboration, "Cosmic ray spectrum and composition from PeV to EeV using 3 years of data from IceTop and IceCube", *Phys. Rev. D*, vol. 100, no. 8, 082002, p. 082 002, 2019. DOI: 10.1103/PhysRevD.100.082002. arXiv: 1906.04317 [astro-ph.HE].

[19] Telescope Array Collaboration, "The Cosmic Ray Energy Spectrum between 2 PeV and 2 EeV Observed with the TALE Detector in Monocular Mode", *ApJ*, vol. 865, no. 1, 74, p. 74, 2018. DOI: 10.3847/1538-4357/aada05. arXiv: 1803.01288 [astro-ph.HE].

[20] Tunka Collaboration, "The primary cosmic-ray energy spectrum measured with the Tunka-133 array", *Astroparticle Physics*, vol. 117, 102406, p. 102 406, 2020. DOI: 10.1016/j.astropartphys.2019.102406. arXiv: 2104.03599 [astro-ph.HE].

[21] J. R. Hörandel, "Models of the knee in the energy spectrum of cosmic rays", *Astroparticle Physics*, vol. 21, no. 3, pp. 241–265, 2004. DOI: 10.1016/j.astropartphys.2004.01.004. arXiv: astro-ph/0402356 [astro-ph].

[22] P. Blasi and E. Amato, "Diffusive propagation of cosmic rays from supernova remnants in the Galaxy. I: spectrum and chemical composition", *J. Cosmology Astropart. Phys.*, vol. 2012, no. 1, 010, p. 010, 2012. DOI: 10.1088/1475-7516/2012/01/010. arXiv: 1105.4521 [astro-ph.HE].

[23] T. K. Gaisser, T. Stanev, and S. Tilav, "Cosmic ray energy spectrum from measurements of air showers", *Frontiers of Physics*, vol. 8, no. 6, pp. 748–758, 2013. DOI: 10.1007/s11467-013-0319-7. arXiv: 1303.3565 [astro-ph.HE].

[24] F. G. Schröder *et al.*, "High-Energy Galactic Cosmic Rays (Astro2020 Science White Paper)", *arXiv e-prints*, arXiv:1903.07713, arXiv:1903.07713, 2019. arXiv: 1903.07713 [astro-ph.HE].

[25] HAWC Collaboration, "Evidence of 200 TeV Photons from HAWC J1825-134", *ApJ*, vol. 907, no. 2, L30, p. L30, 2021. DOI: 10.3847/2041-8213/abd77b. arXiv: 2012.15275 [astro-ph.HE].

[26] Tibet AS-gamma Collaboration, "First Detection of sub-PeV Diffuse Gamma Rays from the Galactic Disk: Evidence for Ubiquitous Galactic Cosmic Rays beyond PeV Energies", *Phys. Rev. Lett.*, vol. 126, no. 14, 141101, p. 141 101, 2021. DOI: 10.1103/PhysRevLett.126.141101. arXiv: 2104.05181 [astro-ph.HE].

[27] LHAASO Collaboration, "Ultrahigh-energy photons up to 1.4 petaelectronvolts from 12 gamma-ray Galactic sources", *Nature*, vol. 594, no. 7861, pp. 33–36, 2021. DOI: 10.1038/s41586-021-03498-z.

[28] P. Cristofari, P. Blasi, and E. Amato, "The low rate of Galactic pevatrons", *Astroparticle Physics*, vol. 123, 102492, p. 102 492, 2020. DOI: 10.1016/j.astropartphys.2020.102492. arXiv: 2007.04294 [astro-ph.HE].

[29] J. Linsley, "Evidence for a Primary Cosmic-Ray Particle with Energy 10^{20} eV", *Phys. Rev. Lett.*, vol. 10, pp. 146–148, 4 1963. DOI: 10.1103/PhysRevLett.10.146. [Online]. Available: https://link.aps.org/doi/10.1103/PhysRevLett.10.146.

[30] A. Addazi *et al.*, "Quantum gravity phenomenology at the dawn of the multi-messenger era-A review", *Progress in Particle and Nuclear Physics*, vol. 125, 103948, p. 103 948, 2022. DOI: 10.1016/j.ppnp.2022.103948. arXiv: 2111.05659 [hep-ph].

[31] Pierre Auger Collaboration, "Properties and performance of the prototype instrument for the Pierre Auger Observatory", *Nuclear Instruments and Methods in Physics Research A*, vol. 523, no. 1-2, pp. 50–95, 2004. DOI: 10.1016/j.nima.2003.12.012.

[32] Telescope Array Collaboration, "Telescope Array Experiment", *Nuclear Physics B Proceedings Supplements*, vol. 175, pp. 221–226, 2008. DOI: 10.1016/j.nuclphysbps.2007.11.002.

[33] Pierre Auger Collaboration, "Observation of a large-scale anisotropy in the arrival directions of cosmic rays above 8×10^{18} eV", *Science*, vol. 357, no. 6357, pp. 1266–1270, 2017. DOI: 10.1126/science.aan4338. eprint: https://www.science.org/doi/pdf/10.1126/science.aan4338. [Online]. Available: https://www.science.org/doi/abs/10.1126/science.aan4338.

[34] Pierre Auger Collaboration, "Arrival Directions of Cosmic Rays above 32 EeV from Phase One of the Pierre Auger Observatory", *ApJ*, vol. 935, no. 2, 170, p. 170, 2022. DOI: 10.3847/1538-4357/ac7d4e. arXiv: 2206.13492 [astro-ph.HE].

[35] R. Alves Batista *et al.*, "Open Questions in Cosmic-Ray Research at Ultrahigh Energies", *Frontiers in Astronomy and Space Sciences*, vol. 6, 23, p. 23, 2019. DOI: 10.3389/fspas.2019.00023. arXiv: 1903.06714 [astro-ph.HE].

[36] Pierre Auger Collaboration, "Measurement of the cosmic-ray energy spectrum above 2.5×10^{18} eV using the Pierre Auger Observatory", *Phys. Rev. D*, vol. 102, no. 6, 062005, p. 062 005, 2020. DOI: 10.1103/PhysRevD.102.062005. arXiv: 2008.06486 [astro-ph.HE].

[37] HiRes Collaboration, "First Observation of the Greisen-Zatsepin-Kuzmin Suppression", *Phys. Rev. Lett.*, vol. 100, no. 10, 101101, p. 101 101, 2008. DOI: 10.1103/PhysRevLett.100.101101. arXiv: astro-ph/0703099 [astro-ph].

[38] Pierre Auger Collaboration, "The energy spectrum of cosmic rays beyond the turn-down around 10^{17} eV as measured with the surface detector of the Pierre Auger Observatory", *European Physical Journal C*, vol. 81, no. 11, 966, p. 966, 2021. DOI: 10.1140/epjc/s10052-021-09700-w. arXiv: 2109.13400 [astro-ph.HE].

[39] Pierre Auger Collaboration, "Energy spectrum of cosmic rays measured using the Pierre Auger Observatory", *PoS*, vol. ICRC2021, p. 324, 2021. DOI: 10.22323/1.395.0324.

[40] Telescope Array Collaboration, "The Cosmic-Ray Energy Spectrum Observed with the Surface Detector of the Telescope Array Experiment", *ApJ*, vol. 768, no. 1, L1, p. L1, 2013. DOI: 10.1088/2041-8205/768/1/L1. arXiv: 1205.5067 [astro-ph.HE].

[41] D. Ivanov and Telescope Array Collaboration, "Energy Spectrum Measured by the Telescope Array Experiment", in *APS April Meeting Abstracts*, ser. APS Meeting Abstracts, vol. 2019, 2019, G08.002, G08.002.

[42] K. Greisen, "End to the Cosmic-Ray Spectrum?", *Phys. Rev. Lett.*, vol. 16, pp. 748–750, 17 1966. DOI: 10.1103/PhysRevLett.16.748. [Online]. Available: https://link.aps.org/doi/10.1103/PhysRevLett.16.748.

[43] G. T. Zatsepin and V. A. Kuzmin, "Upper limit of the spectrum of cosmic rays", *JETP Lett.*, vol. 4, pp. 78–80, 1966.

[44] Pierre Auger Collaboration, "Depth of maximum of air-shower profiles at the Pierre Auger Observatory. II. Composition implications", *Phys. Rev. D*, vol. 90, p. 122 006, 12 2014. DOI: 10.1103/PhysRevD.90.122006. [Online]. Available: https://link.aps.org/doi/10.1103/PhysRevD.90.122006.

[45] J. Bellido, "Depth of maximum of air-shower profiles at the Pierre Auger Observatory: Measurements above $10^{17.2}$ eV and Composition Implications", *PoS*, vol. ICRC2017, p. 506, 2017. DOI: 10.22323/1.301.0506.

[46] Pierre Auger Collaboration, "Evidence for a mixed mass composition at the 'ankle' in the cosmic-ray spectrum", *Physics Letters B*, vol. 762, pp. 288–295, 2016. DOI: 10.1016/j.physletb.2016.09.039. arXiv: 1609.08567 [astro-ph.HE].

[47] A. Yushkov, "Mass Composition of Cosmic Rays with Energies above $10^{17.2}$ eV from the Hybrid Data of the Pierre Auger Observatory", *PoS*, vol. ICRC2019, p. 482, 2019. DOI: 10.22323/1.358.0482.

[48] A. M. Hillas, "TOPICAL REVIEW: Can diffusive shock acceleration in supernova remnants account for high-energy galactic cosmic rays?", *Journal of Physics G Nuclear Physics*, vol. 31, no. 5, R95–R131, 2005. DOI: 10.1088/0954-3899/31/5/R02.

[49] D. Allard, N. G. Busca, G. Decerprit, A. V. Olinto, and E. Parizot, "Implications of the cosmic ray spectrum for the mass composition at the highest energies", *J. Cosmology Astropart. Phys.*, vol. 2008, no. 10, 033, p. 033, 2008. DOI: 10.1088/1475-7516/2008/10/033. arXiv: 0805.4779 [astro-ph].

[50] G. Giacinti, M. Kachelrieß, and D. V. Semikoz, "Escape model for Galactic cosmic rays and an early extragalactic transition", *Phys. Rev. D*, vol. 91, p. 083 009, 8 2015. DOI: 10.1103/PhysRevD.91.083009. [Online]. Available: https://link.aps.org/doi/10.1103/PhysRevD.91.083009.

[51] O. Deligny, "Cosmic rays around 10^{18} eV: Implications of contemporary measurements on the origin of the ankle feature", *Comptes Rendus Physique*, vol. 15, no. 4, pp. 367–375, 2014. DOI: 10.1016/j.crhy.2014.02.009. arXiv: 1403.5569 [astro-ph.HE].

[52] R. Aloisio, V. Berezinsky, and P. Blasi, "Ultra high energy cosmic rays: implications of Auger data for source spectra and chemical composition", *J. Cosmology Astropart. Phys.*, vol. 2014, no. 10, pp. 020–020, 2014. DOI: 10.1088/1475-7516/2014/10/020. arXiv: 1312.7459 [astro-ph.HE].

[53] R. Aloisio and V. Berezinsky, "Towards Solving the Mass-Composition Problem in Ultra High Energy Cosmic Rays", *Soviet Journal of Experimental and Theoretical Physics*, vol. 128, no. 1, pp. 52–63, 2019. DOI: 10.1134/S1063776118120014.

[54] Pierre Auger Collaboration, "Constraining the sources of ultra-high-energy cosmic rays across and above the ankle with the spectrum and composition data measured at the Pierre Auger Observatory", *arXiv e-prints*, astro-ph/2211.02857, astro–ph/2211.02857, 2022. DOI: https://doi.org/10.48550/arXiv.2211.02857. arXiv: 2211.02857 [astro-ph].

[55] Pierre Auger Collaboration, "An Indication of Anisotropy in Arrival Directions of Ultra-high-energy Cosmic Rays through Comparison to the Flux Pattern of Extragalactic Gamma-Ray Sources", *ApJ*, vol. 853, no. 2, L29, p. L29, 2018. DOI: 10.3847/2041-8213/aaa66d. arXiv: 1801.06160 [astro-ph.HE].

[56] M. Erdmann, G. Müller, M. Urban, and M. Wirtz, "The nuclear window to the extragalactic universe", *Astroparticle Physics*, vol. 85, pp. 54–64, 2016. DOI: 10.1016/j.astropartphys.2016.10.002. arXiv: 1607.01645 [astro-ph.HE].

[57] G. R. Farrar and M. S. Sutherland, "Deflections of UHECRs in the Galactic magnetic field", *J. Cosmology Astropart. Phys.*, vol. 2019, no. 5, 004, p. 004, 2019. DOI: 10.1088/1475-7516/2019/05/004. arXiv: 1711.02730 [astro-ph.HE].

[58] Telescope Array Collaboration, "Search for EeV protons of galactic origin", *Astroparticle Physics*, vol. 86, pp. 21–26, 2017. DOI: 10.1016/j.astropartphys.2016.11.001. arXiv: 1608.06306 [astro-ph.HE].

[59] Pierre Auger Collaboration, "Cosmic-Ray Anisotropies in Right Ascension Measured by the Pierre Auger Observatory", *ApJ*, vol. 891, no. 2, 142, p. 142, 2020. DOI: 10.3847/1538-4357/ab7236. arXiv: 2002.06172 [astro-ph.HE].

[60] R. de Almeida and Pierre Auger Collaboration, "Large-scale and multipolar anisotropies of cosmic rays detected at the Pierre Auger Observatory with energies above 4 EeV", *PoS*, vol. ICRC2021, p. 335, 2021. DOI: 10.22323/1.395.0335.

[61] J. P. Huchra *et al.*, "The 2MASS Redshift Survey - Description and Data Release", *ApJS*, vol. 199, no. 2, 26, p. 26, 2012. DOI: 10.1088/0067-0049/199/2/26. arXiv: 1108.0669 [astro-ph.CO].

[62] Telescope Array Collaboration, "Testing a Reported Correlation between Arrival Directions of Ultra-high-energy Cosmic Rays and a Flux Pattern from nearby Starburst Galaxies using Telescope Array Data", *ApJ*, vol. 867, no. 2, L27, p. L27, 2018. DOI: 10.3847/2041-8213/aaebf9. arXiv: 1809.01573 [astro-ph.HE].

[63] A. di Matteo *et al.*, "UHECR arrival directions in the latest data from the original Auger and TA surface detectors and nearby galaxies", *PoS*, vol. ICRC2021, p. 308, 2021. DOI: 10.22323/1.395.0308.

[64] Pierre Auger Collaboration, "Bounds on the density of sources of ultra-high energy cosmic rays from the Pierre Auger Observatory", *J. Cosmology Astropart. Phys.*, vol. 2013, no. 5, 009, p. 009, 2013. DOI: 10.1088/1475-7516/2013/05/009. arXiv: 1305.1576 [astro-ph.HE].

[65] A. M. Hillas, "The Origin of Ultra-High-Energy Cosmic Rays", *ARA&A*, vol. 22, pp. 425–444, 1984. DOI: 10.1146/annurev.aa.22.090184.002233.

[66] K. V. Ptitsyna and S. V. Troitsky, "PHYSICS OF OUR DAYS Physical conditions in potential accelerators of ultra-high-energy cosmic rays: updated Hillas plot and radiation-loss constraints", *Physics Uspekhi*, vol. 53, no. 7, pp. 691–701, 2010. DOI: 10.3367/UFNe.0180.201007c.0723. arXiv: 0808.0367 [astro-ph].

[67] Pierre Auger Collaboration, "Combined fit of spectrum and composition data as measured by the Pierre Auger Observatory", *J. Cosmology Astropart. Phys.*, vol. 2017, no. 4, 038, p. 038, 2017. DOI: 10.1088/1475-7516/2017/04/038. arXiv: 1612.07155 [astro-ph.HE].

[68] "Erratum: Combined fit of spectrum and composition data as measured by the Pierre Auger Observatory", *J. Cosmology Astropart. Phys.*, vol. 2018, no. 3, E02, E02, 2018. DOI: 10.1088/1475-7516/2018/03/E02.

[69] K. Murase and H. Takami, "Implications of Ultra-High-Energy Cosmic Rays for Transient Sources in the Auger Era", *ApJ*, vol. 690, no. 1, pp. L14–L17, 2009. DOI: 10.1088/0004-637X/690/1/L14. arXiv: 0810.1813 [astro-ph].

[70] E. Waxman and J. Miralda-Escude, "Images of Bursting Sources of High-Energy Cosmic Rays: Effects of Magnetic Fields", *ApJ*, vol. 472, p. L89, 1996. DOI: 10.1086/310367. arXiv: astro-ph/9607059 [astro-ph].

[71] N. Gehrels *et al.*, "The Swift Gamma-Ray Burst Mission", *ApJ*, vol. 611, no. 2, pp. 1005–1020, 2004. DOI: 10.1086/422091. arXiv: astro-ph/0405233 [astro-ph].

[72] C. Meegan *et al.*, "The Fermi Gamma-ray Burst Monitor", *ApJ*, vol. 702, no. 1, pp. 791–804, 2009. DOI: 10.1088/0004-637X/702/1/791. arXiv: 0908.0450 [astro-ph.IM].

[73] Fermi-LAT Collaboration, "The Large Area Telescope on the Fermi Gamma-Ray Space Telescope Mission", *ApJ*, vol. 697, no. 2, pp. 1071–1102, 2009. DOI: 10.1088/0004-637X/697/2/1071. arXiv: 0902.1089 [astro-ph.IM].

[74] MAGIC Collaboration, "The major upgrade of the MAGIC telescopes, Part I: The hardware improvements and the commissioning of the system", *Astroparticle Physics*, vol. 72, pp. 61–75, 2016. DOI: 10.1016/j.astropartphys.2015.04.004. arXiv: 1409.6073 [astro-ph.IM].

[75] MAGIC Collaboration, "The major upgrade of the MAGIC telescopes, Part II: A performance study using observations of the Crab Nebula", *Astroparticle Physics*, vol. 72, pp. 76–94, 2016. DOI: 10.1016/j.astropartphys.2015.02.005. arXiv: 1409.5594 [astro-ph.IM].

[76] F. A. Aharonian, W. Hofmann, A. K. Konopelko, and H. J. Völk, "The potential of ground based arrays of imaging atmospheric Cherenkov telescopes. I. Determination of shower parameters", *Astroparticle Physics*, vol. 6, no. 3-4, pp. 343–368, 1997. DOI: 10.1016/S0927-6505(96)00069-2.

[77] F. A. Aharonian, W. Hofmann, A. K. Konopelko, and H. J. Völk, "The potential of the ground based arrays of imaging atmospheric Cherenkov telescopes. II. Gamma ray flux sensitivities", *Astroparticle Physics*, vol. 6, no. 3-4, pp. 369–377, 1997. DOI: 10.1016/S0927-6505(96)00070-9.

[78] T. C. Weekes *et al.*, "VERITAS: the Very Energetic Radiation Imaging Telescope Array System", *Astroparticle Physics*, vol. 17, no. 2, pp. 221–243, 2002. DOI: 10.1016/S0927-6505(01)00152-9. arXiv: astro-ph/0108478 [astro-ph].

[79] HAWC Collaboration, "On the sensitivity of the HAWC observatory to gamma-ray bursts", *Astroparticle Physics*, vol. 35, no. 10, pp. 641–650, 2012. DOI: 10.1016/j.astropartphys.2012.02.001. arXiv: 1108.6034 [astro-ph.HE].

[80] HAWC Collaboration, "Sensitivity of the high altitude water Cherenkov detector to sources of multi-TeV gamma rays", *Astroparticle Physics*, vol. 50, pp. 26–32, 2013. DOI: 10.1016/j.astropartphys.2013.08.002. arXiv: 1306.5800 [astro-ph.HE].

[81] ARGO-YBJ Collaboration, "High Altitude test of RPCs for the ARGO-YBJ experiment", *Nucl. Instr. Meth.*, vol. A443, hep-ex/9909034, hep–ex/9909034, 2000. arXiv: hep-ex/9909034 [hep-ex].

[82] LHAASO Collaboration, "The Large High Altitude Air Shower Observatory (LHAASO) Science Book (2021 Edition)", *arXiv e-prints*, arXiv:1905.02773, arXiv:1905.02773, 2019. arXiv: 1905.02773 [astro-ph.HE].

[83] A. Cooray, "Extragalactic background light measurements and applications", *Royal Society Open Science*, vol. 3, no. 3, p. 150 555, 2016. DOI: 10.1098/rsos.150555. arXiv: 1602.03512 [astro-ph.CO].

[84] A. De Angelis, G. Galanti, and M. Roncadelli, "Transparency of the Universe to gamma-rays", *MNRAS*, vol. 432, no. 4, pp. 3245–3249, 2013. DOI: 10.1093/mnras/stt684. arXiv: 1302.6460 [astro-ph.HE].

[85] J. Biteau and D. A. Williams, "The Extragalactic Background Light, the Hubble Constant, and Anomalies: Conclusions from 20 Years of TeV Gamma-ray Observations", *ApJ*, vol. 812, no. 1, 60, p. 60, 2015. DOI: 10.1088/0004-637X/812/1/60. arXiv: 1502.04166 [astro-ph.CO].

[86] R. Durrer and A. Neronov, "Cosmological magnetic fields: their generation, evolution and observation", *A&A Rev.*, vol. 21, 62, p. 62, 2013. DOI: 10.1007/s00159-013-0062-7. arXiv: 1303.7121 [astro-ph.CO].

[87] R. J. Gould and G. Schréder, "Opacity of the Universe to High-Energy Photons", *Phys. Rev. Lett.*, vol. 16, no. 6, pp. 252–254, 1966. DOI: 10.1103/PhysRevLett.16.252.

[88] I. Bartos and M. Kowalski, *Multimessenger Astronomy*. 2017. DOI: 10.1088/978-0-7503-1369-8.

[89] L. Mohrmann, "Characterizing cosmic neutrino sources: a measurement of the energy spectrum and flavor composition of the cosmic neutrino flux observed with the IceCube Neutrino Observatory", Ph.D. dissertation, Humboldt University of Berlin, Germany, 2015.

[90] E. Vitagliano, I. Tamborra, and G. Raffelt, "Grand unified neutrino spectrum at Earth: Sources and spectral components", *Reviews of Modern Physics*, vol. 92, no. 4, 045006, p. 045 006, 2020. DOI: 10.1103/RevModPhys.92.045006. arXiv: 1910.11878 [astro-ph.HE].

[91] S. Weinberg, *Gravitation and Cosmology: Principles and Applications of the General Theory of Relativity*. 1972.

[92] J. N. Bahcall and R. K. Ulrich, "Solar models, neutrino experiments, and helioseismology", *Reviews of Modern Physics*, vol. 60, no. 2, pp. 297–372, 1988. DOI: 10.1103/RevModPhys.60.297.

[93] S. Fukuda *et al.*, "Solar ^{8}B and hep Neutrino Measurements from 1258 Days of Super-Kamiokande Data", *Phys. Rev. Lett.*, vol. 86, no. 25, pp. 5651–5655, 2001. DOI: 10.1103/PhysRevLett.86.5651. arXiv: hep-ex/0103032 [hep-ex].

[94] L. M. Krauss, S. L. Glashow, and D. N. Schramm, "Antineutrino astronomy and geophysics", *Nature*, vol. 310, no. 5974, pp. 191–198, 1984. DOI: 10.1038/310191a0.

[95] F. Vissani and G. Pagliaroli, "The diffuse supernova neutrino background: expectations and uncertainties derived from SN1987A", *A&A*, vol. 528, L1, p. L1, 2011. DOI: 10.1051/0004-6361/201016109. arXiv: 1102.0447 [astro-ph.HE].

[96] T. K. Gaisser and M. Honda, "Flux of atmospheric neutrinos", *Annual Review of Nuclear and Particle Science*, vol. 52, pp. 153–199, 2002. DOI: 10.1146/annurev.nucl.52.050102.090645. arXiv: hep-ph/0203272 [hep-ph].

[97] F. W. Stecker, C. Done, M. H. Salamon, and P. Sommers, "High-energy neutrinos from active galactic nuclei", *Phys. Rev. Lett.*, vol. 66, no. 21, pp. 2697–2700, 1991. DOI: 10.1103/PhysRevLett.66.2697.

[98] "Erratum: High-energy neutrinos from active galactic nuclei [Phys. Rev. Lett. 66, 2697 (1991)]", *Phys. Rev. Lett.*, vol. 69, no. 18, p. 2738, 1992. DOI: 10.1103/PhysRevLett.69.2738.

[99] F. W. Stecker, "Note on high-energy neutrinos from active galactic nuclei cores", *Phys. Rev. D*, vol. 72, no. 10, 107301, p. 107 301, 2005. DOI: 10.1103/PhysRevD.72.107301. arXiv: astro-ph/0510537 [astro-ph].

[100] J. Bahcall and E. Waxman, "High energy astrophysical neutrinos: The upper bound is robust", *Phys. Rev. D*, vol. 64, no. 2, 023002, p. 023 002, 2001. DOI: 10.1103/PhysRevD.64.023002. arXiv: hep-ph/9902383 [hep-ph].

[101] M. Ahlers, L. A. Anchordoqui, M. C. Gonzalez–Garcia, F. Halzen, and S. Sarkar, "GZK neutrinos after the Fermi-LAT diffuse photon flux measurement", *Astroparticle Physics*, vol. 34, no. 2, pp. 106–115, 2010. DOI: 10.1016/j.astropartphys.2010.06.003. arXiv: 1005.2620 [astro-ph.HE].

[102] T. Stanev, *High energy cosmic rays*. 2004.

[103] M. Honda, T. Kajita, K. Kasahara, S. Midorikawa, and T. Sanuki, "Calculation of atmospheric neutrino flux using the interaction model calibrated with atmospheric muon data", *Phys. Rev. D*, vol. 75, no. 4, 043006, p. 043 006, 2007. DOI: 10.1103/PhysRevD.75.043006. arXiv: astro-ph/0611418 [astro-ph].

[104] R. Enberg, M. H. Reno, and I. Sarcevic, "Prompt neutrino fluxes from atmospheric charm", *Phys. Rev. D*, vol. 78, no. 4, 043005, p. 043 005, 2008. DOI: 10.1103/PhysRevD.78.043005. arXiv: 0806.0418 [hep-ph].

[105] K. A. Olive and Particle Data Group, "Review of Particle Physics", *Chinese Physics C*, vol. 38, no. 9, 090001, p. 090 001, 2014. DOI: 10.1088/1674-1137/38/9/090001.

[106] M. Tanabashi, K. Hagiwara, K. Hikasa, K. Nakamura, Y. Sumino, F. Takahashi, Tanaka, and Particle Data Group, "Review of Particle Physics", *Phys. Rev. D*, vol. 98, no. 3, 030001, p. 030 001, 2018. DOI: 10.1103/PhysRevD.98.030001.

[107] E. Waxman and J. Bahcall, "High energy neutrinos from astrophysical sources: An upper bound", *Phys. Rev. D*, vol. 59, no. 2, 023002, p. 023 002, 1998. DOI: 10.1103/PhysRevD.59.023002. arXiv: hep-ph/9807282 [hep-ph].

[108] M. V. Garzelli, S. Moch, and G. Sigl, "Lepton fluxes from atmospheric charm revisited", *Journal of High Energy Physics*, vol. 2015, 115, p. 115, 2015. DOI: 10.1007/JHEP10(2015)115. arXiv: 1507.01570 [hep-ph].

[109] M. V. Garzelli, S. Moch, O. Zenaiev, A. Cooper-Sarkar, A. Geiser, K. Lipka, R. Placakyte, and G. Sigl, "Prompt neutrino fluxes in the atmosphere with PROSA parton distribution functions", *Journal of High Energy Physics*, vol. 2017, no. 5, 4, p. 4, 2017. DOI: 10.1007/JHEP05(2017)004. arXiv: 1611.03815 [hep-ph].

[110] A. Bhattacharya, R. Enberg, Y. S. Jeong, C. S. Kim, M. H. Reno, I. Sarcevic, and A. Stasto, "Prompt atmospheric neutrino fluxes: perturbative QCD models and nuclear effects", *Journal of High Energy Physics*, vol. 2016, no. 11, 167, p. 167, 2016. DOI: 10.1007/JHEP11(2016)167. arXiv: 1607.00193 [hep-ph].

[111] R. Davis, D. S. Harmer, and K. C. Hoffman, "Search for Neutrinos from the Sun", *Phys. Rev. Lett.*, vol. 20, no. 21, pp. 1205–1209, 1968. DOI: 10.1103/PhysRevLett.20.1205.

[112] K. Hirata *et al.*, "Observation of a neutrino burst from the supernova SN1987A", *Phys. Rev. Lett.*, vol. 58, no. 14, pp. 1490–1493, 1987. DOI: 10.1103/PhysRevLett.58.1490.

[113] R. M. Bionta *et al.*, "Observation of a neutrino burst in coincidence with supernova 1987A in the Large Magellanic Cloud", *Phys. Rev. Lett.*, vol. 58, no. 14, pp. 1494–1496, 1987. DOI: 10.1103/PhysRevLett.58.1494.

[114] IceCube Collaboration, "Evidence for High-Energy Extraterrestrial Neutrinos at the IceCube Detector", *Science*, vol. 342, no. 6161, 1242856, p. 1 242 856, 2013. DOI: 10.1126/science.1242856. arXiv: 1311.5238 [astro-ph.HE].

[115] IceCube Collaboration, "First Observation of PeV-Energy Neutrinos with IceCube", *Phys. Rev. Lett.*, vol. 111, no. 2, 021103, p. 021 103, 2013. DOI: 10.1103/PhysRevLett.111.021103. arXiv: 1304.5356 [astro-ph.HE].

[116] M. Ahlers and F. Halzen, "Opening a new window onto the universe with IceCube", *Progress in Particle and Nuclear Physics*, vol. 102, pp. 73–88, 2018. DOI: 10.1016/j.ppnp.2018.05.001. arXiv: 1805.11112 [astro-ph.HE].

[117] IceCube Collaboration, "IceCube high-energy starting event sample: Description and flux characterization with 7.5 years of data", *Phys. Rev. D*, vol. 104, no. 2, 022002, p. 022 002, 2021. DOI: 10.1103/PhysRevD.104.022002. arXiv: 2011.03545 [astro-ph.HE].

[118] J. Stettner and IceCube Collaboration, "Measurement of the diffuse astrophysical muon-neutrino spectrum with ten years of IceCube data", in *36th International Cosmic Ray Conference (ICRC2019)*, ser. International Cosmic Ray Conference, vol. 36, 2019, 1017, p. 1017. DOI: 10.22323/1.358.01017. arXiv: 1908.09551 [astro-ph.HE].

[119] IceCube Collaboration, "Characteristics of the Diffuse Astrophysical Electron and Tau Neutrino Flux with Six Years of IceCube High Energy Cascade Data", *Phys. Rev. Lett.*, vol. 125, no. 12, 121104, p. 121 104, 2020. DOI: 10.1103/PhysRevLett.125.121104.

[120] IceCube Collaboration, "Measurements using the inelasticity distribution of multi-TeV neutrino interactions in IceCube", *Phys. Rev. D*, vol. 99, no. 3, 032004, p. 032 004, 2019. DOI: 10.1103/PhysRevD.99.032004.

[121] L. A. Fusco, F. Versari, and ANTARES Collaboration, "Study of the high-energy neutrino diffuse flux with the ANTARES neutrino telescope", in *36th International Cosmic Ray Conference (ICRC2019)*, ser. International Cosmic Ray Conference, vol. 36, 2019, 891, p. 891. DOI: 10.22323/1.358.0891.

[122] Baikal-GVD Collaboration, "Diffuse neutrino flux measurements with the Baikal-GVD neutrino telescope", *Phys. Rev. D*, vol. 107, no. 4, 042005, p. 042 005, 2023. DOI: 10.1103/PhysRevD.107.042005.

[123] E. Ganster and IceCube Collaboration, "A Combined Fit of the Diffuse Neutrino Spectrum using IceCube Muon Tracks and Cascades", in *37th International Cosmic Ray Conference*, 2022, 1129, p. 1129. DOI: 10.22323/1.395.01129. arXiv: 2107.10003 [astro-ph.HE].

[124] ANTARES Collaboration, "All-flavor Search for a Diffuse Flux of Cosmic Neutrinos with Nine Years of ANTARES Data", *ApJ*, vol. 853, no. 1, L7, p. L7, 2018. DOI: 10.3847/2041-8213/aaa4f6. arXiv: 1711.07212 [astro-ph.HE].

[125] IceCube Collaboration, D. Gaggero, and D. Grasso, "Joint Constraints on Galactic Diffuse Neutrino Emission from the ANTARES and IceCube Neutrino Telescopes", *ApJ*, vol. 868, no. 2, L20, p. L20, 2018. DOI: 10.3847/2041-8213/aaeecf. arXiv: 1808.03531 [astro-ph.HE].

[126] IceCube Collaboration, Fermi-LAT, MAGIC, AGILE, ASA-SN, HAWC, H.E.S.S, INTEGRAL, Kanata, Kiso, Kapteyn, Liverpool telescopes, Subaru, Swift/NuSTAR, VERITAS, VLA/17B-403, "Multimessenger observations of a flaring blazar coincident with high-energy neutrino IceCube-170922A", *Science*, vol. 361, no. 6398, eaat1378, eaat1378, 2018. DOI: 10.1126/science.aat1378. arXiv: 1807.08816 [astro-ph.HE].

[127] IceCube Collaboration, "Evidence for neutrino emission from the nearby active galaxy NGC 1068", *Science*, vol. 378, no. 6619, pp. 538–543, 2022. DOI: 10.1126/science.abg3395. eprint: https://www.science.org/doi/pdf/10.1126/science.abg3395. [Online]. Available: https://www.science.org/doi/abs/10.1126/science.abg3395.

[128] IceCube Collaboration, "Time-Integrated Neutrino Source Searches with 10 Years of IceCube Data", *Phys. Rev. Lett.*, vol. 124, no. 5, 051103, p. 051 103, 2020. DOI: 10.1103/PhysRevLett.124.051103. arXiv: 1910.08488 [astro-ph.HE].

[129] R. Stein *et al.*, "A tidal disruption event coincident with a high-energy neutrino", *Nature Astronomy*, vol. 5, pp. 510–518, 2021. DOI: 10.1038/s41550-020-01295-8. arXiv: 2005.05340 [astro-ph.HE].

[130] A. Plavin, Y. Y. Kovalev, Y. A. Kovalev, and S. Troitsky, "Observational Evidence for the Origin of High-energy Neutrinos in Parsec-scale Nuclei of Radio-bright Active Galaxies", *ApJ*, vol. 894, no. 2, 101, p. 101, 2020. DOI: 10.3847/1538-4357/ab86bd. arXiv: 2001.00930 [astro-ph.HE].

[131] LIGO Scientific Collaboration and Virgo Collaboration, "Observation of Gravitational Waves from a Binary Black Hole Merger", *Phys. Rev. Lett.*, vol. 116, no. 6, 061102, p. 061 102, 2016. DOI: 10.1103/PhysRevLett.116.061102. arXiv: 1602.03837 [gr-qc].

[132] LIGO Scientific Collaboration and Virgo Collaboration, "GW170817: Observation of Gravitational Waves from a Binary Neutron Star Inspiral", *Phys. Rev. Lett.*, vol. 119, no. 16, 161101, p. 161 101, 2017. DOI: 10.1103/PhysRevLett.119.161101. arXiv: 1710.05832 [gr-qc].

[133] LIGO Scientific Collaboration, Virgo Collaboration, Fermi GBM, INTEGRAL, IceCube Collaboration, AstroSat Cadmium Zinc Telluride Imager Team, IPN Collaboration, The Insight-Hxmt Collaboration, ANTARES Collaboration, The Swift Collaboration, AGILE Team, The 1M2H Team, The Dark Energy Camera GW-EM Collaboration, the DES Collaboration, The DLT40 Collaboration, GRAWITA: GRAvitational Wave Inaf TeAm, The Fermi Large Area Telescope Collaboration, ATCA: Australia Telescope Compact Array, ASKAP: Australian SKA Pathfinder, Las Cumbres Observatory Group, OzGrav, DWF (Deeper, Wider, Faster Program), AST3, CAASTRO Collaborations, The VINROUGE Collaboration, MASTER Collaboration, J-GEM, GROWTH, JAGWAR, Caltech- NRAO, TTU-NRAO, NuSTAR Collaborations, Pan-STARRS, The MAXI Team, TZAC Consortium, KU Collaboration, Nordic Optical Telescope, ePESSTO, GROND, Texas Tech University, SALT Group, TOROS: Transient Robotic Observatory of the South Collaboration, The BOOTES Collaboration, MWA: Murchison Widefield Array, The CALET Collaboration, IKI-GW Follow-up Collaboration, H.E.S.S. Collaboration, LOFAR Collaboration, LWA: Long Wavelength Array, HAWC Collaboration, The Pierre Auger Collaboration, ALMA Collaboration, Euro VLBI Team, Pi of the Sky Collaboration, The Chandra Team at McGill University, DFN: Desert Fireball Network, ATLAS, High Time Resolution Universe Survey, RIMAS, RATIR, SKA South Africa/MeerKAT, "Multi-messenger Observations of a Binary Neutron Star Merger", *ApJ*, vol. 848, no. 2, L12, p. L12, 2017. DOI: 10.3847/2041-8213/aa91c9. arXiv: 1710.05833 [astro-ph.HE].

[134] B. D. Metzger, "Kilonovae", *Living Reviews in Relativity*, vol. 20, no. 1, 3, p. 3, 2017. DOI: 10.1007/s41114-017-0006-z. arXiv: 1610.09381 [astro-ph.HE].

[135] K. Danzmann and LISA Science Team, "LISA — An ESA cornerstone mission for the detection and observation of gravitational waves", *Advances in Space Research*, vol. 32, no. 7, pp. 1233–1242, 2003. DOI: 10.1016/S0273-1177(03)90323-1.

[136] M. Bailes *et al.*, "Gravitational-wave physics and astronomy in the 2020s and 2030s", *Nature Reviews Physics*, vol. 3, no. 5, pp. 344–366, 2021. DOI: 10.1038/s42254-021-00303-8.

[137] E. Fermi, "On the Origin of the Cosmic Radiation", *Physical Review*, vol. 75, no. 8, pp. 1169–1174, 1949. DOI: 10.1103/PhysRev.75.1169.

[138] W. Axford, E. Leer, and G. Skadron, "The Acceleration of Cosmic Rays by Shock Waves", in *International Cosmic Ray Conference*, ser. International Cosmic Ray Conference, vol. 11, 1977, p. 132.

[139] G. F. Krymskii, "A regular mechanism for the acceleration of charged particles on the front of a shock wave", *Akademiia Nauk SSSR Doklady*, vol. 234, pp. 1306–1308, 1977.

[140] A. R. Bell, "The acceleration of cosmic rays in shock fronts - I.", *MNRAS*, vol. 182, pp. 147–156, 1978. DOI: 10.1093/mnras/182.2.147.

[141] A. R. Bell, "The acceleration of cosmic rays in shock fronts - II.", *MNRAS*, vol. 182, pp. 443–455, 1978. DOI: 10.1093/mnras/182.3.443.

[142] R. D. Blandford and J. P. Ostriker, "Particle acceleration by astrophysical shocks.", *ApJ*, vol. 221, pp. L29–L32, 1978. DOI: 10.1086/182658.

[143] A. R. Bell, "Turbulent amplification of magnetic field and diffusive shock acceleration of cosmic rays", *MNRAS*, vol. 353, no. 2, pp. 550–558, 2004. DOI: 10.1111/j.1365-2966.2004.08097.x.

[144] G. R. Blumenthal and R. J. Gould, "Bremsstrahlung, Synchrotron Radiation, and Compton Scattering of High-Energy Electrons Traversing Dilute Gases", *Reviews of Modern Physics*, vol. 42, no. 2, pp. 237–271, 1970. DOI: 10.1103/RevModPhys.42.237.

[145] G. B. Rybicki and A. P. Lightman, *Radiative processes in astrophysics*. 1979.

[146] T. K. Gaisser, R. J. Protheroe, and T. Stanev, "Gamma-Ray Production in Supernova Remnants", *ApJ*, vol. 492, no. 1, pp. 219–227, 1998. DOI: 10.1086/305011. arXiv: astro-ph/9609044 [astro-ph].

[147] A. De Angelis and M. Pimenta, *Introduction to Particle and Astroparticle Physics*. 2018. DOI: 10.1007/978-3-319-78181-5.

[148] N. S. Kardashev, "Nonstationarity of Spectra of Young Sources of Nonthermal Radio Emission", *Soviet Astronomy*, vol. 6, p. 317, 1962.

[149] F. Aharonian *et al.*, "The Crab Nebula and Pulsar between 500 GeV and 80 TeV: Observations with the HEGRA Stereoscopic Air Cerenkov Telescopes", *ApJ*, vol. 614, no. 2, pp. 897–913, 2004. DOI: 10.1086/423931. arXiv: astro-ph/0407118 [astro-ph].

[150] F. W. Stecker, *Cosmic gamma rays*. 1971, vol. 249.

[151] R. J. Murphy, C. D. Dermer, and R. Ramaty, "High-Energy Processes in Solar Flares", *ApJS*, vol. 63, p. 721, 1987. DOI: 10.1086/191180.

[152] C. Pfrommer and T. A. Enßlin, "Constraining the population of cosmic ray protons in cooling flow clusters with γ-ray and radio observations: Are radio mini-halos of hadronic origin?", *A&A*, vol. 413, pp. 17–36, 2004. DOI: 10.1051/0004-6361:20031464.

[153] Y. Ohira, K. Kohri, and N. Kawanaka, "Positron annihilation as a cosmic ray probe", *MNRAS*, vol. 421, no. 1, pp. L102–L106, 2012. DOI: 10.1111/j.1745-3933.2011.01215.x. arXiv: 1103.4140 [astro-ph.HE].

[154] A. Giuliani *et al.*, "AGILE detection of GeV γ-ray emission from the SNR W28", *A&A*, vol. 516, L11, p. L11, 2010. DOI: 10.1051/0004-6361/201014256. arXiv: 1005.0784 [astro-ph.HE].

[155] Fermi-LAT Collaboration, "Detection of the Characteristic Pion-Decay Signature in Supernova Remnants", *Science*, vol. 339, no. 6121, pp. 807–811, 2013. DOI: 10.1126/science.1231160. arXiv: 1302.3307 [astro-ph.HE].

[156] M. Tavani *et al.*, "Direct Evidence for Hadronic Cosmic-Ray Acceleration in the Supernova Remnant IC 443", *ApJ*, vol. 710, no. 2, pp. L151–L155, 2010. DOI: 10.1088/2041-8205/710/2/L151. arXiv: 1001.5150 [astro-ph.HE].

[157] R.-z. Yang, E. Kafexhiu, and F. Aharonian, "Exploring the shape of the γ-ray spectrum around the π^0-bump", *A&A*, vol. 615, A108, A108, 2018. DOI: 10.1051/0004-6361/201730908. arXiv: 1803.05072 [astro-ph.HE].

[158] "Erratum: Energy spectra of gamma rays, electrons, and neutrinos produced at proton-proton interactions in the very high energy regime [Phys. Rev. D 74, 034018 (2006)]", *Phys. Rev. D*, vol. 79, no. 3, 039901, p. 039 901, 2009. DOI: 10.1103/PhysRevD.79.039901.

[159] J. K. Becker, "High-energy neutrinos in the context of multimessenger astrophysics", *Phys. Rep.*, vol. 458, no. 4-5, pp. 173–246, 2008. DOI: 10.1016/j.physrep.2007.10.006. arXiv: 0710.1557 [astro-ph].

[160] Fermi-LAT Collaboration, “The Spectrum of Isotropic Diffuse Gamma-Ray Emission between 100 MeV and 820 GeV”, *ApJ*, vol. 799, no. 1, 86, p. 86, 2015. DOI: 10.1088/0004-637X/799/1/86. arXiv: 1410.3696 [astro-ph.HE].

[161] K. Murase, M. Ahlers, and B. C. Lacki, “Testing the hadronuclear origin of PeV neutrinos observed with IceCube”, *Phys. Rev. D*, vol. 88, no. 12, 121301, p. 121 301, 2013. DOI: 10.1103/PhysRevD.88.121301. arXiv: 1306.3417 [astro-ph.HE].

[162] K. Murase, D. Guetta, and M. Ahlers, “Hidden Cosmic-Ray Accelerators as an Origin of TeV-PeV Cosmic Neutrinos”, *Phys. Rev. Lett.*, vol. 116, no. 7, 071101, p. 071 101, 2016. DOI: 10.1103/PhysRevLett.116.071101. arXiv: 1509.00805 [astro-ph.HE].

[163] POEMMA Collaboration, “The POEMMA (Probe of Extreme Multi-Messenger Astrophysics) observatory”, *J. Cosmology Astropart. Phys.*, vol. 2021, no. 6, 007, p. 007, 2021. DOI: 10.1088/1475-7516/2021/06/007. arXiv: 2012.07945 [astro-ph.IM].

[164] T. K. Gaisser, R. Engel, and E. Resconi, *Cosmic Rays and Particle Physics*. 2016.

[165] M. Kowalski, “Status of High-Energy Neutrino Astronomy”, in *Journal of Physics Conference Series*, ser. Journal of Physics Conference Series, vol. 632, 2015, 012039, p. 012 039. DOI: 10.1088/1742-6596/632/1/012039. arXiv: 1411.4385 [astro-ph.HE].

[166] ANTARES Collaboration, IceCube Collaboration, Pierre Auger Collaboration, Telescope Array Collaboration, “Search for Spatial Correlations of Neutrinos with Ultra-high-energy Cosmic Rays”, *ApJ*, vol. 934, no. 2, 164, p. 164, 2022. DOI: 10.3847/1538-4357/ac6def. arXiv: 2201.07313 [astro-ph.HE].

[167] F. Salesa Greus and A. Sánchez Losa, “Multimessenger Astronomy with Neutrinos”, *Universe*, vol. 7, no. 11, p. 397, 2021. DOI: 10.3390/universe7110397. arXiv: 2110.11817 [astro-ph.HE].

[168] ANTARES Collaboration *et al.*, “Optical and X-ray early follow-up of ANTARES neutrino alerts”, *J. Cosmology Astropart. Phys.*, vol. 2016, no. 2, pp. 062–062, 2016. DOI: 10.1088/1475-7516/2016/02/062. arXiv: 1508.01180 [astro-ph.HE].

[169] H. A. Ayala Solares *et al.*, “The Astrophysical Multimessenger Observatory Network (AMON): Performance and science program”, *Astroparticle Physics*, vol. 114, pp. 68–76, 2020. DOI: 10.1016/j.astropartphys.2019.06.007. arXiv: 1903.08714 [astro-ph.IM].

[170] K. Murase and I. Bartos, “High-Energy Multimessenger Transient Astrophysics”, *Annual Review of Nuclear and Particle Science*, vol. 69, pp. 477–506, 2019. DOI: 10.1146/annurev-nucl-101918-023510. arXiv: 1907.12506 [astro-ph.HE].

[171] IceCube Collaboration, “The IceCube realtime alert system”, *Astroparticle Physics*, vol. 92, pp. 30–41, 2017. DOI: 10.1016/j.astropartphys.2017.05.002. arXiv: 1612.06028 [astro-ph.HE].

[172] IceCube Collaboration, “Follow-up of Astrophysical Transients in Real Time with the IceCube Neutrino Observatory”, *ApJ*, vol. 910, no. 1, 4, p. 4, 2021. DOI: 10.3847/1538-4357/abe123. arXiv: 2012.04577 [astro-ph.HE].

[173] ANTARES Collaboration, “Review of the online analyses of multi-messenger alerts and electromagnetic transient events with the ANTARES neutrino telescope”, *arXiv e-prints*, arXiv:2211.07551, arXiv:2211.07551, 2022. arXiv: 2211.07551 [astro-ph.HE].

[174] M. A. Markov, “On high energy neutrino physics”, in *10th International Conference on High Energy Physics*, 1960, pp. 578–581.

[175] Baikal-GVD Collaboration, “The Gigaton Volume Detector in Lake Baikal”, *Nuclear Instruments and Methods in Physics Research A*, vol. 639, no. 1, pp. 30–32, 2011. DOI: 10.1016/j.nima.2010.09.137.

[176] P. A. Čerenkov, “Visible Radiation Produced by Electrons Moving in a Medium with Velocities Exceeding that of Light”, *Physical Review*, vol. 52, no. 4, pp. 378–379, 1937. DOI: 10.1103/PhysRev.52.378.

[177] R. W. Austin and G. Halikas, “The index of refraction of seawater”, *UC San Diego: Scripps Institution of Oceanography*, 1976. DOI: https://escholarship.org/uc/item/8px2019m.

[178] I. M. Frank and I. G. Tamm, “Coherent visible radiation of fast electrons passing through matter”, *Physics-Uspekhi*, vol. 93, pp. 388–393, 1937.

[179] Katrin Collaboration, “Direct neutrino-mass measurement with sub-electronvolt sensitivity”, *Nature Physics*, vol. 18, no. 2, pp. 160–166, 2022. DOI: 10.1038/s41567-021-01463-1.

[180] J. A. Formaggio and G. P. Zeller, “From eV to EeV: Neutrino cross sections across energy scales”, *Reviews of Modern Physics*, vol. 84, no. 3, pp. 1307–1341, 2012. DOI: 10.1103/RevModPhys.84.1307. arXiv: 1305.7513 [hep-ex].

[181] R. Gandhi, C. Quigg, M. Hall Reno, and I. Sarcevic, “Ultrahigh-energy neutrino interactions”, *Astroparticle Physics*, vol. 5, no. 2, pp. 81–110, 1996. DOI: 10.1016/0927-6505(96)00008-4. arXiv: hep-ph/9512364 [hep-ph].

[182] S. L. Glashow, “Resonant Scattering of Antineutrinos”, *Physical Review*, vol. 118, no. 1, pp. 316–317, 1960. DOI: 10.1103/PhysRev.118.316.

[183] F. Bernard, “Caractérisation des performances d’un télescope sous-marin à neutrinos pour la détection de cascades contenues dans le cadre du projet ANTARES”, Theses, Université de la Méditerranée - Aix-Marseille II, 2000. [Online]. Available: https://tel.archives-ouvertes.fr/tel-00001417.

[184] D. E. Groom, N. V. Mokhov, and S. I. Striganov, “Muon Stopping Power and Range Tables 10 MeV-100 TeV”, *Atomic Data and Nuclear Data Tables*, vol. 78, no. 2, pp. 183–356, 2001. DOI: 10.1006/adnd.2001.0861.

[185] D. E. Groom, N. V. Mokhov, and S. I. Striganov, “Muon Stopping Power and Range Tables 10 MeV-100 TeV”, *Atomic Data and Nuclear Data Tables*, vol. 78, no. 2, pp. 183–356, 2001. DOI: 10.1006/adnd.2001.0861.

[186] C. Kopper, “Performance studies for the KM3NeT Neutrino Telescope”, Ph.D. dissertation, Erlangen - Nuremberg U., 2010.

[187] J. G. Learned and K. Mannheim, “High-Energy Neutrino Astrophysics”, *Annual Review of Nuclear and Particle Science*, vol. 50, pp. 679–749, 2000. DOI: 10.1146/annurev.nucl.50.1.679.

[188] ANTARES Collaboration, “Transmission of light in deep sea water at the site of the ANTARES neutrino telescope”, *Astroparticle Physics*, vol. 23, no. 1, pp. 131–155, 2005. DOI: 10.1016/j.astropartphys.2004.11.006. arXiv: astro-ph/0412126 [astro-ph].

[189] F. R. S. Lord Rayleigh, “X. On the electromagnetic theory of light”, *The London, Edinburgh, and Dublin Philosophical Magazine and Journal of Science*, vol. 12, no. 73, pp. 81–101, 1881. DOI: 10.1080/14786448108627074. eprint: https://doi.org/10.1080/14786448108627074. [Online]. Available: https://doi.org/10.1080/14786448108627074.

[190] F. R. S. Lord Rayleigh, “XXXIV. On the transmission of light through an atmosphere containing small particles in suspension, and on the origin of the blue of the sky”, *The London, Edinburgh, and Dublin Philosophical Magazine and Journal of Science*, vol. 47, no. 287, pp. 375–384, 1899. DOI: 10.1080/14786449908621276. eprint: https://doi.org/10.1080/14786449908621276. [Online]. Available: https://doi.org/10.1080/14786449908621276.

[191] G. Mie, “Beiträge zur Optik trüber Medien, speziell kolloidaler Metallösungen”, *Annalen der Physik*, vol. 330, no. 3, pp. 377–445, 1908. DOI: https://doi.org/10.1002/andp.19083300302. eprint: https://onlinelibrary.wiley.com/doi/pdf/10.1002/andp.19083300302. [Online]. Available: https://onlinelibrary.wiley.com/doi/abs/10.1002/andp.19083300302.

[192] U. F. Katz and C. Spiering, “High-energy neutrino astrophysics: Status and perspectives”, *Progress in Particle and Nuclear Physics*, vol. 67, no. 3, pp. 651–704, 2012. DOI: 10.1016/j.ppnp.2011.12.001. arXiv: 1111.0507 [astro-ph.HE].

[193] T. Chiarusi and M. Spurio, “High-energy astrophysics with neutrino telescopes”, *European Physical Journal C*, vol. 65, no. 3-4, pp. 649–701, 2010. DOI: 10.1140/epjc/s10052-009-1230-9. arXiv: 0906.2634 [astro-ph.HE].

[194] F. Ameli, M. Bonori, and F. Massa, “Optical background measurement in a potential site for the NEMO KM undersea neutrino telescope”, *European Physical Journal C*, vol. 25, no. 1, pp. 67–75, 2002. DOI: 10.1007/s10052-002-1015-x.

[195] H. van Haren, I. Taupier-Letage, and ANTARES Collaboration, “Acoustic and optical variations during rapid downward motion episodes in the deep north-western Mediterranean Sea”, *Deep Sea Research Part I: Oceanographic Research*, vol. 58, no. 8, pp. 875–884, 2011. DOI: 10.1016/j.dsr.2011.06.006. arXiv: 1111.6482 [physics.geo-ph].

[196] R. Lahmann, “Acoustic Detection of Neutrinos: Review and Future Potential”, *Nuclear and Particle Physics Proceedings*, vol. 273-275, pp. 406–413, 2016. DOI: 10.1016/j.nuclphysbps.2015.09.059.

[197] T. Huege and D. Besson, “Radio-wave detection of ultra-high-energy neutrinos and cosmic rays”, *Progress of Theoretical and Experimental Physics*, vol. 2017, no. 12, 12A106, 12A106, 2017. DOI: 10.1093/ptep/ptx009. arXiv: 1701.02987 [astro-ph.IM].

[198] Y. Becherini, A. Margiotta, M. Sioli, and M. Spurio, “A parameterisation of single and multiple muons in the deep water or ice”, *Astroparticle Physics*, vol. 25, no. 1, pp. 1–13, 2006. DOI: 10.1016/j.astropartphys.2005.10.005. arXiv: hep-ph/0507228 [hep-ph].

[199] A. L’Abbate, T. Montaruli, and I. Sokalski, “Effect of neutral current interactions on high energy muon and electron neutrino propagation through the earth”, *Astroparticle Physics*, vol. 23, no. 1, pp. 57–63, 2005. DOI: 10.1016/j.astropartphys.2004.11.004. arXiv: hep-ph/0406133 [hep-ph].

[200] S. Cecchini, E. Korolkova, A. Margiotta, and L. Thompson, "Atmospheric muon background in the ANTARES detector", in *29th International Cosmic Ray Conference (ICRC29), Volume 5*, ser. International Cosmic Ray Conference, vol. 5, 2005, p. 51. arXiv: astro-ph/0510799 [astro-ph].

[201] G. C. Hill, J. Hodges, B. Hughey, A. Karle, and M. Stamatikos, "Examining the Balance Between Optimising an Analysis for Best Limit Setting and Best Discovery Potential", in *Statistical Problems in Particle Physics, Astrophysics and Cosmology*, L. Lyons and M. Karagöz ünel, Eds., 2006, p. 108. DOI: 10.1142/9781860948985_0025.

[202] G. J. Feldman and R. D. Cousins, "Unified approach to the classical statistical analysis of small signals", *Phys. Rev. D*, vol. 57, no. 7, pp. 3873–3889, 1998. DOI: 10.1103/PhysRevD.57.3873. arXiv: physics/9711021 [physics.data-an].

[203] *Statistical Problems in Particle Physics, Astrophysics and Cosmology: proceedings of PHYSTAT05*, 2006.

[204] F. Halzen and U. Katz, "The Era of Kilometer-Scale Neutrino Detectors", *Advances in High Energy Physics*, vol. 2013, J. Bernabeu, Ed., p. 680 584, 2013, Publisher: Hindawi Publishing Corporation, ISSN: 1687-7357. DOI: 10.1155/2013/680584. [Online]. Available: https://doi.org/10.1155/2013/680584.

[205] ANTARES Collaboration, "ANTARES: The first undersea neutrino telescope", *Nuclear Instruments and Methods in Physics Research A*, vol. 656, no. 1, pp. 11–38, 2011. DOI: 10.1016/j.nima.2011.06.103. arXiv: 1104.1607 [astro-ph.IM].

[206] ANTARES Collaboration, "The ANTARES optical module", *Nuclear Instruments and Methods in Physics Research A*, vol. 484, no. 1-3, pp. 369–383, 2002. DOI: 10.1016/S0168-9002(01)02026-5. arXiv: astro-ph/0112172 [astro-ph].

[207] C. Spiering, "Neutrino detectors under water and ice", in *Particle Physics Reference Library: Volume 2: Detectors for Particles and Radiation*, C. W. Fabjan and H. Schopper, Eds. Cham: Springer International Publishing, 2020, pp. 785–822, ISBN: 978-3-030-35318-6. DOI: 10.1007/978-3-030-35318-6_17. [Online]. Available: https://doi.org/10.1007/978-3-030-35318-6_17.

[208] ANTARES Collaboration, "The ANTARES optical beacon system", *Nuclear Instruments and Methods in Physics Research A*, vol. 578, no. 3, pp. 498–509, 2007. DOI: 10.1016/j.nima.2007.05.325. arXiv: astro-ph/0703355 [astro-ph].

[209] ANTARES Collaboration, "The positioning system of the ANTARES Neutrino Telescope", *Journal of Instrumentation*, vol. 7, no. 8, T08002, 2012. DOI: 10.1088/1748-0221/7/08/T08002. arXiv: 1202.3894 [astro-ph.IM].

[210] ANTARES Collaboration, "The data acquisition system for the ANTARES neutrino telescope", *Nuclear Instruments and Methods in Physics Research A*, vol. 570, no. 1, pp. 107–116, 2007. DOI: 10.1016/j.nima.2006.09.098. arXiv: astro-ph/0610029 [astro-ph].

[211] KM3NeT Collaboration, "Letter of intent for KM3NeT 2.0", *Journal of Physics G Nuclear Physics*, vol. 43, no. 8, 084001, p. 084 001, 2016. DOI: 10.1088/0954-3899/43/8/084001.

[212] KM3NeT Collaboration, "The KM3NeT multi-PMT optical module", *Journal of Instrumentation*, vol. 17, no. 7, P07038, P07038, 2022. DOI: 10.1088/1748-0221/17/07/P07038.

[213] G. Mul, E. M. Berbee, H. B. Rookhuizen, E. Heine, J. Hogenbirk, S. Mos, E. de Wolf, and KM3NeT Consortium, "A vertical electro-optical data cable for KM3NeT", *Nuclear Instruments and Methods in Physics Research A*, vol. 725, pp. 230–233, 2013. DOI: 10.1016/j.nima.2012.12.099.

[214] J. Barrios Martí, "Search for cosmic sources in neutrino telescopes and time calibration in the ANTARES neutrino telescope", Ph.D. dissertation, University of Valencia, Spain, 2018.

[215] T. van Eeden, J. Seneca, A. Heijboer, and KM3NeT Collaboration, "High-energy reconstruction for single and double cascades using the KM3NeT detector", in *37th International Cosmic Ray Conference*, 2022, 1089, p. 1089. DOI: 10.22323/1.395.01089.

[216] KM3NeT Collaboration, "Sensitivity of the KM3NeT/ARCA neutrino telescope to point-like neutrino sources", *Astroparticle Physics*, vol. 111, pp. 100–110, 2019. DOI: 10.1016/j.astropartphys.2019.04.002. arXiv: 1810.08499 [astro-ph.HE].

[217] IceCube Collaboration, "Time-Integrated Neutrino Source Searches with 10 Years of IceCube Data", *Phys. Rev. Lett.*, vol. 124, no. 5, 051103, p. 051 103, 2020. DOI: 10.1103/PhysRevLett.124.051103. arXiv: 1910.08488 [astro-ph.HE].

[218] R. Muller, A. Heijboer, A. Garcia Soto, B. Caiffi, M. Sanguineti, V. Kulikovskiy, and KM3NeT Collaboration, "Sensitivity estimates for diffuse, point-like and extended neutrino sources with KM3NeT/ARCA", in *37th International Cosmic Ray Conference*, 2022, 1077, p. 1077. DOI: 10.22323/1.395.1077. arXiv: 2107.13050 [astro-ph.IM].

[219] G. Illuminati and ANTARES Collaboration, "Searches for point-like sources of cosmic neutrinos with 13 years of ANTARES data", in *37th International Cosmic Ray Conference*, 2022, 1161, p. 1161. DOI: 10.22323/1.395.01161.

[220] KM3NeT Collaboration, "Determining the neutrino mass ordering and oscillation parameters with KM3NeT/ORCA", *European Physical Journal C*, vol. 82, no. 1, 26, p. 26, 2022. DOI: 10.1140/epjc/s10052-021-09893-0. arXiv: 2103.09885 [hep-ex].

[221] IceCube Collaboration, "All-sky Search for Time-integrated Neutrino Emission from Astrophysical Sources with 7 yr of IceCube Data", *ApJ*, vol. 835, no. 2, 151, p. 151, 2017. DOI: 10.3847/1538-4357/835/2/151. arXiv: 1609.04981 [astro-ph.HE].

[222] R. Le Breton *et al.*, "The calibration units of KM3NeT", in *Journal of Instrumentation*, vol. 16, 2021. DOI: 10.1088/1748-0221/16/09/C09004.

[223] G. Riccobene and KM3NeT Collaboration, "The Positioning system for KM3NeT", in *EPJ Web of Conferences*, 2019. DOI: https://doi.org/10.1051/epjconf/201920707005.

[224] ANTARES Collaboration, "Time calibration of the ANTARES neutrino telescope", *Astroparticle Physics*, vol. 34, no. 7, pp. 539–549, 2011. DOI: 10.1016/j.astropartphys.2010.12.004. arXiv: 1012.2204 [astro-ph.IM].

[225] R. Coniglione, A. Creusot, I. Di Palma, D. Guderian, J. Hofestaedt, G. Riccobene, and A. Sánchez-Losa, "KM3NeT Time Calibration", *PoS*, vol. ICRC2019, p. 868, 2019. DOI: 10.22323/1.358.0868.

[226] S. Aiello et al. (KM3NeT Collaboration), "Nanobeacon: A time calibration device for the KM3NeT neutrino telescope", *Nuclear Inst. and Methods in Physics Research*, 2022. DOI: 10.1016/j.nima.2022.167132.

[227] IceCube Collaboration, "Sensitivity of the IceCube detector to astrophysical sources of high energy muon neutrinos", *Astroparticle Physics*, vol. 20, no. 5, pp. 507–532, 2004. DOI: 10.1016/j.astropartphys.2003.09.003.

[228] IceCube Collaboration, "The design and performance of icecube and deepcore", *ApJ*, vol. 35, no. 10, pp. 615–624, 2012, ISSN: 0927-6505. DOI: https://doi.org/10.1016/j.astropartphys.2012.01.004. [Online]. Available: https://www.sciencedirect.com/science/article/pii/S0927650512000254.

[229] T. K. Gaisser and IceCube Collaboration, "IceTop: The Surface Component of IceCube", in *International Cosmic Ray Conference*, ser. International Cosmic Ray Conference, vol. 2, 2003, p. 1117.

[230] IceCube-Gen2 Collaboration, "IceCube-Gen2: A Vision for the Future of Neutrino Astronomy in Antarctica", *arXiv e-prints*, arXiv:1412.5106, arXiv:1412.5106, 2014. DOI: 10.48550/arXiv.1412.5106. arXiv: 1412.5106 [astro-ph.HE].

[231] I. A. Belolaptikov *et al.*, "The Baikal-experiment", *Nuclear Physics B Proceedings Supplements*, vol. 14, no. 2, pp. 51–60, 1990. DOI: 10.1016/0920-5632(90)90364-Z.

[232] V. Aynutdinov *et al.*, "Search for a diffuse flux of high-energy extraterrestrial neutrinos with the NT200 neutrino telescope", *Astroparticle Physics*, vol. 25, no. 2, pp. 140–150, 2006. DOI: 10.1016/j.astropartphys.2005.12.005. arXiv: astro-ph/0508675 [astro-ph].

[233] A. Zegarelli, S. Celli, A. Capone, S. Gagliardini, S. Campion, and I. Di Palma, "Detection prospects for multi-GeV neutrinos from collisionally heated GRBs", *Phys. Rev. D*, vol. 105, no. 8, 083023, p. 083 023, 2022. DOI: 10.1103/PhysRevD.105.083023. arXiv: 2112.14188 [astro-ph.HE].

[234] D. Band *et al.*, "BATSE Observations of Gamma-Ray Burst Spectra. I. Spectral Diversity", *ApJ*, vol. 413, p. 281, 1993. DOI: 10.1086/172995.

[235] C. Kouveliotou, C. A. Meegan, G. J. Fishman, N. P. Bhat, M. S. Briggs, T. M. Koshut, W. S. Paciesas, and G. N. Pendleton, "Identification of Two Classes of Gamma-Ray Bursts", *ApJ*, vol. 413, p. L101, 1993. DOI: 10.1086/186969.

[236] C. A. Meegan, G. J. Fishman, R. B. Wilson, W. S. Paciesas, G. N. Pendleton, J. M. Horack, M. N. Brock, and C. Kouveliotou, "Spatial distribution of γ-ray bursts observed by BATSE", *Nature*, vol. 355, no. 6356, pp. 143–145, 1992. DOI: 10.1038/355143a0.

[237] A. Cucchiara *et al.*, "A Photometric Redshift of z ~9.4 for GRB 090429B", *ApJ*, vol. 736, no. 1, 7, p. 7, 2011. DOI: 10.1088/0004-637X/736/1/7. arXiv: 1105.4915 [astro-ph.CO].

[238] R. Salvaterra *et al.*, "GRB090423 at a redshift of z~8.1", *Nature*, vol. 461, no. 7268, pp. 1258–1260, 2009. DOI: 10.1038/nature08445. arXiv: 0906.1578 [astro-ph.CO].

[239] N. R. Tanvir *et al.*, "A γ-ray burst at a redshift of z~8.2", *Nature*, vol. 461, no. 7268, pp. 1254–1257, 2009. DOI: 10.1038/nature08459. arXiv: 0906.1577 [astro-ph.CO].

[240] L. Amati, "The $E_{p,i}$-E_{iso} correlation in gamma-ray bursts: updated observational status, re-analysis and main implications", *MNRAS*, vol. 372, no. 1, pp. 233–245, 2006. DOI: 10.1111/j.1365-2966.2006.10840.x. arXiv: astro-ph/0601553 [astro-ph].

[241] J. .-. Atteia, V. Heussaff, J. .-. Dezalay, A. Klotz, D. Turpin, A. E. Tsvetkova, D. D. Frederiks, Y. Zolnierowski, F. Daigne, and R. Mochkovitch, "The Maximum Isotropic Energy of Gamma-ray Bursts", *ApJ*, vol. 837, no. 2, 119, p. 119, 2017. DOI: 10.3847/1538-4357/aa5ffa.

[242] J. .-. Atteia, V. Heussaff, J. .-. Dezalay, A. Klotz, D. Turpin, A. E. Tsvetkova, D. D. Frederiks, Y. Zolnierowski, F. Daigne, and R. Mochkovitch, "Erratum:The Maximum Isotropic Energy of Gamma-Ray Bursts", *ApJ*, vol. 852, no. 2, 144, p. 144, 2018. DOI: 10.3847/1538-4357/aaa414.

[243] R. W. Klebesadel, I. B. Strong, and R. A. Olson, "Observations of Gamma-Ray Bursts of Cosmic Origin", *ApJ*, vol. 182, p. L85, 1973. DOI: 10.1086/181225.

[244] M. J. Rees and P. Mészáros, "Unsteady Outflow Models for Cosmological Gamma-Ray Bursts", *ApJ*, vol. 430, p. L93, 1994. DOI: 10.1086/187446.

[245] E. Costa *et al.*, "Discovery of an X-ray afterglow associated with the γ-ray burst of 28 February 1997", *Nature*, vol. 387, no. 6635, pp. 783–785, 1997. DOI: 10.1038/42885. arXiv: astro-ph/9706065 [astro-ph].

[246] M. J. Rees and P. Meszaros, "Relativistic fireballs - Energy conversion and time-scales.", *MNRAS*, vol. 258, p. 41, 1992. DOI: 10.1093/mnras/258.1.41P.

[247] A. von Kienlin *et al.*, "The Fourth Fermi-GBM Gamma-Ray Burst Catalog: A Decade of Data", *ApJ*, vol. 893, no. 1, 46, p. 46, 2020. DOI: 10.3847/1538-4357/ab7a18. arXiv: 2002.11460 [astro-ph.HE].

[248] E. Nakar and T. Piran, "Time-scales in long gamma-ray bursts", *MNRAS*, vol. 331, no. 1, pp. 40–44, 2002. DOI: 10.1046/j.1365-8711.2002.05158.x. arXiv: astro-ph/0103210 [astro-ph].

[249] P. Kumar and B. Zhang, "The physics of gamma-ray bursts & relativistic jets", *Phys. Rep.*, vol. 561, pp. 1–109, 2015. DOI: 10.1016/j.physrep.2014.09.008.

[250] M. Ruderman, "Theories of gamma -ray bursts.", in *Seventh Texas Symposium on Relativistic Astrophysics*, P. G. Bergman, E. J. Fenyves, and L. Motz, Eds., vol. 262, 1975, pp. 164–180. DOI: 10.1111/j.1749-6632.1975.tb31430.x.

[251] W. K. H. Schmidt, "Distance limit for a class of model γ-ray burst sources", *Nature*, vol. 271, no. 5645, pp. 525–527, 1978. DOI: 10.1038/271525a0.

[252] A. Pe'er, "Physics of Gamma-Ray Bursts Prompt Emission", *Advances in Astronomy*, vol. 2015, 907321, p. 907 321, 2015. DOI: 10.1155/2015/907321. arXiv: 1504.02626 [astro-ph.HE].

[253] A. Goldstein, R. D. Preece, R. S. Mallozzi, M. S. Briggs, G. J. Fishman, C. Kouveliotou, W. S. Paciesas, and J. M. Burgess, "The BATSE 5B Gamma-Ray Burst Spectral Catalog", *ApJS*, vol. 208, no. 2, 21, p. 21, 2013. DOI: 10.1088/0067-0049/208/2/21. arXiv: 1311.7135 [astro-ph.HE].

[254] L. Salmon, L. Hanlon, and A. Martin-Carrillo, "Two Dimensional Clustering of Swift/BAT and Fermi/GBM Gamma-ray Bursts", *Galaxies*, vol. 10, no. 4, p. 77, 2022. DOI: 10.3390/galaxies10040077.

[255] A. Shahmoradi and R. J. Nemiroff, "Short versus long gamma-ray bursts: a comprehensive study of energetics and prompt gamma-ray correlations", *MNRAS*, vol. 451, no. 1, pp. 126–143, 2015. DOI: 10.1093/mnras/stv714. arXiv: 1412.5630 [astro-ph.HE].

[256] S. E. Woosley and J. S. Bloom, "The Supernova Gamma-Ray Burst Connection", *ARA&A*, vol. 44, no. 1, pp. 507–556, 2006. DOI: 10.1146/annurev.astro.43.072103.150558. arXiv: astro-ph/0609142 [astro-ph].

[257] T. J. Galama *et al.*, "An unusual supernova in the error box of the γ-ray burst of 25 April 1998", *Nature*, vol. 395, no. 6703, pp. 670–672, 1998. DOI: 10.1038/27150. arXiv: astro-ph/9806175 [astro-ph].

[258] R. Ruffini, M. Muccino, C. L. Bianco, M. Enderli, L. Izzo, M. Kovacevic, A. V. Penacchioni, G. B. Pisani, J. A. Rueda, and Y. Wang, "On binary-driven hypernovae and their nested late X-ray emission", *A&A*, vol. 565, L10, p. L10, 2014. DOI: 10.1051/0004-6361/201423812. arXiv: 1404.3946 [astro-ph.HE].

[259] J. A. Rueda, R. Ruffini, R. Moradi, and Y. Wang, "A brief review of binary-driven hypernova", *International Journal of Modern Physics D*, vol. 30, no. 15, 2130007, p. 2 130 007, 2021. DOI: 10.1142/S021827182130007X. arXiv: 2201.03500 [astro-ph.HE].

[260] N. Gehrels *et al.*, "A new γ-ray burst classification scheme from GRB060614", *Nature*, vol. 444, no. 7122, pp. 1044–1046, 2006. DOI: 10.1038/nature05376. arXiv: astro-ph/0610635 [astro-ph].

[261] M. Della Valle *et al.*, "An enigmatic long-lasting γ-ray burst not accompanied by a bright supernova", *Nature*, vol. 444, no. 7122, pp. 1050–1052, 2006. DOI: 10.1038/nature05374. arXiv: astro-ph/0608322 [astro-ph].

[262] A. Gal-Yam *et al.*, "A novel explosive process is required for the γ-ray burst GRB 060614", *Nature*, vol. 444, no. 7122, pp. 1053–1055, 2006. DOI: 10.1038/nature05373. arXiv: astro-ph/0608257 [astro-ph].

[263] J. P. U. Fynbo *et al.*, "No supernovae associated with two long-duration γ-ray bursts", *Nature*, vol. 444, no. 7122, pp. 1047–1049, 2006. DOI: 10.1038/nature05375. arXiv: astro-ph/0608313 [astro-ph].

[264] E. Troja *et al.*, "A nearby long gamma-ray burst from a merger of compact objects", *Nature*, vol. 612, no. 7939, pp. 228–231, 2022, ISSN: 1476-4687. DOI: 10.1038/s41586-022-05327-3. [Online]. Available: https://doi.org/10.1038/s41586-022-05327-3.

[265] A. Mei *et al.*, "Gigaelectronvolt emission from a compact binary merger", *Nature*, vol. 612, no. 7939, pp. 236–239, 2022, ISSN: 1476-4687. DOI: 10.1038/s41586-022-05404-7. [Online]. Available: https://doi.org/10.1038/s41586-022-05404-7.

[266] B. Paczynski, "Gamma-ray bursters at cosmological distances", *ApJ*, vol. 308, pp. L43–L46, 1986. DOI: 10.1086/184740.

[267] J. Goodman, "Are gamma-ray bursts optically thick?", *ApJ*, vol. 308, p. L47, 1986. DOI: 10.1086/184741.

[268] T. Piran, "Gamma-ray bursts and the fireball model", *Phys. Rep.*, vol. 314, no. 6, pp. 575–667, 1999. DOI: 10.1016/S0370-1573(98)00127-6.

[269] A. M. Beloborodov and P. Mészáros, "Photospheric Emission of Gamma-Ray Bursts", *Space Sci. Rev.*, vol. 207, no. 1-4, pp. 87–110, 2017. DOI: 10.1007/s11214-017-0348-6.

[270] D. Giannios, "Prompt GRB emission from gradual energy dissipation", *A&A*, vol. 480, no. 2, pp. 305–312, 2008. DOI: 10.1051/0004-6361:20079085.

[271] J. C. McKinney and D. A. Uzdensky, "A reconnection switch to trigger gamma-ray burst jet dissipation", *MNRAS*, vol. 419, no. 1, pp. 573–607, 2012. DOI: 10.1111/j.1365-2966.2011.19721.x.

[272] L. Sironi, M. Petropoulou, and D. Giannios, "Relativistic jets shine through shocks or magnetic reconnection?", *MNRAS*, vol. 450, no. 1, pp. 183–191, 2015. DOI: 10.1093/mnras/stv641.

[273] P. Beniamini and J. Granot, "Properties of GRB light curves from magnetic reconnection", *MNRAS*, vol. 459, no. 4, pp. 3635–3658, 2016. DOI: 10.1093/mnras/stw895.

[274] P. Joss, E. Salpeter, and J. Ostriker, "On the "Critical Luminosity" in Stellar Interiors and Stellar Surface Boundary Conditions", *ApJ*, vol. 181, pp. 429–438, 1973. DOI: 10.1086/152060.

[275] M. Bustamante, P. Baerwald, K. Murase, and W. Winter, "Neutrino and cosmic-ray emission from multiple internal shocks in gamma-ray bursts", *Nature Communications*, vol. 6, 6783, p. 6783, 2015. DOI: 10.1038/ncomms7783.

[276] D. Guetta, D. Hooper, J. Alvarez-Muniz, F. Halzen, and E. Reuveni, "Neutrinos from individual gamma-ray bursts in the BATSE catalog", *Astroparticle Physics*, vol. 20, no. 4, pp. 429–455, 2004. DOI: 10.1016/S0927-6505(03)00211-1.

[277] Y. Kaneko, R. D. Preece, M. S. Briggs, W. S. Paciesas, C. A. Meegan, and D. L. Band, "The Complete Spectral Catalog of Bright BATSE Gamma-Ray Bursts", *ApJS*, vol. 166, no. 1, pp. 298–340, 2006. DOI: 10.1086/505911.

[278] F. Frontera, L. Amati, C. Guidorzi, R. Landi, and V. La Parola, "The spectral evolution in the 2-700 keV energy band of the entire sample of GRBs observed with WFC and GRBM aboard BeppoSAX .", *Mem. Soc. Astron. Italiana*, vol. 81, p. 426, 2010.

[279] L. Nava, G. Ghirlanda, G. Ghisellini, and A. Celotti, "Spectral properties of 438 GRBs detected by Fermi/GBM", *A&A*, vol. 530, A21, A21, 2011. DOI: 10.1051/0004-6361/201016270.

[280] Fermi GBM Collaboration, "The Fermi GBM Gamma-Ray Burst Spectral Catalog: Four Years of Data", *ApJS*, vol. 211, no. 1, 12, p. 12, 2014. DOI: 10.1088/0067-0049/211/1/12.

[281] Fermi GBM Collaboration, "The Fourth Fermi-GBM Gamma-Ray Burst Catalog: A Decade of Data", *ApJ*, vol. 893, no. 1, 46, p. 46, 2020. DOI: 10.3847/1538-4357/ab7a18.

[282] R. D. Preece, M. S. Briggs, R. S. Mallozzi, G. N. Pendleton, W. S. Paciesas, and D. L. Band, "The BATSE Gamma-Ray Burst Spectral Catalog. I. High Time Resolution Spectroscopy of Bright Bursts Using High Energy Resolution Data", *ApJS*, vol. 126, no. 1, pp. 19–36, 2000. DOI: 10.1086/313289.

[283] G. Ghirlanda, G. Ghisellini, and A. Celotti, "The spectra of short gamma-ray bursts", *A&A*, vol. 422, pp. L55–L58, 2004. DOI: 10.1051/0004-6361:20048008.

[284] G. Ghirlanda, L. Nava, G. Ghisellini, A. Celotti, and C. Firmani, "Short versus long gamma-ray bursts: spectra, energetics, and luminosities", *A&A*, vol. 496, no. 3, pp. 585–595, 2009. DOI: 10.1051/0004-6361/200811209.

[285] P. Mészáros, E. Ramirez-Ruiz, M. J. Rees, and B. Zhang, "X-Ray-rich Gamma-Ray Bursts, Photospheres, and Variability", *ApJ*, vol. 578, no. 2, pp. 812–817, 2002. DOI: 10.1086/342611.

[286] M. J. Rees and P. Mészáros, "Dissipative Photosphere Models of Gamma-Ray Bursts and X-Ray Flashes", *ApJ*, vol. 628, no. 2, pp. 847–852, 2005. DOI: 10.1086/430818.

[287] D. Lazzati, B. J. Morsony, and M. C. Begelman, "Very High Efficiency Photospheric Emission in Long-Duration γ-Ray Bursts", *ApJ*, vol. 700, no. 1, pp. L47–L50, 2009. DOI: 10.1088/0004-637X/700/1/L47.

[288] F. Ryde *et al.*, "Observational evidence of dissipative photospheres in gamma-ray bursts", *MNRAS*, vol. 415, no. 4, pp. 3693–3705, 2011. DOI: 10.1111/j.1365-2966.2011.18985.x.

[289] A. M. Beloborodov, "Collisional mechanism for gamma-ray burst emission", *MNRAS*, vol. 407, no. 2, pp. 1033–1047, 2010. DOI: 10.1111/j.1365-2966.2010.16770.x.

[290] I. Vurm, A. M. Beloborodov, and J. Poutanen, "Gamma-Ray Bursts from Magnetized Collisionally Heated Jets", *ApJ*, vol. 738, no. 1, 77, p. 77, 2011. DOI: 10.1088/0004-637X/738/1/77.

[291] C. Thompson, "A model of gamma-ray bursts.", *MNRAS*, vol. 270, pp. 480–498, 1994. DOI: 10.1093/mnras/270.3.480.

[292] H. C. Spruit, F. Daigne, and G. Drenkhahn, "Large scale magnetic fields and their dissipation in GRB fireballs", *A&A*, vol. 369, pp. 694–705, 2001. DOI: 10.1051/0004-6361:20010131.

[293] D. Giannios and H. C. Spruit, "Spectra of Poynting-flux powered GRB outflows", *A&A*, vol. 430, pp. 1–7, 2005. DOI: 10.1051/0004-6361:20047033.

[294] B. Zhang and H. Yan, "The Internal-collision-induced Magnetic Reconnection and Turbulence (ICMART) Model of Gamma-ray Bursts", *ApJ*, vol. 726, no. 2, 90, p. 90, 2011. DOI: 10.1088/0004-637X/726/2/90.

[295] M. A. Abramowicz, I. D. Novikov, and B. Paczynski, "The Appearance of Highly Relativistic, Spherically Symmetric Stellar Winds", *ApJ*, vol. 369, p. 175, 1991. DOI: 10.1086/169748.

[296] A. Pe'er, "Temporal Evolution of Thermal Emission from Relativistically Expanding Plasma", *ApJ*, vol. 682, no. 1, pp. 463–473, 2008. DOI: 10.1086/588136.

[297] Fermi GBM Collaboration, "Fermi Observations of GRB 090902B: A Distinct Spectral Component in the Prompt and Delayed Emission", *ApJ*, vol. 706, no. 1, pp. L138–L144, 2009. DOI: 10.1088/0004-637X/706/1/L138.

[298] S. Guiriec *et al.*, "Detection of a Thermal Spectral Component in the Prompt Emission of GRB 100724B", *ApJ*, vol. 727, no. 2, L33, p. L33, 2011. DOI: 10.1088/2041-8205/727/2/L33. arXiv: 1010.4601 [astro-ph.HE].

[299] S. Iyyani *et al.*, "Variable jet properties in GRB 110721A: time resolved observations of the jet photosphere", *MNRAS*, vol. 433, no. 4, pp. 2739–2748, 2013. DOI: 10.1093/mnras/stt863.

[300] E. Waxman and J. Bahcall, "High Energy Neutrinos from Cosmological Gamma-Ray Burst Fireballs", *Phys. Rev. Lett.*, vol. 78, no. 12, pp. 2292–2295, 1997. DOI: 10.1103/PhysRevLett.78.2292.

[301] P. Mészáros and M. J. Rees, "Multi-GEV Neutrinos from Internal Dissipation in Gamma-Ray Burst Fireballs", *ApJ*, vol. 541, no. 1, pp. L5–L8, 2000. DOI: 10.1086/312894.

[302] J. N. Bahcall and P. Mészáros, "5-10 GeV Neutrinos from Gamma-Ray Burst Fireballs", *Phys. Rev. Lett.*, vol. 85, no. 7, pp. 1362–1365, 2000. DOI: 10.1103/PhysRevLett.85.1362.

[303] I. Bartos, A. M. Beloborodov, K. Hurley, and S. Márka, "Detection Prospects for GeV Neutrinos from Collisionally Heated Gamma-ray Bursts with IceCube/DeepCore", *Phys. Rev. Lett.*, vol. 110, no. 24, 241101, p. 241 101, 2013. DOI: 10.1103/PhysRevLett.110.241101.

[304] K. Murase, K. Kashiyama, and P. Mészáros, "Subphotospheric Neutrinos from Gamma-Ray Bursts: The Role of Neutrons", *Phys. Rev. Lett.*, vol. 111, no. 13, 131102, p. 131 102, 2013. DOI: 10.1103/PhysRevLett.111.131102.

[305] J. P. Rachen and P. Mészáros, "Photohadronic neutrinos from transients in astrophysical sources", *Phys. Rev. D*, vol. 58, no. 12, 123005, p. 123 005, 1998. DOI: 10.1103/PhysRevD.58.123005.

[306] K. Murase and S. Nagataki, "High energy neutrino emission and neutrino background from gamma-ray bursts in the internal shock model", *Phys. Rev. D*, vol. 73, no. 6, 063002, p. 063 002, 2006. DOI: 10.1103/PhysRevD.73.063002.

[307] B. Zhang and P. Kumar, "Model-Dependent High-Energy Neutrino Flux from Gamma-Ray Bursts", *Phys. Rev. Lett.*, vol. 110, no. 12, 121101, p. 121 101, 2013. DOI: 10.1103/PhysRevLett.110.121101.

[308] E. V. Derishev, V. V. Kocharovsky, and V. V. Kocharovsky, "The Neutron Component in Fireballs of Gamma-Ray Bursts: Dynamics and Observable Imprints", *ApJ*, vol. 521, no. 2, pp. 640–649, 1999. DOI: 10.1086/307574.

[309] A. M. Beloborodov, "Hyper-accreting black holes", in *Cool Discs, Hot Flows: The Varying Faces of Accreting Compact Objects*, M. Axelsson, Ed., ser. American Institute of Physics Conference Series, vol. 1054, 2008, pp. 51–70. DOI: 10.1063/1.3002509.

[310] A. M. Beloborodov, "Nuclear Composition of Gamma-Ray Burst Fireballs", *ApJ*, vol. 588, no. 2, pp. 931–944, 2003. DOI: 10.1086/374217.

[311] A. M. Beloborodov, "Neutron-fed Afterglows of Gamma-Ray Bursts", *ApJ*, vol. 585, no. 1, pp. L19–L22, 2003. DOI: 10.1086/374258.

[312] ANTARES Collaboration, "Search for muon neutrinos from gamma-ray bursts with the ANTARES neutrino telescope using 2008 to 2011 data", *A&A*, vol. 559, A9, A9, 2013. DOI: 10.1051/0004-6361/201322169.

[313] ANTARES Collaboration, "Search for high-energy neutrinos from bright GRBs with ANTARES", *MNRAS*, vol. 469, no. 1, pp. 906–915, 2017. DOI: 10.1093/mnras/stx902.

[314] ANTARES Collaboration, "Constraining the contribution of Gamma-Ray Bursts to the high-energy diffuse neutrino flux with 10 yr of ANTARES data", *MNRAS*, vol. 500, no. 4, pp. 5614–5628, 2021. DOI: 10.1093/mnras/staa3503.

[315] IceCube Collaboration, "Extending the Search for Muon Neutrinos Coincident with Gamma-Ray Bursts in IceCube Data", *ApJ*, vol. 843, no. 2, 112, p. 112, 2017. DOI: 10.3847/1538-4357/aa7569.

[316] IceCube Collaboration, "An All-sky Search for Three Flavors of Neutrinos from Gamma-ray Bursts with the IceCube Neutrino Observatory", *ApJ*, vol. 824, no. 2, 115, p. 115, 2016. DOI: 10.3847/0004-637X/824/2/115.

[317] IceCube Collaboration, "Search for sub-TeV neutrino emission from transient sources with three years of IceCube data", *arXiv e-prints*, arXiv:2011.05096, arXiv:2011.05096, 2020.

[318] C. Chen, P. Dave, and I. Taboada, "Search for Astrophysical Neutrino Transients with IceCube DeepCore", *PoS*, vol. ICRC2021, p. 1143, 2021. DOI: 10.22323/1.395.1143".

[319] K. Asano and P. Mészáros, "Photon and neutrino spectra of time-dependent photospheric models of gamma-ray bursts", *J. Cosmology Astropart. Phys.*, vol. 2013, no. 9, 008, p. 008, 2013. DOI: 10.1088/1475-7516/2013/09/008.

[320] The IceCube-PINGU Collaboration, "Letter of Intent: The Precision IceCube Next Generation Upgrade (PINGU)", *arXiv e-prints*, arXiv:1401.2046, arXiv:1401.2046, 2014. arXiv: 1401.2046 [physics.ins-det].

[321] KM3NeT Collaboration, "Deep-sea deployment of the KM3NeT neutrino telescope detection units by self-unrolling", *Journal of Instrumentation*, vol. 15, no. 11, P11027, 2020. DOI: 10.1088/1748-0221/15/11/P11027.

[322] A. Kouchner and J. Coelho, "Measuring the Neutrino Mass Ordering and other oscillation parameters with KM3NeT-ORCA", *PoS*, vol. ICRC2017, p. 1027, 2017. DOI: 10.22323/1.301.1027.

[323] J. S. Bloom, D. A. Frail, and R. Sari, "The Prompt Energy Release of Gamma-Ray Bursts using a Cosmological k-Correction", *AJ*, vol. 121, no. 6, pp. 2879–2888, 2001. DOI: 10.1086/321093.

[324] S. Poolakkil *et al.*, "The Fermi-GBM Gamma-Ray Burst Spectral Catalog: 10 yr of Data", *ApJ*, vol. 913, no. 1, 60, p. 60, 2021. DOI: 10.3847/1538-4357/abf24d. arXiv: 2103.13528 [astro-ph.HE].

[325] T. K. Gaisser and A. M. Hillas, "Reliability of the Method of Constant Intensity Cuts for Reconstructing the Average Development of Vertical Showers", in *International Cosmic Ray Conference*, ser. International Cosmic Ray Conference, vol. 8, 1977, p. 353.

[326] W. Assal, D. Dornic, E. Le Guirriec, M. Lincetto, G. Vannoye, and KM3NeT Collaboration, "Real-time Multi-Messenger Analysis Framework of KM3NeT", *PoS*, vol. ICRC2021, p. 941, 2021. DOI: 10.22323/1.395.0941.

[327] G. Ghirlanda, F. Nappo, G. Ghisellini, A. Melandri, G. Marcarini, L. Nava, O. S. Salafia, S. Campana, and R. Salvaterra, "Bulk Lorentz factors of gamma-ray bursts", *A&A*, vol. 609, A112, A112, 2018. DOI: 10.1051/0004-6361/201731598. arXiv: 1711.06257 [astro-ph.HE].

[328] IceCube Collaboration, "Search for Prompt Neutrino Emission from Gamma-Ray Bursts with IceCube", *ApJ*, vol. 805, no. 1, L5, p. L5, 2015. DOI: 10.1088/2041-8205/805/1/L5. arXiv: 1412.6510 [astro-ph.HE].

[329] IceCube Collaboration, "An All-sky Search for Three Flavors of Neutrinos from Gamma-ray Bursts with the IceCube Neutrino Observatory", *ApJ*, vol. 824, no. 2, 115, p. 115, 2016. DOI: 10.3847/0004-637X/824/2/115. arXiv: 1601.06484 [astro-ph.HE].

[330] IceCube Collaboration, "Extending the Search for Muon Neutrinos Coincident with Gamma-Ray Bursts in IceCube Data", *ApJ*, vol. 843, no. 2, 112, p. 112, 2017. DOI: 10.3847/1538-4357/aa7569. arXiv: 1702.06868 [astro-ph.HE].

[331] S. Adrián-Martínez *et al.*, "Search for muon neutrinos from gamma-ray bursts with the ANTARES neutrino telescope using 2008 to 2011 data", *A&A*, vol. 559, A9, A9, 2013. DOI: 10.1051/0004-6361/201322169. arXiv: 1307.0304 [astro-ph.HE].

[332] S. Adrián-Martínez *et al.*, "Stacked search for time shifted high energy neutrinos from gamma ray bursts with the Antares neutrino telescope", *European Physical Journal C*, vol. 77, no. 1, 20, p. 20, 2017. DOI: 10.1140/epjc/s10052-016-4496-8.

[333] A. Albert *et al.*, "Search for high-energy neutrinos from bright GRBs with ANTARES", *MNRAS*, vol. 469, no. 1, pp. 906–915, 2017. DOI: 10.1093/mnras/stx902. arXiv: 1612.08589 [astro-ph.HE].

[334] D. Gruber *et al.*, "The Fermi GBM Gamma-Ray Burst Spectral Catalog: Four Years of Data", *ApJS*, vol. 211, no. 1, 12, p. 12, 2014. DOI: 10.1088/0067-0049/211/1/12. arXiv: 1401.5069 [astro-ph.HE].

[335] A. von Kienlin *et al.*, "The Second Fermi GBM Gamma-Ray Burst Catalog: The First Four Years", *ApJS*, vol. 211, no. 1, 13, p. 13, 2014. DOI: 10.1088/0067-0049/211/1/13. arXiv: 1401.5080 [astro-ph.HE].

[336] P. Narayana Bhat *et al.*, "The Third Fermi GBM Gamma-Ray Burst Catalog: The First Six Years", *ApJS*, vol. 223, no. 2, 28, p. 28, 2016. DOI: 10.3847/0067-0049/223/2/28. arXiv: 1603.07612 [astro-ph.HE].

[337] M. Ajello *et al.*, "A Decade of Gamma-Ray Bursts Observed by Fermi-LAT: The Second GRB Catalog", *ApJ*, vol. 878, no. 1, 52, p. 52, 2019. DOI: 10.3847/1538-4357/ab1d4e. arXiv: 1906.11403 [astro-ph.HE].

[338] W. B. Atwood *et al.*, "The Large Area Telescope on the Fermi Gamma-Ray Space Telescope Mission", *ApJ*, vol. 697, no. 2, pp. 1071–1102, 2009. DOI: 10.1088/0004-637X/697/2/1071. arXiv: 0902.1089 [astro-ph.IM].

[339] C. Meegan *et al.*, "The Fermi Gamma-ray Burst Monitor", *ApJ*, vol. 702, no. 1, pp. 791–804, 2009. DOI: 10.1088/0004-637X/702/1/791. arXiv: 0908.0450 [astro-ph.IM].

[340] R. L. Aptekar *et al.*, "Konus-W Gamma-Ray Burst Experiment for the GGS Wind Spacecraft", *Space Sci. Rev.*, vol. 71, no. 1-4, pp. 265–272, 1995. DOI: 10.1007/BF00751332.

[341] D. Guetta, D. Hooper, J. Alvarez-Muniz, F. Halzen, and E. Reuveni, "Neutrinos from individual gamma-ray bursts in the BATSE catalog", *Astroparticle Physics*, vol. 20, no. 4, pp. 429–455, 2004. DOI: 10.1016/S0927-6505(03)00211-1. arXiv: astro-ph/0302524 [astro-ph].

[342] F. Daigne and R. Mochkovitch, "Gamma-ray bursts from internal shocks in a relativistic wind: temporal and spectral properties", *MNRAS*, vol. 296, no. 2, pp. 275–286, 1998. DOI: 10.1046/j.1365-8711.1998.01305.x. arXiv: astro-ph/9801245 [astro-ph].

[343] K. Asano and T. Terasawa, "Slow Heating Model of Gamma-ray Burst: Photon Spectrum and Delayed Emission", *ApJ*, vol. 705, no. 2, pp. 1714–1720, 2009. DOI: 10.1088/0004-637X/705/2/1714. arXiv: 0905.1392 [astro-ph.HE].

[344] M. Lyutikov, "Did Swift measure gamma-ray burst prompt emission radii?", *MNRAS*, vol. 369, no. 1, pp. L5–L8, 2006. DOI: 10.1111/j.1745-3933.2006.00161.x. arXiv: astro-ph/0601557 [astro-ph].

[345] P. Kumar and E. McMahon, "A general scheme for modelling γ-ray burst prompt emission", *MNRAS*, vol. 384, no. 1, pp. 33–63, 2008. DOI: 10.1111/j.1365-2966.2007.12621.x. arXiv: 0802.2704 [astro-ph].

[346] K. Murase, K. Ioka, S. Nagataki, and T. Nakamura, "High-energy cosmic-ray nuclei from high- and low-luminosity gamma-ray bursts and implications for multimessenger astronomy", *Phys. Rev. D*, vol. 78, no. 2, 023005, p. 023 005, 2008. DOI: 10.1103/PhysRevD.78.023005. arXiv: 0801.2861 [astro-ph].

[347] H.-N. He, R.-Y. Liu, X.-Y. Wang, S. Nagataki, K. Murase, and Z.-G. Dai, "Icecube Nondetection of Gamma-Ray Bursts: Constraints on the Fireball Properties", *ApJ*, vol. 752, no. 1, 29, p. 29, 2012. DOI: 10.1088/0004-637X/752/1/29. arXiv: 1204.0857 [astro-ph.HE].

[348] B. Zhang and P. Kumar, "Model-Dependent High-Energy Neutrino Flux from Gamma-Ray Bursts", *Phys. Rev. Lett.*, vol. 110, no. 12, 121101, p. 121 101, 2013. DOI: 10.1103/PhysRevLett.110.121101. arXiv: 1210.0647 [astro-ph.HE].

[349] K. Murase, "Prompt high-energy neutrinos from gamma-ray bursts in photospheric and synchrotron self-Compton scenarios", *Phys. Rev. D*, vol. 78, no. 10, 101302, p. 101 302, 2008. DOI: 10.1103/PhysRevD.78.101302. arXiv: 0807.0919 [astro-ph].

[350] K. Murase, K. Kashiyama, and P. Mészáros, "Subphotospheric Neutrinos from Gamma-Ray Bursts: The Role of Neutrons", *Phys. Rev. Lett.*, vol. 111, no. 13, 131102, p. 131 102, 2013. DOI: 10.1103/PhysRevLett.111.131102. arXiv: 1301.4236 [astro-ph.HE].

[351] B. Paczynski and G. Xu, "Neutrino Bursts from Gamma-Ray Bursts", *ApJ*, vol. 427, p. 708, 1994. DOI: 10.1086/174178.

[352] E. Waxman and J. Bahcall, "High Energy Neutrinos from Cosmological Gamma-Ray Burst Fireballs", *Phys. Rev. Lett.*, vol. 78, no. 12, pp. 2292–2295, 1997. DOI: 10.1103/PhysRevLett.78.2292. arXiv: astro-ph/9701231 [astro-ph].

[353] S. Hümmer, M. Rüger, F. Spanier, and W. Winter, "Simplified Models for Photohadronic Interactions in Cosmic Accelerators", *ApJ*, vol. 721, no. 1, pp. 630–652, 2010. DOI: 10.1088/0004-637X/721/1/630. arXiv: 1002.1310 [astro-ph.HE].

[354] S. Hümmer, P. Baerwald, and W. Winter, "Neutrino Emission from Gamma-Ray Burst Fireballs, Revised", *Phys. Rev. Lett.*, vol. 108, no. 23, 231101, p. 231 101, 2012. DOI: 10.1103/PhysRevLett.108.231101. arXiv: 1112.1076 [astro-ph.HE].

[355] A. R. Bell, "The acceleration of cosmic rays in shock fronts - I.", *MNRAS*, vol. 182, pp. 147–156, 1978. DOI: 10.1093/mnras/182.2.147.

[356] P. Kumar and B. Zhang, "The physics of gamma-ray bursts & relativistic jets", *Phys. Rep.*, vol. 561, pp. 1–109, 2015. DOI: 10.1016/j.physrep.2014.09.008. arXiv: 1410.0679 [astro-ph.HE].

[357] M. Bustamante, P. Baerwald, K. Murase, and W. Winter, "Neutrino and cosmic-ray emission from multiple internal shocks in gamma-ray bursts", *Nature Communications*, vol. 6, 6783, p. 6783, 2015. DOI: 10.1038/ncomms7783. arXiv: 1409.2874 [astro-ph.HE].

[358] M. Bustamante, J. Heinze, K. Murase, and W. Winter, "Multi-messenger Light Curves from Gamma-Ray Bursts in the Internal Shock Model", *ApJ*, vol. 837, no. 1, 33, p. 33, 2017. DOI: 10.3847/1538-4357/837/1/33. arXiv: 1606.02325 [astro-ph.HE].

[359] R. Sari and T. Piran, "Predictions for the Very Early Afterglow and the Optical Flash", *ApJ*, vol. 520, no. 2, pp. 641–649, 1999. DOI: 10.1086/307508. arXiv: astro-ph/9901338 [astro-ph].

[360] Y. Lithwick and R. Sari, "Lower Limits on Lorentz Factors in Gamma-Ray Bursts", *ApJ*, vol. 555, no. 1, pp. 540–545, 2001. DOI: 10.1086/321455. arXiv: astro-ph/0011508 [astro-ph].

[361] N. Gupta and B. Zhang, "Diagnosing the site of gamma-ray burst prompt emission with spectral cut-off energy", *MNRAS*, vol. 384, no. 1, pp. L11–L15, 2008. DOI: 10.1111/j.1745-3933.2007.00411.x. arXiv: 0708.2763 [astro-ph].

[362] Fermi LAT Collaboration and Fermi GBM Collaboration, "Fermi Observations of High-Energy Gamma-Ray Emission from GRB 080916C", *Science*, vol. 323, no. 5922, p. 1688, 2009. DOI: 10.1126/science.1169101.

[363] Fermi LAT Collaboration, "A limit on the variation of the speed of light arising from quantum gravity effects", *Nature*, vol. 462, no. 7271, pp. 331–334, 2009. DOI: 10.1038/nature08574. arXiv: 0908.1832 [astro-ph.HE].

[364] A. A. Abdo *et al.*, "Fermi Observations of GRB 090902B: A Distinct Spectral Component in the Prompt and Delayed Emission", *ApJ*, vol. 706, no. 1, pp. L138–L144, 2009. DOI: 10.1088/0004-637X/706/1/L138. arXiv: 0909.2470 [astro-ph.HE].

[365] Y.-C. Zou and T. Piran, "Lorentz factor constraint from the very early external shock of the gamma-ray burst ejecta", *MNRAS*, vol. 402, no. 3, pp. 1854–1862, 2010. DOI: 10.1111/j.1365-2966.2009.15863.x. arXiv: 0908.4418 [astro-ph.HE].

[366] J. Lü, Y.-C. Zou, W.-H. Lei, B. Zhang, Q. Wu, D.-X. Wang, E.-W. Liang, and H.-J. Lü, "Lorentz-factor-Isotropic-luminosity/Energy Correlations of Gamma-Ray Bursts and Their Interpretation", *ApJ*, vol. 751, no. 1, 49, p. 49, 2012. DOI: 10.1088/0004-637X/751/1/49. arXiv: 1109.3757 [astro-ph.HE].

[367] V. Z. Golkhou, N. R. Butler, and O. M. Littlejohns, "The Energy Dependence of GRB Minimum Variability Timescales", *ApJ*, vol. 811, no. 2, 93, p. 93, 2015. DOI: 10.1088/0004-637X/811/2/93. arXiv: 1501.05948 [astro-ph.HE].

[368] V. Z. Golkhou and N. R. Butler, "Uncovering the Intrinsic Variability of Gamma-Ray Bursts", *ApJ*, vol. 787, no. 1, 90, p. 90, 2014. DOI: 10.1088/0004-637X/787/1/90. arXiv: 1403.4254 [astro-ph.HE].

[369] E. Sonbas, G. A. MacLachlan, K. S. Dhuga, P. Veres, A. Shenoy, and T. N. Ukwatta, "Gamma-ray Bursts: Temporal Scales and the Bulk Lorentz Factor", *ApJ*, vol. 805, no. 2, 86, p. 86, 2015. DOI: 10.1088/0004-637X/805/2/86. arXiv: 1408.3042 [astro-ph.HE].

[370] D. Xu, A. J. Levan, S. B. Cenko, D. A. Perley, and N. R. Tanvir, "GRB 141028A: VLT/X-shooter redshift of z=2.33", *GRB Coordinates Network*, vol. 16983, p. 1, 2014.

[371] A. J. Levan, S. B. Cenko, D. A. Perley, and N. R. Tanvir, "GRB 130427A: gemini-north redshift.", *GRB Coordinates Network*, vol. 14455, p. 1, 2013.

[372] G. Ghirlanda, L. Nava, G. Ghisellini, A. Celotti, D. Burlon, S. Covino, and A. Melandri, "Gamma-ray bursts in the comoving frame", *MNRAS*, vol. 420, no. 1, pp. 483–494, 2012. DOI: 10.1111/j.1365-2966.2011.20053.x. arXiv: 1107.4096 [astro-ph.HE].

[373] R. D. Blandford and C. F. McKee, "Fluid dynamics of relativistic blast waves", *Physics of Fluids*, vol. 19, pp. 1130–1138, 1976. DOI: 10.1063/1.861619.

[374] S. Adrián-Martínez *et al.*, "The positioning system of the ANTARES Neutrino Telescope", *Journal of Instrumentation*, vol. 7, no. 8, T08002, 2012. DOI: 10.1088/1748-0221/7/08/T08002. arXiv: 1202.3894 [astro-ph.IM].

[375] ANTARES Collaboration, "First all-flavor neutrino pointlike source search with the ANTARES neutrino telescope", *Phys. Rev. D*, vol. 96, no. 8, 082001, p. 082 001, 2017. DOI: 10.1103/PhysRevD.96.082001. arXiv: 1706.01857 [astro-ph.HE].

[376] A. Albert *et al.*, "The cosmic ray shadow of the Moon observed with the ANTARES neutrino telescope", *European Physical Journal C*, vol. 78, no. 12, 1006, p. 1006, 2018. DOI: 10.1140/epjc/s10052-018-6451-3. arXiv: 1807.11815 [astro-ph.HE].

[377] ANTARES Collaboration, "Observation of the cosmic ray shadow of the Sun with the ANTARES neutrino telescope", *Phys. Rev. D*, vol. 102, no. 12, 122007, p. 122 007, 2020. DOI: 10.1103/PhysRevD.102.122007. arXiv: 2007.00931 [astro-ph.HE].

[378] L. F. Rayleigh, "Xii. on the resultant of a large number of vibrations of the same pitch and of arbitrary phase", *The London, Edinburgh, and Dublin Philosophical Magazine and Journal of Science*, vol. 10, no. 60, pp. 73–78, 1880. DOI: 10.1080/14786448008626893. eprint: https://doi.org/10.1080/14786448008626893. [Online]. Available: https://doi.org/10.1080/14786448008626893.

[379] R. Barlow, "Extended maximum likelihood", *Nuclear Instruments and Methods in Physics Research A*, vol. 297, no. 3, pp. 496–506, 1990. DOI: 10.1016/0168-9002(90)91334-8.

[380] ANTARES Collaboration, "Search for Cosmic Neutrino Point Sources with Four Years of Data from the ANTARES Telescope", *ApJ*, vol. 760, no. 1, 53, p. 53, 2012. DOI: 10.1088/0004-637X/760/1/53. arXiv: 1207.3105 [hep-ex].

[381] A. Schneider, "Characterization of the Astrophysical Diffuse Neutrino Flux with IceCube High-Energy Starting Events", in *36th International Cosmic Ray Conference (ICRC2019)*, ser. International Cosmic Ray Conference, vol. 36, 2019, 1004, p. 1004. DOI: 10.22323/1.358.01004. arXiv: 1907.11266 [astro-ph.HE].

[382] R.-Y. Liu and X.-Y. Wang, "Diffuse PeV Neutrinos from Gamma-Ray Bursts", *ApJ*, vol. 766, no. 2, 73, p. 73, 2013. DOI: 10.1088/0004-637X/766/2/73. arXiv: 1212.1260 [astro-ph.HE].

[383] N. Gupta and B. Zhang, "Neutrino spectra from low and high luminosity populations of gamma ray bursts", *Astroparticle Physics*, vol. 27, no. 5, pp. 386–391, 2007. DOI: 10.1016/j.astropartphys.2007.01.004. arXiv: astro-ph/0606744 [astro-ph].

[384] P. Mészáros and E. Waxman, "TeV Neutrinos from Successful and Choked Gamma-Ray Bursts", *Phys. Rev. Lett.*, vol. 87, no. 17, 171102, p. 171 102, 2001. DOI: 10.1103/PhysRevLett.87.171102. arXiv: astro-ph/0103275 [astro-ph].

[385] K. Murase and K. Ioka, "TeV-PeV Neutrinos from Low-Power Gamma-Ray Burst Jets inside Stars", *Phys. Rev. Lett.*, vol. 111, no. 12, 121102, p. 121 102, 2013. DOI: 10.1103/PhysRevLett.111.121102. arXiv: 1306.2274 [astro-ph.HE].

[386] N. Senno, K. Murase, and P. Mészáros, "Choked jets and low-luminosity gamma-ray bursts as hidden neutrino sources", *Phys. Rev. D*, vol. 93, no. 8, 083003, p. 083 003, 2016. DOI: 10.1103/PhysRevD.93.083003. arXiv: 1512.08513 [astro-ph.HE].

[387] M. Fasano, S. Celli, D. Guetta, A. Capone, A. Zegarelli, and I. Di Palma, "Estimating the neutrino flux from choked gamma-ray bursts", *J. Cosmology Astropart. Phys.*, vol. 2021, no. 9, 044, p. 044, 2021. DOI: 10.1088/1475-7516/2021/09/044. arXiv: 2101.03502 [astro-ph.HE].

[388] KM3NeT Collaboration, "The KM3NeT multi-PMT optical module", *Journal of Instrumentation*, vol. 17, no. 7, P07038, P07038, 2022. DOI: 10.1088/1748-0221/17/07/P07038.

[389] D. Calvo, D. Real, and KM3NeT Collaboration, "Status of the central logic board (CLB) of the KM3NeT neutrino telescope", *Journal of Instrumentation*, vol. 10, no. 12, C12027, p. C12027, 2015. DOI: 10.1088/1748-0221/10/12/C12027.

[390] A. Zwart, E. Heine, J. Hogenbirk, P. Jansweijer, G. Kieft, S. Mos, E. de Wolf, and KM3NeT Consortium, "A TDC for the characterization of KM3NeT PMTs", *Nuclear Instruments and Methods in Physics Research A*, vol. 725, pp. 170–174, 2013. DOI: 10.1016/j.nima.2012.12.101.

[391] KM3NeT Collaboration, "KM3NeT front-end and readout electronics system: hardware, firmware, and software", *Journal of Astronomical Telescopes, Instruments, and Systems*, vol. 5, 046001, p. 046 001, 2019. DOI: 10.1117/1.JATIS.5.4.046001. arXiv: 1907.06453 [astro-ph.IM].

[392] KM3NeT Collaboration, "Architecture and performance of the KM3NeT front-end firmware", *Journal of Astronomical Telescopes, Instruments, and Systems*, vol. 7, 016001, p. 016 001, 2021. DOI: 10.1117/1.JATIS.7.1.016001.

[393] C. Pellegrino and T. Chiarusi, "The Trigger and Data Acquisition System for the KM3NeT neutrino telescope", in *European Physical Journal Web of Conferences*, ser. European Physical Journal Web of Conferences, vol. 116, 2016, 05005, p. 05 005. DOI: 10.1051/epjconf/201611605005.

[394] KM3NeT Collaboration, "The Control Unit of the KM3NeT Data Acquisition System", *Computer Physics Communications*, vol. 256, 107433, p. 107 433, 2020. DOI: 10.1016/j.cpc.2020.107433. arXiv: 1910.00112 [astro-ph.IM].

[395] KM3NeT Collaboration, "Implementation and first results of the KM3NeT real-time core-collapse supernova neutrino search", *European Physical Journal C*, vol. 82, no. 4, 317, p. 317, 2022. DOI: 10.1140/epjc/s10052-022-10137-y.

[396] M. G. Allen, "CDS - Strasbourg Astronomical Data Centre", in *Astronomical Data Analysis Software and Systems XXIX*, R. Pizzo, E. R. Deul, J. D. Mol, J. de Plaa, and H. Verkouter, Eds., ser. Astronomical Society of the Pacific Conference Series, vol. 527, 2020, p. 751.

[397] P. Antonioli *et al.*, "SNEWS: the SuperNova Early Warning System", *New Journal of Physics*, vol. 6, p. 114, 2004. DOI: 10.1088/1367-2630/6/1/114. arXiv: astro-ph/0406214 [astro-ph].

[398] S. Al Kharusi *et al.*, "SNEWS 2.0: a next-generation supernova early warning system for multimessenger astronomy", *New Journal of Physics*, vol. 23, no. 3, 031201, p. 031 201, 2021. DOI: 10.1088/1367-2630/abde33. arXiv: 2011.00035 [astro-ph.HE].

[399] https://docs.docker.com.

[400] https://www.rabbitmq.com.

[401] S. Dichiara, J. D. Gropp, J. A. Kennea, N. P. M. Kuin, A. Y. Lien, F. E. Marshall, A. Tohuvavohu, M. A. Williams, and Neil Gehrels Swift Observatory Team, "Swift J1913.1+1946 a new bright hard X-ray and optical transient", *GRB Coordinates Network*, vol. 32632, p. 1, 2022.

[402] P. Veres, E. Burns, E. Bissaldi, S. Lesage, O. Roberts, and Fermi GBM Team, "GRB 221009A: Fermi GBM detection of an extraordinarily bright GRB", *GRB Coordinates Network*, vol. 32636, p. 1, 2022.

[403] R. Pillera, E. Bissaldi, N. Omodei, G. La Mura, and F. Longo, "GRB 221009A: Fermi-LAT refined analysis", *The Astronomer's Telegram*, vol. 15656, p. 1, 2022.

[404] Y. Huang, S. Hu, S. Chen, M. Zha, C. Liu, Z. Yao, Z. Cao, and LHAASO experiment, "LHAASO observed GRB 221009A with more than 5000 VHE photons up to around 18 TeV", *GRB Coordinates Network*, vol. 32677, p. 1, 2022.

[405] A. de Ugarte Postigo *et al.*, "GRB 221009A: Redshift from X-shooter/VLT", *GRB Coordinates Network*, vol. 32648, p. 1, 2022.

[406] S. Balaji, M. E. Ramirez-Quezada, J. Silk, and Y. Zhang, "Light scalar explanation for 18 TeV GRB 221009A", *arXiv e-prints*, arXiv:2301.02258, arXiv:2301.02258, 2023. DOI: 10.48550/arXiv.2301.02258. arXiv: 2301.02258 [hep-ph].

[407] IceCube Collaboration, "GRB 221009A: Upper limits from a neutrino search with IceCube", *GRB Coordinates Network*, vol. 32665, p. 1, 2022.

[408] D. D. Dzhappuev *et al.*, "Swift J1913.1+1946/GRB 221009A: detection of a 250-TeV photon-like air shower by Carpet-2", *The Astronomer's Telegram*, vol. 15669, p. 1, 2022.

[409] N. Fraija, M. Gonzalez, and HAWC Collaboration, "Swift J1913.1+1946/GRB 221009A: Galactic sources of > 100 TeV-photon in spatial coincidence with the 250-TeV photon-like air shower reported by Carpet-2", *The Astronomer's Telegram*, vol. 15675, p. 1, 2022.

[410] KM3NeT Collaboration, "GRB 221009A: search for neutrinos with KM3NeT", *GRB Coordinates Network*, vol. 32741, p. 1, 2022.

[411] https://ohwr.org/project/white-rabbit.git.

[412] B. Jung, M. de Jong, P. Fermani, and KM3NeT Collaboration, "PMT gain calibration and monitoring based on highly compressed hit information in KM3NeT", *Journal of Instrumentation*, vol. 16, no. 9, C09011, p. C09011, 2021. DOI: 10.1088/1748-0221/16/09/C09011. arXiv: 2108.11467 [astro-ph.IM].

[413] B. J. Jung and P. Fermani et al. (KM3NeT Collaboration), "PMT gain calibration and monitoring based on highly compressed hit information in KM3NeT", in *37th International Cosmic Ray Conference. 12-23 July 2021. Berlin*, 2022, 1081, p. 1081.

[414] KM3NeT Collaboration, "gSeaGen: The KM3NeT GENIE-based code for neutrino telescopes", *Computer Physics Communications*, vol. 256, 107477, p. 107 477, 2020. DOI: 10.1016/j.cpc.2020.107477. arXiv: 2003.14040 [astro-ph.IM].

[415] D. Bailey, "Monte Carlo tools and analysis methods for understanding the ANTARES experiment and predicting its sensitivity to dark matter", Ph.D. dissertation, Oxford U., 2002.

[416] C. Andreopoulos *et al.*, “The GENIE neutrino Monte Carlo generator”, *Nuclear Instruments and Methods in Physics Research A*, vol. 614, no. 1, pp. 87–104, 2010. DOI: 10.1016/j.nima.2009.12.009. arXiv: 0905.2517 [hep-ph].

[417] C. Distefano, A. Garcia, and P. Kalaczyński, *Gseagen v7.4.0*, version v7.4.0, 2022. DOI: 10.5281/zenodo.7253732. [Online]. Available: https://doi.org/10.5281/zenodo.7253732.

[418] G. Carminati, M. Bazzotti, A. Margiotta, and M. Spurio, “Atmospheric MUons from PArametric formulas: a fast GEnerator for neutrino telescopes (MUPAGE)”, *Computer Physics Communications*, vol. 179, no. 12, pp. 915–923, 2008. DOI: 10.1016/j.cpc.2008.07.01410.48550/arXiv.0802.0562. arXiv: 0802.0562 [physics.ins-det].

[419] E. Scapparone, “HEMAS: a Monte Carlo code for hadronic, electromagnetic and TeV muon components in air shower”, *arXiv e-prints*, physics/9902043, physics/9902043, 1999. arXiv: physics/9902043 [physics.data-an].

[420] A. J. Heijboer, “Track reconstruction and point source searches with Antares”, Ph.D. dissertation, University of Amsterdam, Netherlands, 2004.

[421] ANTARES Collaboration, “A fast algorithm for muon track reconstruction and its application to the ANTARES neutrino telescope”, *Astroparticle Physics*, vol. 34, no. 9, pp. 652–662, 2011. DOI: 10.1016/j.astropartphys.2011.01.003. arXiv: 1105.4116 [astro-ph.IM].

[422] ANTARES Collaboration, “Muon energy reconstruction in the ANTARES detector”, *Nuclear Instruments and Methods in Physics Research A*, vol. 725, pp. 106–109, 2013. DOI: 10.1016/j.nima.2012.12.109.

[423] K. Melis, A. Heijboer, M. De Jong, and KM3NeT Collaboration, “KM3NeT/ARCA Event Reconstruction Algorithms”, in *35th International Cosmic Ray Conference (ICRC2017)*, ser. International Cosmic Ray Conference, vol. 301, 2017, 950, p. 950. DOI: 10.22323/1.301.0950.

[424] K. LEVENBERG, “A method for the solution of certain non-linear problems in least squares”, *Quarterly of Applied Mathematics*, vol. 2, no. 2, pp. 164–168, 1944, ISSN: 0033569X, 15524485. [Online]. Available: http://www.jstor.org/stable/43633451 (visited on 02/02/2023).

[425] D. W. Marquardt, “An algorithm for least-squares estimation of nonlinear parameters”, *Journal of the Society for Industrial and Applied Mathematics*, vol. 11, no. 2, pp. 431–441, 1963. DOI: 10.1137/0111030. eprint: https://doi.org/10.1137/0111030. [Online]. Available: https://doi.org/10.1137/0111030.

[426] ANTARES Collaboration, “An Algorithm for the Reconstruction of Neutrino-induced Showers in the ANTARES Neutrino Telescope”, *AJ*, vol. 154, no. 6, 275, p. 275, 2017. DOI: 10.3847/1538-3881/aa9709.

[427] F. Filippini *et al.*, “Search for neutrino counterpart to the blazar PKS0735+178 potentially associated with IceCube-211208A and Baikal-GVD-211208A with the KM3NeT neutrino detectors.”, *The Astronomer's Telegram*, vol. 15290, p. 1, 2022.

[428] IceCube Collaboration, “IceCube-211208A - IceCube observation of a high-energy neutrino candidate track-like event”, *GRB Coordinates Network*, vol. 31191, p. 1, 2021.

[429] Z. A. Dzhilkibaev, O. Suvorova, and Baikal-GVD Collaboration, “Baikal-GVD observation of a high-energy neutrino candidate event from the blazar PKS 0735+17 at the day of the IceCube-211208A neutrino alert from the same direction”, *The Astronomer's Telegram*, vol. 15112, p. 1, 2021.